Durham University

Durham E-Theses

Computer simulations of large cosmic ray showers using recent models of hadronic collisions

Protheroe, Raymond John

How to cite:

Protheroe, Raymond John (1977) *Computer simulations of large cosmic ray showers using recent models of hadronic collisions*, Durham theses, Durham University. Available at Durham E-Theses Online: http://etheses.dur.ac.uk/8221/

Use policy

The full-text may be used and/or reproduced, and given to third parties in any format or medium, without prior permission or charge, for personal research or study, educational, or not-for-profit purposes provided that:

- a full bibliographic reference is made to the original source
- a link is made to the metadata record in Durham E-Theses
- the full-text is not changed in any way

The full-text must not be sold in any format or medium without the formal permission of the copyright holders.

Please consult the full Durham E-Theses policy for further details.

Academic Support Office, The Palatine Centre, Durham University, Stockton Road, Durham, DH1 3LE
e-mail: e-theses.admin@durham.ac.uk Tel: +44 0191 334 6107
http://etheses.dur.ac.uk

COMPUTER SIMULATIONS OF LARGE COSMIC RAY SHOWERS

USING RECENT MODELS OF HADRONIC COLLISIONS

by

Raymond John Protheroe, B.Sc.

A Thesis submitted to the University of Durham in accordance with the regulations for admittance to the degree of Doctor of Philosophy

The copyright of this thesis rests with the author
No quotation from it should be published without his prior written consent and information derived from it should be acknowledged

Department of Physics
University of Durham

November 1977

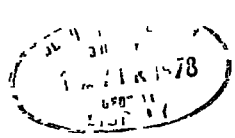

to my parents

ABSTRACT

This thesis is concerned with the computer simulation of large cosmic ray showers. After a general introduction to cosmic rays and extensive air showers (EAS), a review of the nuclear physics and electromagnetic processes relevant to EAS studies is presented.

The method of computer simulation of the hadronic core, electromagnetic cascade, muon component and atmospheric Cerenkov light component of cosmic ray showers is described in detail. Results of the present calculations using Feynman scaling for the momentum distribution of secondary particles in nuclear interactions are given for primary energies ranging from 10^{16} eV to 10^{18} eV.

A novel method of imaging the development of EAS by using information contained in the time structure of Cerenkov light pulses is described. Calculations of the response of experiments designed to detect the isotropic optical emission from EAS are also described, with particular reference to the detection of scattered Cerenkov light.

The results of the present calculations are compared with a broad range of experimental data in an attempt to clarify the implications of the data for particle physics and for the primary mass composition at EAS energies.

CONTENTS

CHAPTER ONE

THE COSMIC RADIATION

INTRODUCTION

The cosmic radiation which continually bombards the Earth's atmosphere from outer space has led, since its discovery over sixty years ago, to a greater understanding of the nature of the universe, both on a microscopic and a gigantic scale. As Heisenberg said in his inaugural lecture to the cosmic ray conference at Munich in 1975 "This cosmic radiation contains information on the behaviour of matter in smallest dimensions and it contributes to our knowledge about the structure of the universe, of the world in the largest dimension."

1-1 THE DISCOVERY OF COSMIC RADIATION AND SUBSEQUENT RESEARCH

Around 1900, an extra-terrestrial radiation was proposed to account for the leakage of charge from an insulated gold leafelectroscope by the ionization of the air in the electroscope. An experiment by C T.R. Wilson (Wilson 1901)) to determine whether the radiation was terrestrial or extra-terrestrial in origin by taking an electroscope underground was inconclusive. It was shown that there was no significant decrease in the electrical leakage underground and so it was assumed that the radiation was of terrestrial origin.

In 1912 Hess (Hess (1912)) made a series of balloon flights to altitudes greater than 5 km and found that, after an initial decrease in the ionization in an electroscope, the intensity of the ionization increased with altitude. This result showed that part of the ionizing radiation was of extra-terrestrial origin and thus marked the beginning of cosmic ray physics. Hess' results were confirmed by

12 APR 1978 LIBRARY

Kolhorster (1914) who made dangerous ascents to an altitude of 9 km. Furthermore, it was found that this radiation was more penetrating than gamma-radiation, the most penetrating radiation then known.

1-1.1 Early experiments

In 1927, the first tracks of cosmic rays were seen in cloud chamber photographs by Skobelzyn (1927) working in Leningrad. In the same year the Geiger-Muller counter (Geiger and Muller (1928)) was invented. Both the cloud chamber and the Geiger-Muller counter were to become very important tools with which many fruitful experiments were performed.

In 1929 Bothe and Kolhorster (Bothe and Kolhorster (1929)) established the corpuscular nature of the radiation by investigating the simultaneous discharge of two Geiger-Muller counters shielded with lead and iron. In 1932 Anderson (Anderson (1932)) discovered tracks of positrons in cloud chamber photographs of cosmic rays. Rossi (1932, 1933) and Anderson and Neddermeyer (1934) showed that the sea level cosmic radiation consisted of a "hard component" which was capable of penetrating 1 m of lead and a "soft component" which cascaded in dense materials and was readily absorbed. In 1934 Bethe and Heitler (Bethe and Heitler (1934)) showed from theoretical arguments that the soft component probably consisted of electrons and concluded that the hard component consisted of more massive particles.

1-1.2 Discovery of mesons

In 1937 Neddermeyer and Anderson (Neddermeyer and Anderson (1937)) proved the existence in the hard component of the cosmic radiation of particles, mesons, with mass intermediate between that of the electron and proton. Rossi, Hilberry and Hoag (1940) pointed out that the hard component of cosmic rays appeared to be absorbed more strongly in air

than in dense media and concluded that the particles were unstable and decayed with a mean lifetime of 2.7 microseconds (this was revised to 2.15 microseconds by Rossi and Nereson (1942) using improved techniques).

In 1940 the first meson decay was observed by Williams and Roberts (1940) in a cloud chamber. Later, Lattes, Occhialini and Powell (1947) observed the decay of a meson into another meson of lower mass in nuclear emulsion and identified the daughter meson as the particle with mean lifetime 2.15 microseconds. They called it the μ-meson and its parent, the π-meson. Brown et al (1949), working with electron sensitive emulsions observed the π-μ-e decay chain. Since the hard component consisted mainly of muons (μ-mesons) and the source of those muons were pions (π-mesons), the mean lifetime of the pion was concluded to be much less than that of the muon.

1-1.3 Discovery of multiparticle production

The discovery by Anderson (1932) of the positron confirmed the existence of a particle-antiparticle conjugation which had been theoretically predicted by Dirac. A consequence of this discovery was that the particle number was no longer a good quantum number, although it was thought that mesons would be produced in pairs in a similar way to the electron-positron pairs of Dirac.

In 1937 Blau and Wambacher (Blau and Wambacher (1937)) discovered possible candidates for multiparticle production in nuclear disintegrations which appeared as "stars" in their photographic emulsions. About 15 years later, multiparticle production was established and many new particles (K^+, K^-, K^o,Λ,$\bar{\Lambda}$,Σ^+ and Ξ^-) were discovered by observing the tracks of particles produced in cosmic ray interactions either in cloud chambers or nuclear emulsions.

1-2 THE COSMIC RADIATION IN THE ATMOSPHERE

A cosmic ray proton entering the atmosphere will collide with air atoms, giving rise to the production of secondary particles, e.g. pions, kaons, etc. After successive collisions the proton will lose energy and disappear from the cascade. The charged pions will either interact with air atoms and produce more secondaries or they will decay into muons but some of the pions may survive to sea level. The muons interact weakly and the majority will survive to sea level but some will decay into electrons. The neutral pions produced in nuclear interactions will decay almost instantly into two gamma-ray photons which will initiate an electromagnetic cascade of electrons, positrons and photons in the atmosphere. In this way, the local cosmic radiation in the atmosphere (consisting mainly of nucleons, pions, muons, electrons and gamma-rays) can be understood. The vertical flux of the important constituents of the local radiation are given in figure 1 as a function of depth in the atmosphere (the constituents of the soft component are shown as dashed lines and the hard component as solid lines).

1-3 THE PRIMARY COSMIC RADIATION

The primary cosmic radiation, the cosmic radiation above the atmosphere, provides us with a direct sample of matter outside the solar system. The radiation consists mainly of protons, alpha-particles, heavier nuclei, gamma-rays and electrons.

1-3.1 Nuclear component up to 10^{12} eV

Figure 2 gives a summary of the primary energy spectra of protons and nuclei up to an energy per nucleon of 10^{12} eV. These spectra were obtained from measurements made using detectors above the Earth's atmosphere in satellites or in balloons at high altitudes. The

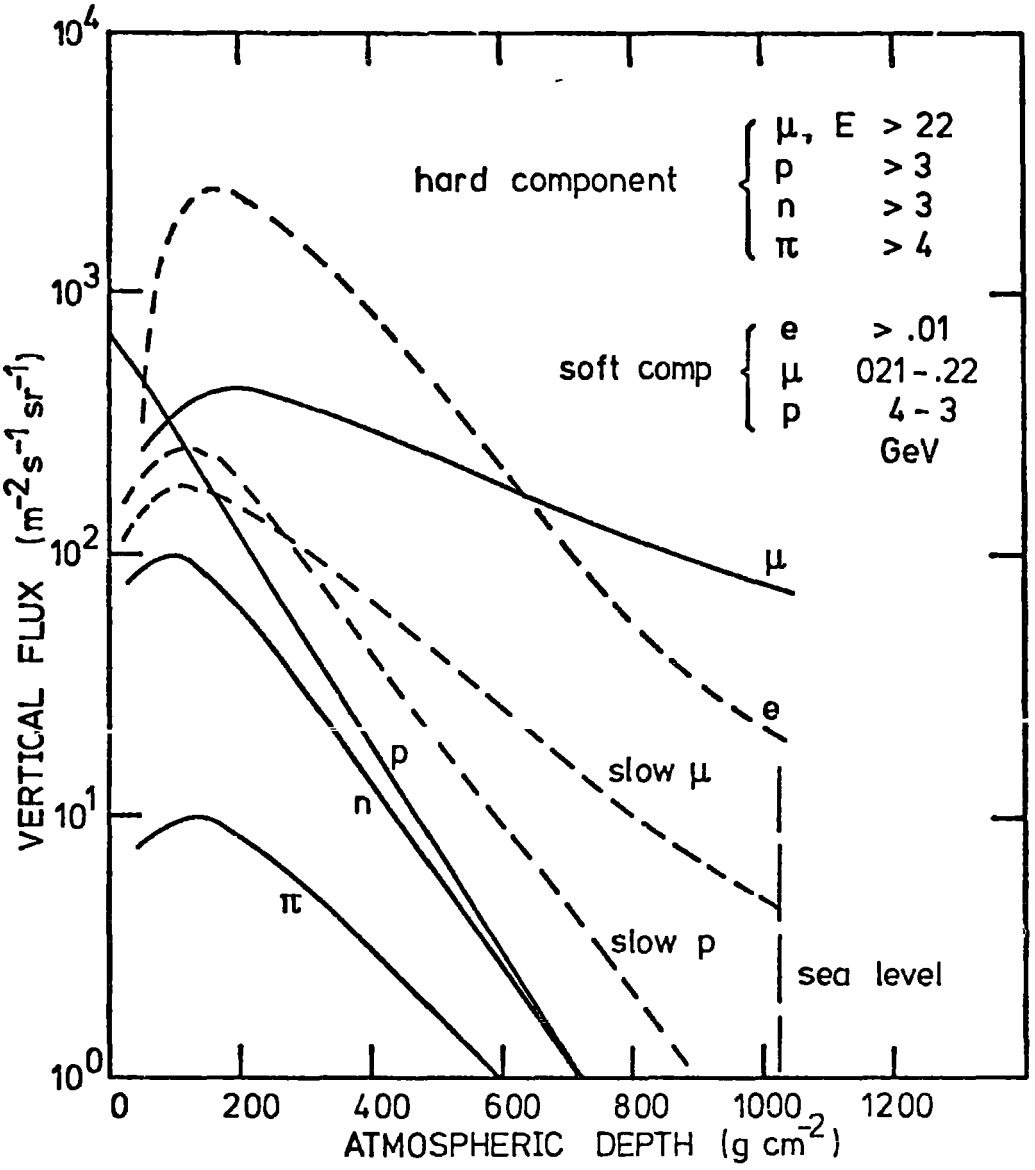

FIGURE 1-1 The components of the radiation in the atmosphere at a geomagnetic latitutde of 45° (from Hillas (1972)).

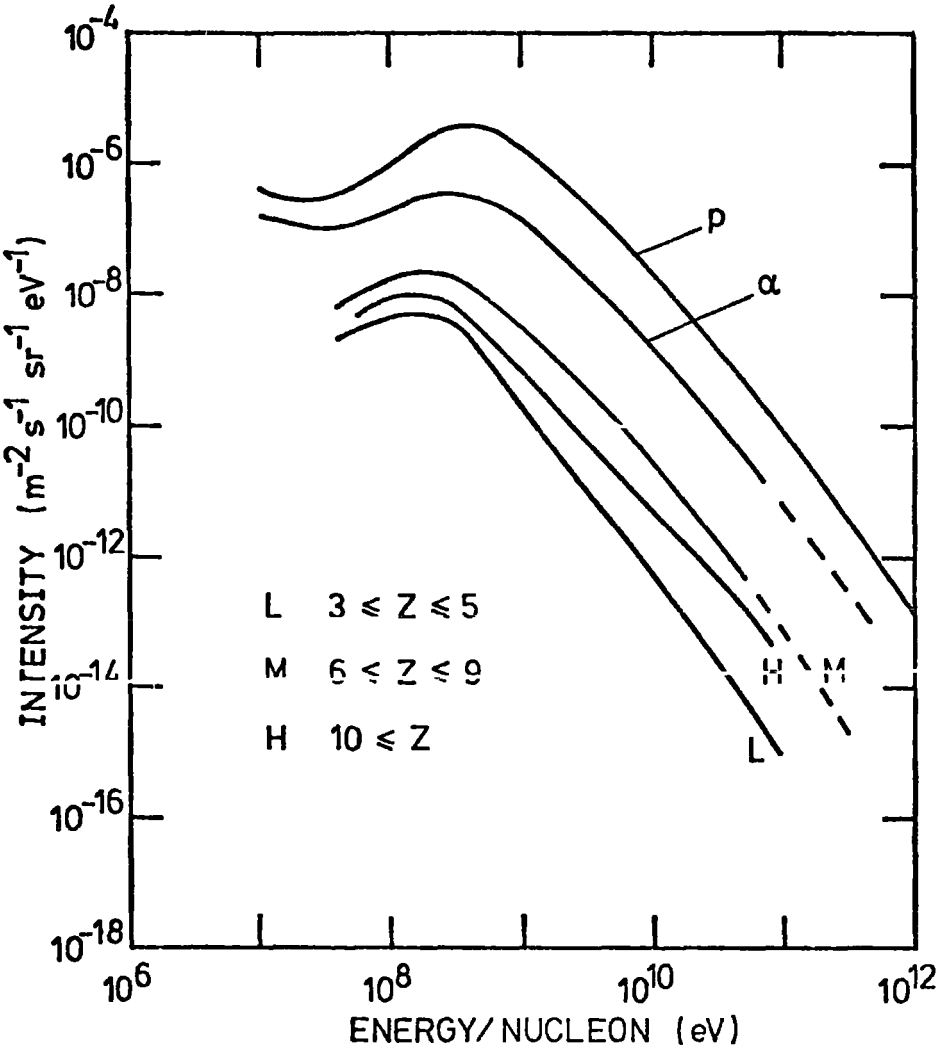

FIGURE 1-2 Summary of measurements on the primary energy spectrum of protons and nuclei (from Wolfendale (1975)).

flattening of the spectrum of heavy nuclei may be due to spallation effects and does not necessarily imply a separate source for this component of the radiation (Orth et al (1977)).

The primary nuclei are thought to be created in the nuclear burning processes of stellar evolution and their chemical composition is thus an important source of information about nucleosynthesis in stars. The observed composition differs from that on production due to the various processes the cosmic rays go through from their production (e.g. spallation). To obtain the source spectrum it is first necessary to know the isotopic composition of the primary radiation as this enables the age of the cosmic rays to be obtained by radioactive dating and may also give information about their propagation through interstellar space.

The composition of the nearby cosmic rays is in fairly good agreement with the "universal abundances", particularly for the elements most prominent in the nuclear burning stages of stars (H, He, C, O, Ne, Mg, Si and Fe) and is thought to indicate that information on the source composition is still present.

1-3.2 Electron component

The existence of an electron component of the primary cosmic radiation was suggested to explain the observation of a continuous spectrum of radio waves from our galaxy. This could be accounted for by synchrotron emission from electrons spiralling in the galactic magnetic field. Direct observation of the electron component, which is of galactic origin, has been made and the energy spectrum is shown in figure 3 which summarizes the main components of the primary radiation.

1-3.3 Cosmic gamma-radiation

Cosmic gamma-rays, being uncharged, are not deflected by the galactic magnetic field and travel directly to us from their source.

They are produced in the various interactions between the primary nuclear component and the fields, photons and matter in space. They thus provide information about the distribution of both the primary nuclear cosmic rays and matter in the galaxy. The primary energy spectrum of the cosmic gamma-radiation obtained from satellite and balloon experiments is shown in figure 3.

1-3.4 Primary radiation at energies greater than 10^{14} eV

The steepness of the primary energy spectrum renders direct observation of the primary radiation above energies of about 10^{12} eV impractical. This is because the flux is low (see figure 3) and detectors required to give a reasonable event rate would be much larger than could be carried by balloons or satellites. It is therefore necessary to measure the energy of the primary radiation indirectly by using the Earth's atmosphere as a detector and observing the resulting extensive air showers (EAS) at ground level.

1-4 EXTENSIVE AIR SHOWERS

The first evidence for showers developing in the air was obtained by Rossi who noticed more simultaneous discharges of Geiger-Muller counters separated by up to 0.4 m than could be accounted for by accidental coincidences. This work was extended by Auger et al (1938) who found simultaneous discharges at separations of up to 300 m. By estimating the density of shower particles for such events they were able to estimate (from considerations of ionization loss in the atmosphere) that the energy of the primary particle must be about 10^{16} eV. Before then, such high primary energies had not been considered.

Extensive air showers were initially thought to consist only of electrons and photons but later Cocconi et al (1946) observed the

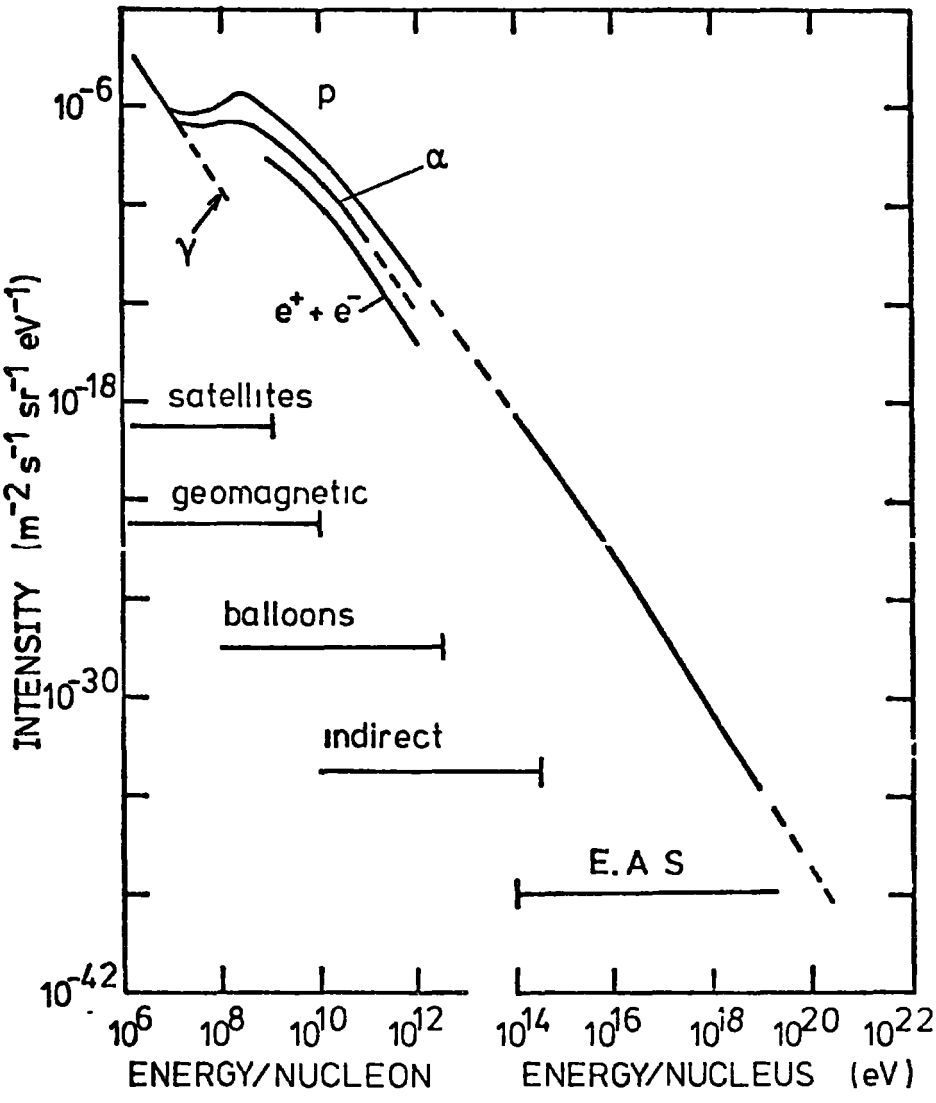

FIGURE 1-3 Summary of measurements of some of the primary components (from Wolfendale (197ɔ)).

presence of a few percent of muons in the shower which were more broadly spread than the electrons and, in addition, it also became evident that the attenuation of the soft component was slower than expected for pure electron-photon cascades. Both these observations suggested that the showers were of nuclear origin and that the hadronic cascade produced the hard component by the decay of pions and continually regenerated the soft component by the production of gamma-rays in nuclear interactions (neutral pions had not then been discovered).

1-4.1 Detection of extensive air showers

The particle formation in an extensive air shower is illustrated in figure 4. In figure 5 the average numbers of pions, muons, electrons and gamma-rays are shown as a function of atmospheric depth calculated for vertical showers from primary protons of energy 10^{15} eV. The lateral distribution of these components at sea level is shown in figure 6 where the particle density is plotted against distance from the air shower core (the point where the primary particle would have hit the ground had it not interacted in the atmosphere). It is noted that the density of electrons, gamma-rays and pions falls off much more rapidly with core distance than the density of muons.

Measurement of the electron and muon components of extensive air showers with ground based particle detectors has enabled the energy spectrum of primary nuclei to be estimated up to energies of 10^{20} eV as shown in figure 3. An extensive air shower array consists of many particle detectors spread in a (usually) regular pattern over a large area (several km^2) of ground. The densities measured by each detector are recorded when the array triggering criterion (usually coincidences in two or more detectors) is satisfied. When the data are analysed, a "contour map" of the shower in the particular component to which the detectors are sensitive is reconstructed from the measured

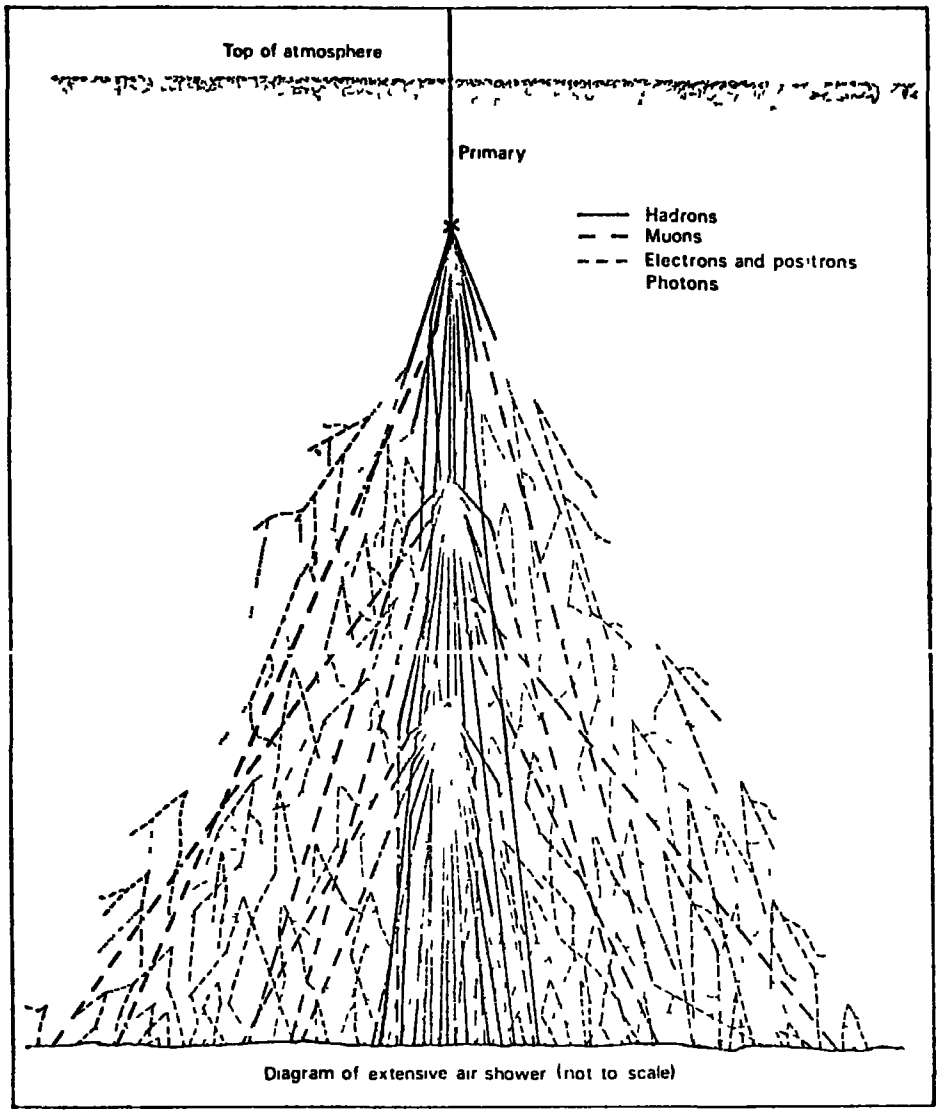

FIGURE 1-4 The particle formation in an extensive air shower (not to scale). From Kellermann (1976)

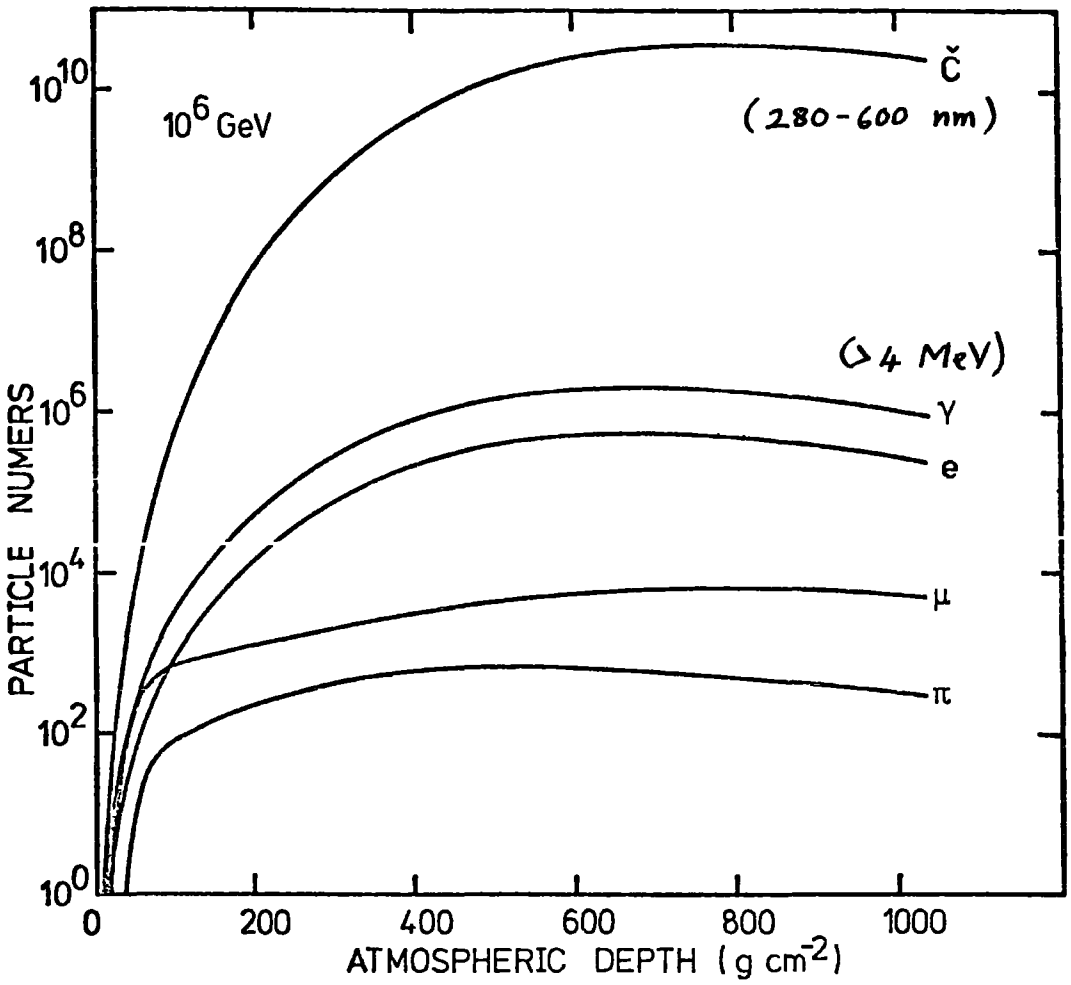

FIGURE 1-5 The average numbers of pions (π), muons (μ), electrons (e) and gamma-rays (γ) as a function of atmospheric depth. The number of Cerenkov light photons ($\check{C}$) is also shown.

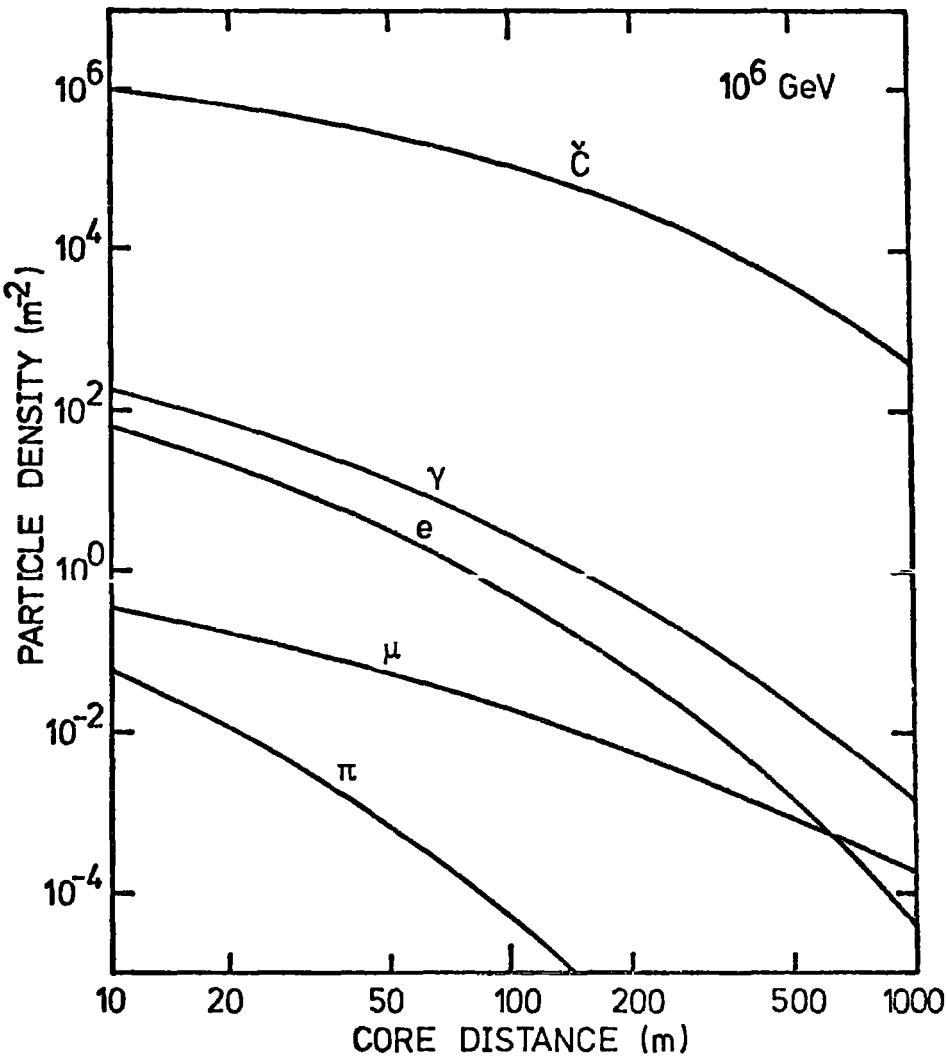

FIGURE 1-6 The lateral distribution at sea level of pions (π), muons (μ), electrons (e), gamma-rays (γ) and Cerenkov light photons ($\check{C}$).

densities. The arrival direction of the shower is obtained by trigonometry from the times at which the detectors recorded the arrival of particles and the position of the core on the ground is found by fitting a structure function to the contour map with the core position as a free parameter but with the core direction as a constraint. The lateral distribution may be integrated to estimate the total number of particles of this component in the shower from which it is possible to estimate the energy of the primary particle. The electron number obtained in this way is used as the primary energy estimator at the Volcano Ranch array, New Mexico, and the muon number is used as the primary energy estimator at the S.U.G.A.R. array, Sydney. The total particle number does vary for showers of the same primary energy which develop at different rates in the atmosphere It has been found from computer simulations that the density of a particular component at a particular core distance may fluctuate less than the total number of particles in this particular component for showers of the same primary energy. At the Haverah Park array, Harrogate, the energy densities recorded by water Cerenkov detectors (sensitive to both the soft and hard components) are interpolated at 500 m and 600 m from the core and these values are used as primary energy estimators.

1-4.2 Optical emission from extensive air showers

High energy electrons in a cosmic ray shower emit Cerenkov light in the air. This radiation may be detected on clear moonless nights and measurement of this component is now popular. The first measurements were made in 1953 by Galbraith and Jelley (Galbraith and Jelley (1953)) soon after they suggested it may be possible to detect Cerenkov light in air showers and since this time, much effort (both theoretical and experimental) has been devoted to the study of Cerenkov light from cosmic ray showers.

The measurement of this component has advantages over the measurement of other components of extensive air showers. The density of optical photons is much higher than the density of electrons or muons (see figure 6) and hence lacks the sampling problems associated with the measurement of these components. Furthermore, much information is contained in the time structure of the Cerenkov light pulse and this has recently been exploited by the Durham group in a new technique to image the development of the electron cascade.

Cosmic ray showers have also been detected through the emission of atmospheric scintillation light. Shower particles excite nitrogen molecules in the air which subsequently emit light on de-excitation. This fluorescence light is emitted isotropically enabling showers to be viewed from any direction. With a suitable set of detectors therefore, the event rate is high as the showers need not hit the detectors and remote showers may be observed.

1-5 COMPUTER SIMULATION OF EXTENSIVE AIR SHOWERS

The role of the computer simulation of large cosmic ray showers is twofold firstly, to provide a design study for future cosmic ray experiments and secondly, to attempt to interpret cosmic ray data in order to obtain information about the primary beam and the nature of ultra-high energy nuclear interactions. To comment about these high energy interactions it is necessary to simulate in detail the propagation of the observed components of showers with various primary masses using plausible models for nuclear processes. Comparison of simulation results with the available cosmic ray data may yield a consistent picture of the gross features of high energy interactions and the primary mass composition.

1-6 THE SCOPE OF THE PRESENT WORK

This thesis is concerned with the computer simulation of cosmic ray extensive air showers. In this chapter an introduction to cosmic radiation in general and to extensive air showers in particular has been given. In chapter 2 a review of the nuclear physics relevant to the present work is given and the computer simulation of the hadron core of an air shower is described. In chapter 3 the interaction of electrons and photons with matter, those aspects of cascade theory relevant to the present work and the computer simulation of the electron-photon component of extensive air showers are described and the results of these simulations of the electron-photon component are given. In chapter 4 simulation of the propagation of pions and muons through the atmosphere is described in detail and results of these simulations of the muon component are given. A detailed account of the computer simulation of atmospheric Cerenkov light in extensive air showers is given in chapter 5. In chapter 6 results of calculations to determine the response of detectors designed to receive the isotropic optical emission from extensive air showers to the nitrogen fluorescence light and the direct and scattered Cerenkov light from air showers are reported. In chapter 7, the results of the computer simulations reported in chapters 3, 4 and 5 are compared with the relevant experimental data and the conclusions drawn from this comparison are given in chapter 8.

CHAPTER TWO

HIGH ENERGY COLLISIONS AND THE HADRON CASCADE IN COSMIC RAY SHOWERS

INTRODUCTION

Simulations of extensive air showers require speculation about the nature of nuclear processes at energies which can never be explored using particle accelerators. Data on nuclear interactions at present accelerator energies ($\lesssim 2 \times 10^3$ GeV) must therefore be extrapolated over several decades in energy. We look to theoretical models describing the nuclear processes to tell us how to make the extrapolation. A number of different hypotheses about the nature of strong interaction processes are able to account for the present accelerator data but give differing predictions at EAS energies.

In this chapter data on inclusive processes in p-p and π-p interactions from accelerator experiments are examined and discussed with reference to the predictions of some important hypotheses. A model based on the above data and the scaling hypothesis is described in detail together with a model based on Landau's hydrodynamical model. The predictions of these two models at EAS energies for the mean multiplicity and the momentum distribution of secondaries in p-p and π-p interactions are compared.

The differences between hadron-nucleon and hadron-nucleus collisions (i.e. the effect on cross sections and multiplicities of target air nuclei) and between nucleon-nucleus and nucleus-nucleus collisions (the case of heavy primary nuclei) are described. In the latter case a description of the breakup of projectile nuclei into fragments and nucleons is included. The incorporation of the above processes into an EAS calculation is outlined. The computer program used in the present work is described and tests of the program are reported.

2-1 KINEMATICS OF MULTIPARTICLE REACTIONS

The momentum 4-vector, p_c, of a particle c is defined by

$$p_c = (E_c, \underline{p}_{c_t}, p_{c_l}) \qquad 1$$

where E_c is the (total) energy of c, $\underline{p}_{c_t}$ its transverse momentum 2-vector and p_{c_l} its longitudinal momentum (throughout this chapter the convention c=1 is used). The 4-momentum of c as seen in a frame moving with velocity v in the longitudinal direction is obtained by Lorentz transformation

$$p_c' = \begin{pmatrix} \gamma & 0 & -v\gamma \\ 0 & 1 & 0 \\ -v\gamma & 0 & \gamma \end{pmatrix} p_c \qquad 2$$

where $\gamma = (1 - v^2)^{-\frac{1}{2}}$.

Consider the inclusive process $a + b \longrightarrow c + X$ (shown schematically in figure 1), where X can be anything and has mass M_x. Useful Lorentz invariant quantities exist, e.g. the centre of momentum energy squared,

$$s = (p_a + p_b)^2 \qquad 3$$

the square of momentum transfer,

$$t = (p_a - p_c)^2 \qquad 4$$

and the missing mass squared,

$$M_x^2 = (p_a + p_b - p_c)^2 \qquad 5$$

Often it is inconvenient to use $\underline{p}_{c_t}$ and p_{c_l} to describe inclusive reactions and other (derived) variables are better suited for this purpose. Some of these are defined in a particular Lorentz frame and are best used for certain physical pictures of the process.

2-1.1 Rapidity

A longitudinal kinematic variable which does not favour any particular frame and is thus of particular value when assessing the

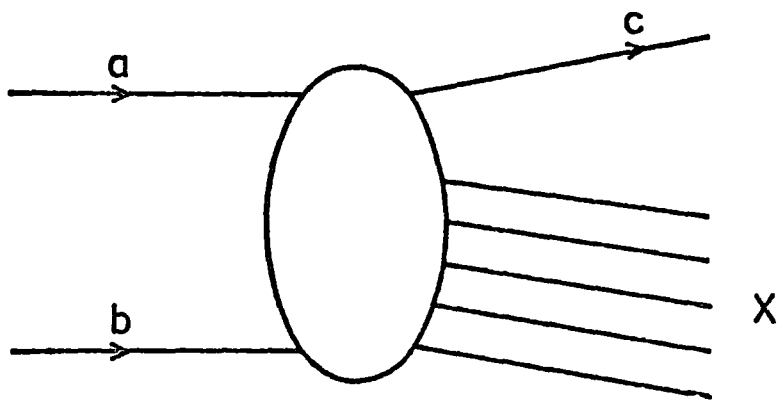

FIGURE 2-1 Schematic representation of the inclusive process $a + b \rightarrow c +$ "anything".

KINEMATIC VARIABLES	INVARIANT CROSS SECTION
p_l , p_t	$\frac{E}{\pi}\frac{d^2\sigma}{dp_l\,dp_t^2}$
x , p_t	$\frac{E^*}{p_m^*}\frac{1}{\pi}\frac{d^2\sigma}{dx\,dp_t^2}$
y , p_t	$\frac{1}{\pi}\frac{d^2\sigma}{dy\,dp_t^2}$

TABLE 2-1 The invariant cross section in terms of three commonly used sets of kinematic variables.

implications of data is rapidity. For the above inclusive process the rapidity of c is defined as,

$$y_c = \tfrac{1}{2} \ln \left\{ \frac{E_c + p_{c_l}}{E_c - p_{c_l}} \right\} = \tfrac{1}{2} \ln \left\{ \frac{1 + v_l}{1 - v_l} \right\} \quad 6$$

where v_l is the longitudinal velocity of c. Also,

$$y_c = \ln \left\{ \frac{E_c + p_{c_l}}{m_{c_t}} \right\} \quad 7$$

where m_{c_t} is the transverse mass of c defined by,

$$m_{c_t} = (m_c^2 + \underline{p}_{c_t}^2)^{\frac{1}{2}}$$

hence the 4-momentum of c in terms of rapidity and transverse mass is,

$$p_c = (m_{c_t} \cosh y_c, \underline{p}_{c_t}, m_{c_t} \sinh y_c) \quad 8$$

Under Lorentz transformation to a frame moving with velocity u along the longitudinal direction the rapidity becomes,

$$y_c' = y_c - \tfrac{1}{2} \ln \left(\frac{1 + u}{1 - u} \right) \quad 9$$

i.e. Lorentz transformation is achieved simply by subtracting the rapidity of the second frame relative to the first, ensuring that the shape of distributions plotted against rapidity is independent of choice of frame of reference.

The maximum and minimum possible longitudinal momenta in the C M system (achieved when $M_x \to 0$) are,

$$p_{c_l}{}^*_{\substack{\max \\ \min}} = \pm \tfrac{1}{2} s^{\frac{1}{2}} \quad 10$$

(where * is used to indicate C M system),

hence,

$$y_c{}^*_{\substack{\max \\ \min}} = \pm \tfrac{1}{2} \ln \left\{ \frac{s}{m_{c_t}^2} \right\} \quad 11$$

thus the length in rapidity of the kinematically allowed region (the maximum rapidity gap) is,

$$Y = (y_{c_{max}} - y_{c_{min}}) = \ln \left\{ \frac{s}{m_{c_t}^2} \right\} \quad 12$$

which depends only on s and the transverse mass of the produced particle c.

2-1.2 Feynman x

An alternative longitudinal kinematic variable used by Feynman (1969) is x defined by,

$$x = \frac{p_{c_l}^*}{p_{c^*_{max}}} \rightarrow 2\, p_{c_l}^*\, s^{-\frac{1}{2}} \qquad 13$$

In the C M system x is thus the reduced longitudinal momentum and ranges from -1 to +1. In EAS calculations where the cascade is considered in the LAB system it is useful to relate x to LAB variables

$$x = 2\, s^{-\frac{1}{2}} \gamma (p_{c_l} - v\, E_c) \qquad 14$$

where, $\gamma = s^{-\frac{1}{2}}(E_a + m_b)$

and $v = p_{a_l}\,(E_a + m_b)^{-1}$

$$\therefore \quad x = \frac{2}{s}\,(E_a + m_b)\, p_{c_l} - \frac{2}{s}\, p_{a_l}\, E_c \qquad 15$$

At high energies $(E_a \gg m_{a,b})$

$$s \rightarrow 2\, m_b\, p_{a_l}$$

$$\therefore \quad x \approx p_{c_l} m_b^{-1} + p_{c_l} E_a^{-1} - E_c\, m_b^{-1}$$

$$= \frac{(E_c^2 - m_{c_t}^2)^{\frac{1}{2}}}{E_a} - \frac{E_c - p_{c_l}}{m_b}$$

$$= \left(\frac{E_c}{E_a} - \tfrac{1}{2}\,\frac{m_{c_t}^2}{E_c^2}\,\frac{E_c}{E_a} + \ldots\right) - \frac{m_{c_t}^2}{(E_c + p_{c_l})\, m_b}$$

$$\therefore \quad x \approx \frac{E_c}{E_a} - \frac{m_{c_t}^2}{(E_c + p_{c_l})\, m_b} \qquad 16$$

At non low X_{lab} $(E_c \gg m_{c_t})$,

$$x \approx X_{lab} - \frac{m_{c_t}^2}{2\, m_b\, E_a\, X_{lab}} \qquad 17$$

where $X_{lab} = E_c/E_a$.

2-1.3 Single particle inclusive cross section

The momentum distribution of particles of type c which is measured, $\frac{d^3\sigma}{d^3 p_c}$ (being the probability per unit incident flux that a particle of type c is produced in the phase space element d^3p_c) is dependent on the measurement frame. The invariance of d^3p_c/E_c enables an invariant differential cross section to be defined

$$f_{ab}^{c}(\underline{p}_c, s) = E_c \frac{d^3\sigma}{d^3 p_c} \qquad 18$$

The invariant cross section in terms the variables described in the previous section is given in table 1.

The mean multiplicity of particles of type c is obtained from the invariant cross section

$$\langle n_c \rangle = \frac{1}{\sigma^{inel}} \int f_{ab}^{c}(\underline{p}_c, s) \frac{d^3 p_c}{E_c} \qquad 19$$

and conservation of energy requires that

$$\sum_c \int f_{ab}^{c}(\underline{p}_c, s)\, d^3 p_c = \sigma^{inel}\, s^{\frac{1}{2}} \qquad 20$$

Since the transverse momentum of particles produced in strong interactions is limited it is useful to integrate f_{ab}^{c} over transverse momentum and derive an energy weighted number distribution (see e.g. Gaisser (1974))

$$F_{ac}(p_{c_l}, s) = \frac{\pi}{\sigma^{inel}} \int f_{ab}^{c}(\underline{p}_c, s)\, dp_{c_t}^2 \qquad 21$$

$$= E_c \frac{dN_c}{dE_c}$$

2-2 PHENOMENOLOGY OF HIGH ENERGY HADRONIC INTERACTIONS

A great wealth of information on high energy hadronic interactions has become available over the past few years from experiments performed at the intersecting storage rings (ISR) at CERN, Geneva, Switzerland ($\leq$ 2000 GeV) and at the proton synchrotron (PS) at Fermilab, Batavia, U.S.A. ($\leq$ 400 GeV). Prior to the commissioning of these accelerators the highest energy attained was $\sim$70 GeV at the Serpukov accelerator near Moscow, U.S.S R. At these high energies the mean number of produced particles is large rendering a complete (exclusive) description of the final state of the interaction impracticable. Experiments to study inclusive processes are therefore usually performed. The zero-particle inclusive process (a + b $\rightarrow$ anything) and the one-particle inclusive process (a + b $\rightarrow$ c + anything) are perhaps the most useful to study.

2-2.1 Hadron - nucleon total cross sections

A survey of the high energy behaviour of the total cross sections of K^+, K^-, π^+, π^-, p and $\bar{p}$ on protons at LAB momenta up to $\sim$300 GeV/c, and in the case of p-p up to $\sim$2000 GeV/c, is given in figure 2. The rise in p-p total cross section with energy observed at the ISR was anticipated from the comparison of measurements of the cosmic ray unaccompanied hadron spectra at different mountain altitudes by Yodh et al (1972). A number of fits to the data using a variety of models have been made (see e.g. Diddens (1974)) and some of these will be discussed later.

2-2.2 Mean multiplicity of different charged particles in p-p interactions

Data on the mean number of charged particles produced in p-p interactions up to ISR energies are shown in figure 3 (reproduced from Antinucci et al (1973)) where the contributions from pion, kaon and nucleon production are given. The best fit to the mean charged

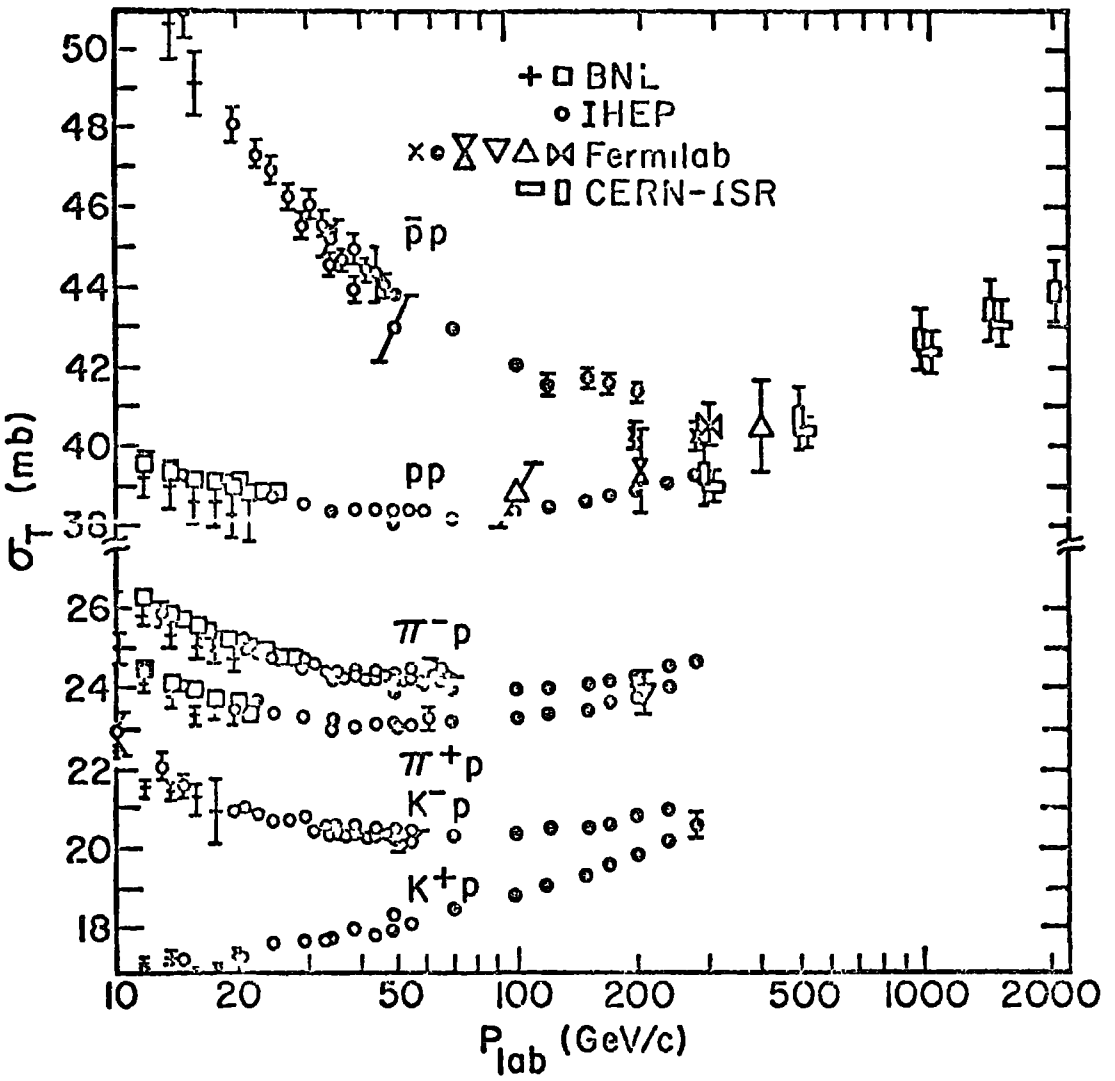

FIGURE 2-2 A survey of the high energy behaviour of the total cross sections for hadron-proton interactions.

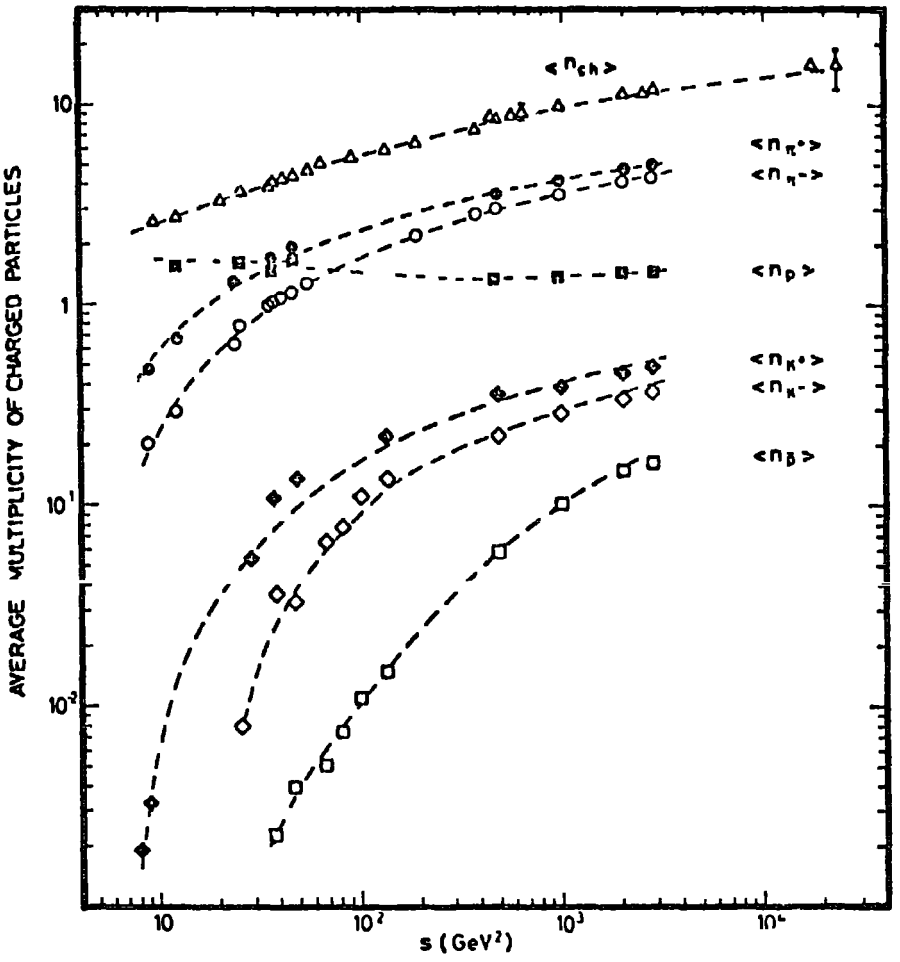

FIGURE 2-3 The energy dependence of the mean number of various types of charged particles produced in proton-proton collisions.

multiplicity is given by Antinucci et al (1973) as,

$$\langle n_{ch} \rangle = (-3.8 \pm 0.4) + (1.88 \pm 0.07) \ln s + (6.4 \pm 0.7) s^{-\frac{1}{2}} \quad 23$$

with s in GeV^2.

2-2.3 Limited transverse momentum

The invariant cross section is observed to fall off rapidly with increasing transverse momentum as illustrated in figure 4 where the invariant cross section for the reaction $p + p \rightarrow \pi^+ + X$ given by Albrow et al (1974) is plotted against p_t for two values of x. The mean transverse momentum is small, $\langle p_t \rangle \sim 0.33$ GeV/c for pions and 0.4 - 0.5 GeV/c for kaons and nucleons. $\langle p_t \rangle$ is not independent of longitudinal momentum (notice the fall off is steeper for the x=0.8 data than for the x=0.5 data shown in figure 4) and when plotted against x there is a dip in $\langle p_t \rangle$ at x=0 making the data points cluster resembling a sea-gull in flight - hence this effect is called the "sea-gull effect". If instead $\langle p_t \rangle$ is plotted against rapidity the data show a monotonic decrease away from y*=0 showing the sea-gull effect to be due to artificial kinematic constraints (see Bosetti et al (1973)).

2-2.4 Longitudinal momentum distributions

Whereas for all types of produced particles transverse momentum is limited and essentially similar, there are important differences in the distributions in longitudinal momentum, p_l, between types of produced particles depending on the nature of the beam and target particles. The p_l distribution is perhaps best illustrated by plotting the invariant cross section integrated over transverse momentum space at fixed x (or y) and plotting against x (or y). This has been done for the reaction $p + p \longrightarrow \pi^+ + X$ in figure 5 for $x \geq 0$ using low energy data from DESY (Blobel et al (1974), $s^{\frac{1}{2}}=7$ GeV) and ISR data (Alper et al (1975), Capiluppi et al (1974) and Albrow et al (1974)) where

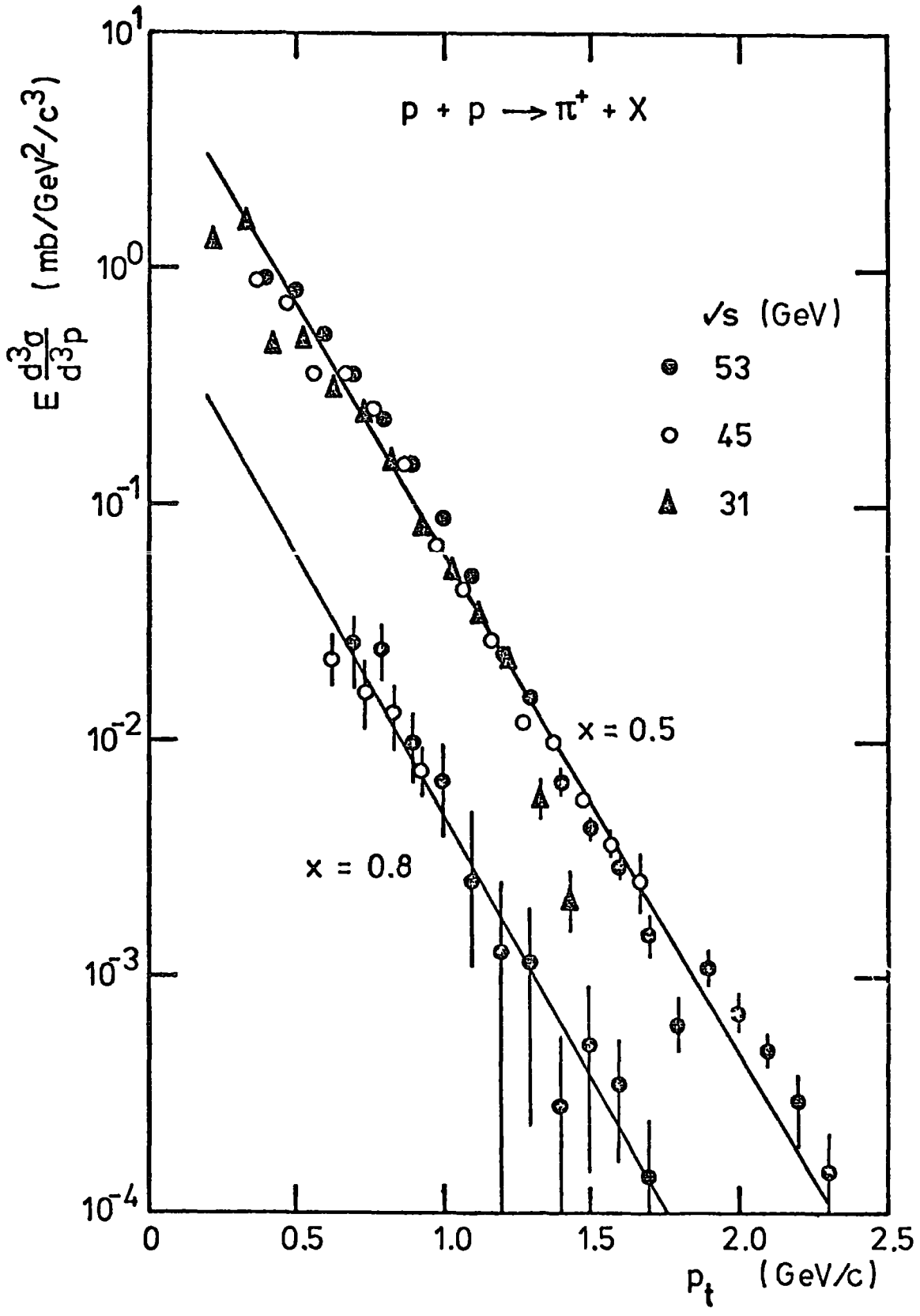

FIGURE 2-4 The invariant cross section for $p+p \rightarrow \pi^+ + X$ from the data of Albrow et al (1974) plotted against transverse momentum.

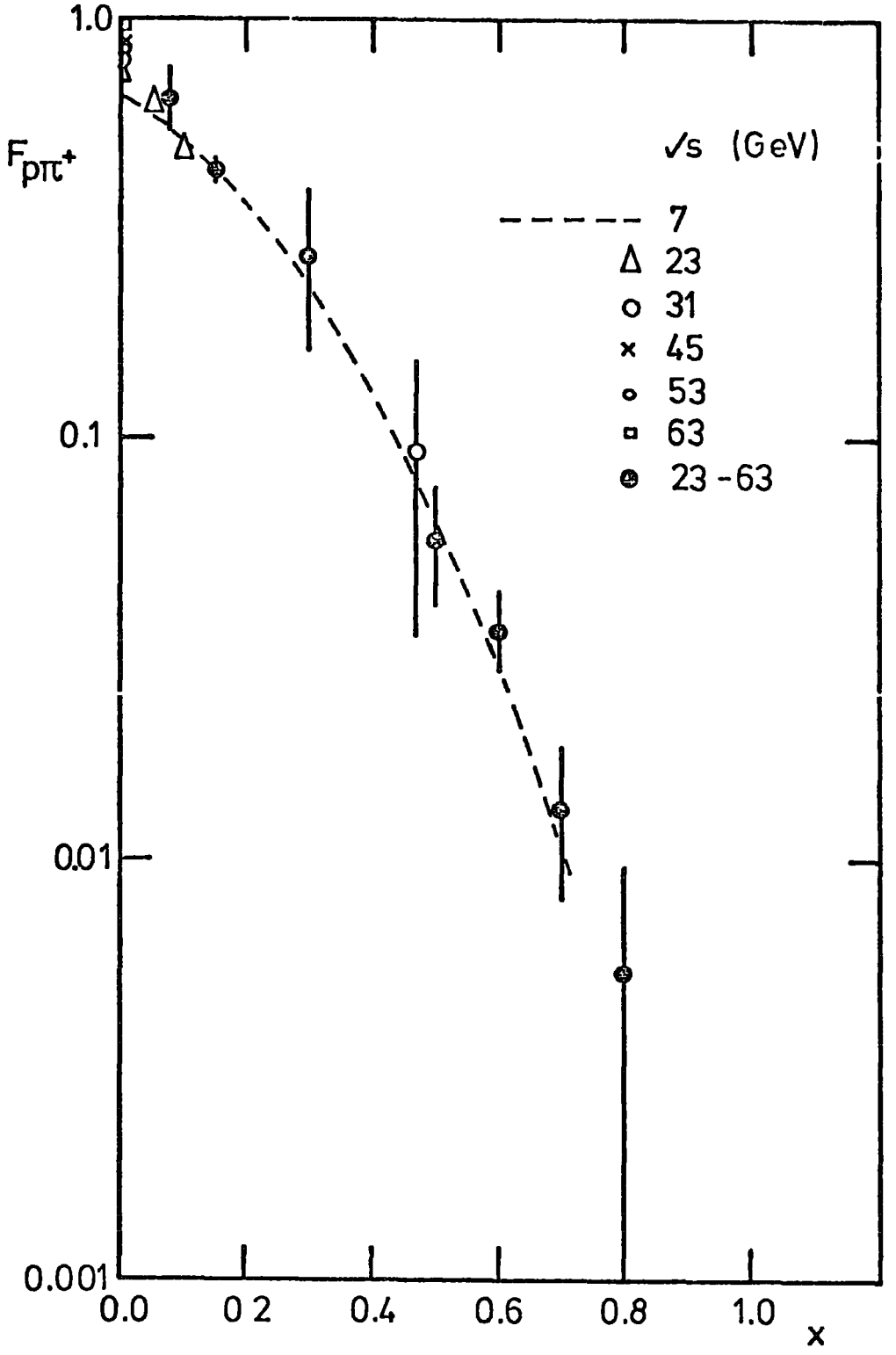

FIGURE 2-5 The invariant cross section for $p+p \rightarrow \pi^+ + X$ integrated over transverse momentum (and normalised to the total inelastic cross section) is plotted against x. The sources of the data are given in section 2-2.4.

it is noted that data from experiments with different beam energies appear to lie on a common curve, indicative of scaling to be discussed later.

Data from experiments at Fermilab presented in a similar form (although not normalized to σ^{inel}) for the reactions $\pi^- + p \rightarrow \pi^- + X$ and $\pi^+ + p \rightarrow \pi^+ + X$ are compiled in figure 6(a) (taken from Whitmore (1976)) which shows a distinct peak at $x \approx 1$ for both distributions. This peak which is not present in figure 5 is due to diffractive excitation of the target proton. In contrast distributions given in figure 6(b) (again from Whitmore (1976)) for the reactions $\pi^- + p \rightarrow \pi^+ + X$ and $\pi^+ + p \rightarrow \pi^- + X$ (i.e. the production of beam-unlike pions) show no such peak. As with the p-p data the shapes of the distributions are approximately independent of energy.

2-3 LIMITING FRAGMENTATION, SCALING AND CORRELATION LENGTH HYPOTHESES

Scaling hypotheses have a long history going back to the pioneering work of Amati et al (1962) and Wilson (1963) and being restated by Feynman (1969) ("Feynman scaling hypothesis") and Benecke et al (1969) ("hypothesis of limiting fragmentation").

2-3.1 Limiting fragmentation

The LAB frame and the projectile rest frame are preferred by Benecke, Chou, Yang and Yen (BCYY) for a description of high energy collisions because, they believe, that in these systems some of the outgoing particles aporoached limiting distributions, i.e. for fragments of the target

$$f(\underline{p}^{lab},s) \longrightarrow f(\underline{p}^{lab}) \qquad 25$$

and for fragments of the projectile

$$f(\underline{p}^{proj},s) \longrightarrow f(\underline{p}^{proj}). \qquad 26$$

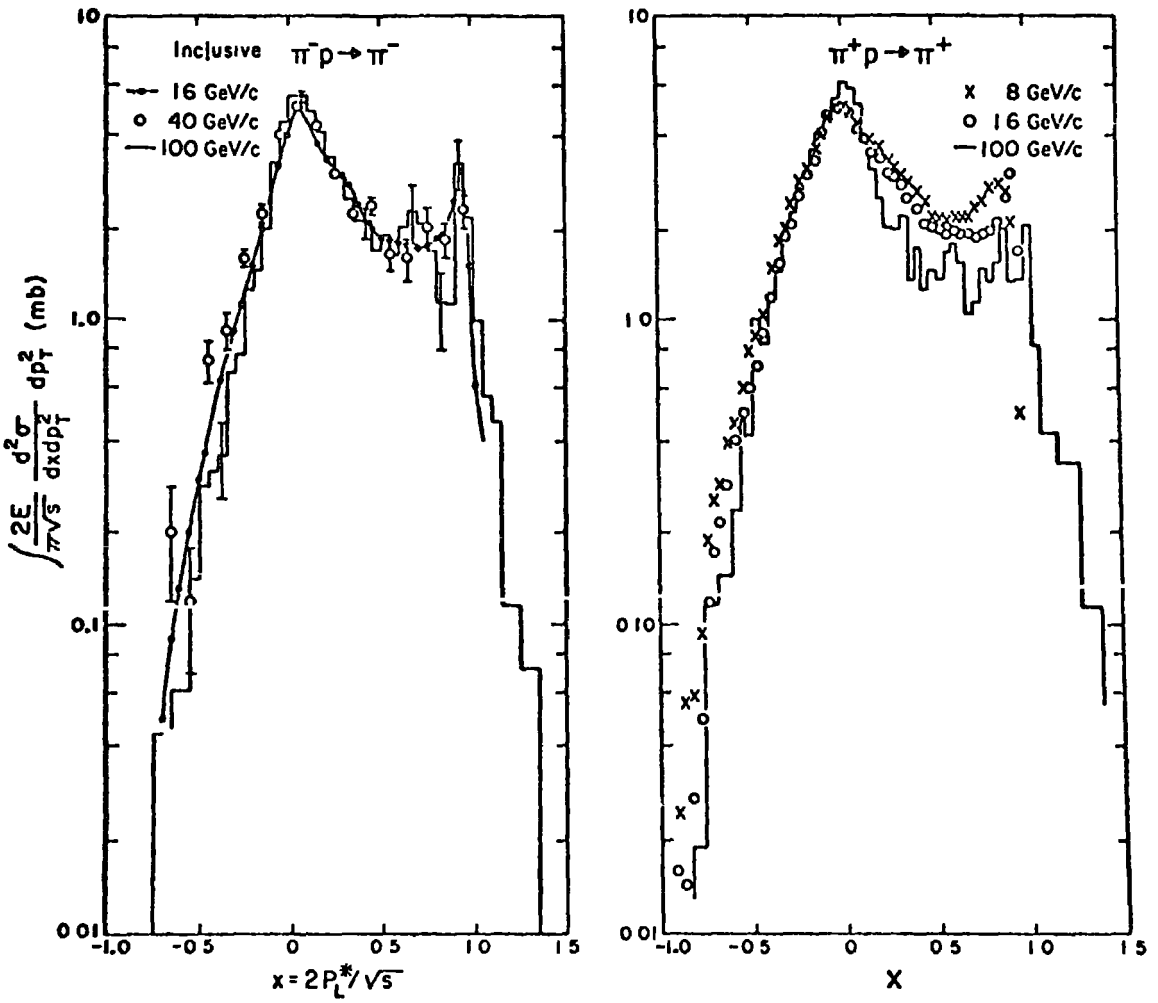

FIGURE 2-6(a) A survey of data on the inclusive cross sections for $\pi^- + p \to \pi^- + X$ and $\pi^+ + p \to \pi^+ + X$ given by Whitmore (1976).

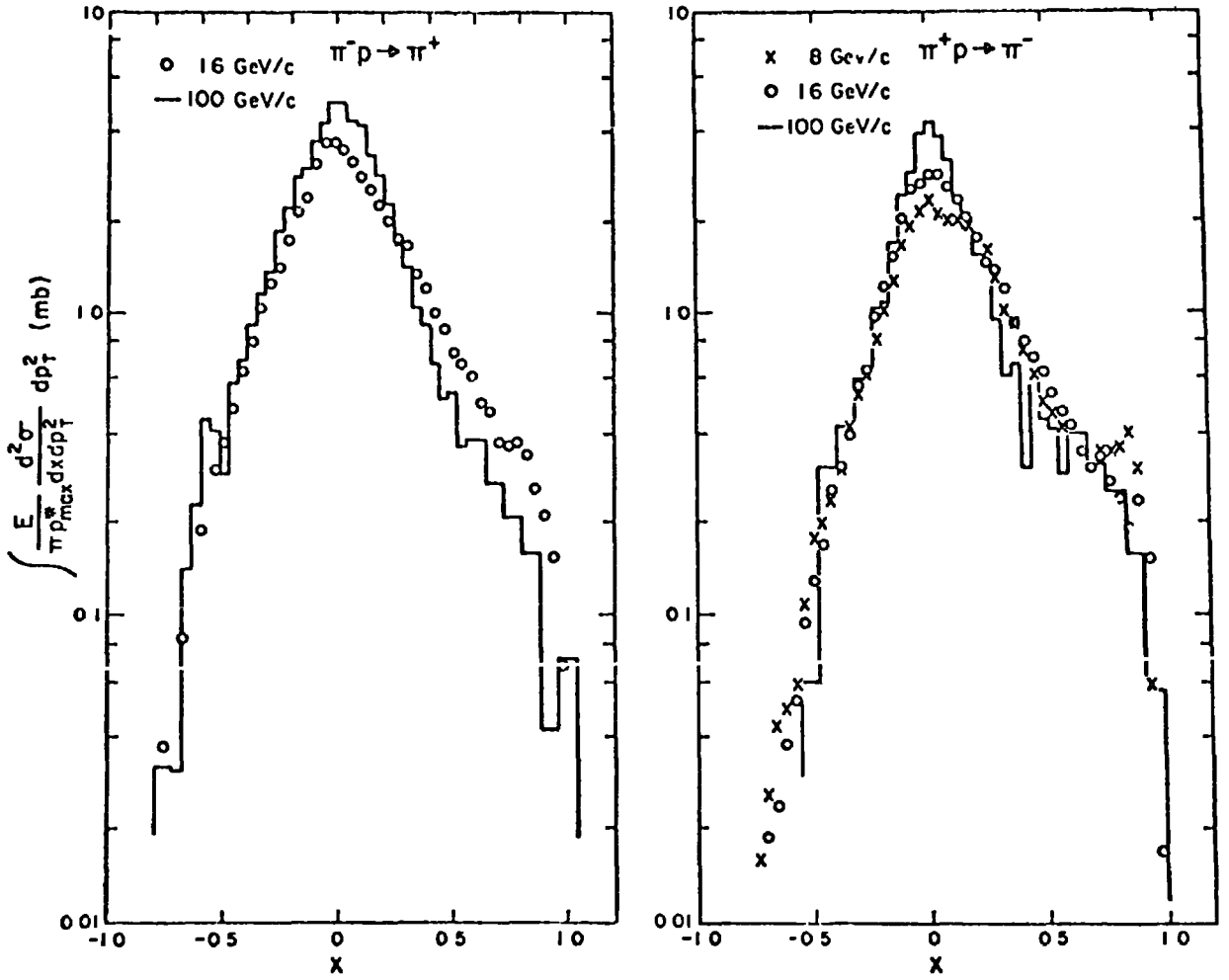

FIGURE 2-6(b) A survey of data on the inclusive cross sections for $\pi^- + p \rightarrow \pi^+ + X$ and $\pi^+ + p \rightarrow \pi^- + X$ given by Whitmore (1976).

These distributions represent distributions of broken-up fragments of the target and projectile and in the case of very high energies form a complete description of the inclusive process, there being no pionization process in their picture illustrated in figure 7(a), taken from Morrison (1973).

BCYY give a droplet picture to illustrate this process. At high energies the projectile is Lorentz contracted to a disc and so, at even higher energies the projectile looks essentially the same to the target. Furthermore, the time of passage of the projectile disc through the target $\sim$(proton size)/c is independent of energy in this simple picture at high energies with the expectation that the excitation and breakup of the target approaches a limiting distribution.

2-3.2 Scaling

Feynman's hypothesis,

$$f_{ab}^{c}(\underline{p}_c, s) \longrightarrow f_{ab}^{c}(x, p_{c_t}^{2}) \qquad 27$$

which is based on a bremstrahlung - parton picture goes further than the hypothesis of limiting fragmentation in that the distribution is predicted to scale in the "central region" (i.e. about x=0) in addition to the projectile and target "fragmentation regions" ($x \approx \pm 1$). These ideas are shown schematically in figure 7(b), also taken from Morrison (1973). Two important consequences of this hypothesis are firstly, the inelastic cross section $\sigma^{ab \to cX}$ should approach a constant value (when s is sufficiently large that thresholds for production of particles are exceeded) and secondly, the multiplicity of particles of type c, $\langle n_c \rangle$, should rise as ln s.

2-3.3 Correlation length hypothesis

This hypothesis (see Frazer et al (1972) for discussion) which has been abstracted from multiperipheral models provides a simple

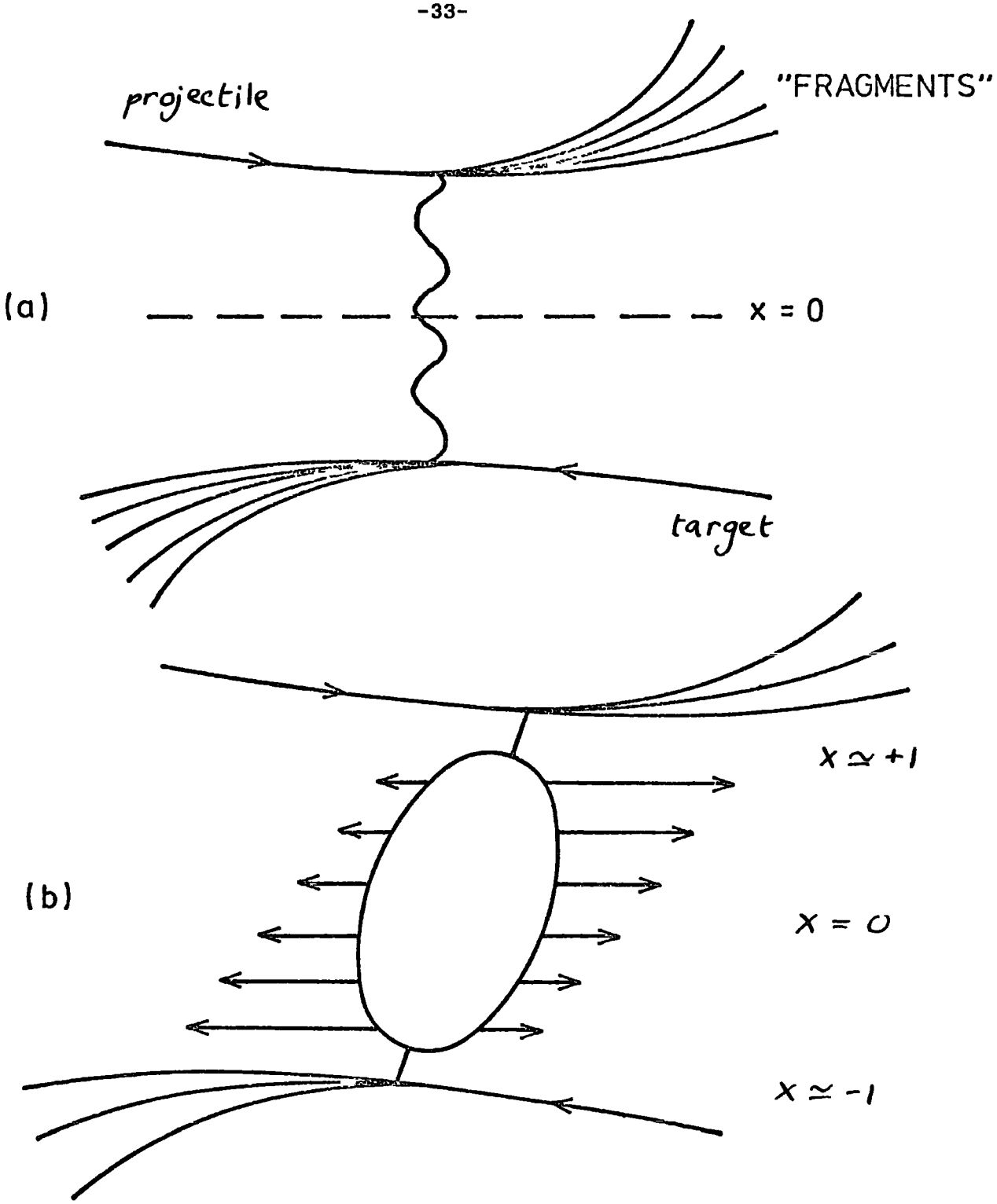

FIGURE 2-7 Schematic representations of a) limiting fragmentation, and b) scaling.

motivation for scaling by invoking short range order in longitudinal momenta. The hypothesis states that there is no correlation between particles separated in rapidity space by a distance large compared to a "correlation length" L. This suggests a natural division of rapidity distributions at high energies into the three regions discussed earlier.

i) target fragmentation region $y < L$

ii) central region $L < y < (Y - L)$

iii) projectile fragmentation region $(Y - L) < y$.

It also suggests that as the energy is increased the behaviour of the rapidity distribution will change. At low energies ($Y \lesssim L$) particles are correlated with both target and projectile. As the energy is increased and $Y \gg L$, particles at opposite ends of the spectrum become uncorrelated and limiting fragmentation is expected. When $Y \gg 2L$ the central part of the distribution is uncorrelated with either fragmentation region and a uniform distribution (the plateau) is expected, in agreement with the scaling hypothesis. Theoretical arguments and data on low energy resonances suggest $L \approx 2$.

2-4 THE SCALING MODEL USED IN THE PRESENT WORK

The model for particle production in pion-nucleon and nucleon-nucleon interactions used in the present work is based on that described by Gaisser (1974). Nuclear target effects are small and have been neglected as discussed later. Kaon production and $N\bar{N}$ production are neglected, the energy instead going into pion production. These simplifications are not unreasonable (except for calculations of hadron spectra and muon charge ratios in EAS which are not undertaken here) since kaon production is low (~10% of pion production), kaon initiated interactions are similar to those of pions and 64% of charged

kaons have decay modes similar to those of charged pions. If $\bar{N}N$ production becomes large at EAS energies its inclusion will be necessary but the data indicate ~3% of the interaction energy goes into $\bar{N}N$ production at high energies (Gaisser and Maurer (1973)). No distinction is made between protons and neutrons (nucleons, N) or between π^+ and π^- (charged pions, π^c)

The distribution of fragment nucleons in N-N interactions is approximated by

$$F_{NN}(x) = x \qquad 28$$

corresponding to a nucleon elasticity of 0.5. This approximation has been found to make little difference to cascade development when compared to that obtained using a more realistic distribution (see figure 8).

The distributions of charged pions produced in N-N and π-N interactions,

$$F_{N\pi^c} \approx (F_{p\pi^+} + F_{p\pi^-}) \qquad 29$$

and

$$F_{\pi^c\pi^c} = \tfrac{1}{2}(F_{\pi^+\pi^+} + F_{\pi^+\pi^-} + F_{\pi^-\pi^+} + F_{\pi^-\pi^-}) \qquad 30$$

have been renormalized up by ~10% to account for kaon production as described by Fishbane et al (1974) and are shown in figures 9 and 10. Neutral pion production is assumed from charge independence to be half that of charged pion production. $F_{\pi^c\pi^c}$ has been decomposed into distributions for a fragment pion and produced pions (see Figure 10) as given by Gaisser (1974).

2-5 NUCLEAR TARGET EFFECTS

The multiplicity of charged particles produced in hadron-nucleus interactions is greater than that for hadron-nucleon interactions due to cascading within the nucleus. The nature of the intra-nuclear cascade is uncertain - see e.g. Fishbane and Trefil (1973) who describe

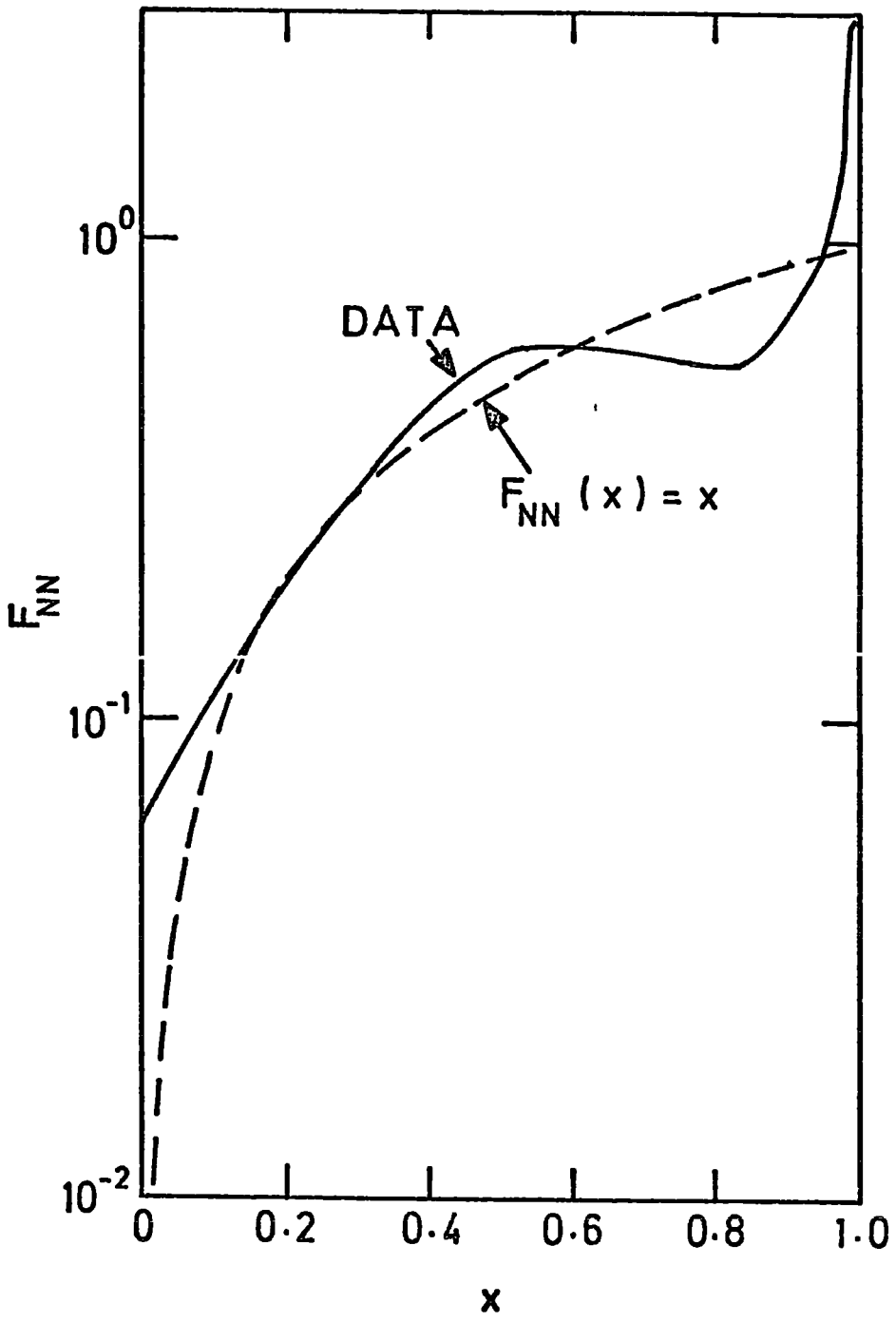

Figure 2-8 The approximate distribution of fragment nucleons, $F_{NN}(x) = x$ is compared to a survey of the experimental data (Gaisser (1974)).

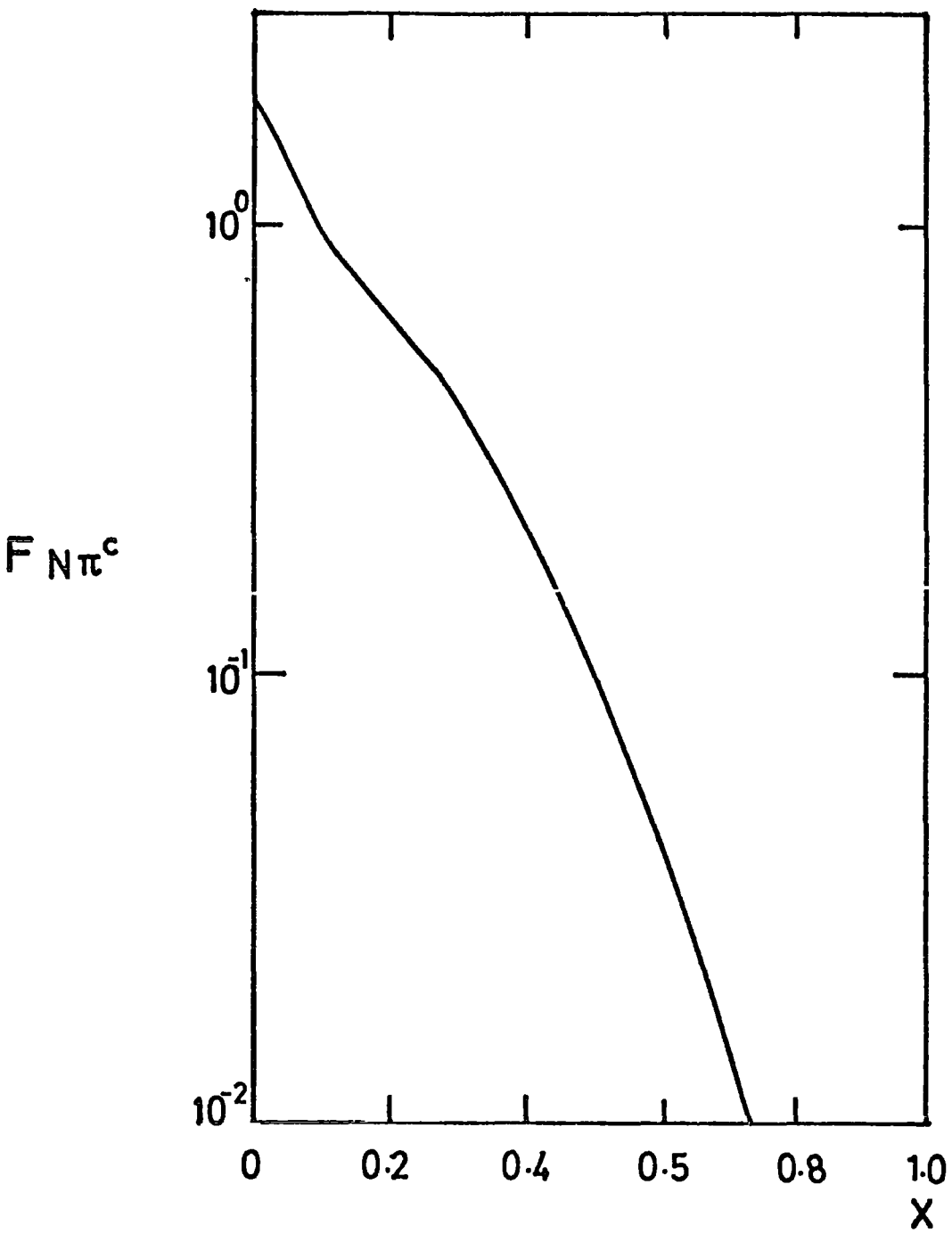

FIGURE 2-9 The distribution of charged pions produced in nucleon-nucleon interactions used in the present calculations.

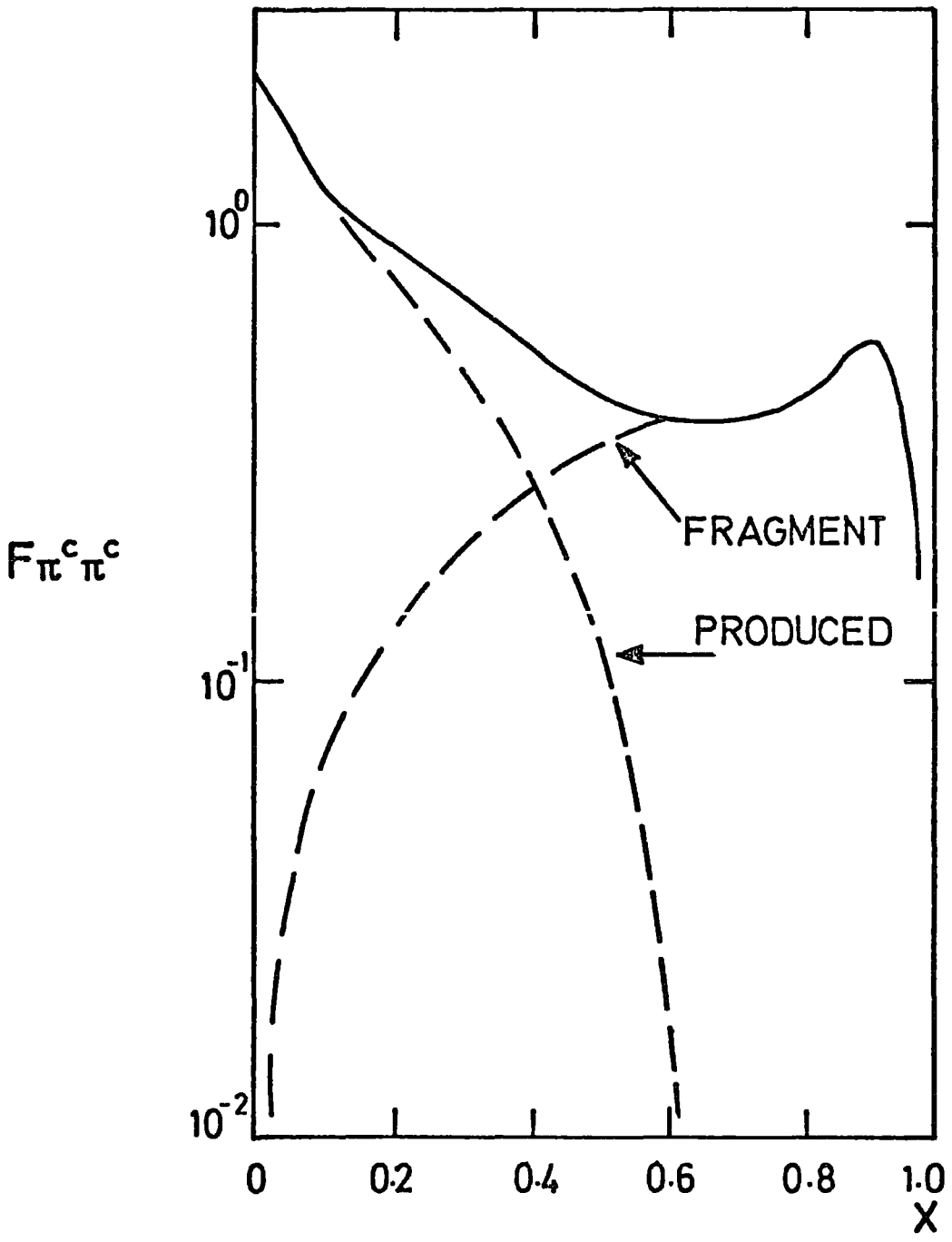

FIGURE 2-10 The distribution of charged pions produced in pion-nucleon interactions used in the present calculations.

coherent production and incoherent production models predicting quite different multiplicities.

Recent experiments at Fermilab by Busza et al (1975) have measured the variation with nuclear size of the number of particles produced in pion-nucleus interactions, $\langle n \rangle_A$, at 100 and 175 GeV/c relative to the number produced in pion-nucleon interactions, $\langle n \rangle_H$, for four angular regions. Their result is shown in figure 11 where $\langle n \rangle_A / \langle n \rangle_H$ is plotted against the average number of absorption mean free paths, $\bar{\nu}$, encountered in the nucleus of mass number A calculated from,

$$\bar{\nu} = A \sigma_{hN} / \sigma_{hA} \qquad 31$$

Their data show that there is no increase in the number of particles produced in the forward direction ($\vartheta_{lab} < 3.5^o$) while at other angles the increase grows slowly with atomic mass and is apparently independent of energy. These authors also point out that their data averaged over all angles are similar tc those from nucleon-nucleus interactions when plotted against $\bar{\nu}$ indicating that the intra-nuclear cascade depends on the absorption cross section of the incident particle and not that of the secondaries. A number of models are able to account for the absence of cascading (e.g. Gottfried (1976), Dar et al (1976), Capella and Krzywicki (1977) and Masuda (1977)) but since cascading is minimal for the light atmospheric nuclei, target effects are ignored in the present work.

2-6 SIMULATIONS OF N-N AND π-N INTERACTIONS

The data of figures 8 - 10 were reduced to a table with elements corresponding to 41 bins of equal width spanning the range of x (-1 — +1). $F_{N\pi^c}$ is symmetrical about x=0 but $F_{\pi^c\pi^c}$ for negative x (near the target nucleon fragmentation region) is similarto $F_{N\pi^c}$ and account was taken of this.

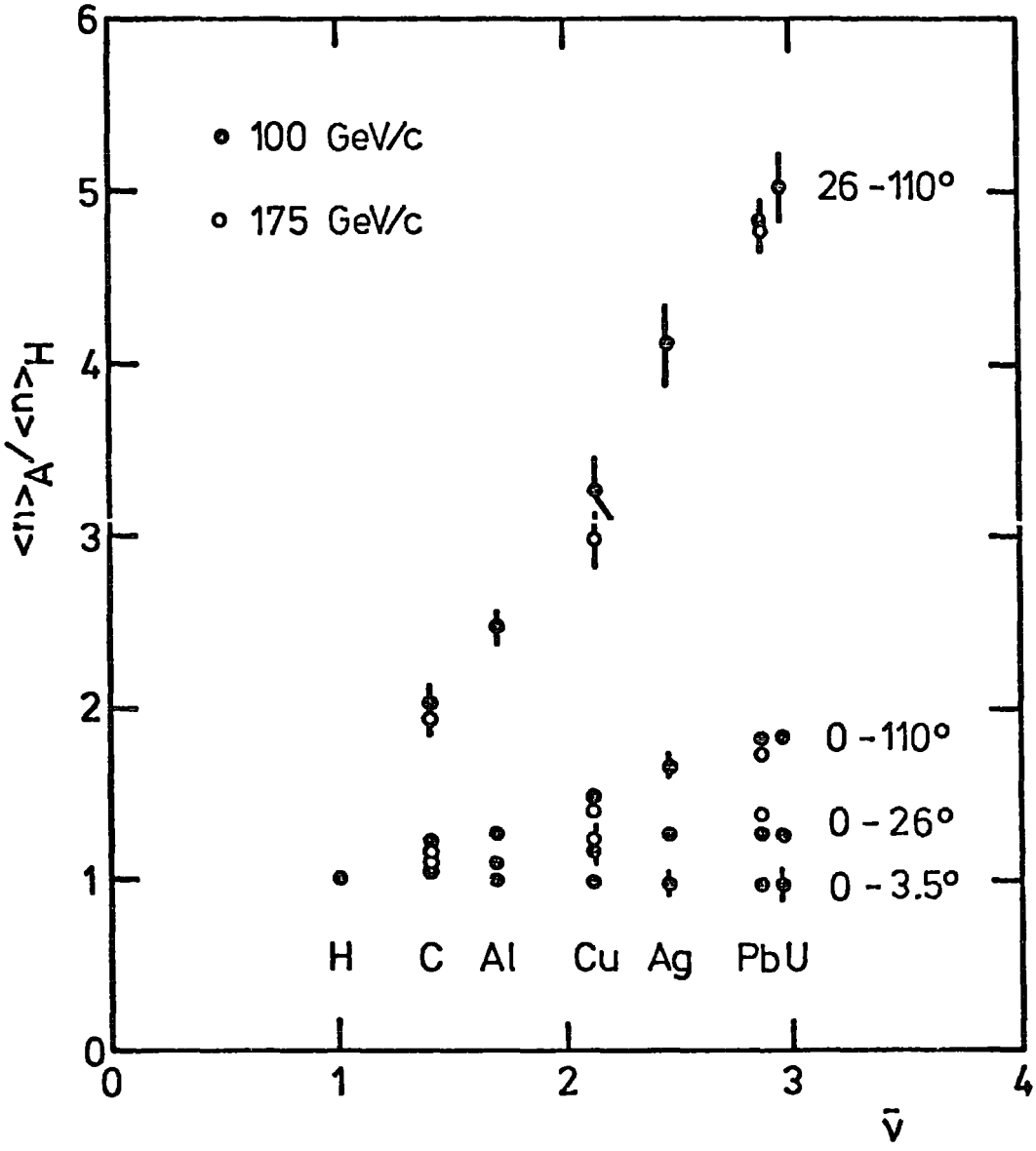

FIGURE 2-11 The number of particles produced in pion-nucleus interactions divided by the number produced in pion-nucleon interactions (from Busza et al (1975)).

Simulation of a N-N interaction was achieved in the LAB frame by first sampling the nucleon elasticity from a uniform distribution (corresponding to $F_{NN}(x) = x$ and a further approximation, $x = X_{lab}$, which holds for leading particles) and second, pions were sampled using $F_{N\pi}^{c}$ (1/3 being randomly chosen as neutral) until the energy remaining for pion production was exhausted.

Sampling of pion LAB energies was carried out in four stages (i) The minimum value of X_{lab} was calculated from

$$X_{min} = \langle m_{\pi_t} \rangle / E_o \qquad 32$$

where E_o is the LAB energy of the incident nucleon. (ii) A possible X_{lab} is then chosen randomly on a logarithmic scale between X_{min} and 1 (this is done since $F(x) = E\frac{dN}{dE} = \frac{dN}{d(\ln E)}$). (iii) The value of (Feynman) x is obtained from X_{lab} using equation 17 and the appropriate value of $F_{N\pi}$ is taken from the table. (iv) A random number is then generated to decide, by comparision with $F_{N\pi}$ whether to accept or reject X_{lab}.

2-6.1 Practical difficulties of sampling

In a simulated interaction where a pion is sampled having more energy than is available, a choice has to be made between giving the sampled pion all the available energy or rejecting the pion altogether. The latter option was used since the distribution obtained by this method was in better agreement with the input distribution. In the full computer program energy conservation was ensured by feeding the remaining energy into the previous interaction (see later).

A related problem is the distortion of the shape of the distribution after energy has been sampled. This arises since a pion is effectively sampled from the distribution from $-1 < x < x_{max}$ where $x_{max} \sim$ energy remaining available for pion production. This effect

is not too serious for $F_{N\pi^c}$ but when pions are sampled directly from $F_{\pi^c\pi^c}$ the distortion is severe as shown in figure 12 since the tendency is to sample first the produced pions (which have higher probability) and then run out of energy before the fragment pion is sampled. In the present work this situation was remedied by independent use of distributions for fragment and produced pions (see figure 10), sampling the fragment pion first. This method is analogous to N-N interactions in which the leading particle, in this case a nucleon, is first sampled from F_{NN}.

2-6.2 Mean multiplicity from sampled events

The mean charged multiplicity obtained from 50 Monte Carlo π-N interactions sampled using $F_{\pi^c\pi^c}$ at given interaction energies are shown in figure 13 where it is compared with the logarithmic multiplicity law obtained from $F_{\pi^c\pi^c}$ (see Appendix A) and with experimental data surveyed by Trilling (1974). At high energies the sampled multiplicity is in excellent agreement with the calculated logarithmic law while at low energies it agrees with the data. This $E^{\frac{1}{4}}$ law approach to the scaling multiplicity at low energies comes naturally from the sampling method used!

2-7 THE COMPUTER PROGRAM FOR NUCLEON INITIATED SHOWERS

The job of this program is to calculate for a vertically incident primary nucleon of given energy the pion production spectrum at 40 levels in the atmosphere. The muon, electron-photon and Cerenkov light components of the shower are calculated from the pion production spectrum by separate programs described in their appropriate chapters. All pions are binned in one of two atmospheric depth/energy arrays (depending on charge) at production. These arrays in the present work

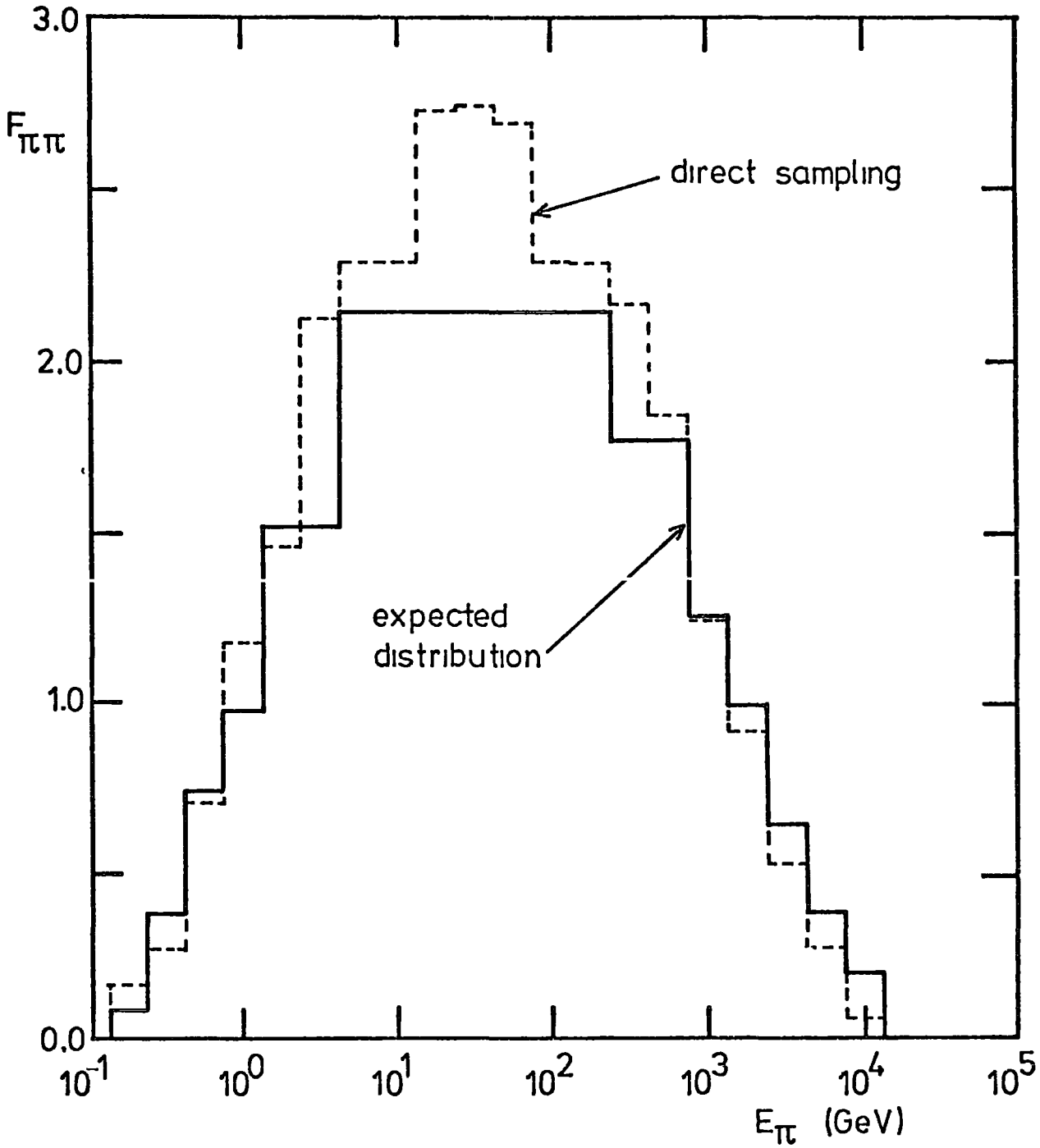

FIGURE 2-12 The distortion in the distribution of sampled pions resulting from sampling directly from the distribution given in figure 10.

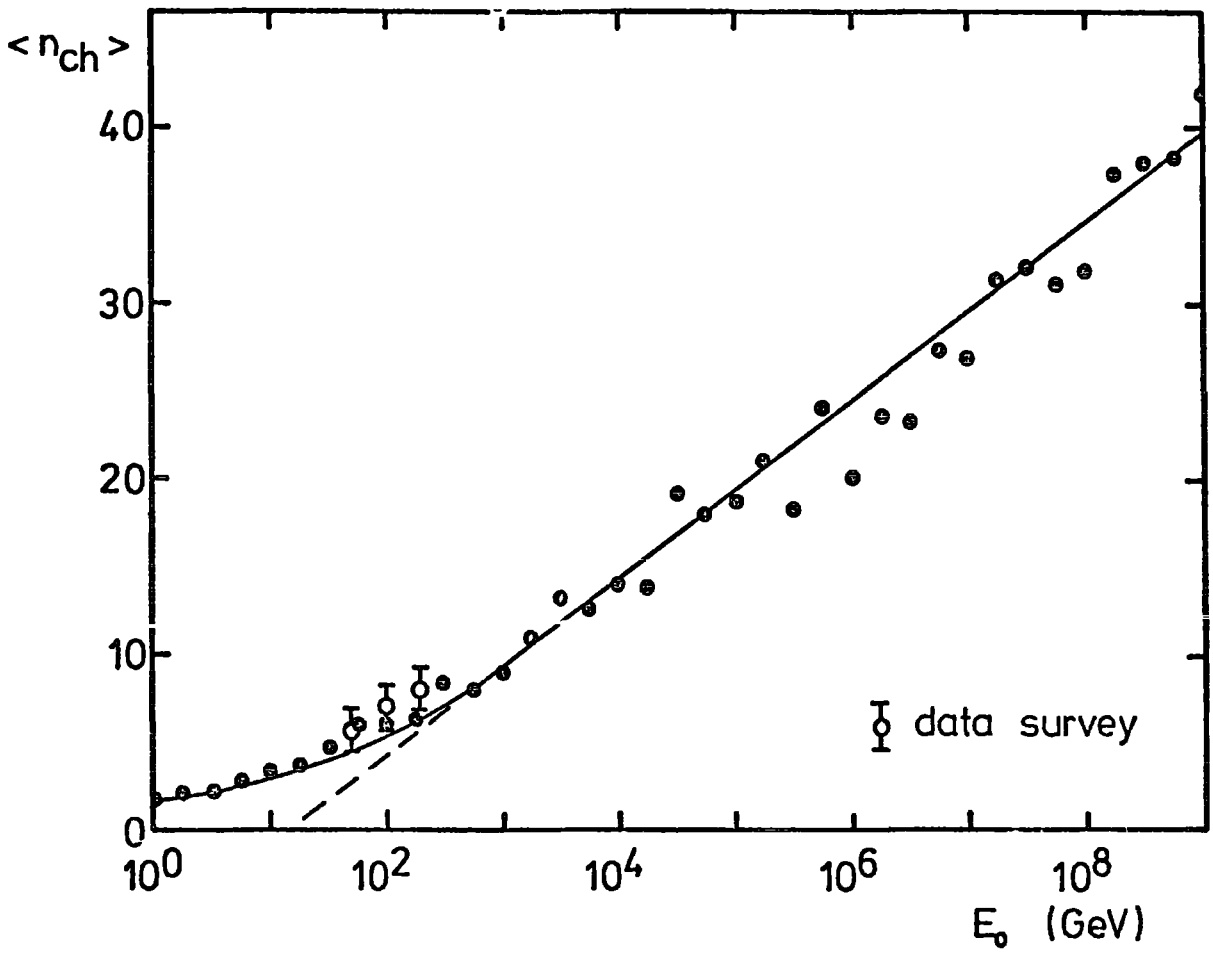

FIGURE 2-13 The mean charged multiplicity for pion-nucleon interactions obtained from the Monte Carlo sampling routines is compared to the expected logarithmic multiplicity law and the experimental data.

have the same format as those used by Dixon (1974) and are,

for charged pions PITOT(IH,IE)

for neutral pions PIZOT(IH,IE).

A pion created at depth x (g cm^{-2}) with energy E (GeV) would cause the value of PITOT(IH, IE) (if e.g. the pion was charged) to be increased by 1.0 where

$$\left.\begin{aligned} IH &= 1 + x/25.75 \\ IE &= 4.5 + 4 \log E \end{aligned}\right\} \text{rounded down to nearest integer.}$$

A fully Monte Carlo simulation is described schematically in figure 14. The atmospheric depth of first interaction, x_1 (g cm^{-2}), of the nucleon is chosen from the distribution,

$$f(x_1)dx_1 = \exp(-x_1/x_{int})dx_1/x_{int} \qquad 33$$

where x_{int} is the mean free path (g cm^{-2}), simply by taking $x_1 = -x_{int}\ln(R)$ where R is a number randomly chosen such that $0 < R \leqslant 1$. At this chosen point of interaction the energy of the leading nucleon is sampled and the energy of a pion is sampled using $F_{N\pi}$. This pion is considered as one of the first generation of pions. Its progress through the atmosphere is considered next (before further pions are sampled from the first interaction). If the pion is neutral it will decay before interaction and another 1^{st} generation pion is sampled. If it is charged, an interaction depth and decay depth (below point of production) are sampled and if the pion interacts before decaying the products of this interaction (the second generation of pions) are considered next, etc., etc... When the energy for production of n^{th} generation pions is exhausted the $(n-1)^{th}$ interation is reconsidered, a further $(n-1)^{th}$ generation being sampled. This process is repeated until all the shower energy is exhausted.

The above procedure enables an individual shower comparable

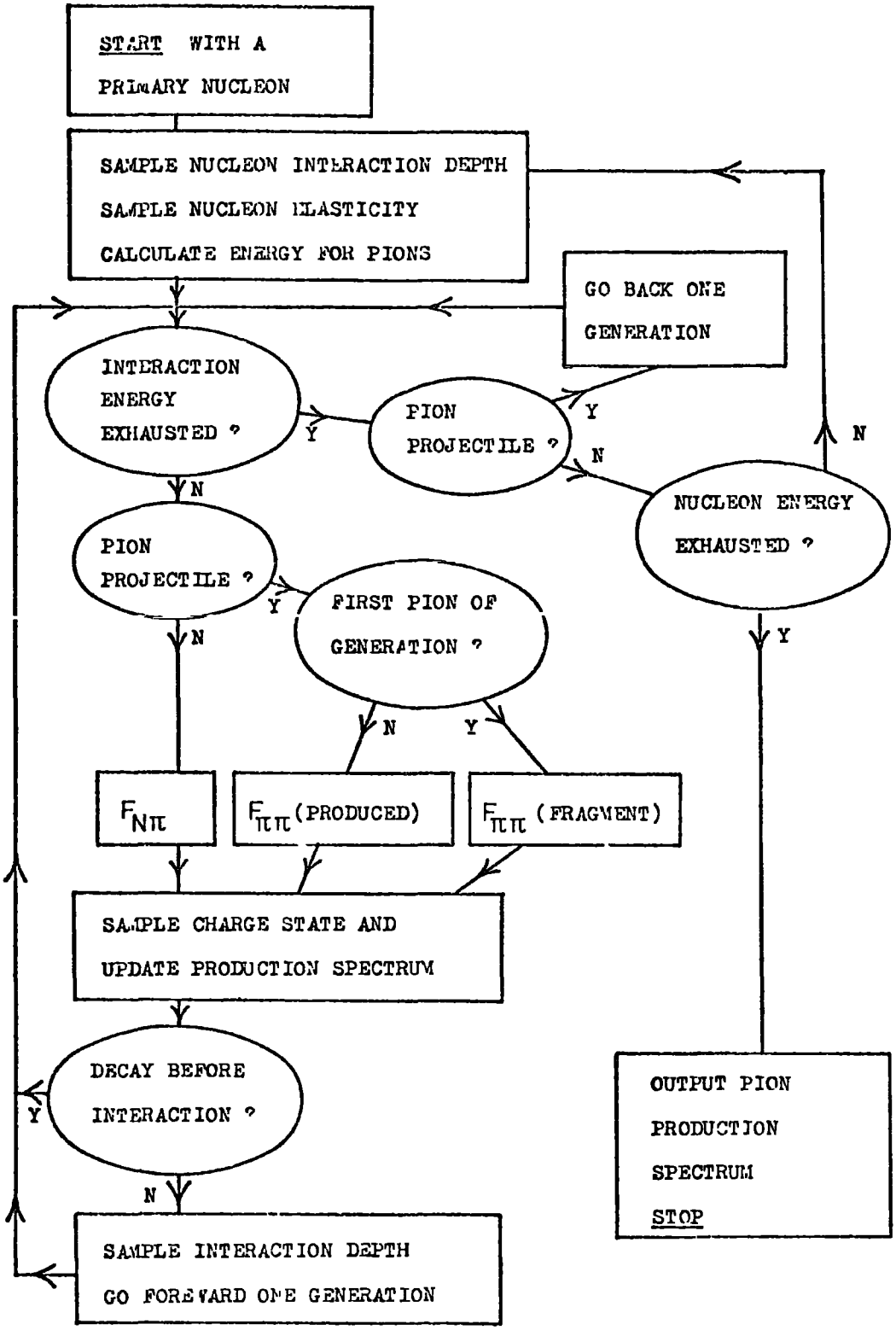

FIGURE 2-14 Flow diagram for the simulation of the hadronic core of a nucleon initiated cascade.

(assuming input cross sections are correct) to a real shower to be simulated since all interactions are considered in detail. A sample of such simulated showers should show similar fluctuations to a real sample of showers. The Monte Carlo technique requires considerable computer time however, and in practice only the high energy interactions (those mainly responsible for fluctuations) are considered in this way. The interactions of all particles with energies greater than a threshold energy (usually chosen as 10^{-3} of primary nucleon energy) are treated by the Monte Carlo method, its secondaries being stored in PITOT and PIZOT. The cascade resulting from pions produced below the threshold energy is treated numerically as described in Appendix B.

2-7.1 Comparison of the present work with that of Gaisser

Results of the average of 50 runs of the computer program at 10^6 GeV are compared to the results of T.K. Gaisser's program (Gaisser (1976, private communication)) using the same scaling model and input. Gaisser's program solves analytically the cascade equations describing the shower.

In figure 15 the differential energy spectra of charged pions are seen to be in agreement at a depth of 500 g cm^{-2} in the atmosphere. The discrepancy at higher energies lower in the atmosphere (at 800 and 1000 g cm^{-2}) is thought to be due to large statistical uncertainties in the present work resulting from the Monte Carlo technique (the error bars correspond to $n^{\frac{1}{2}}$ where n is the number of pions contributing to the point on the energy spectrum). Figure 16 compares the longitudinal electron cascade development from the two programs calculated under Approximation B (see Greisen (1956)) which are seen to be in reasonable agreement.

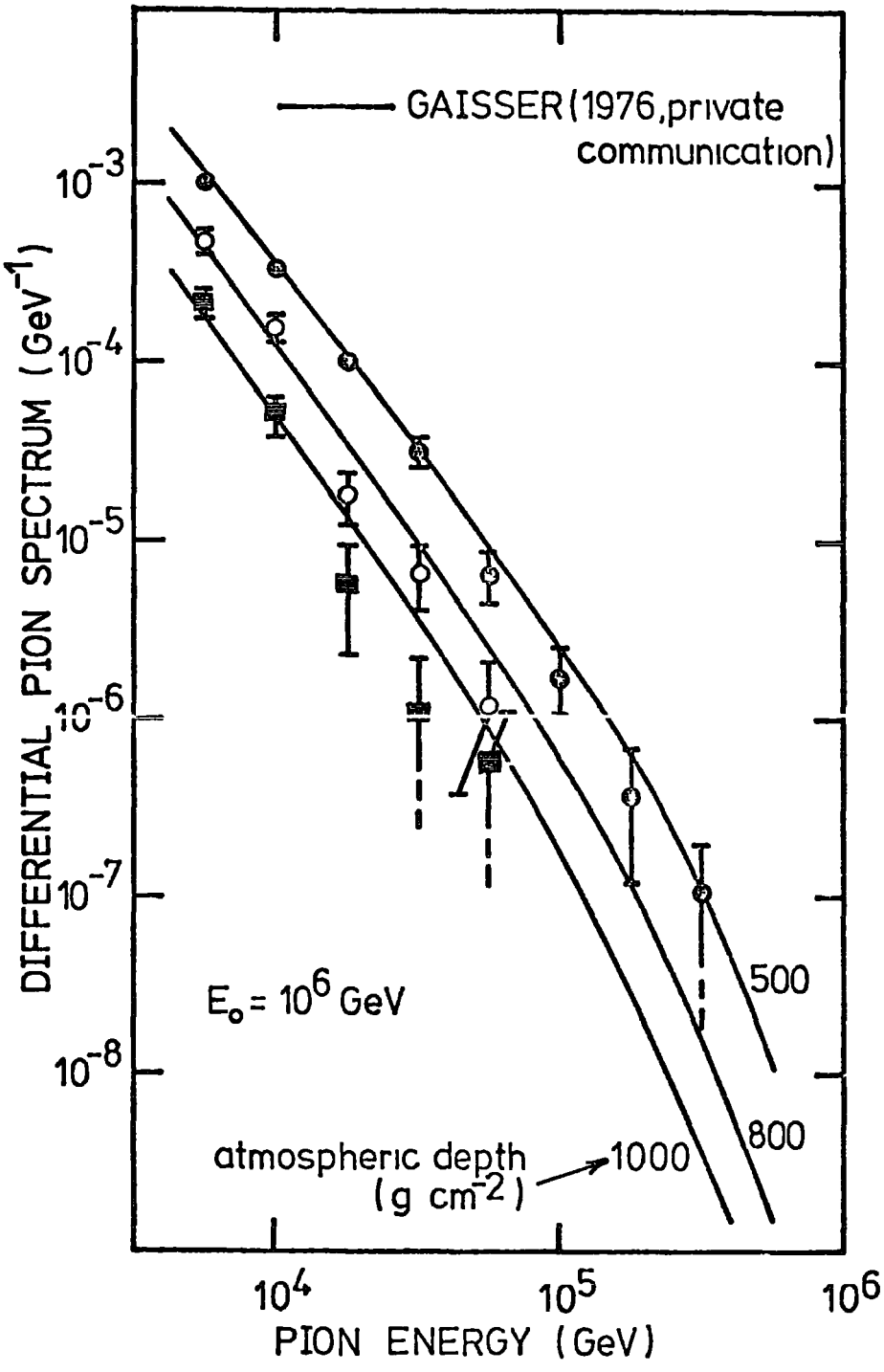

FIGURE 2-15 The differential energy spectra of pions from the present work are compared to those calculated by Gaisser.

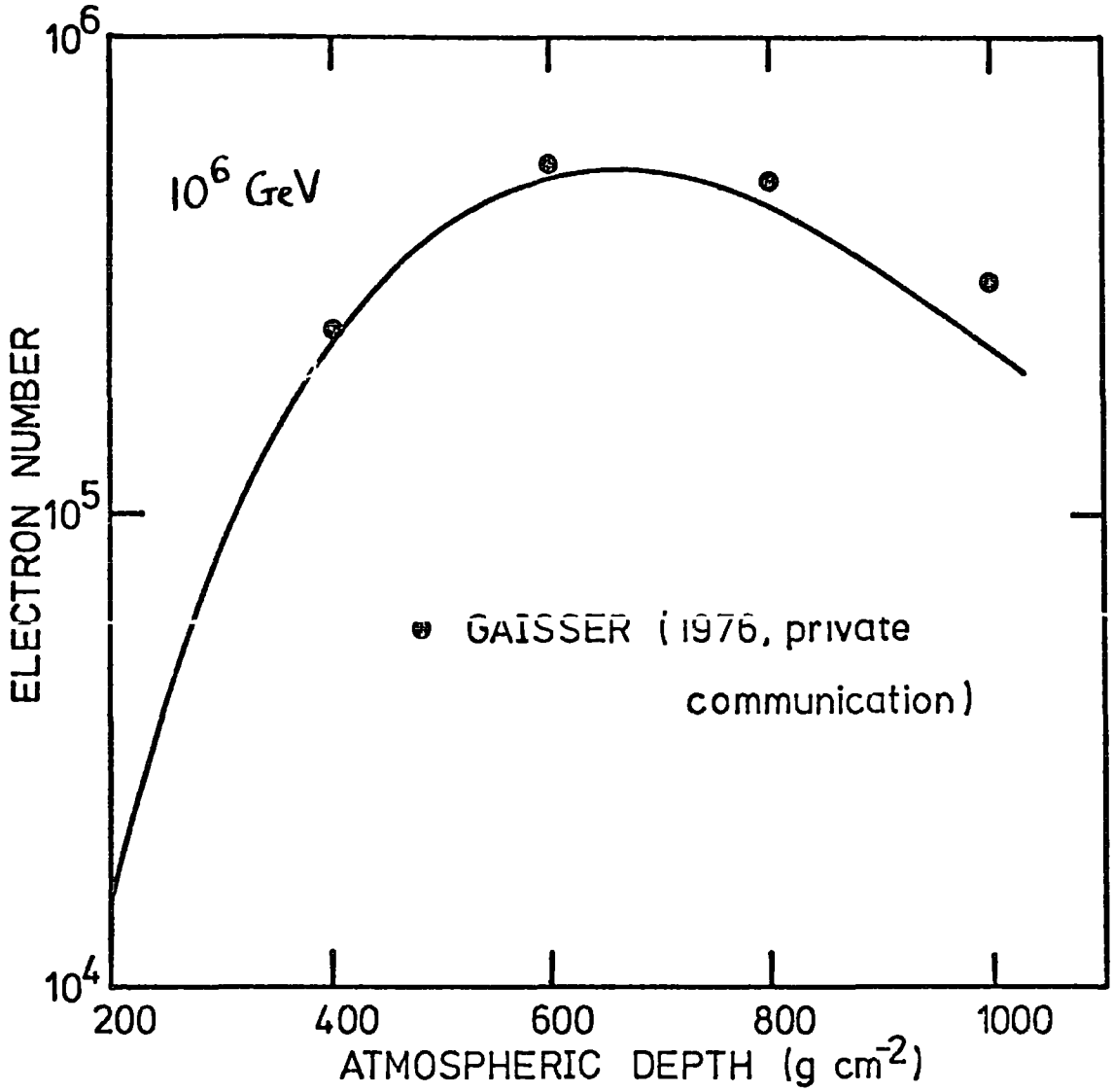

FIGURE 2-16 The longitudinal electron cascade development from the present work is compared to that calculated by Gaisser.

2-7.2 Energy dependent mean free paths

Simulations have been made to test the effect of the increase with energy of total cross sections observed at the ISR. Inelastic cross sections for N-air nucleus and π-air nucleus interations have been obtained from p-p and π-p total cross sections (Gaisser (1976, private communication)) extrapolated from accelerator data according to three different models. The input total cross sections are an extreme extrapolation given by Leader and Maor (1973), a ln s and a $\ln^2 s$ extrapolation given by Bartell and Diddens (see Diddens (1974)). The dependence of these cross sections on LAB energy is shown in figure 17 and the corresponding N-air nucleus and π-air nucleus inelastic cross sections are shown in figure 18. Results showing the effect of these cross sections on EAS cascade development will be presented in chapter 3.

2-8 THE LANDAU HYDRODYNAMICAL MODEL

It has been pointed out by Andersson et al (1976) and Carruthers and Minh Duong-van (1973) that the Landau model (Landau (1953)) can provide an equally good representation of the data at ISR energies as scaling models. This model can be regarded as an extension of the statistical model due to Fermi (Fermi (1950)).

A thin slab of hadronic matter is considered to be in thermal equilibrium after the collision and to expand adiabatically. The expansion is greatest in the longitudinal direction due to a higher pressure gradient (resulting from Lorentz contraction) causing a longitudinal-transverse asymmetry. The adiabatic nature of the process gives rise to an $E^{\frac{1}{4}}$ multiplicity law.

Carruthers and Minh Duong-van (1973) give an approximate formula for the invariant cross section in factorized form

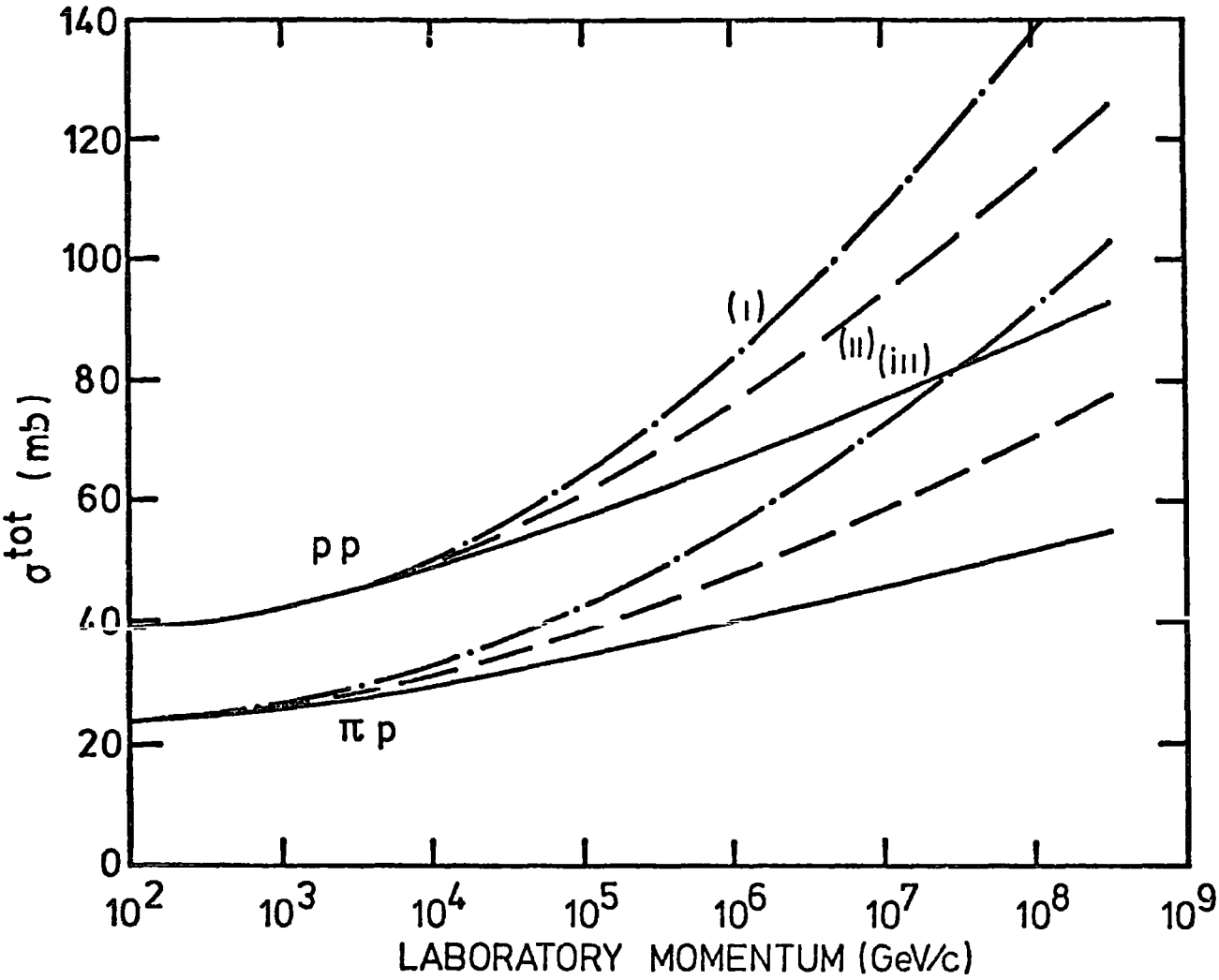

FIGURE 2-17 Energy dependent extrapolations of the total cross sections for pp and πp interactions

(i) Leader and Maor (1973),

(ii) $\ln^2 s$, Bartell and Diddens,

(iii) $\ln s$, Bartell and Diddens

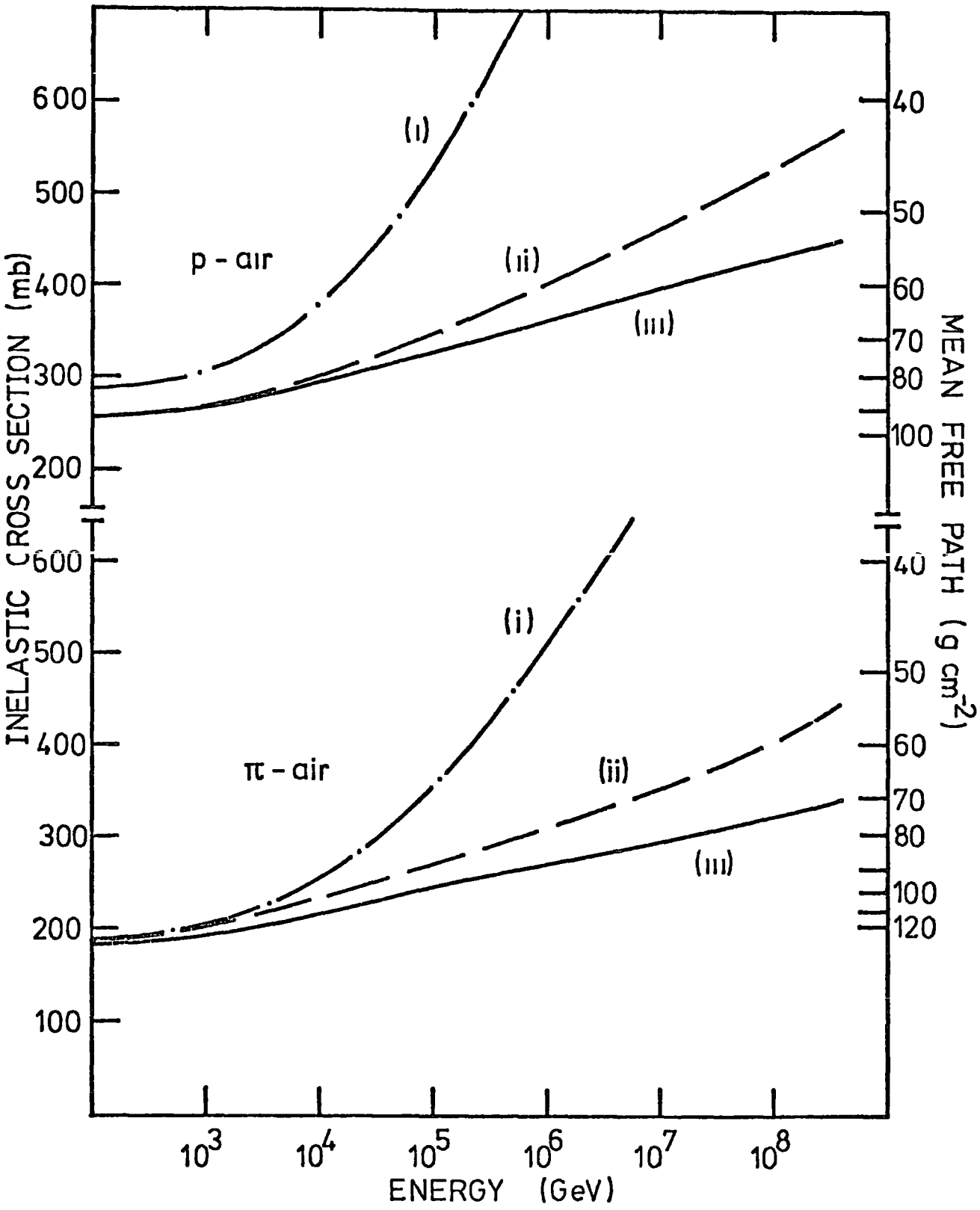

FIGURE 2-18 The total inelastic proton-air nucleus and pion-air nucleus cross sections corresponding to the proton-proton and pion-proton total cross sections given in figure 17.

$$E\frac{d\sigma}{d^3p} = \frac{\sigma^{inel}\ N\ B^2\ e^{-Bp_t}\ e^{-y^{*2}/2L}}{2\pi\ (2\pi L)^{\frac{1}{2}}} \qquad 34$$

where $B \approx 6\ (GeV)^{-1}$

$L = \frac{1}{2} \ln(s/4m_p^2)$

and $N \approx 2\ E^{\frac{1}{4}}$.

$F_{N\pi c}$ has been obtained by numerical integration over p_t^2 and is compared for ISR energies with the standard model in figure 19. The discrepancy between the predictions of equation 34 and the standard scaling model (which is a summary of ISR data) for $x>0.3$ is thought to be due to the simplicity of this version of the model which includes protons as well as pions.

The effect of using the Landau model in EAS calculations has been investigated by using the standard scaling model for $|x|>0.025$ while for $|x|<0.025$, using

$$F_{N\pi c}(x) = F(0,s)\ e^{-a(s)\ x^2} \qquad 35$$

where F(0,s) is calculated from equation 34 except that $N = 1.438\ E^{\frac{1}{4}}$ (which gives an energy dependence for $F_{N\pi c}(0)$ in agreement with that inferred from the data of Alper et al (1975) and consistent with more recent data of Guettler et al (1976)) and a(s) is such that $F_{N\pi c}(x)$ is continuous at $x = \pm 0.025$. For π-p interactions where only low energy data is available a similar model was used for produced pions with $N = b\ E^{\frac{1}{4}}$ where b was chosen such that $F_{\pi c \pi c}(0)$ agrees with the data at 16 GeV/c.

The distribution in LAB energy of pions produced in π-p interactions according to this model is compared in figure 20 to that obtained using the standard scaling model for 10^2 to 10^8 GeV primary pions. The distributions were obtained from the averages over 50 events sampled from the above distributions.

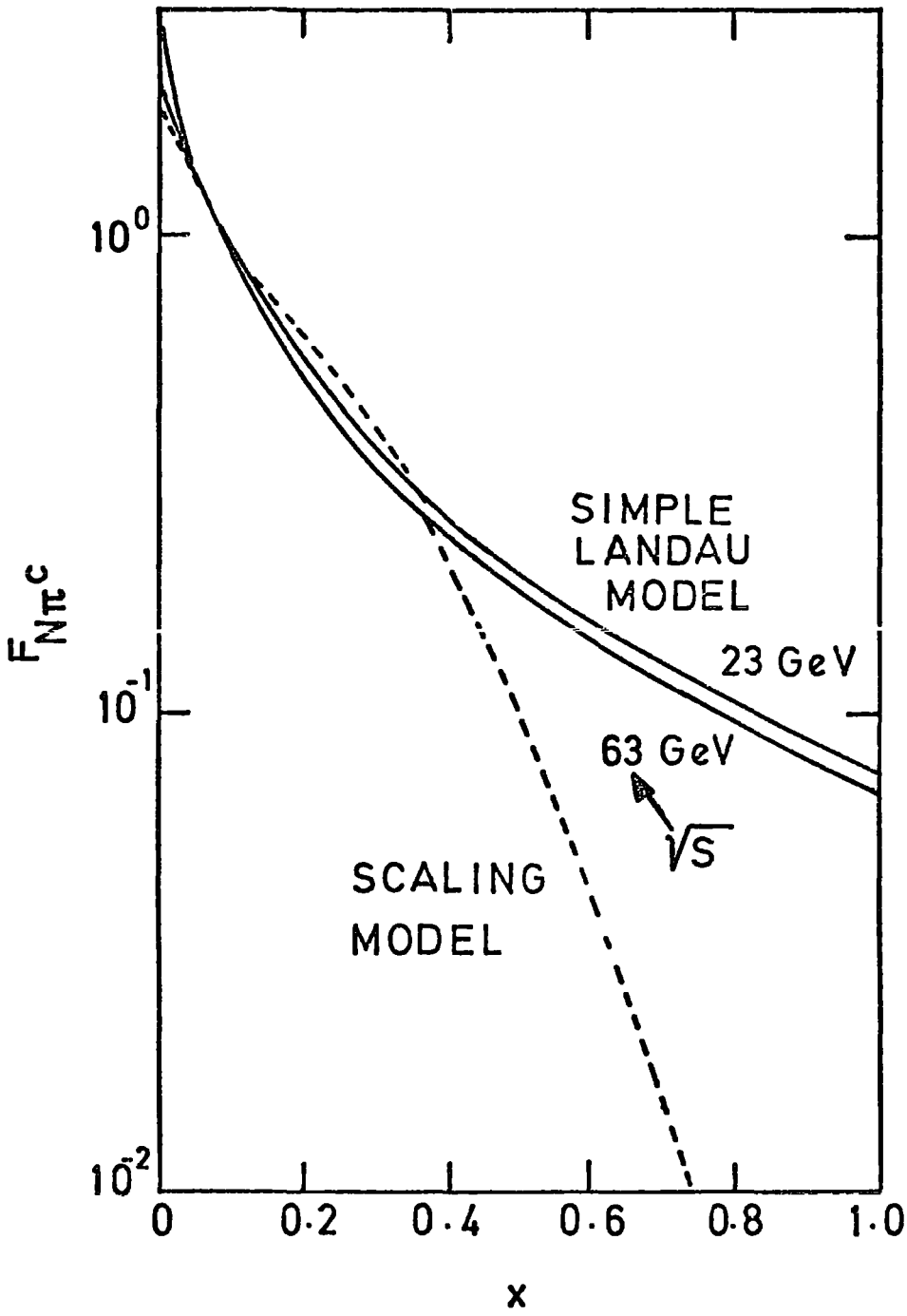

FIGURE 2-19 The distribution of charged pions produced in nucleon-nucleon interactions predicted by a simple version of Landau's hydrodynamical model is compared to the standard scaling model.

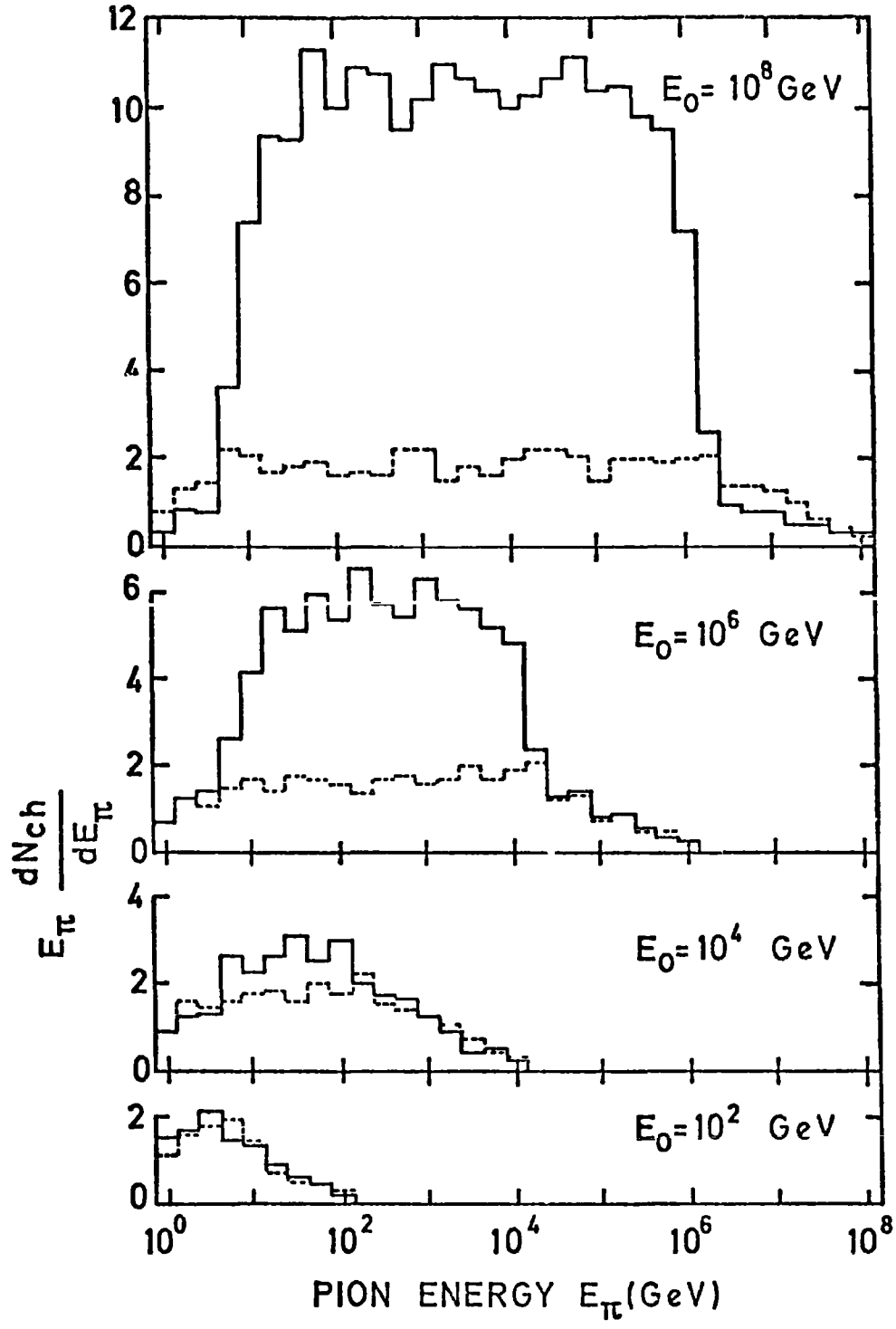

FIGURE 2-20: The distribution in LAB energy of pions produced in pion-nucleon interactions sampled according to the Landau model (solid lines) and the scaling model (dashed lines) at at four different energies.

The effect of a model where pion production in the central region relative to production near the fragmentation regions rises like $E^{\frac{1}{2}}$ (to be referred to as the Landau enhanced model) was investigated by using $N = c + d\ E^{\frac{1}{2}}$ in equation 34 where c and d were again chosen such that the energy dependence of $F_{N\pi}^{c}(0)$ agreed with the data.

The mean charged multiplicity in π-p interactions for the two above models is compared in figure 21 to that obtained from the standard scaling model (again averaged over 50 simulated events). While for the Landau model $\langle n_{ch} \rangle = 1.68\ E^{\frac{1}{4}}$ is proportional to N, for the Landau enhanced model, $\langle n_{ch} \rangle = E^{0.33}$, which is not. This is because at high energies the central region is enhanced so much that production in this region takes away a large amount of the available energy which is however finite.

2-9 PRIMARY NUCLEUS INITIATED SHOWERS

In many calculations of nucleus initiated EAS the superposition model has been used (de Beer et al (1966), Hillas (1966), Gaisser (1974), etc.). This model assumes that the shower from a primary nucleus of energy E and mass A is equivalent to the sum of A nucleon initiated showers of primary energy E/A. This simple treatment has been shown to underestimate fluctuations in cascade development by Dixon et al (1974). The present treatment of primary nuclei is based on that of Dixon et al (1974a) which uses data for the fragmentation similar to that described in detail by Freier and Waddington (1975).

The problem is to calculate the depths at which each of the A nucleons first interact after which the simulation proceeds as described for nucleon initiated showers. The depth at which the primary interacts is sampled from a distribution with mean free path given by Cleghorn et al (1968). In the interaction the primary nucleus breaks up into

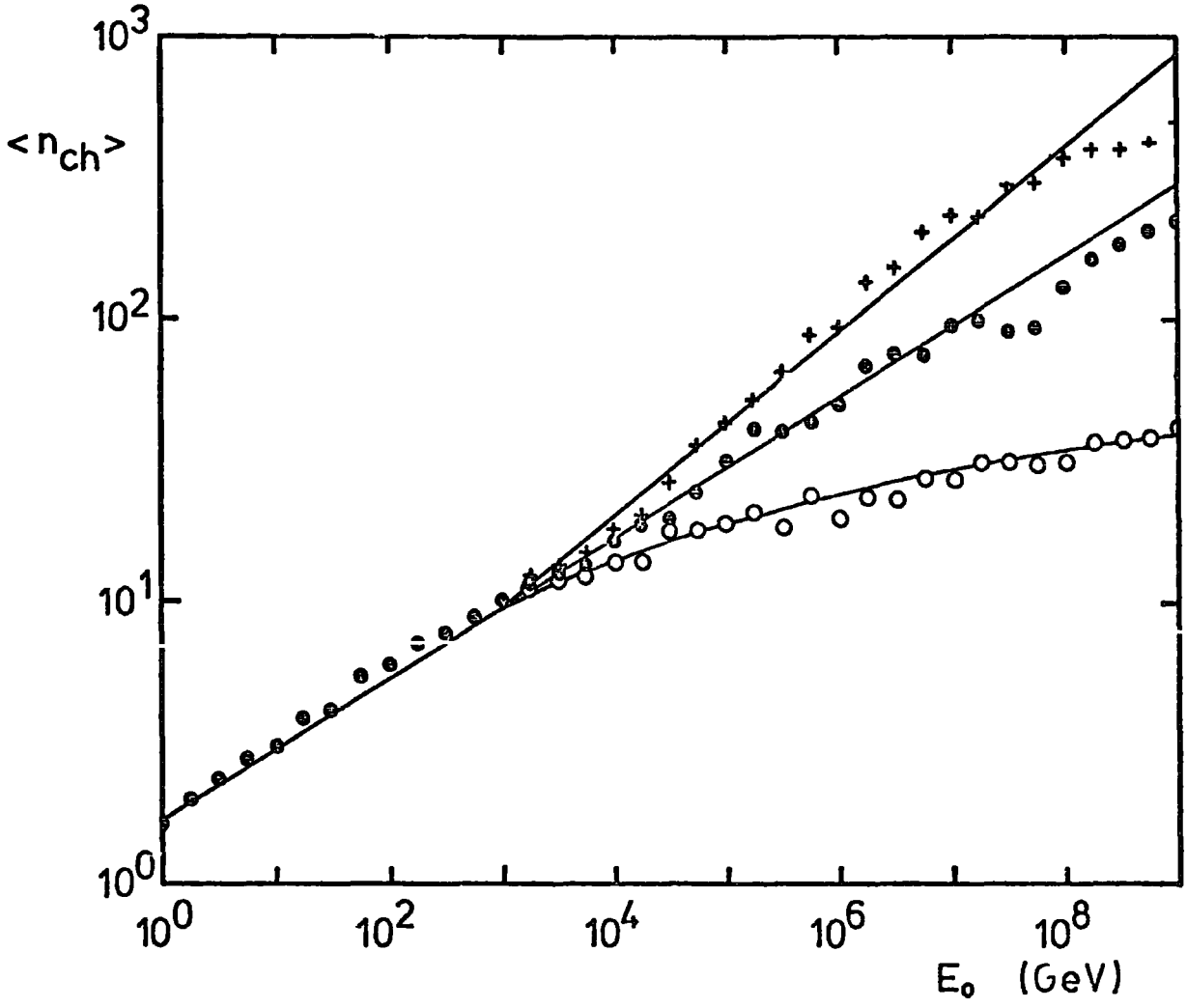

FIGURE 2-21 The mean charged multiplicity in pion-nucleon interactions as a function of interaction energy sampled according to the scaling model (o), the Landau model (●) and the Landau enhanced model (+).

fragment nuclei, α-particles and nucleons. A fraction of the nucleons released in the fragmentation interacted with the target air nucleus to produce pions. Dixon et al assumed this fraction to be 0.25 but measurements by Tomaszewski and Wdowczyk (1975) conclude the fraction of interacting nucleons should be ~0.75 for medium nuclei varying to ~ 0.5 for very heavy nuclei. These higher values have been used in the present work.

The probability of nucleon interaction as a function of atmospheric depth averaged over 20 iron nucleus showers obtained using the fragmentation model of Dixon et al, with nucleus mean free paths as given by Cleghorn et al, a nucleon mean free path of 80 g cm^{-2} and the fraction of interacting nuclei given by Tomaszewski and Wdowczyk is shown in figure 22. Also shown is the probability of interaction obtained from the superposition model (using nucleon mean free path = 80 g cm^{-2}) which is seen on average to give approximately the same distribution, suggesting that the superposition model may be used for calculations of average cascade development. The full fragmentation treatment should however be used to study fluctuations in nucleus initiated showers as has been done in the present work.

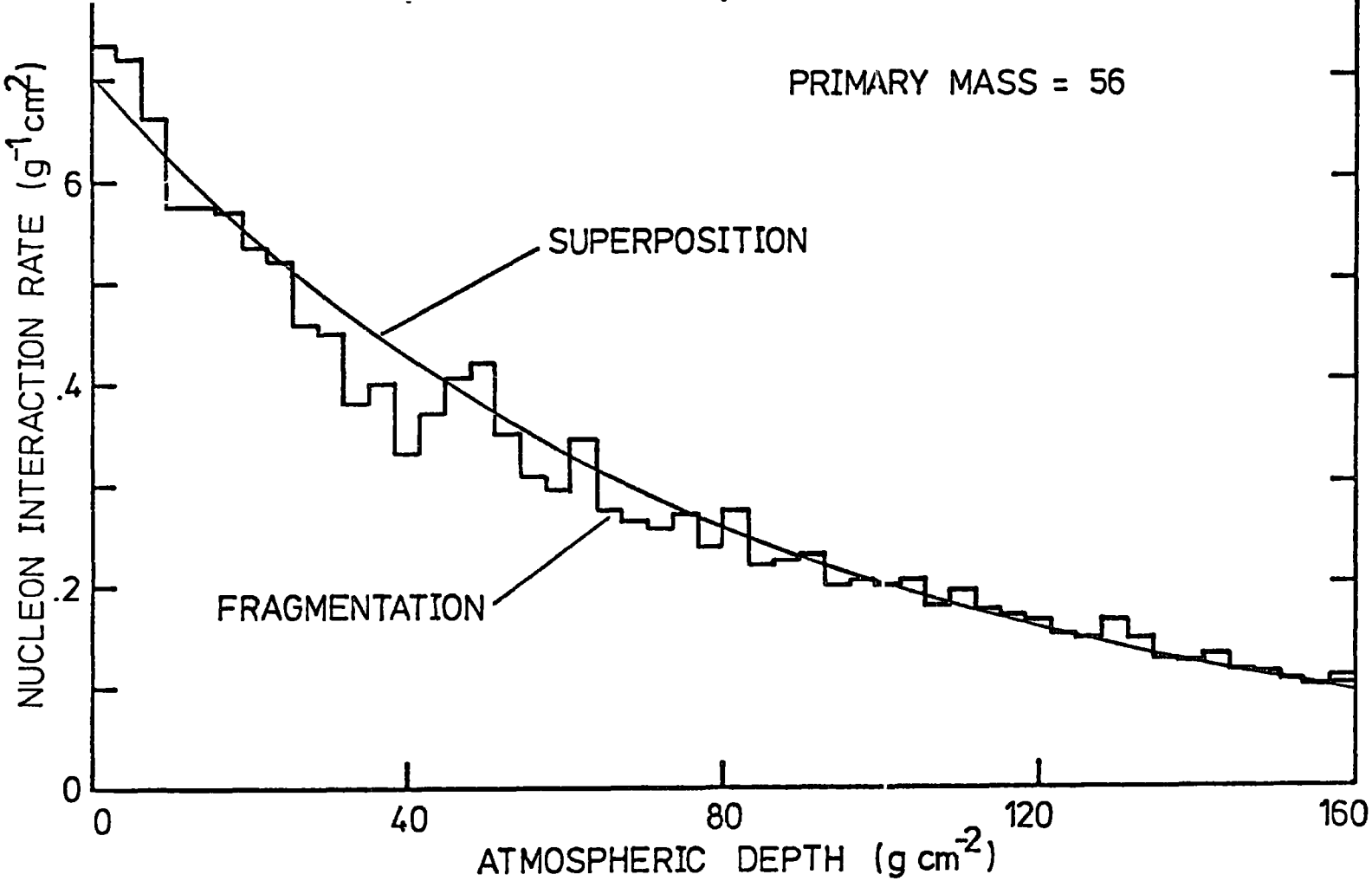

FIGURE 2-22 The probability of nucleon interaction as a function of atmospheric depth from the fragmentation model of Dixon et al (1974) compared to the superposition model for primary iron nuclei.

CHAPTER THREE

THE ELECTRON-PHOTON COMPONENT OF COSMIC RAY SHOWERS

INTRODUCTION

The electron-photon component of cosmic ray showers, the most numerous component at sea level, is fed primarily by the decay into two gamma-rays of neutral pions produced in high energy hadronic interactions. These gamma-rays will initiate a cascade of electrons and photons in the atmosphere. The number of cascade particles approximately doubles after each radiation length until particle energies are reduced such that ionization loss dominates over radiation processes. As the cascade grows it also develops laterally, mainly due to Coulomb scattering of the electrons.

In this chapter electromagnetic interactions are described and approximations commonly used in cascade theory are discussed. Results of cascade calculations using "approximation B" are compared to the results of recent detailed calculations. The method of calculating the electron-photon component of large cosmic ray showers using the results of recent Monte Carlo calculations is described and results of these calculations are given. The response of water Cerenkov particle detectors of the type deployed at the Haverah Park EAS array to the electron-photon component is also calculated.

3-1 ELECTROMAGNETIC INTERACTIONS

Electromagnetic interactions are accurately described by the theorey of quantum electrodynamics, but many processes may be adequately treated by classical electromagnetic theory and the methods of quantum mechanics.

The result of the interaction of an electron with an atom depends on its distance of closest approach to the atomic nucleus. If this distance is larger than the atomic dimensions, then the atom as a whole reacts to the field of the passing electron resulting in its

excitation or ionization. If the distance of closest approach is of the order of the dimensions of the atom, the problem is that of the collision between an atomic electron (which may be considered as free) and the incident electron. These "collision processes" may be treated by quantum mechanical methods. As the distance of closest approach becomes smaller than the atomic dimensions, the deflection of the electron in the Coulomb field of the nucleus becomes increasingly important. The deflection results in the emission of electromagnetic radiation (bremsstrahlung). This "radiation process" must be treated by quantum electrodynamics.

The interaction of a photon with an atom may be split up into three cases as with electron-atom interactions. The photo-electric effect results from the interaction of the photon with the atom as a whole. The interaction of a photon with a free electron results in the Compton effect and the interaction of a photon with the Coulomb field of the nucleus results in pair production.

The relative importance of the main processes mentioned above for the interaction of electrons and photons in air are illustrated in figures 1 and 2, where radiation processes are seen to dominate at high energies.

3-1.1 Bremsstrahlung

Radiation processes of electrons take place at distances from the nucleus which are large in comparison to the dimensions of the nucleus, thus the electric field of the nucleus may be considered as the Coulomb field of a point charge of magnitude Ze. If this distance is of the order of, or larger than the atomic radius, the screening of the electric field by the atomic electrons becomes important.

The probability of an electron with energy E traversing a thickness

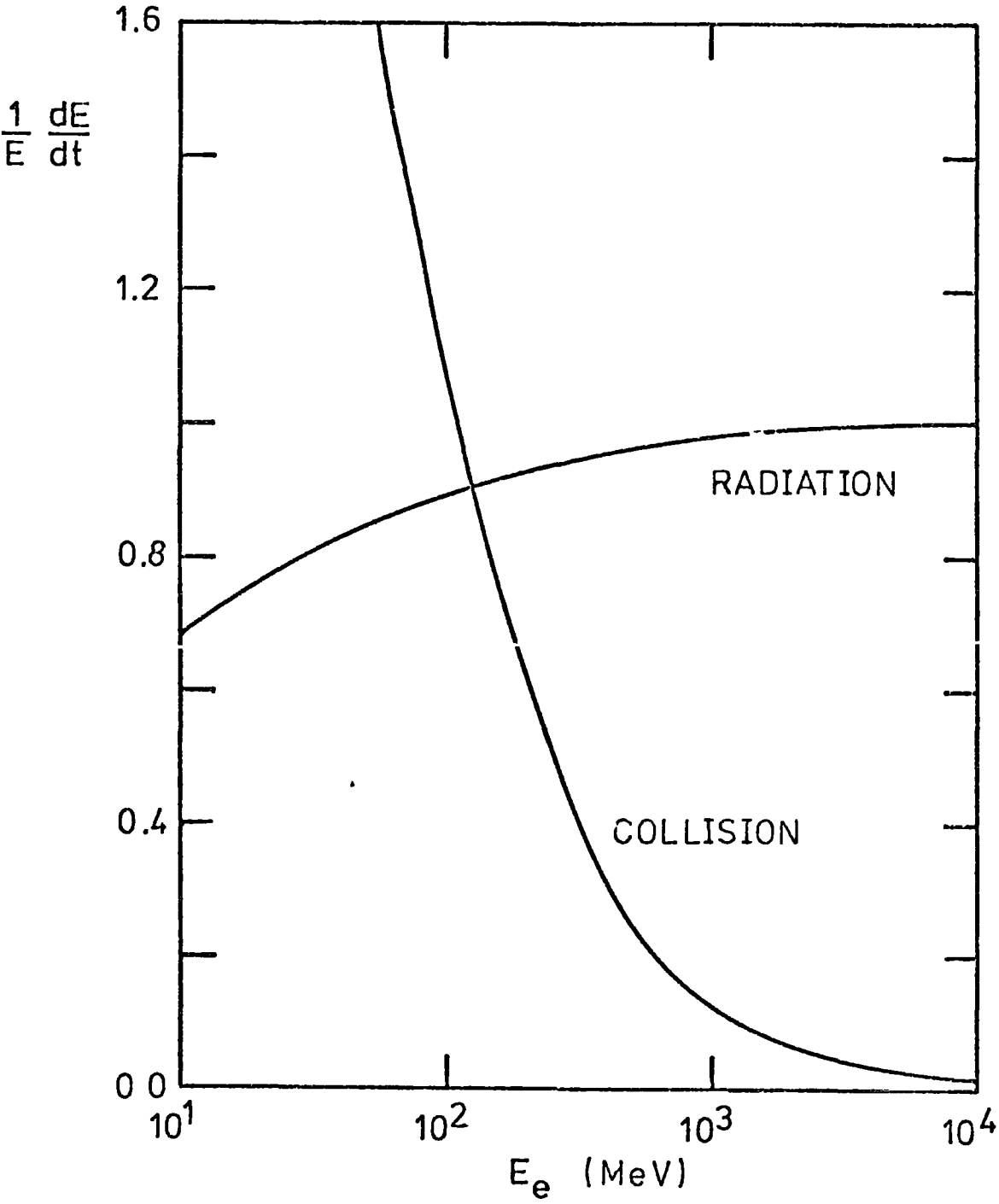

FIGURE 3-1 Fractional energy loss by collision and radiation for electrons per radiation length of air (From Rossi and Greisen (1941)).

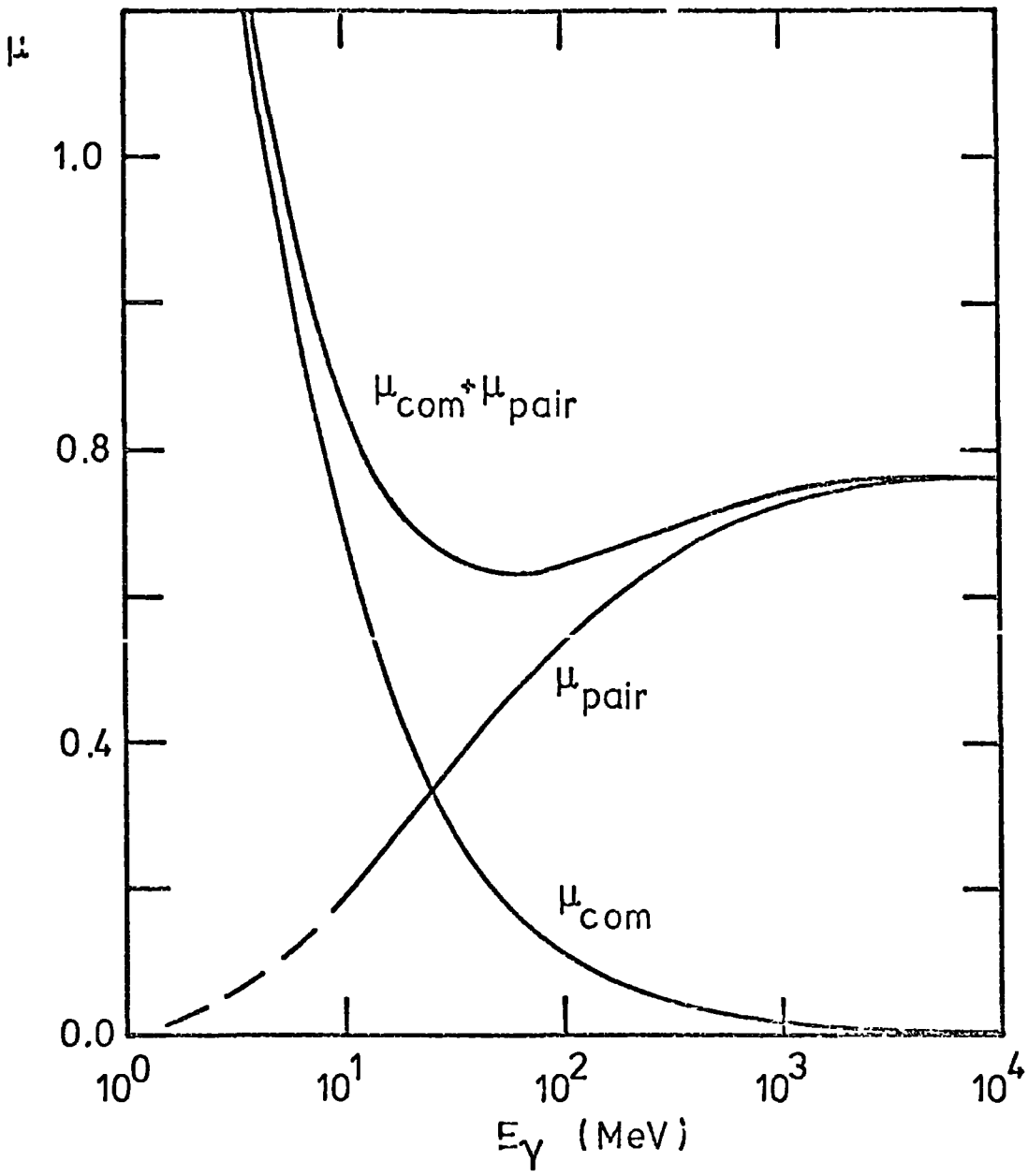

FIGURE 3-2 The total probability per radiation length of air for Compton scattering (μ_{com}), for pair production (μ_{pair}), and for either effect (From Rossi and Greisen (1941)).

dx emitting a photon with energy E' in dE' is,

$$\Phi_{rad}(E,E')dE'dx = 4\alpha\frac{N}{A} Z^2 \; r_e^{\;2} \; \frac{dE'}{E'} F(E,E')dx \qquad 1$$

where. $r_e = \frac{e^2}{m_e c^2}$ is the classical electron radius,

N is Avogadro's number,

F(E,E') depends on the degree of screening and is given by Rossi (1952). The differential radiation probability for electrons in air is plotted against E'/E for various electron energies in figure 3.

The average energy loss per g cm^{-2} due to bremsstrahlung is,

$$-\frac{dE}{dx}_{rad} = \int_{0}^{E - m_e c^2} E \; \Phi_{rad}(E,E')dE' \qquad 2$$

For the case of complete screening this becomes

$$-\frac{dE}{dx}_{rad} = 4\,\alpha\,\frac{N}{A}\,Z^2\,r_e^{\;2}\,E\left[\ln(183\,Z^{-1/3}) + 1/18\right] \qquad 3$$

For radiation processes it is thus useful to measure thickness in units of the "radiation length", X_o, defined by,

$$X_o^{-1} = 4\,\alpha\,\frac{N}{A}\,Z^2\,r_e^{\;2}\ln(183\,Z^{-1/3}) \qquad 4$$

If the effect of atomic electrons and the inaccuracy of the Born approximation used to derive equation 4 are taken into account, a more accurate formula for the radiation length is obtained

$$X_o^{-1} = 4\,\alpha\,\frac{N}{A}\,Z(Z+1)\;\;r_e^{\;2}\ln(183\,Z^{-1/3})\left[1 + 0.12\,(Z/82)^2\right]^{-1} \qquad 5$$

3-1.2 Pair production

The production of electron-positron pairs may be considered as the inverse process of bremsstrahlung. The materialization of a photon into an electron-positron pair is induced by the strong electric field

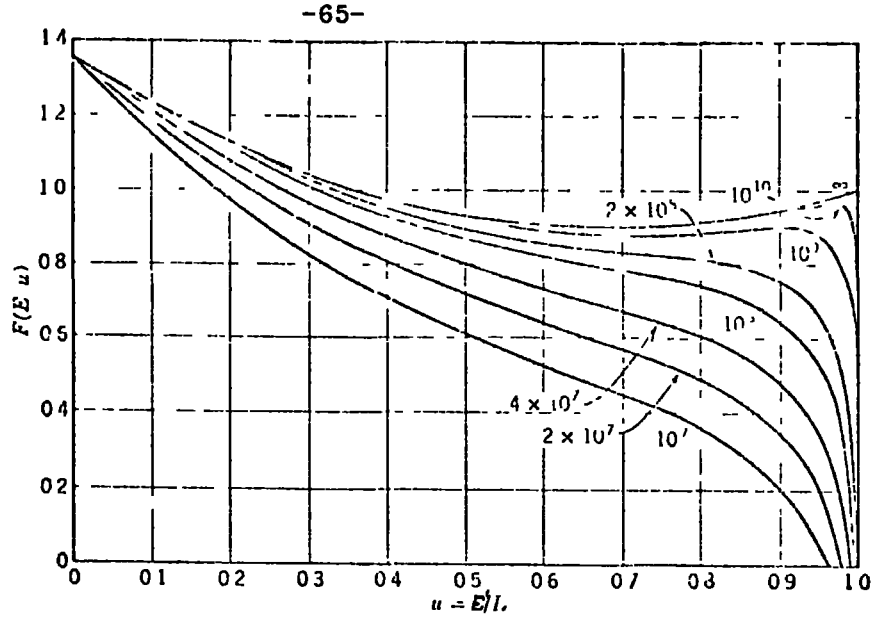

FIGURE 3-3 Differential radiation probability per radiation length of air for electrons of various energies. The numbers attached to the curves are the electron energies (eV). (From Rossi and Greisen (1941)).

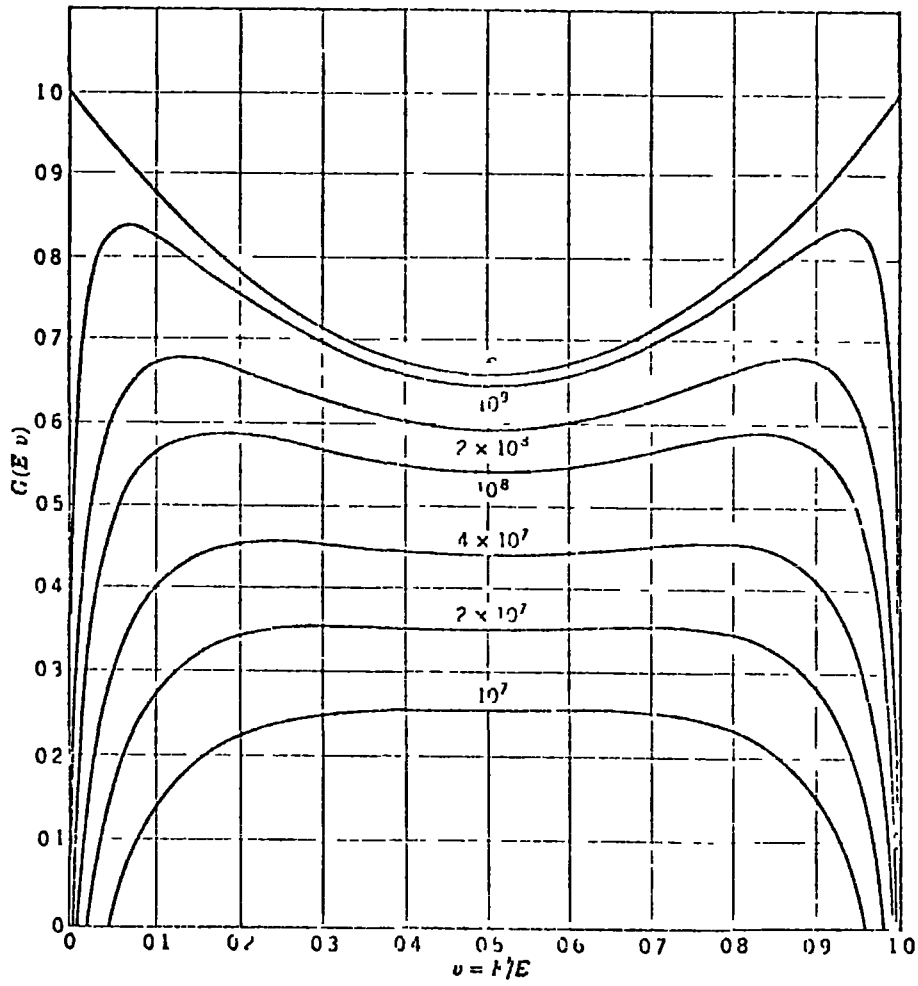

FIGURE 3-4 Differential probability of pair production per radiation length of air for photons of various energies. The numbers attached to the curves are the energies (eV) of primary photons. (From Rossi and Greisen (1941)).

surrounding an atomic nucleus.

The probability of a photon with energy E traversing a thickness dx and producing a pair where the positron has energy E' in dE' is given by

$$\Phi_{pair}(E,E')dE'dx = 4\alpha N \frac{Z^2}{A} r_e^2 \frac{dE'}{E} G(E,E')dx \qquad 6$$

where G(E,E') depends on the degree of screening and is given by Rossi (1952). The differential probability of pair production is plotted against E'/E for various photon energies in figure 4 where it is seen to be symmetric with respect to exchange of v and (1 - v) where v = E'/E, (i.e. with respect to the positron and electron energy).

The total probability for a photon with energy E to produce a pair per radiation length is,

$$\mu_{pair}(E) = \int_0^E \varphi_{pair}(E,E')dE' \qquad 7$$

where $\varphi_{pair}(E,E') = X_o \Phi_{pair}(E,E')$.

For the case of complete screening

$$\mu_{pair}(E \longrightarrow \infty) \approx 7/9 \qquad 8$$

3-2 NUCLEAR INTERACTIONS OF ELECTRONS AND PHOTONS

The cross sections for nuclear interactions of electrons and photons are much smaller than the corresponding electromagnetic cross sections and it has been found (McComb, Protheroe and Turver (1977, unpublished)) that these processes may be completely neglected in calculations of the electron-photon component of cosmic ray showers. The treatment of these nuclear interactions may, however, be necessary in calculations of the muon component of large cosmic ray showers where the nuclear interactions of just a small fraction of the numerous electron-photon

component may make an important contribution (through the decay of the charged pions produced) to the less numerous muon component.

3-2.1 Photomeson production

The total inelastic cross sections for photon-hadron interactions (photomeson production) and electron-hadron interactions (deep inelastic scattering) are of the order of α and α^2 of the total inelastic cross sections for hadron-hadron interactions respectively (α is the fine structure constant $\sim 1/137$) and for this reason photon-hadron interactions only are considered here. The total inelastic cross section for photon-proton interactions displays resonances at photon energies below 2 GeV but is fairly constant in the high energy region (> 2 GeV) up to 20 GeV with values of about 125 μb (see e.g. Luke and Soding (1971) for a survey of data in the range 0.2 GeV $< E_\gamma <$ 20 GeV). Recent measurements at Fermilab (Nash (1977)) up to photon energies of 185 GeV show the rise in the total inelastic cross section expected from the increase in the proton-proton total cross section observed at the ISR. The energy dependence of the photon-proton total inelastic cross section predicted from the behaviour of hadron-hadron cross sections is (P.D.P. Collins (1977, private communication))

$$\sigma_{\gamma p}^{tot} = 100\ s^{0.07} + 100\ s^{-\frac{1}{2}}\ \mu b \qquad 9$$

where s is in GeV^2. This energy dependence of the cross section has been assumed in the present work.

The total inelastic cross section for photon-nucleus interactions is obtained from the photon-proton cross section (see e.g. Weise (1974)) by,

$$\sigma_{\gamma A} = A^{0.91}\,\sigma_{\gamma p} \qquad 10$$

where A is the atomic mass number of the nucleus.

The inclusive cross sections for pion production in photon-hadron interactions are essentially similar to those for hadron-hadron interactions (see e.g Burfeindt et al (1973) for data on $\gamma + p \rightarrow \pi^+ + X$, Swanson et al (1971) and Moffeit et al (1972) for data on $\gamma + p \rightarrow \pi^- + X$ and Berger et al (1973) and Eisner et al (1974) for data on $\gamma + p \rightarrow \pi^o + X$) although Eisner et al have pointed out that in the kinematic region of their experiment π^o production is only 80% of the π^+ production.

3-2.2 The importance of photomeson production

The total inelastic cross section for photon-air nucleus interactions is $\sim$1.5 mb from equation 10 (assuming $\sigma_{\gamma p} = 125$ μb and A = 14.8) which is about 0.3% of the corresponding pair production cross section. The mean free path corresponding to photomeson production in air is thus approximately sixteen times the thickness of the atmosphere. It is quite conceivable therefore that the number of photon-hadron interactions in a cosmic ray shower may be as high as 10^{-2} times the electron number at shower maximum, N_{max}. In the majority of these interactions a small number of low energy pions will be produced and it is energetically favourable for the charged pions to decay into muons rather than interact with air nuclei. It is expected therefore that $\sim 10^{-3}$ to 10^{-2} N_{max} additional muons in the shower may arise from photomeson production. Furthermore, the energy dependence of the number of muons arising from photomeson production is expected to be approximately proportional to N_{max} which in turn is approximately proportional to the primary energy of the shower, E_p. The energy dependence of muons arising from the decay of pions produced in the hadron core is approximately proportional to E_p^{β} where β depends on the model for the hadronic interactions and is usually less than unity. It is feasible therefore that for high primary energies muons arising from photomeson production may even dominate the muon component.

A description of the treatment of photomeson production in these calculations together with preliminary results (McComb, Protheroe and Turver (1977, in preparation)) showing the effect of muons arising from photomeson production on the muon component will be given in chapter 4.

3-3 CASCADE SHOWERS

High energy electrons lose most of their energy by radiation. Since the energy distribution of both the surviving electron and the photon radiated in bremsstrahlung are almost flat, the electron and photon have sufficient energy on average to produce further photons and to materialize electron-positron pairs. If the primary particle has sufficient energy these processes take place successively, the total number of particles increasing with each interaction This continues until the energy of the particles is reduced below that at which collision processes dominate and the cascade shower decays.

3-3.1 Approximations of cascade shower theory

The properties of cascade showers may be derived analytically by solution of the cascade equations provided simplifying assumptions are made. Two sets of approximations frequently used are "approximation A" and "approximation B" (see Rossi and Greisen (1941)).

Under approximation A only radiation processes are considered, the asymptotic formulae for bremsstrahlung and pair production being used. The results of shower theory under approximation A are identical for all substances provided thicknesses are measured in radiation lengths.

Under approximation B radiation processes are considered in the same way as under approximation A but, in addition, ionization losses are taken into account and are described by a constant energy deposition of ε_o per radiation length. ε_o is the critical energy defined by

$$\varepsilon_o = \varepsilon(\varepsilon_o) \qquad 11$$

where $\varepsilon(E)$ is the collision loss per radiation length of electrons with energy E.

3-3.2 Results of cascade theory under approximation B

A solution of the cascade equations under approximation B by Snyder (1949) for the total number of electrons at a depth of t radiation lengths in a cascade initiated by a primary photon of energy E_γ has been conveniently given by Greisen (1956) as,

$$N_e(E_e > 0, \quad t) = \frac{0.31}{\beta_o^{\frac{1}{2}}} \exp\left\{ t\left(1 - \frac{3}{2} \ln(s)\right)\right\} \qquad 12$$

where $s = 3t/(t + 2\beta_o)$,

$$\beta_o = \ln(E_\gamma / \varepsilon_o).$$

s is called the "age parameter" of the shower $s < 1$ before cascade maximum, $s = 1$ at cascade maximum and $s > 1$ after cascade maximum.

Calculations of the lateral development of showers have been made under approximation B by Nishimura and Kamata (see Nishimura (1967)). Their result for the lateral distribution of electrons has been parameterized by Greisen (1956), the "NKG distribution", as

$$f(x) \propto x^{s-2} (x + 1)^{s-4.5} \qquad 13$$

where x is the radial distance measured in "Moliere units", r_m, defined by,

$$r_m = X_o \frac{\varepsilon_o}{E_s} \qquad 14$$

where E_s is the characteristic energy for multiple scattering $E_s \simeq 21$ MeV for electrons.

3-3.3 Detailed Monte Carlo calculations

The analytic method is unable to accurately describe the behaviour of low energy shower particles because the approximations become invalid as the energy is reduced, the cross sections depending strongly on energy. Use of Monte Carlo method enables the energy dependence of

the cross sections to be faithfully reproduced and processes which become important at low energies (e.g. Coulomb scattering and the Compton and photo-electric effects) to be considered rigorously.

A number of comprehensive calculations of cascades in a variety of media were made by Butcher and Messel (1958, 1960), Crawford and Messel (1962), Messel et al (1962) and Messel and Crawford (1970). Recent work by the Durham group (Browning, Protheroe and Turver (1976, unpublished)) which is reported here has been based on the techniques of Butcher and Messel (1962) and the computer program devised by Baxter (1969). Many improvements to this program (e.g. the inclusion of the geomagnetic deflection of electrons) have been made by Smith and Hough (1973,unpublished), Browning (1975, unpublished), Allan et al (1975), Browning and Turver (1977) and the present author in order to make calculations of the radio emission, Cerenkov light emission and nitrogen fluorescence light emission from large cosmic ray showers. The above work utilises the cross sections for electromagnetic proceses by Rossi (1952) but ionization loss is calculated using the data of Sternheimer (1959).

Recently, Allan et al (1975) have shown that the lateral distribution of electrons given by the NKG distribution is considerably broader than that obtained by detailed Monte Carlo calculations. This result was supported by Browning, Protheroe and Turver (1976, unpublished) who found a lateral spread midway between that given by Allan et al and the NKG distribution. More recent calculations by Hillas and Lapikens (1977) are in agreement with the present work.

3-3.4 Comparison between results of present Monte Carlo calculations and other work

Monte Carlo simulations of cascades developing in a real atmosphere from the present work are compared with other simulations. The

average longitudinal cascade development of electrons (E>4 MeV) in photon initiated showers is compared with the cascade development calculated under approximation B (equation 10) in figure 5. The data from the present work comprise results obtained for primary gamma-rays injected at different depths in a real atmosphere (the atmospheric density has little effect on longitudinal development when plotted against atmospheric depth). Except for the difference in normalization (due to the different energy thresholds), the longitudinal cascade development in the present work is in agreement with the approximation B cascades. Monte Carlo simulations of Marsden (1971) are in excellent agreement with the electron and photon number development from the present work as shown in figure 6. The discrepancy in the photon number development given by Messel and Crawford (1970) was noted by Marsden and is again evident in this figure.

The lateral distribution of electrons in photon initiated showers is compared with that obtained from the NKG distribution in figure 7. As noted earlier, the NKG distribution predicts more electrons at large core distances than obtained from the present work. Better agreement is seen at large core distances in figure 8 between the present work and the parameterization of Monte Carlo results given by Marsden (1971).

The integral energy spectrum of electrons integrated over the whole shower is found to be in good agreement with the results of Richards and Nordheim (1948) which are shown in figure 9. The integral energy spectra of electrons integrated over the length of the shower (at different core distances) and thus indicative of the spectra at cascade maximum are shown in figure 10.

For comparison with the work of Allan et al (1975) and Hillas and Lapikens (1977), a sample of 40 photon initiated showers of primary energy 10 GeV were generated in a linear atmosphere of density 1 kg m^{-3}.

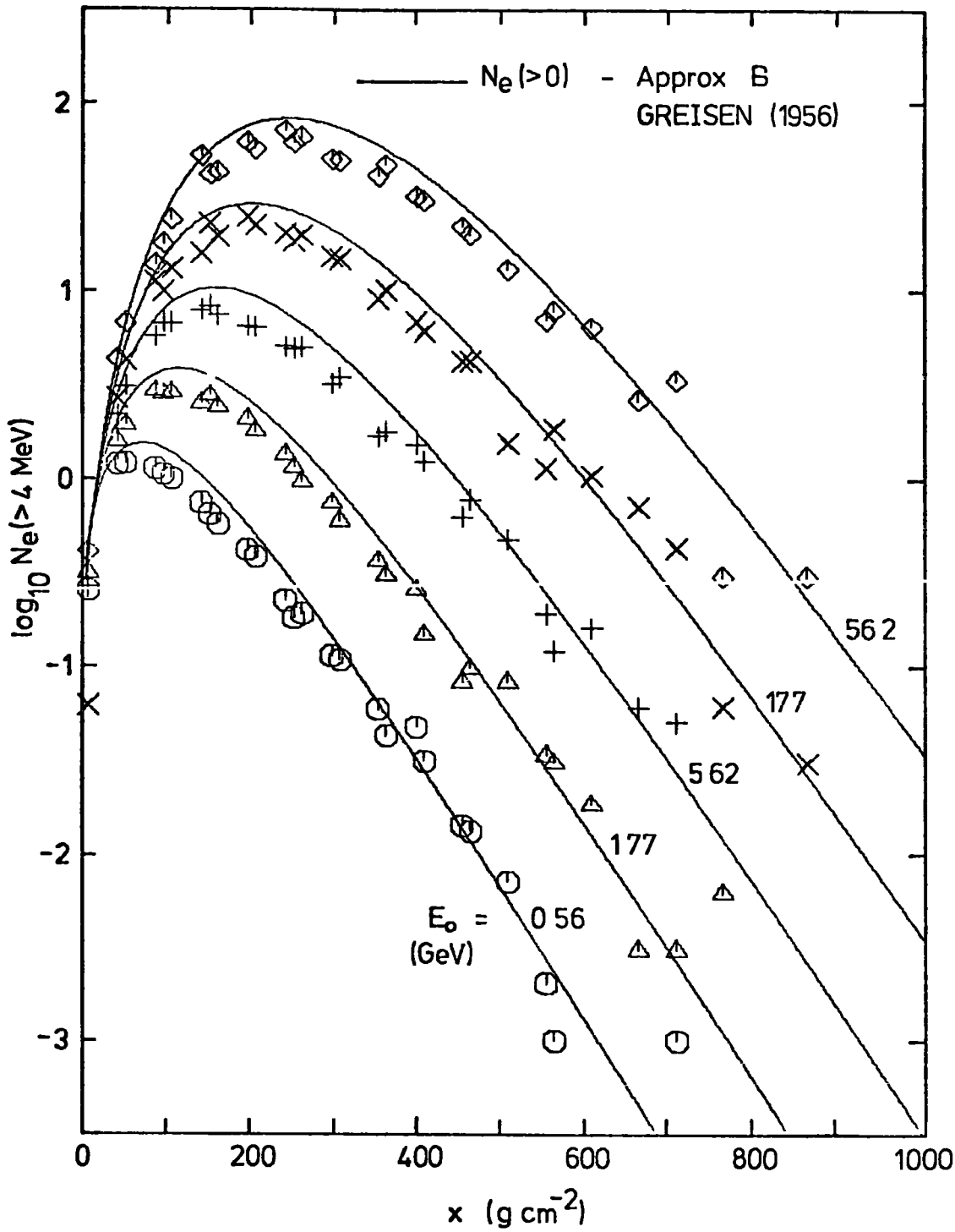

FIGURE 3-5 The average longtiduinal electron cascade development from the present work is compared to that calculated under approximation B for various primary photon energies, E_o.

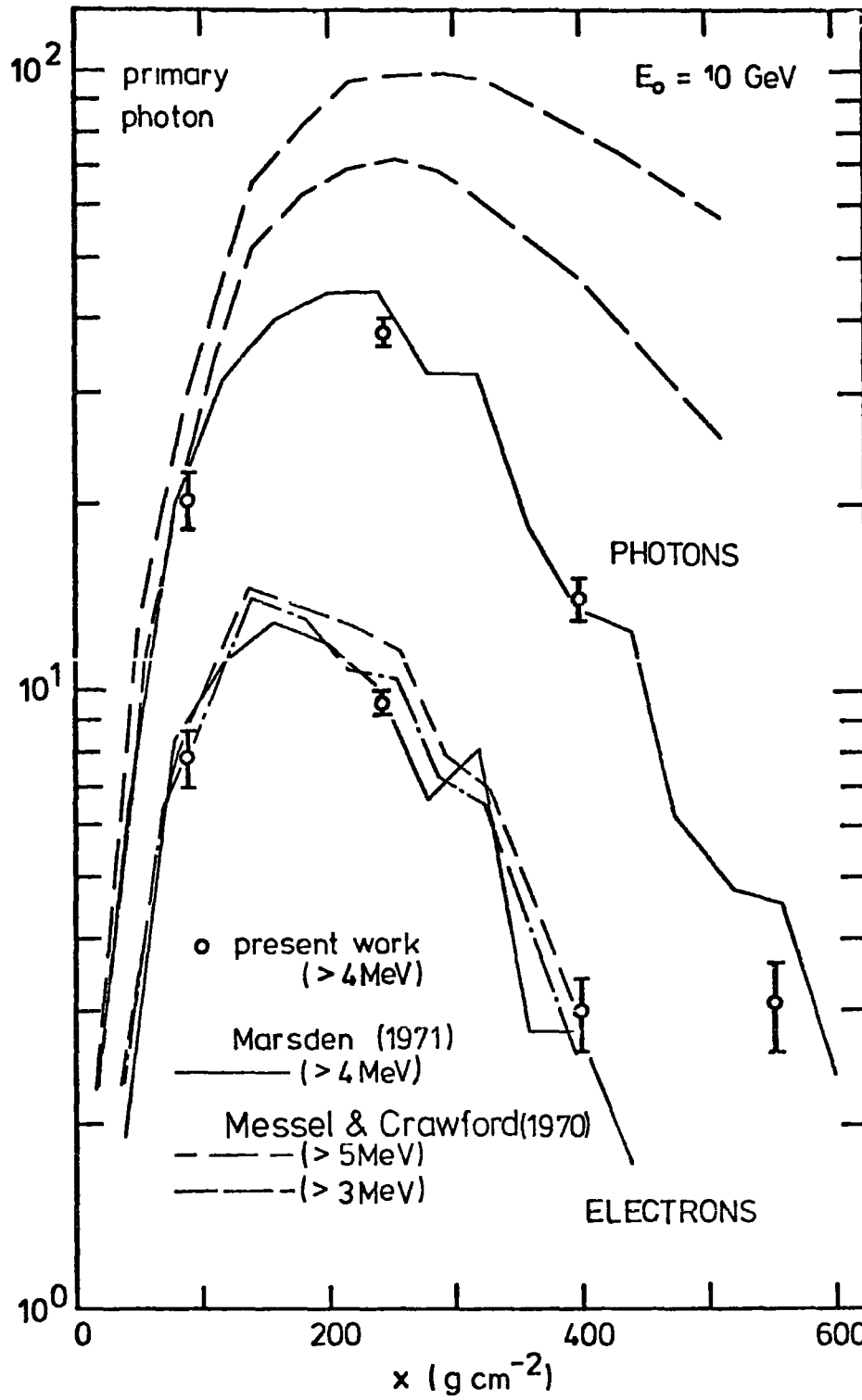

FIGURE 3-6 The average electron and photon cascade development from the present work is compared to that calculated by Marsden (1971) and Messel and Crawford (1970) for a primary photon energy of 10 GeV

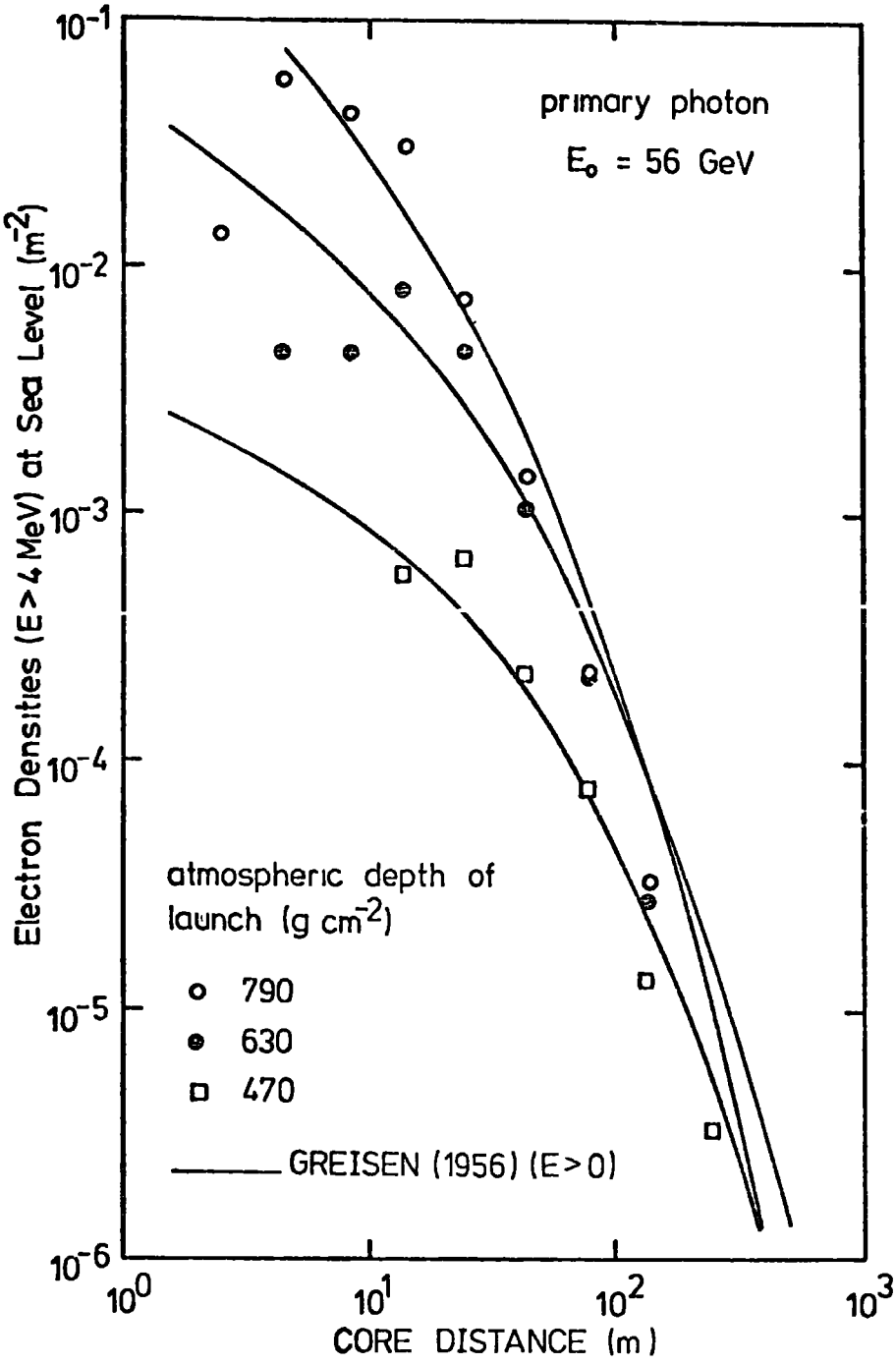

FIGURE 3-7 The lateral distribution of electrons from the present work is compared to that given by the NKG distribution. The deficiency of points from the present work near the core is due to sampling.

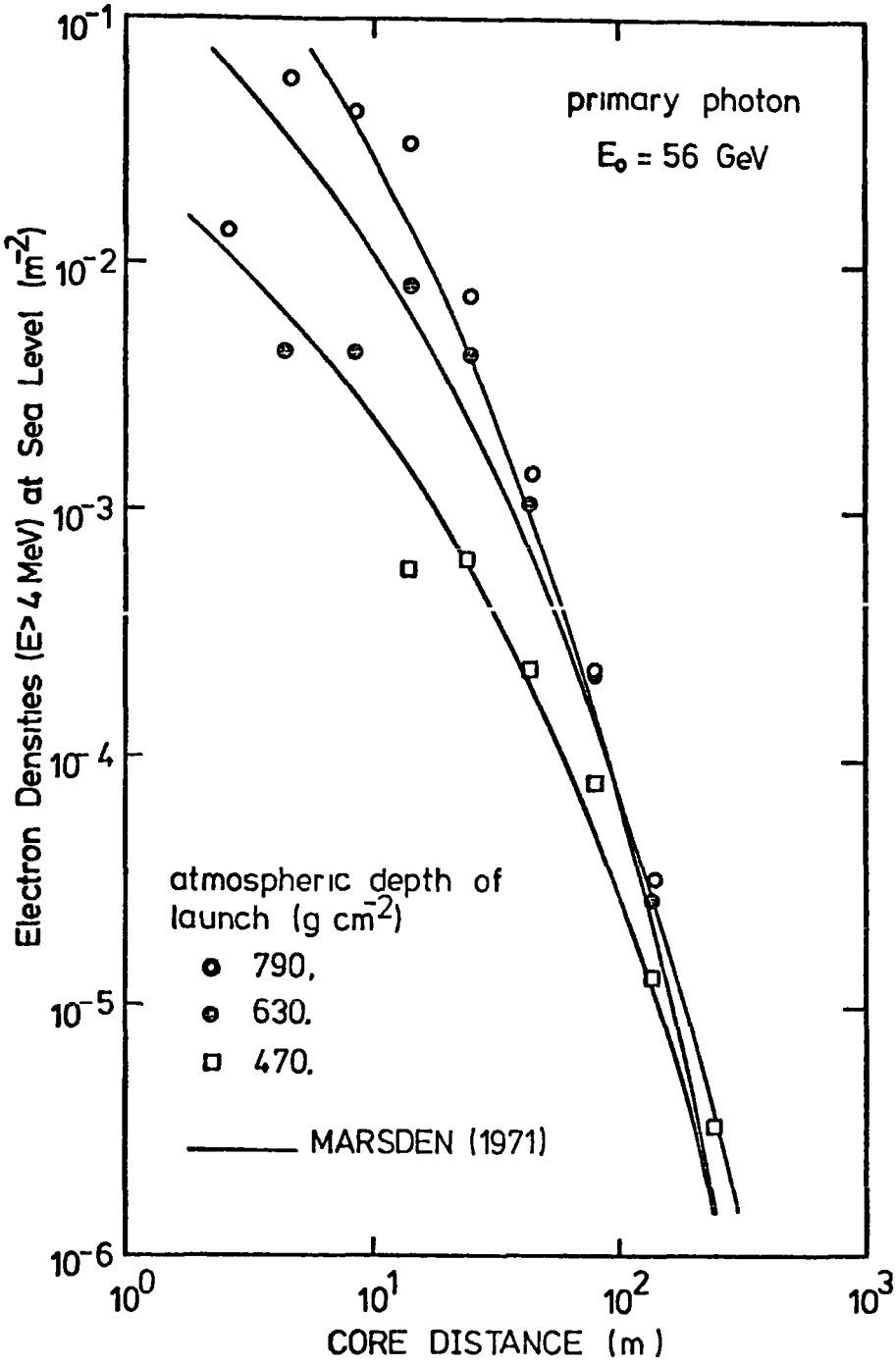

FIGURE 3-8. The lateral distribution of electrons from the present work is compared to that calculated by Marsden (1971).

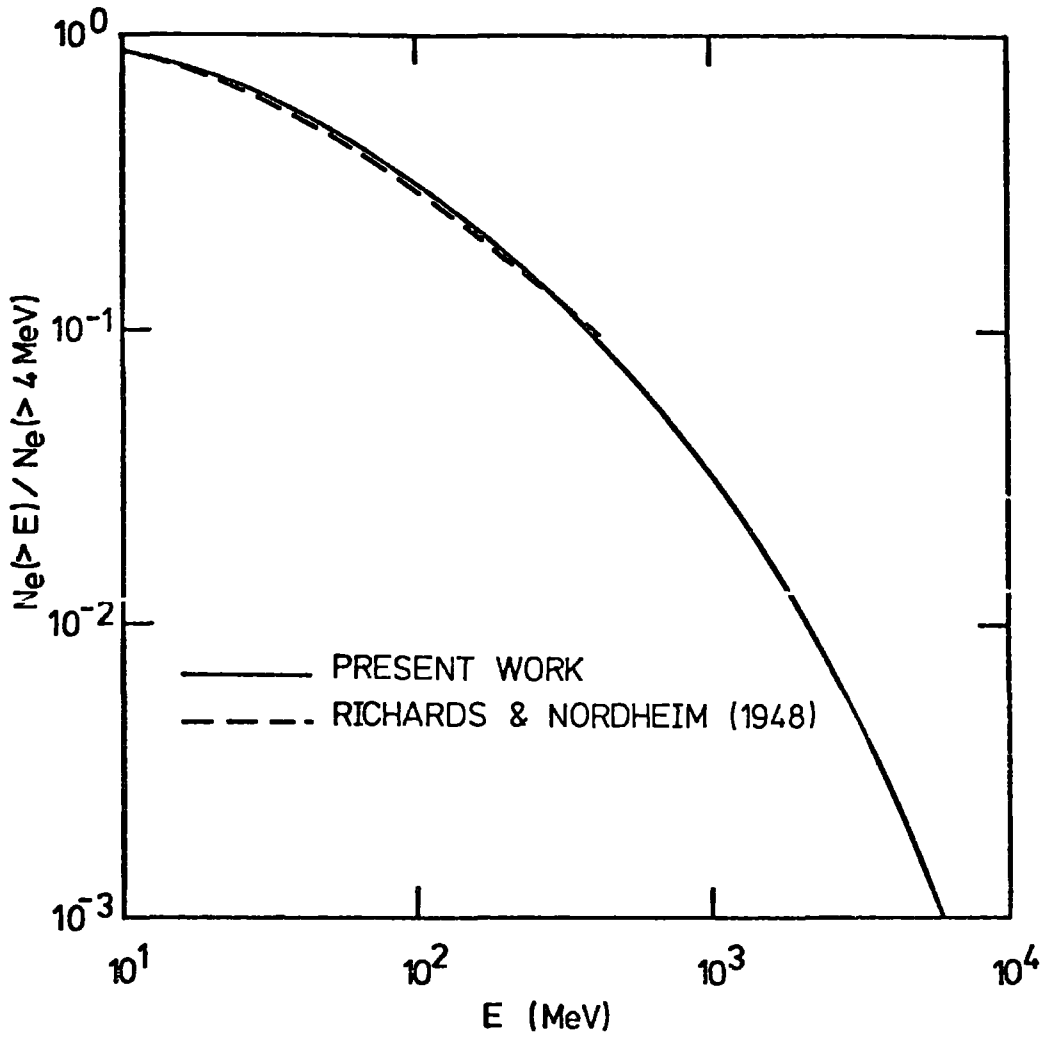

FIGURE 3-9 The integral energy spectrum of electrons from the present work, integrated over the whole shower, is compared to that given by Richards and Nordheim (1948).

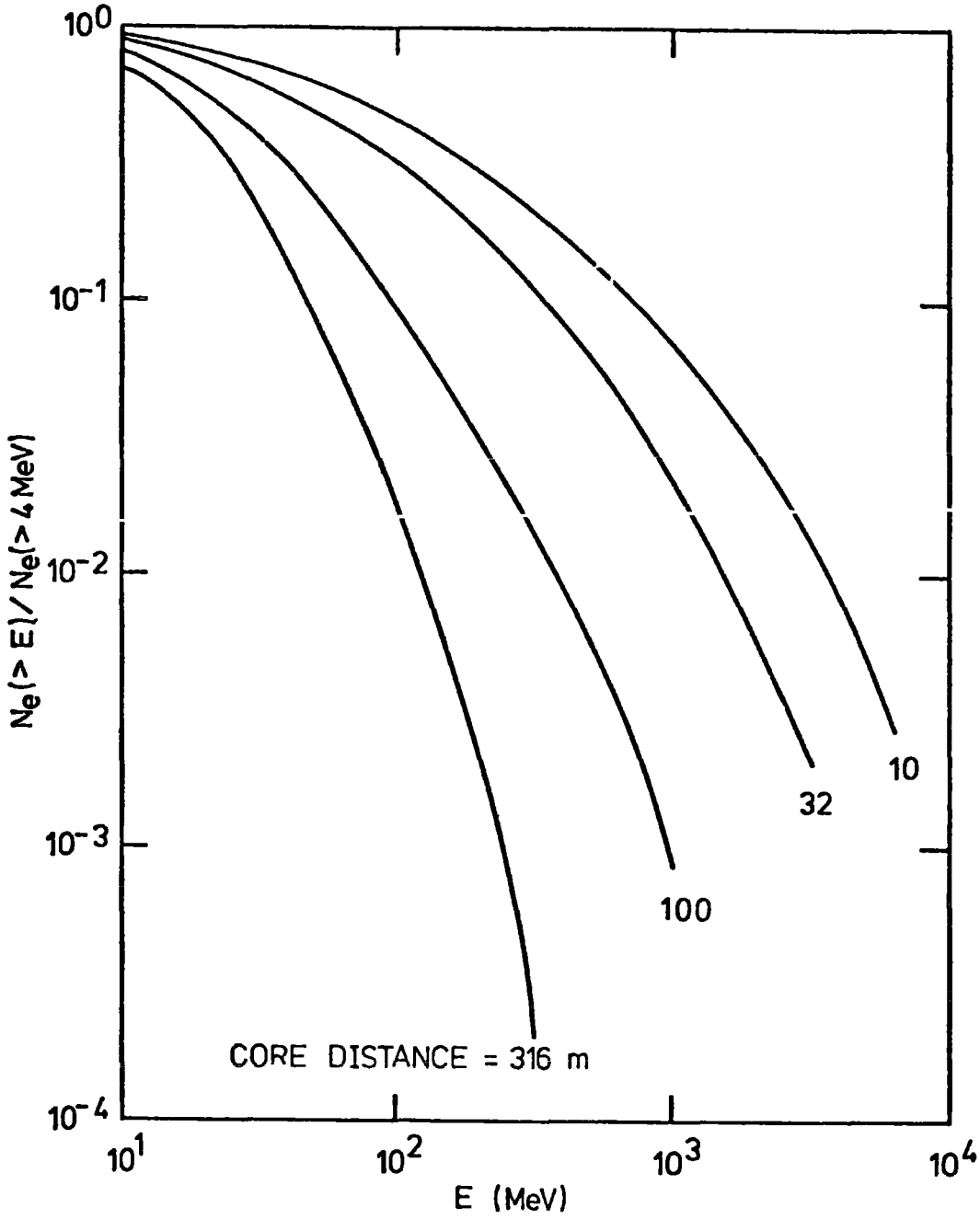

FIGURE 3-10 The integral energy spectra of electrons integrated over the length of the shower at various core distances (from the present work).

The r.m.s. and median cascade widths of electrons (E>4 MeV) from this calculation are compared with those obtained by Allan et al, Hillas and Lapikens in figure 11. The cascade widths are found to be broader than those of Allan et al, but in excellent agreement with those of Hillas and Lapikens.

The lateral distribution of electrons at a depth of 5 radiation lengths according to the present work is seen in figure 12 to be in excellent agreement with that obtained by Hillas but narrower than predicted by the NKG distribution. Figure 13 shows the r.m.s. angles of electrons and photons as a function of energy (particularly important in the calculation of the Cerenkov light component of cosmic ray showers) from the present work which are compared to those of Rossi and Nordheim (1949), Allan et al (1975) and Hillas and Lapikens (1977).

3-4 ELECTRON-PHOTON CASCADES IN LARGE COSMIC RAY SHOWERS

The electron-photon cascade of a large cosmic ray shower is fed by the decay of neutral pions (and kaons) into gamma-rays and by the decay of muons into electrons (and neutrinos, which are essentially lost from the cascade). Since in large cosmic ray showers at sea level the muon number is at least 100 times smaller than the electron number, muon decay may be neglected as a source of electrons in calculations of the electron-photon component.

In the rest system of a neutral pion, the decay is into two photons with equal and opposite momenta. The angular distribution of either photon is isotropic in the pion rest system resulting in a flat energy spectrum in the LAB system

$$f(E)dE = \frac{2\,dE}{E_\pi} \qquad (E < E_\pi) \qquad 15$$

where E_π is the energy of the neutral pion and E is the energy of a photon.

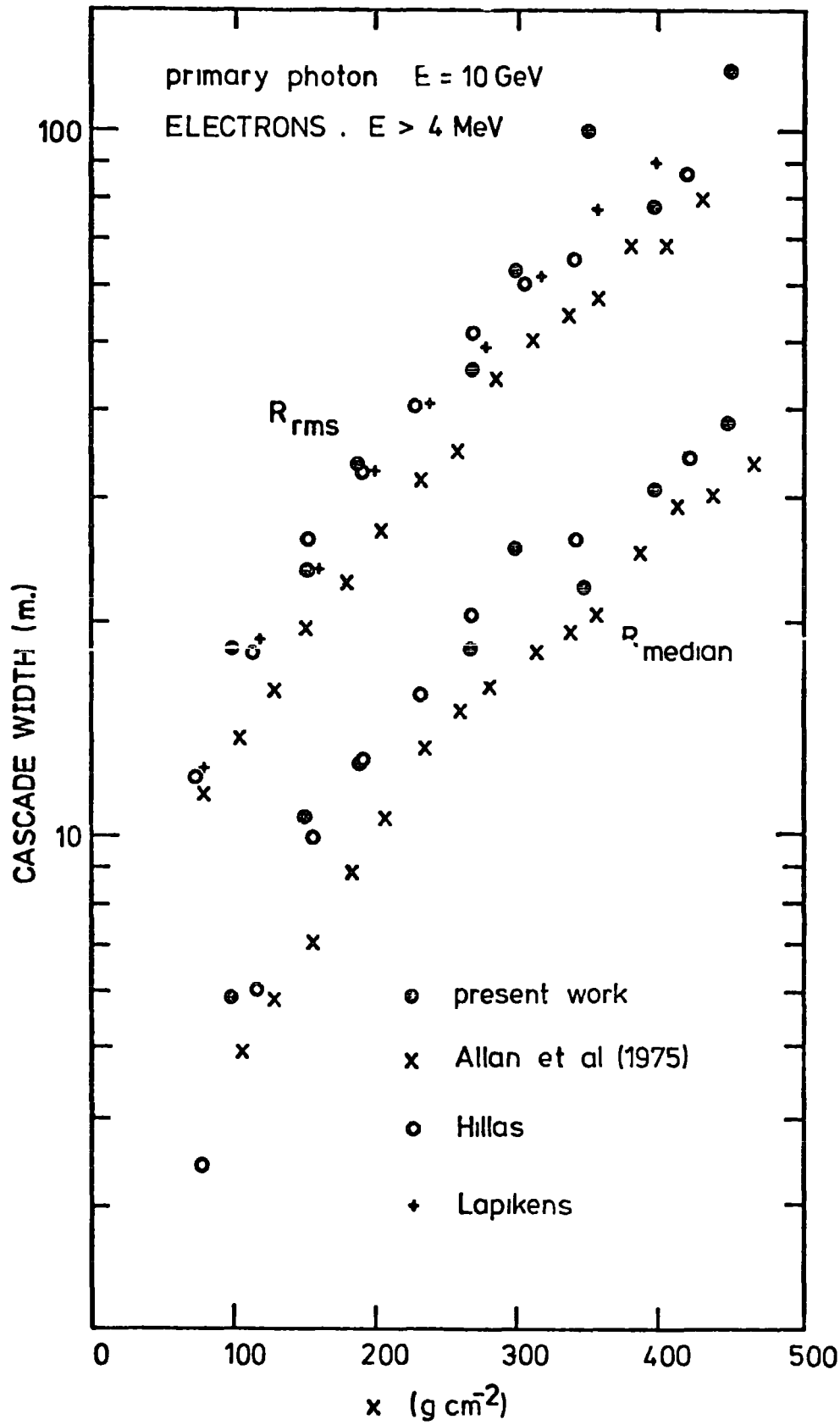

FIGURE 3-11 The r.m.s. and median electron radius from the present work is compared to that given by Allan et al (1975) and those given in Hillas and Lapikens (1977).

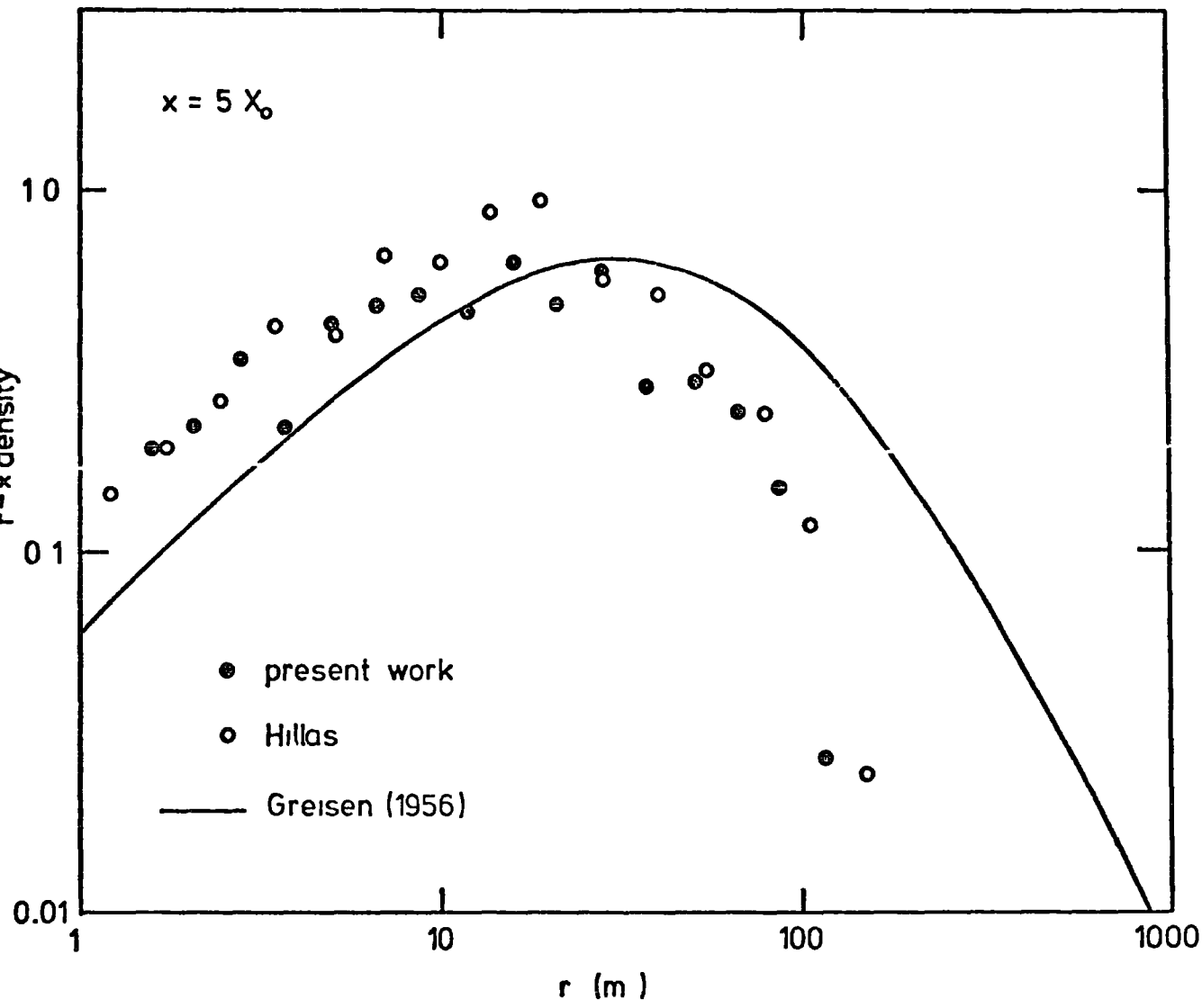

FIGURE 3-12 The lateral distribution of electrons (multiplied by core distance squared) from the present work is compared to that given in Hillas and Lapikens (1977) and to the NKG distribution

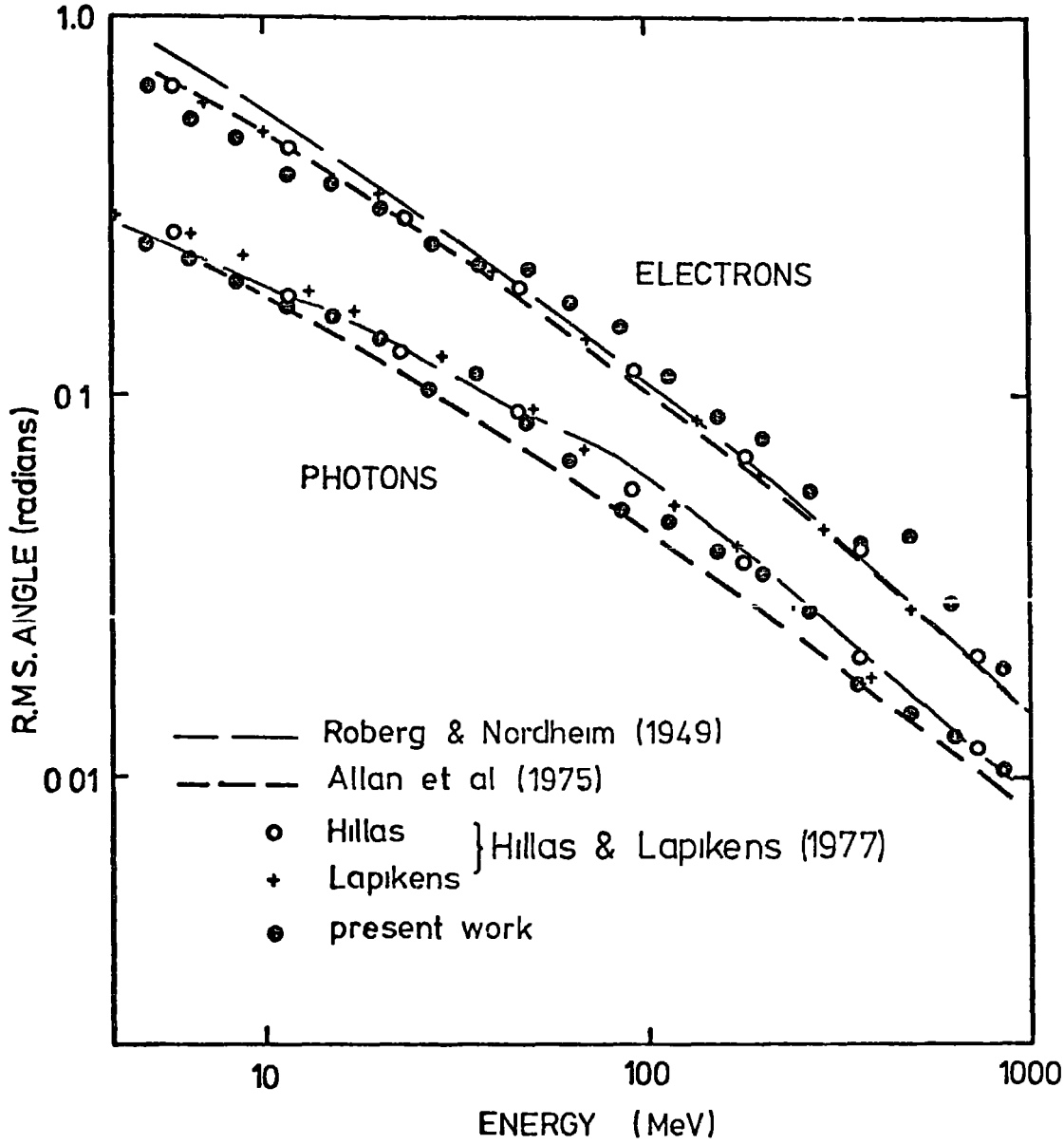

FIGURE 3-13 The r.m s. angle of electrons and photons from the present work is plotted as a function of energy and compared with other results.

3-4.1 Average cascade development under approximation B

The production spectra of neutral pions at 40 depths in the atmosphere are calculated by the hadron core program as described in chapter 2 and are converted using equation 15 to the spectra of photons resulting from pion decay at the 40 depths. These spectra are then used to weight electron cascades under approximation B given in equation 12 to give the electron cascade in the cosmic ray shower.

Results for average shower development calculated using the standard scaling model for pion production described in chapter 2 with the electron cascade calculated as described above for proton, helium nucleus and iron nucleus primaries are given in figures 14, 15 and 16 respectively for primary energies ranging from 10^6 GeV to 10^9 GeV.

The average development of electron cascades in proton initiated showers calculated using the standard scaling model but with the energy dependent inelastic hadron-air nucleus cross sections of figure 18 of chapter 2, are given in figures 17, 18 and 19. It is noted that as the cross sections become larger the number of electrons at cascade maximum increases.

3-4.2 Fluctuations in cascade development

Results from a sample of 20 individual proton initiated showers and 10 individual iron nucleus initiated showers with primary energy 5×10^8 GeV are given in figure 20. The thick lines give the mean electron number, $\bar{N}$, and the dashed lines give $\bar{N} \pm \sigma$ where σ is the r.m.s. deviation of N from $\bar{N}$. Also shown are the r.m.s.electron number, N_{rms}, which reproduce the cascade development as observed by the constant intensity cut method (see Gaisser and Hillas (1977)). For iron nucleus initiated showers the difference between $\bar{N}$ and N_{rms} is negligible due to the small fluctuations in cascade development whereas for proton initiated showers the difference is greater (the

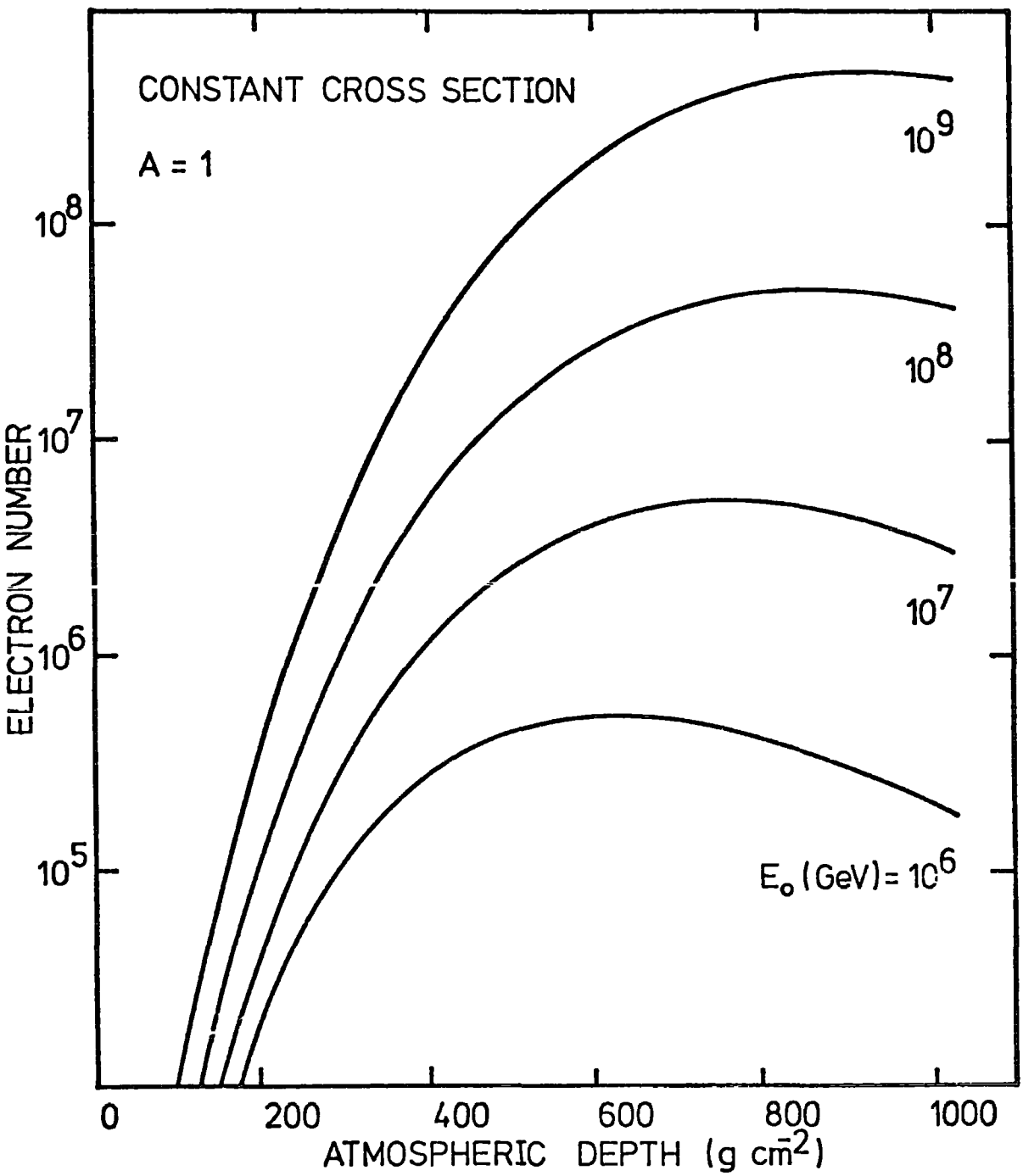

FIGURE 3-14 Average electron cascade development for primary proton initiated showers.

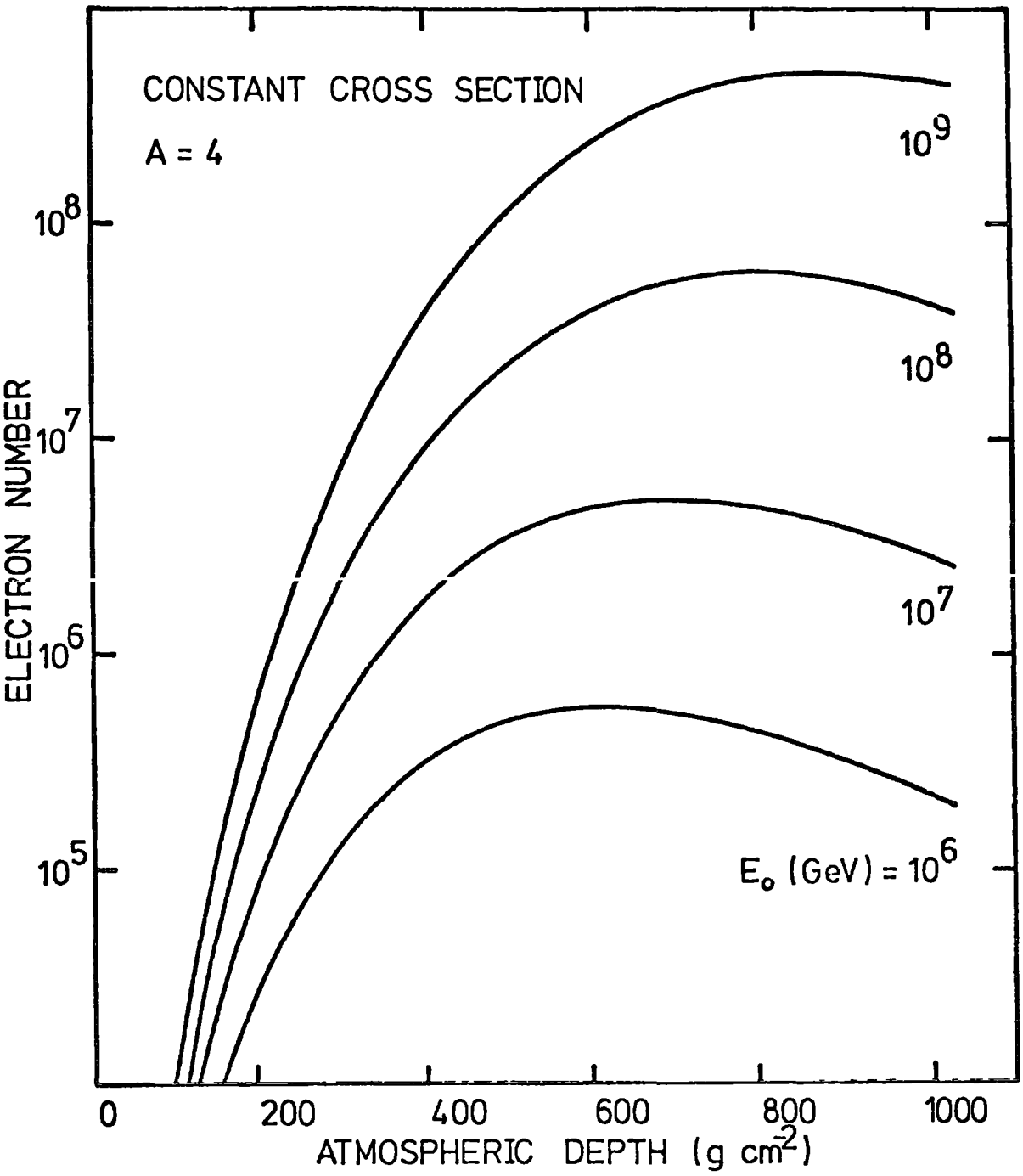

FIGURE 3-15 Average electron cascade development for primary helium nucleus initiated showers.

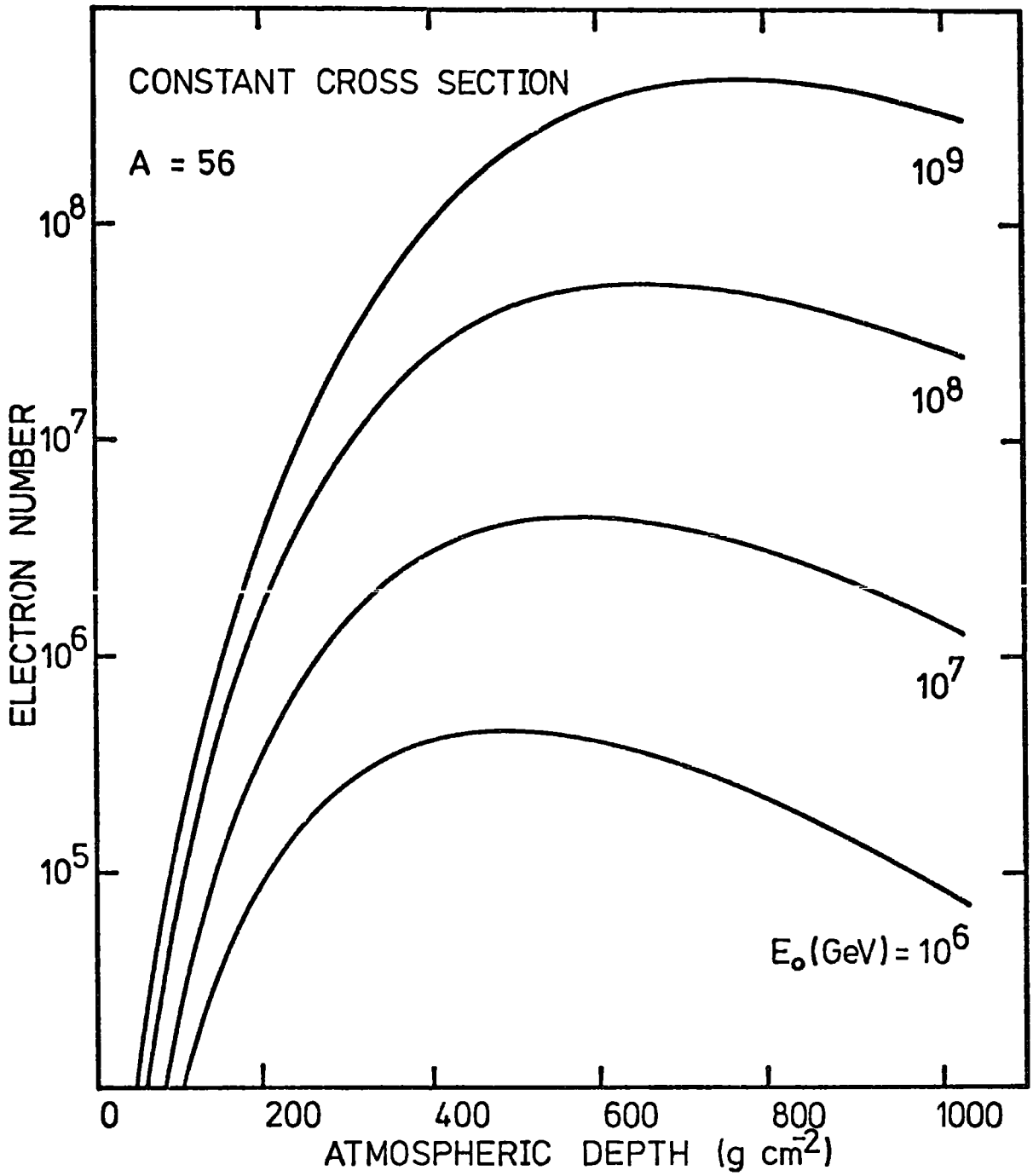

FIGURE 3-16 Average electron cascade development for primary iron nucleus initiated showers.

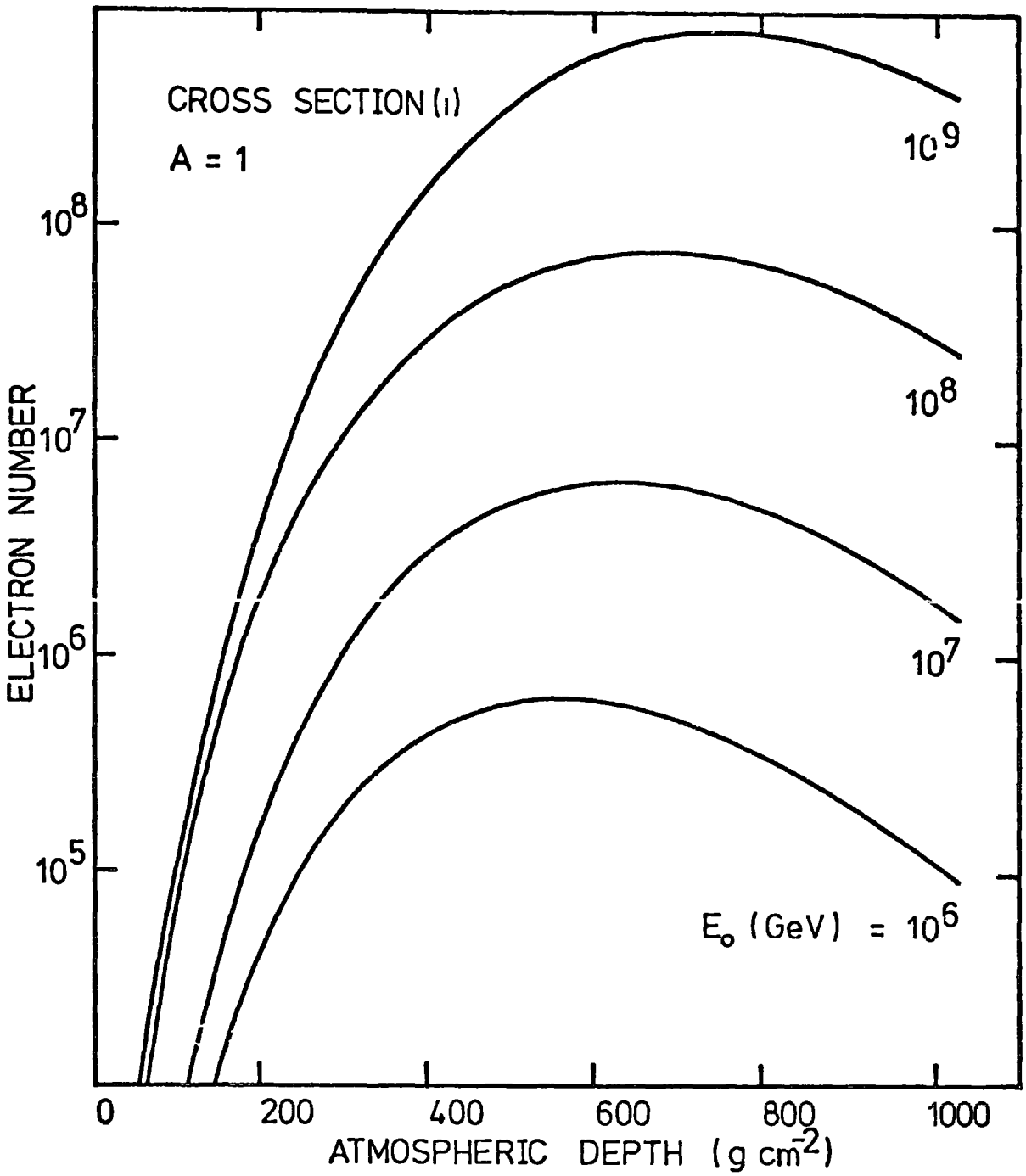

FIGURE 3-17 Average electron cascade development for primary proton initiated showers using the energy dependent cross sections (1) given in figure 18 of chapter 2.

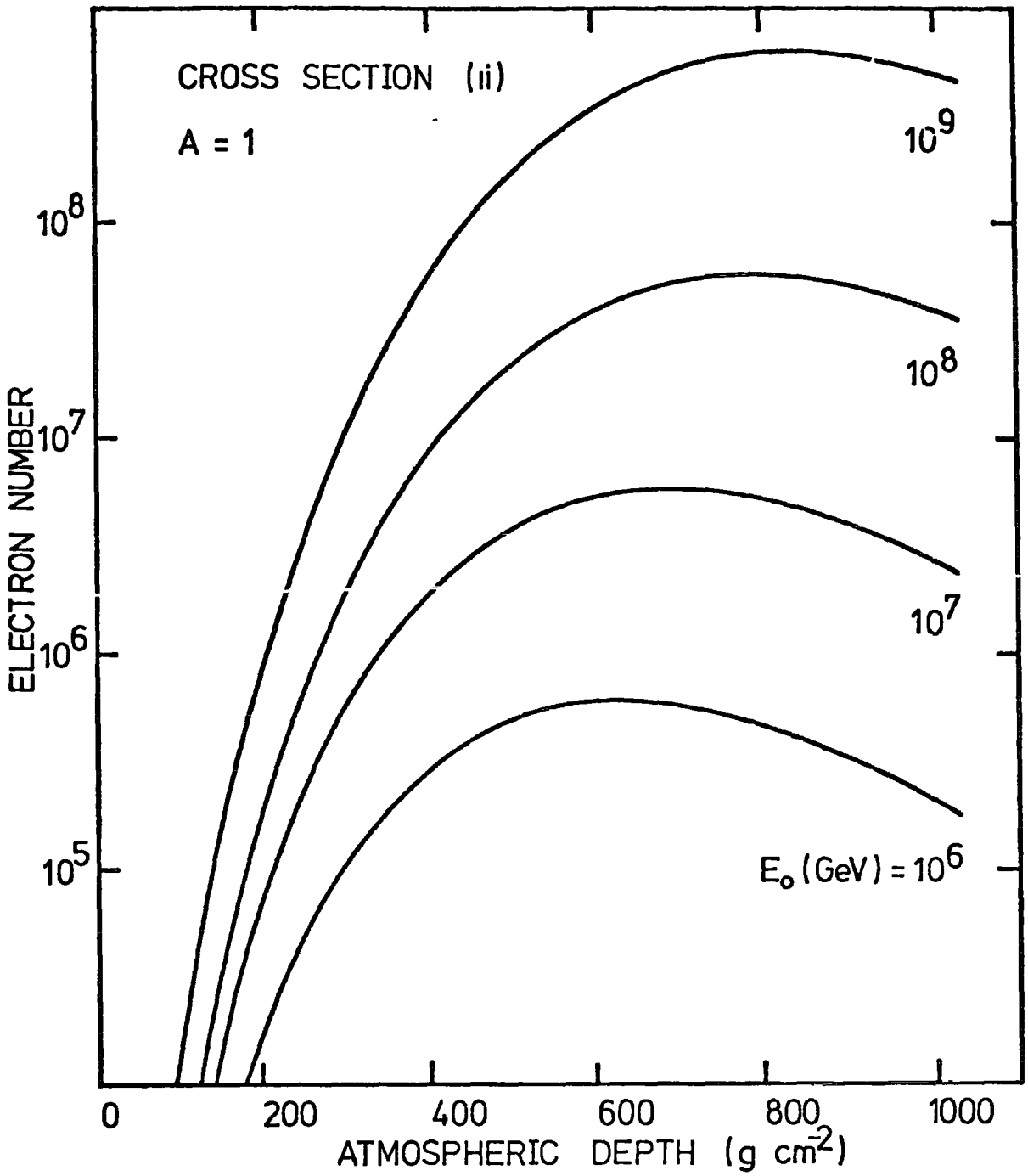

FIGURE 3-18 Average electron cascade development for primary proton initiated showers using the energy dependent cross sections (ii) given in figure 18 of chapter 2.

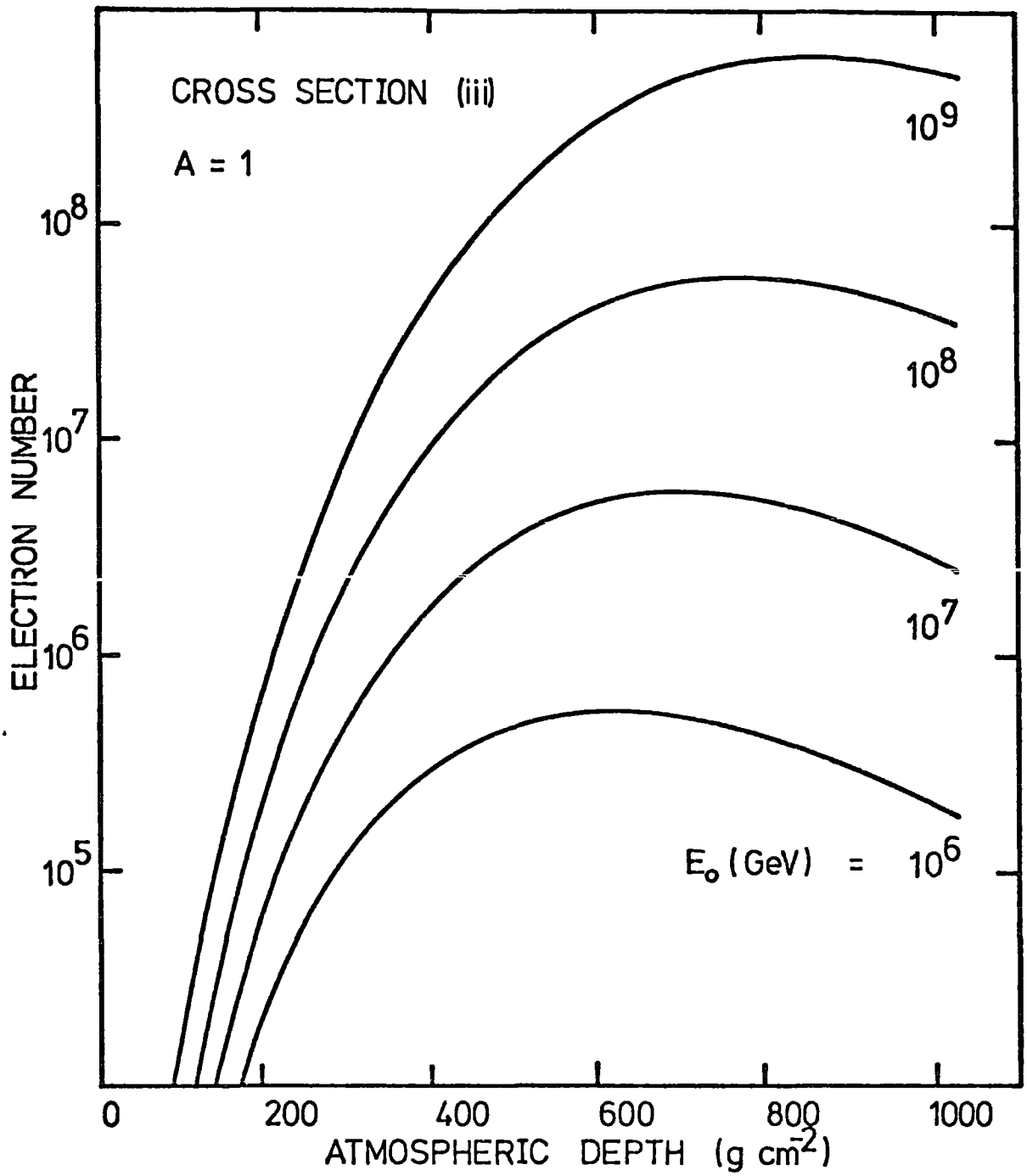

FIGURE 3-19 Average electron cascade development for primary proton initiated showers using the energy dependent cross sections (iii) given in figure 18 of chapter 2.

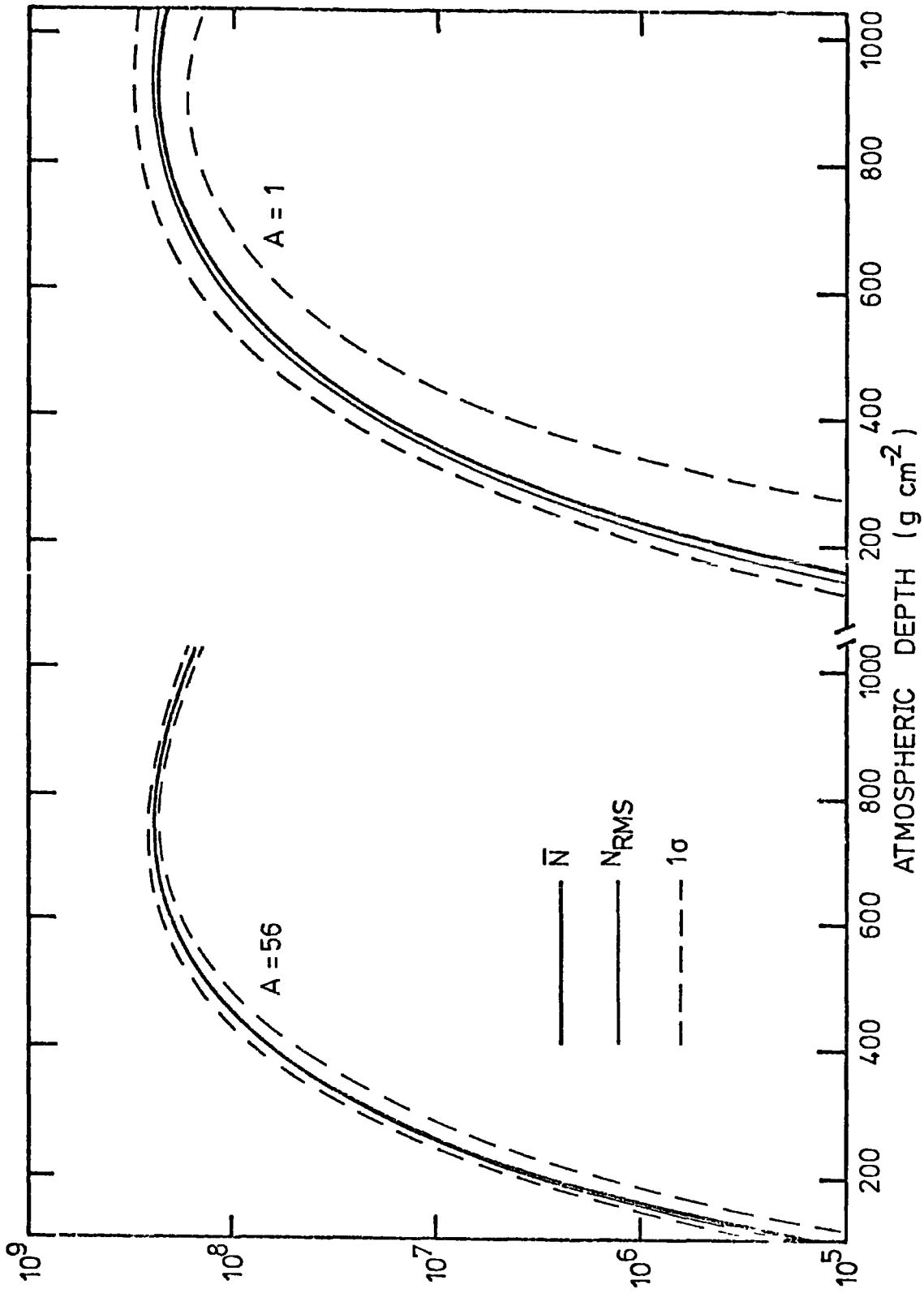

FIGURE 3-20 The mean and r.m.s. electron number development for iron nucleus and proton initiated showers with primary energy 5 x 10^{17}eV.

apparent depth of cascade maximum may be ~15 g cm^{-2} higher in the atmosphere than the true depth of cascade maximum) but is small in comparison to the accuracy obtained in typical experiments.

3-5 CALCULATION OF THE ELECTRON-PHOTON COMPONENT USING THE APPROXIMATION A + MONTE CARLO TECHNIQUE

It has been customary to calculate the lateral distribution of electrons in cosmic ray showers from the NKG distribution but, as has been pointed out earlier in this chapter, recent Monte Carlo calculations have shown that the NKG function overestimates the electron cascade width. The analytic approach is also unsuitable for the calculation of Cerenkov light emission where detailed information about shower structure is required.

It is impractical to use the Monte Carlo technique to simulate the electron-photon cascade in large cosmic ray showers because the number of particles which would have to be followed is so large that the computing time required for the calculation would be prohibitive. This problem is overcome by following the development of the high energy part of the cascade in one-dimension using numerical methods and then using the results of detailed three dimensional Monte Carlo calculations to consider the low energy part of the cascade. In the present work the cascade of particles with energies greater than 75 GeV is followed under approximation A (at these energies the cascade is essentially one-dimensional and approximation A is valid) using the "step-by-step" method (see Dedenko (1966) and Hillas (1966)). Particles generated in this way with energies below 75 GeV are removed from the cascade and binned in a standard depth-energy matrix (similar to those used to store pion production spectra described in chapter 2) and used to weight the results of the detailed Monte Carlo calculations in order to obtain the electron and photon lateral distributions for the large cosmic ray shower.

3-5.1 Numerical calculations under appoximation A

The equations which analytically describe the development of an electron-photon cascade are given by Rossi (1952),

$$\left.\begin{aligned}\frac{\partial \pi(E,t)}{\partial t} &= -\pi(E,t)\mu_{\pi}(E) + \int_{E}^{\infty} \pi(E',t)\ \varphi_{\pi\pi}(E',E)dE' \\ &\quad + \int_{E}^{\infty} \gamma(E',t)\ \varphi_{\gamma\pi}(E',E)dE' \\ \frac{\partial \gamma(E,t)}{\partial t} &= \int_{E}^{\infty} \pi(E',t)\ \varphi_{\pi\gamma}(E',E)dE' \\ &\quad + \int_{E}^{\infty} \gamma(E',t)\ \varphi_{\gamma\gamma}(E',E)dE' - \gamma(E,t)\ \mu_{\gamma}(E)\end{aligned}\right\} \quad 16$$

where $\pi(E,t)dE$ and $\gamma(E,t)dE$ are the numbers of electrons and photons, respectively, with energies between E and (E + dE) at a depth of t radiation lengths,

$\varphi_{ab}(E',E)dE$ is the probability per radiation length for a particle of type a with energy E' to produce a particle of type b with energy E in dE,

$\mu_{a}(E)$ is the probability per radiation length of a particle of type a with energy E interacting.

Under approximation A only radiation processes are considered, the assymptotic cross sections being used to describe bremsstrahlung and pair production as shown in figure 21.

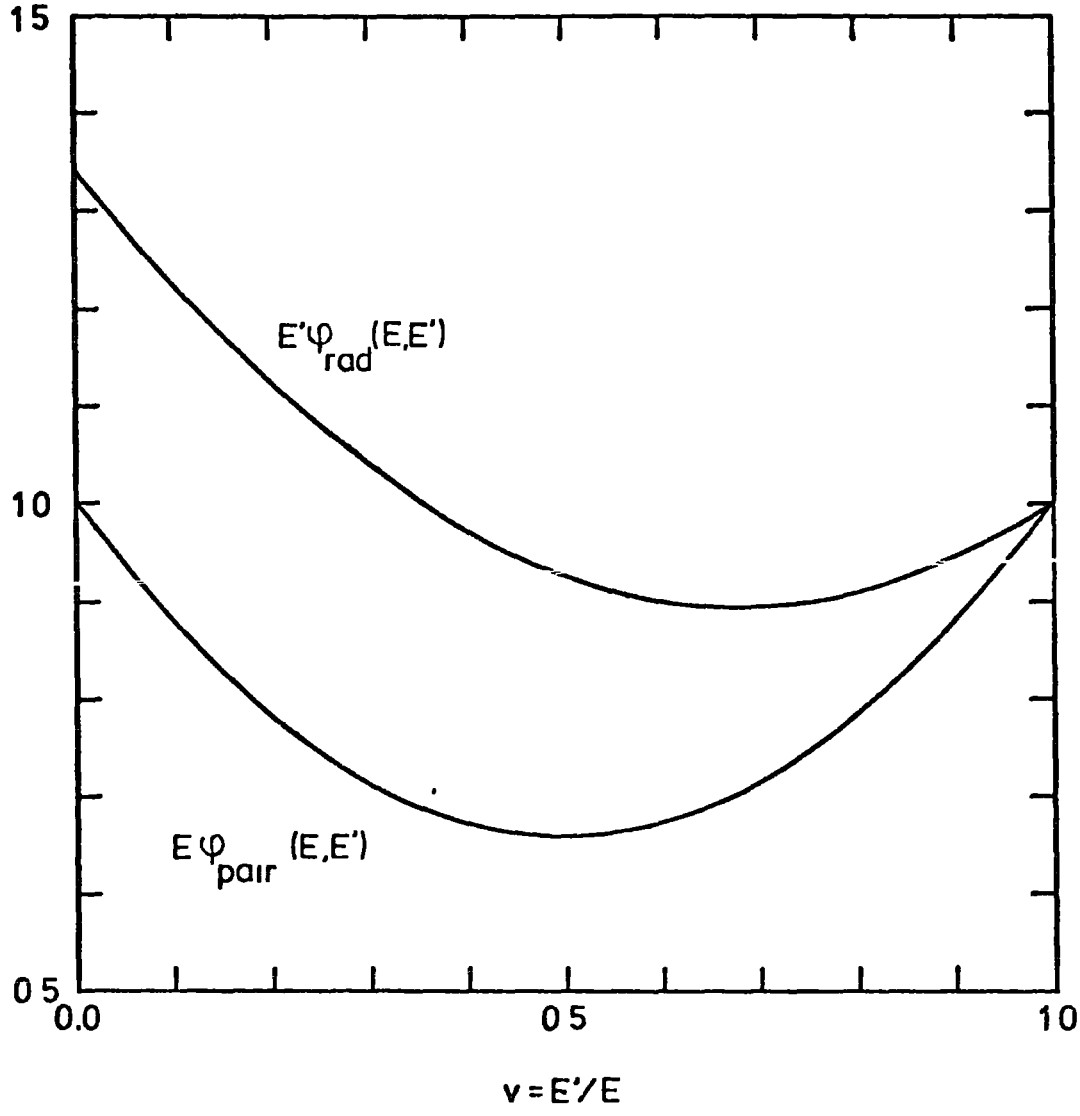

FIGURE 3-21 The assymptotic cross sections for bremsstrahlung and pair production (see text for explanation).

Hence,

$$\left.\begin{aligned} \varphi_{\gamma\pi}(E',E) &= 2\,\varphi_{pair}(E',E) = \frac{2}{E'}\,\psi_{pair}(E/E'), \\ \varphi_{\pi\pi}(E',E) &= \varphi_{rad}(E',E'-E) = \frac{1}{E'}\,\psi_{rad}\left(\frac{E'-E}{E'}\right), \\ \varphi_{\pi\gamma}(E',E) &= \varphi_{rad}(E',E) = \frac{1}{E'}\,\psi_{rad}(E/E'), \\ \varphi_{\gamma\gamma}(E',E) &= 0\ , \end{aligned}\right\} \quad 17$$

and,

$$\left.\begin{aligned} \mu_{\pi}(E') &= \int_0^{E'} \psi_{rad}(E/E')\,dE/E', \\ \mu_{\gamma}(E') &= \int_0^{E'} \psi_{pair}(E/E')\,dE/E' = \mu_o\ , \end{aligned}\right\} \quad 18$$

where

$$\left.\begin{aligned} \psi_{rad}(v) &= \frac{1}{v}\left[1 + (1-v)^2 - (1-v)\left(\frac{2}{3} - 2b\right)\right]\ , \\ \psi_{pair}(v) &= v^2 + (1-v)^2 + \left(\frac{2}{3} - 2b\right)(1-v)v\ , \\ b &= \left[18\,\ln(183\,Z^{-1/3})\right]^{-1}\ , \end{aligned}\right\} \quad 19$$

then,

$$\mu_o = \frac{7}{9} - \frac{b}{3}\ . \qquad 20$$

In the present work the electron-photon cascade development was calculated by the step-by-step method using procedures similar to those described by Marsden (1971). A series of logarithmic energy bins was used to store the differential energy spectra $\pi(E,t)$ and $\gamma(E,t)$ at a given

depth. The mid energy of the $(i+1)^{th}$ bin, E_{i+1}, is related to the mid energy of the i^{th} bin, E_i, by

$$E_{i+1} = F^2 E_i \quad . \qquad 21$$

Given the number of electrons and photons in all energy bins, i, at depth t, $\Pi(i,t)$ and $\gamma(i,t)$ the spectra at depth $(t+\Delta t)$ may be obtained from

$$\left.\begin{aligned} \Pi(i,t+\Delta t) &= \sum_{n=0}^{\infty} \left\{ ee_n \Pi(i+n,t) + ge_n \gamma(i+n,t) \right\} \\ \gamma(i,t+\Delta t) &= \sum_{n=0}^{\infty} \left\{ gg_n \gamma(i+n,t) + eg_n \Pi(i+n,t) \right\} \end{aligned}\right\} \qquad 22$$

where ee_n, ge_n, gg_n and eg_n are the "approximation A operators". Calculation of the approximation A operators is described in Appendix C. A computer program based on equation 22 was used to calculate electron-photon cascades under approximation A.

3-5.2 Tests of the step-by-step program

The sensitivity of the calculated electron development to the "step size", Δt in radiation lengths, is given in figure 22 which shows the electron longitudinal development calculated for three values of Δt. It is apparent that the minimum step size for reasonable accuracy is less than one eighth of a radiation length.

The sensitivity of the calculated electron development to F^2 (related to the width of the energy bins) is shown in figure 23 from which it isseen that for reasonable accuracy F^2 should be less than $10^{\frac{1}{8}}$ (the value used by Marsden (1971)).

Results of the step-by-step program using $\Delta t = X_o/32$ and $F^2 = 10^{1/32}$ for an electron primary are given in figure 24 where they are found to be in good agreement with the results of analytic calculations by Rossi

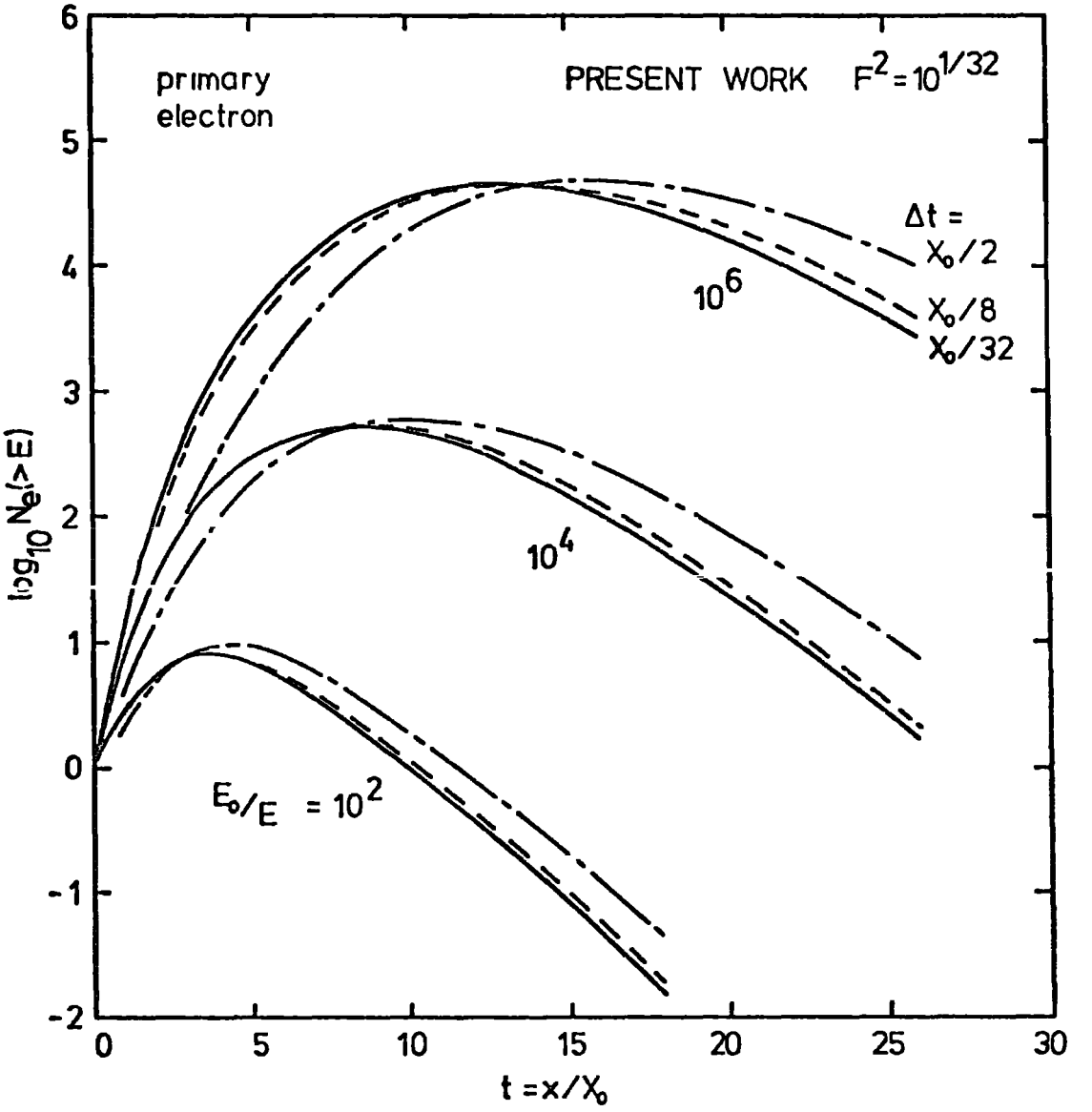

FIGURE 3-22 The sensitivity of the step-by-step calculations to step size Δt (see text).

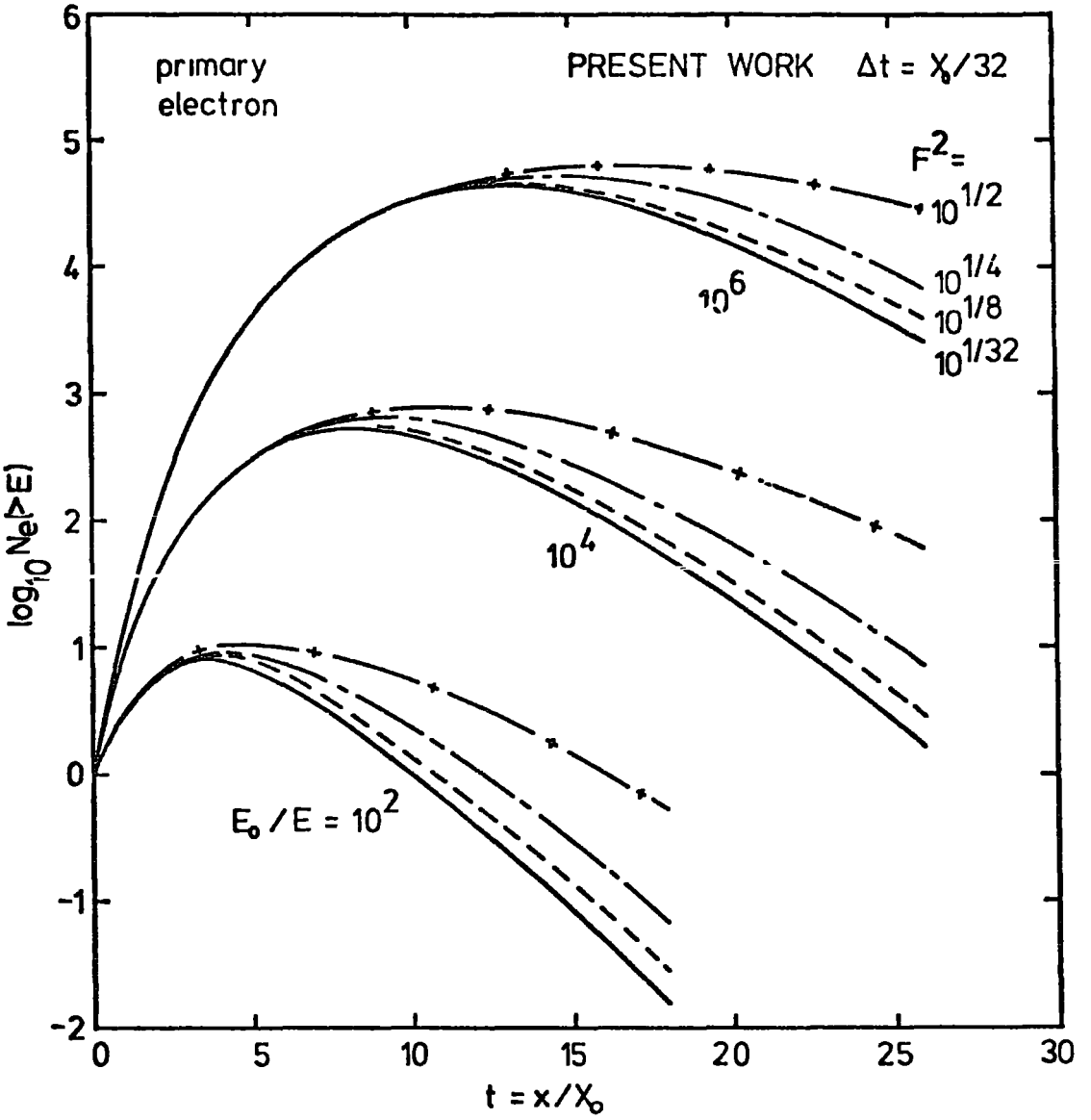

FIGURE 3-23 The sensitivity of the step-by-step calculations to energy bin size (related to F^2, see text).

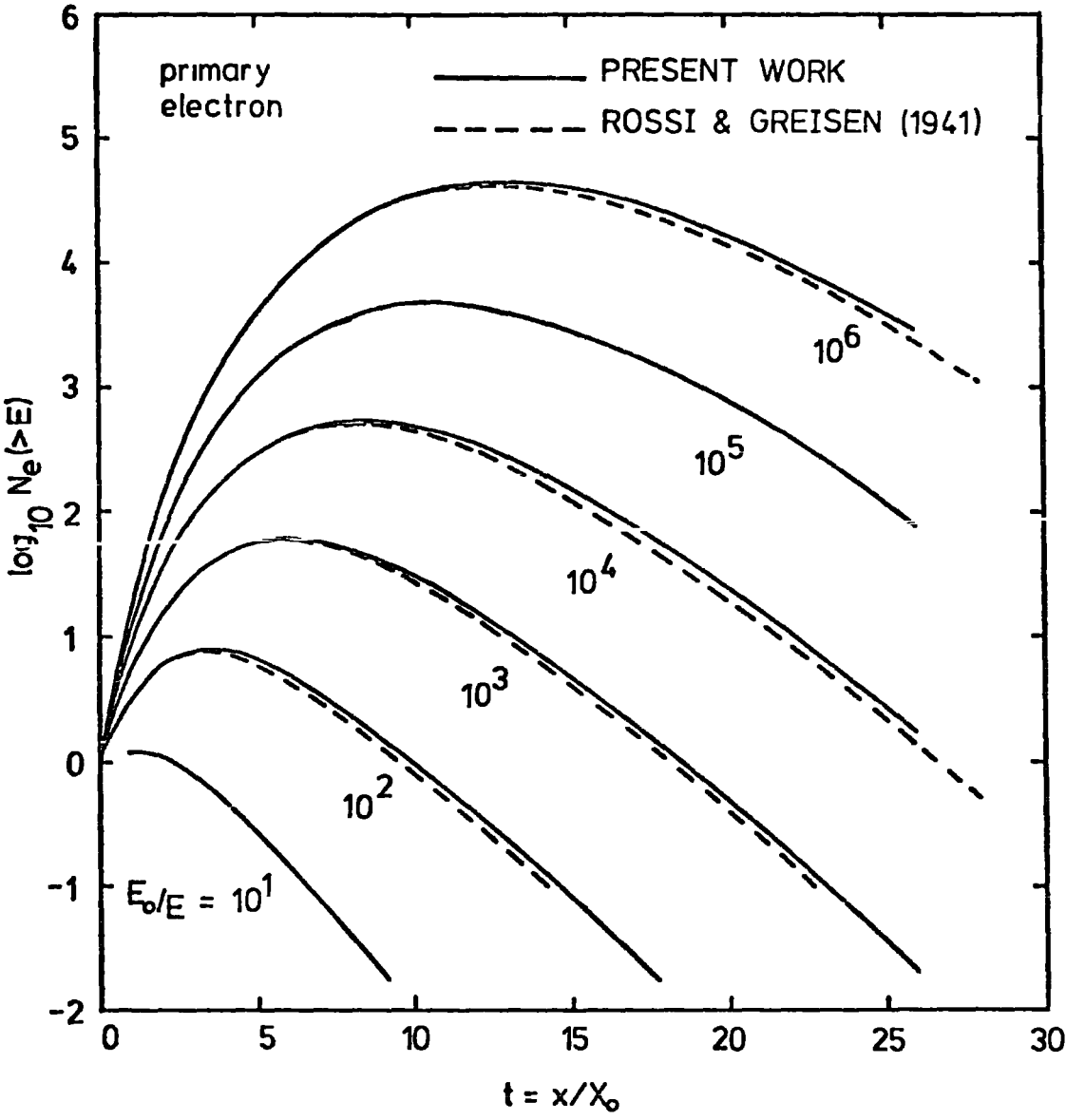

FIGURE 3-24 Comparison of the longitudinal development of the electron cascade under approximation A from the present work with the analytic result of Rossi and Greisen (1941).

and Greisen (1941). The electron and photon cascade development under approximation A in the present work (using the same step size and energy bins) are shown in figure 25 for a primary photon and in figure 26 for a primary electron.

3-5.3 Tests of the approximation A + Monte Carlo technique

The approximation A + Monte Carlo technique may be readily checked by using the parameterization of results calculated under approximation B (given in equation 12) in place of the results of the detailed Monte Carlo calculations of low energy cascades. The result obtained in this way from the pion production spectrum of a given cosmic ray shower should then be identical to that obtained by using the approximation B results for the whole cascade. This is because approximation B reduces to approximation A for electron and photon energies much in excess of the critical energy.

The longitudinal electron cascade development for a 10^{18} eV shower has been calculated under Approximation B and also under approximation A (E>75 GeV) + Approximation B (E<75 GeV) and is shown in figure 27 where the good agreement shows that the approximation A + Monte Carlo technique is valid.

The longitudinal cascade development of electrons with kinetic energy greater than 4 MeV and 20 MeV calculated using the approximation A + Monte Carlo technique is compared to that calculated completely under approximation B (all electrons, kinetic energy>0) in figure 28 for the same shower. The result is consistent with the energy spectrum of electrons given by Richards and Nordheim (1948) (see figure 9) at all depths in the atmosphere.

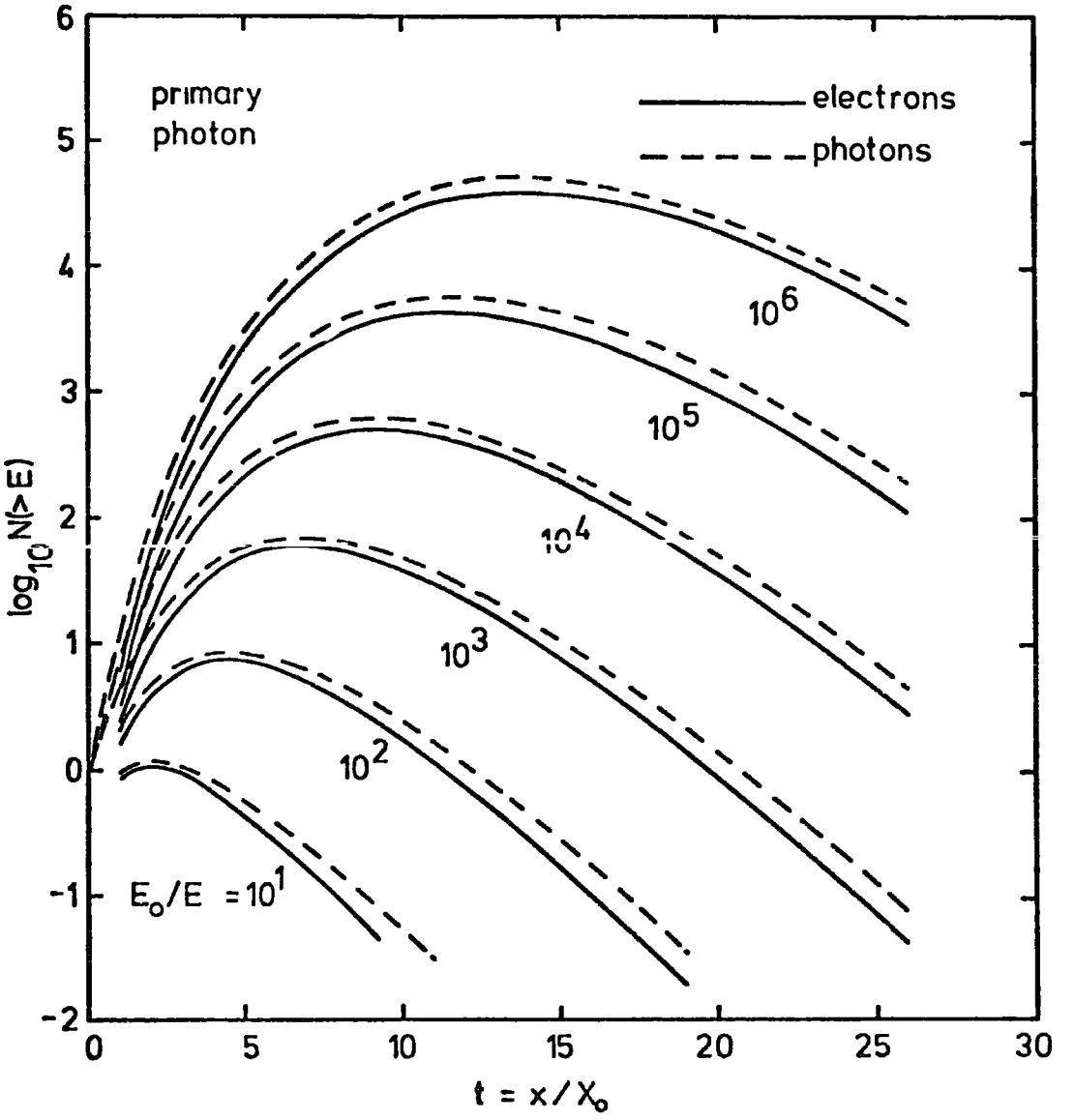

FIGURE 3-25 The electron and photon cascade development under approximation A for a primary photon.

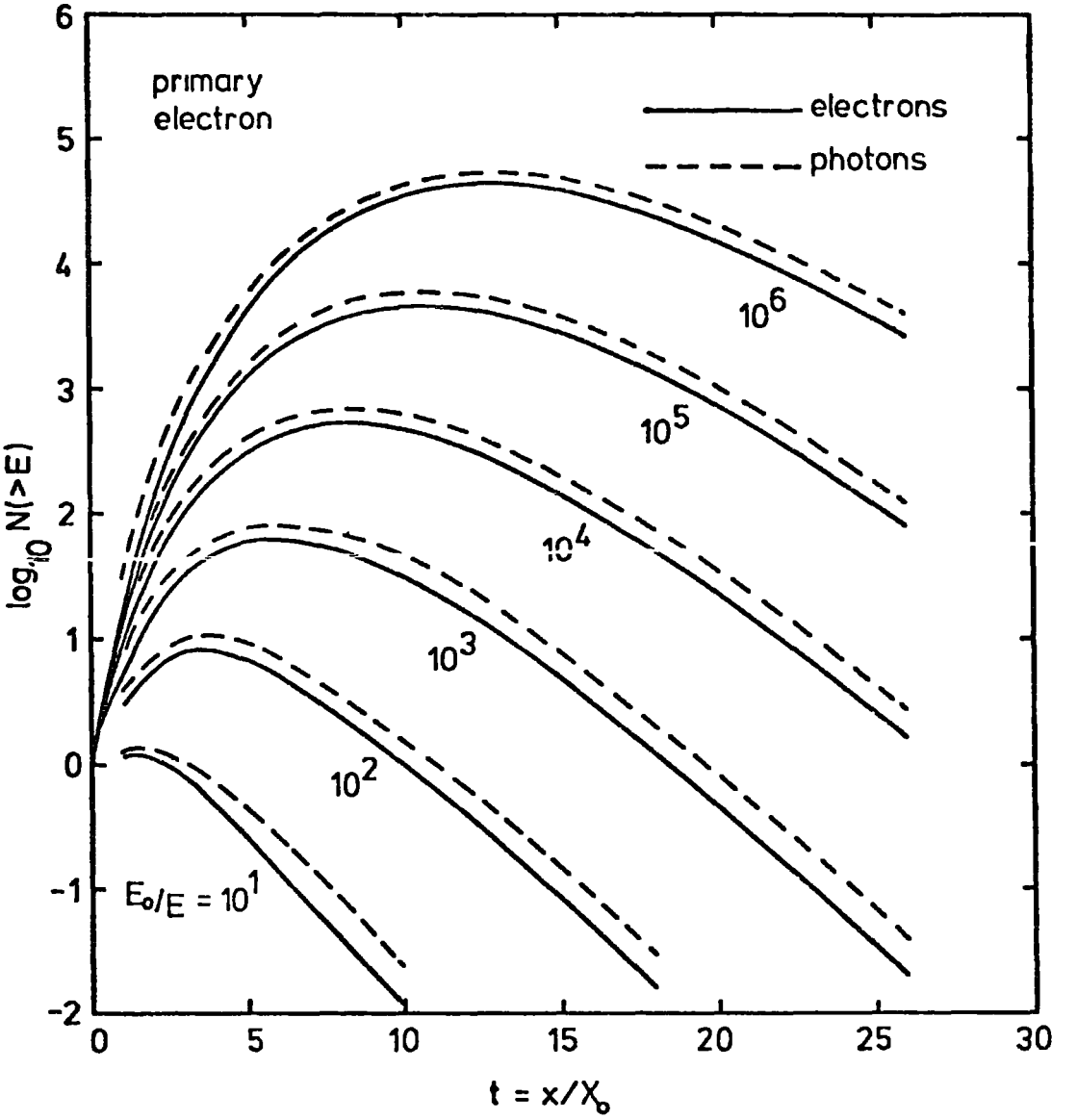

FIGURE 3-26 The electron and photon cascade development under approximation A for a primary electron.

12 APR 1978
SECTION LIBRARY

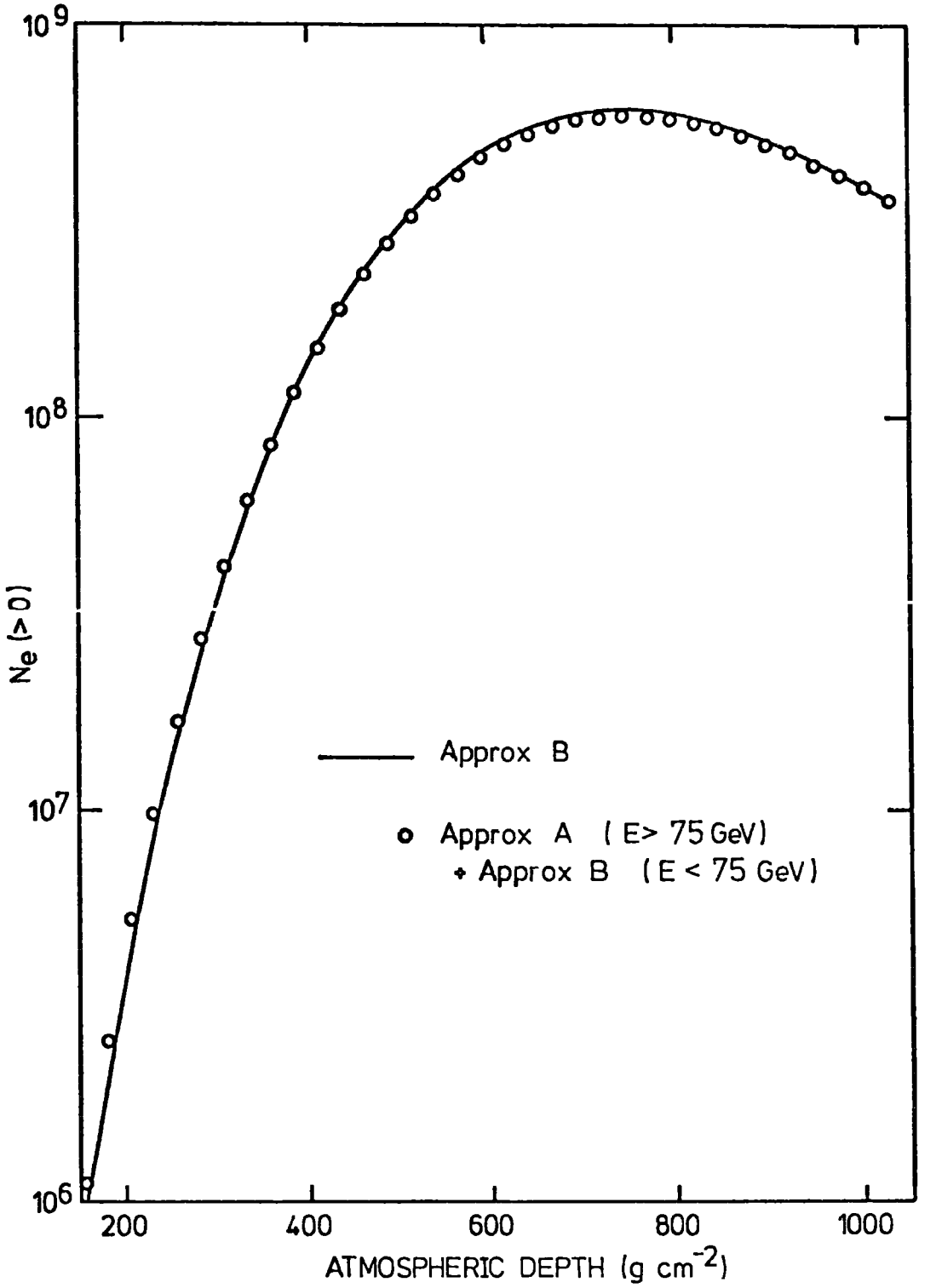

FIGURE 3-27 The electron cascade development for a 10^{18}eV shower calculated under approximation B and using "approximation A + approximation B" (see text for explanation)

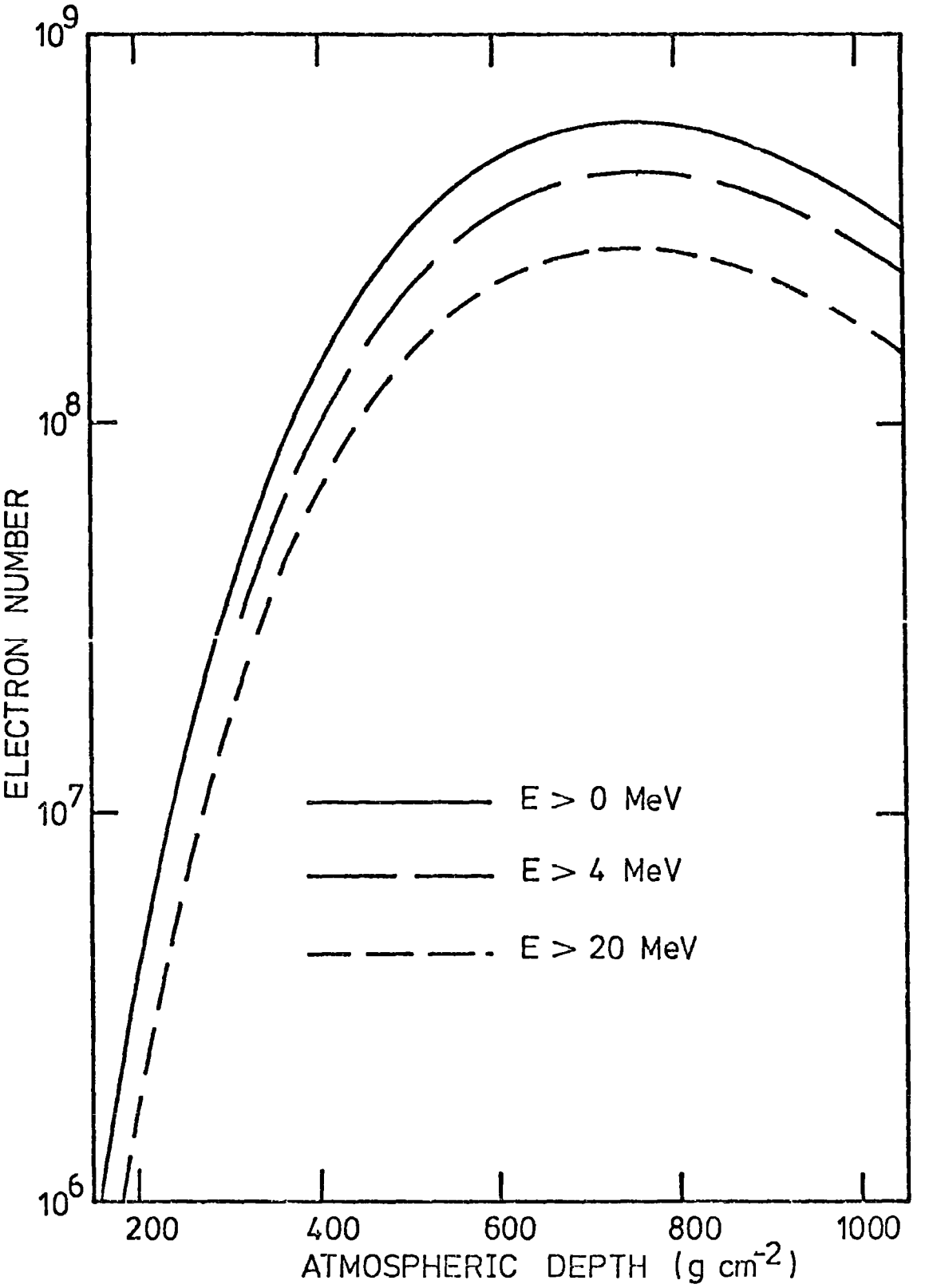

FIGURE 3-28 The longitudinal cascade development of electrons with kinetic energies greater than 0, 4 and 20 MeV in the same shower.

3-6 LATERAL DISTRIBUTION OF ELECTRONS AND PHOTONS IN LARGE COSMIC RAY SHOWERS

The lateral distribution of electrons and photons (>4 MeV) in the average 10^{17} eV proton initiated shower calculated using the CKP model (Cocconi et al (1961)) for pion production and the approximation A + Monte Carlo technique for the electron-photon cascade is compared in figure 29 with the results of Marsden (1971) who used essentially similar techniques. The discrepancy is thought to arise from the difference between the primary zenith angle used in the present work ($\vartheta = 0$) and by Marsden ($\vartheta = 25^{o}$).

Results for the standard scaling model are given in figure 30 which shows the lateral distribution of electrons and photons (>4 MeV) in proton and iron nucleus initiated showers of primary energy 10^{16} eV, 10^{17}eV and 10^{18} eV. Showers which develop high in the atmosphere are seen to have flatter lateral distributions than showers developing low in the atmosphere.

3-7 RESPONSE OF HAVERAH PARK DETECTORS TO THE ELECTRON-PHOTON COMPONENT

The Haverah Park particle detector array consists of water Cerenkov detectors ~1.2 m deep viewed by photomultiplier tubes. These detectors are sensitive both to the electron-photon and muon components of cosmic ray showers. A muon passing vertically through the tank will produce $\sim 2.47 \times 10^{4}$ optical photons by Cerenkov radiation whereas an electron or photon incident on the detector will initiate an electron-photon cascade in the water, the number of optical photons emitted depending on the energy deposited by the cascade.

Simulations of electron-photon cascades in 1.2 m of water initiated by electrons and photons with energies up to 1 GeV have been made by Browning, Protheroe and Turver (1976, unpublished) to calculate the Cerenkov light photon yield of the Haverah Park detectors. The

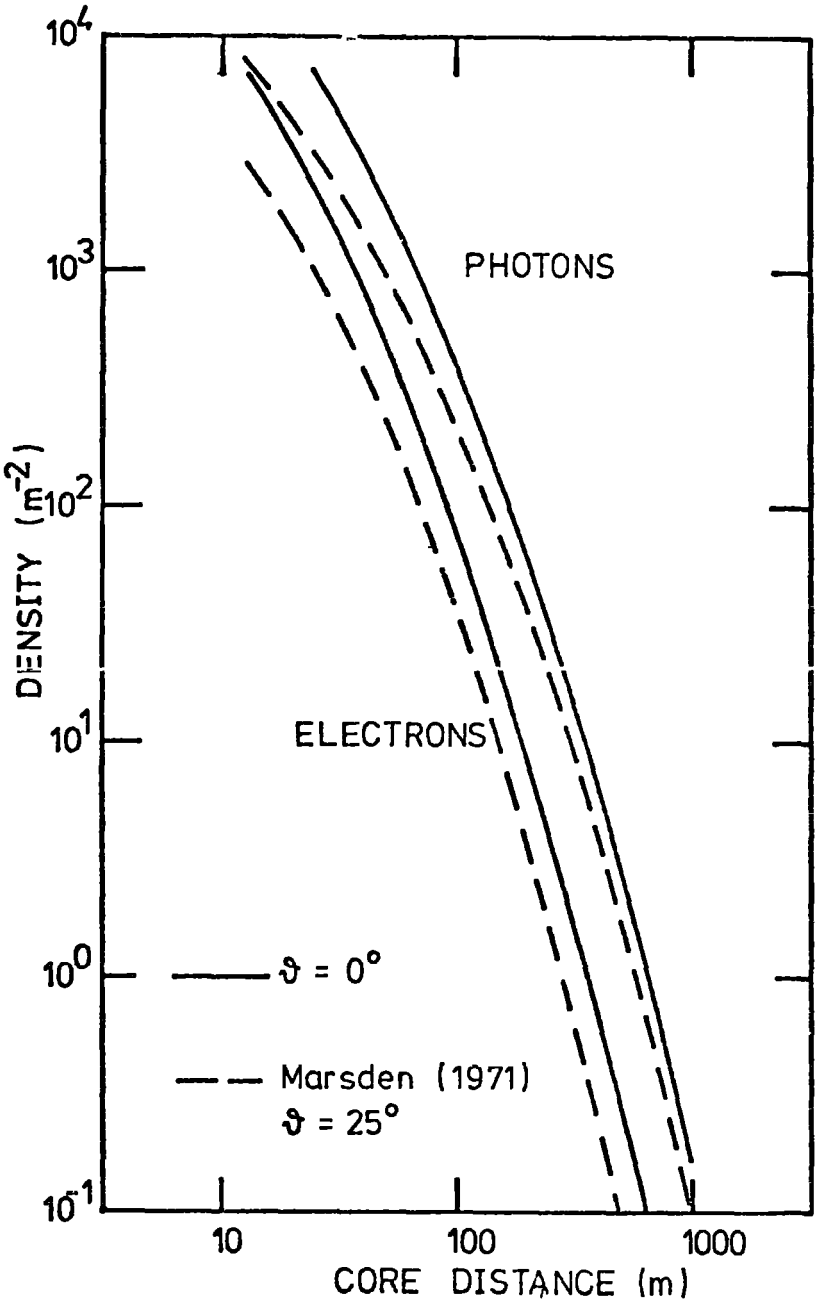

FIGURE 3-29 The lateral distribution of electrons and photons (>4 MeV) for a 10^{17} eV CKP proton initiated shower from the present work is compared to that given by Marsden (1971).

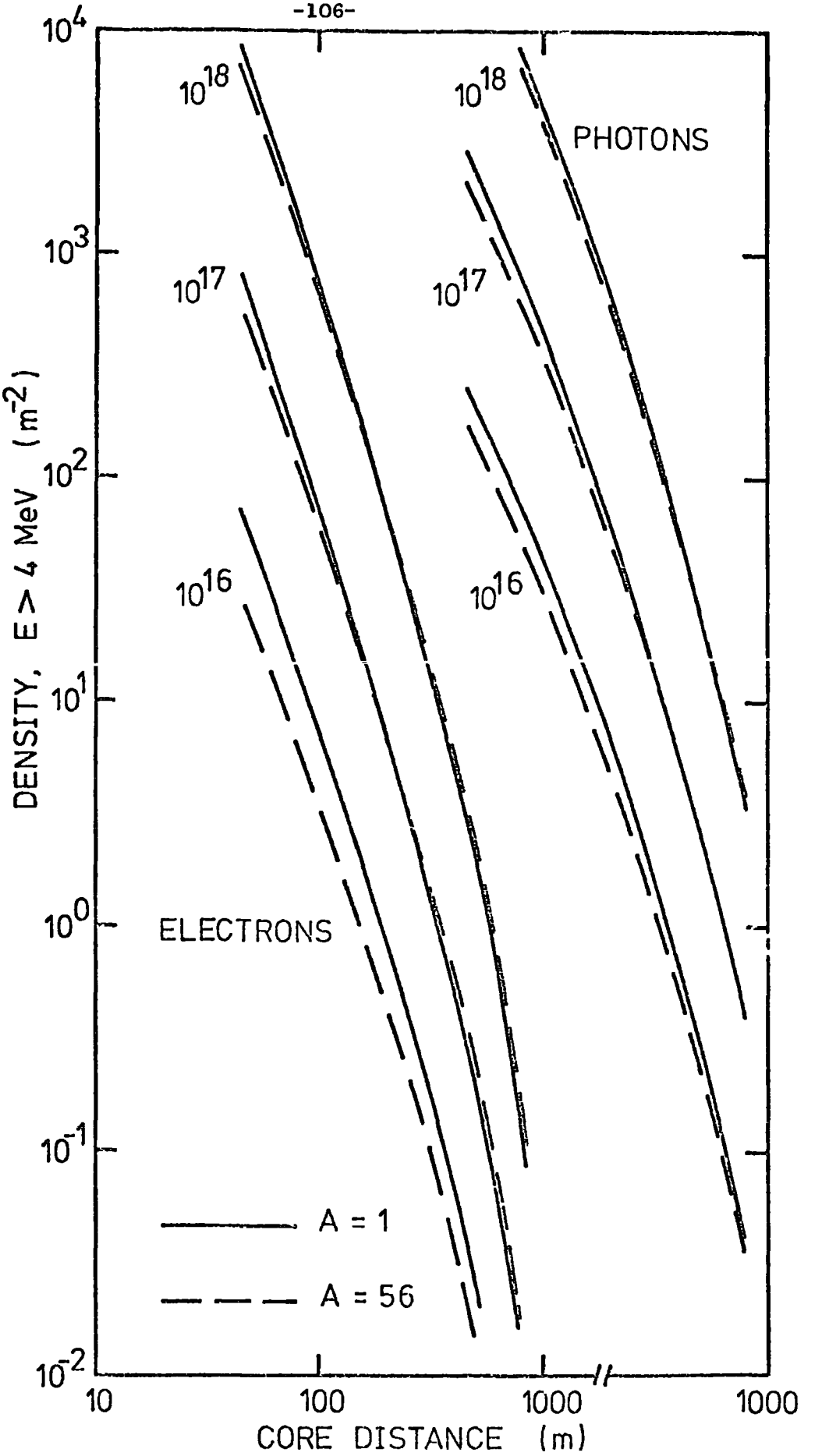

FIGURE 3-30 The lateral distribution of electrons and photons in proton and iron nucleus initiated showers. The numbers attached to the curves are the primary energies (eV).

mean optical photon yield as a function of the energy of an electron or photon incident on a 1.2 m deep water detector is given in figure 31. In practice the detector response depends on the position on the detector at which the particle is incident as the light received by the photo-multiplier is reflected within the walls of the detector, but no attempt has been made to include these effects.

The particle densities recorded by the Haverah Park detectors are given in vertical equivalent muons m^{-2} since their response is calibrated by observing the photon yield of a single vertical cosmic ray muon. Results from the present work for the lateral distribution of electrons, photons and deep water detector response are given in figure 32 for the average 10^{18} eV proton initiated shower calculated using the CKP model for pion production. The results of Dixon and Turver (1974) based on the data of Messel and Crawford (1970) for the electron densities and data of Marsden (1971) for the deep detector response are also shown.

The Haverah Park deep detector response to the soft (electron-photon) component for showers calculated using the standard scaling model for pion production will be given in chapter 4 where it will be discussed together with the response of these detectors to the hard (muon) component.

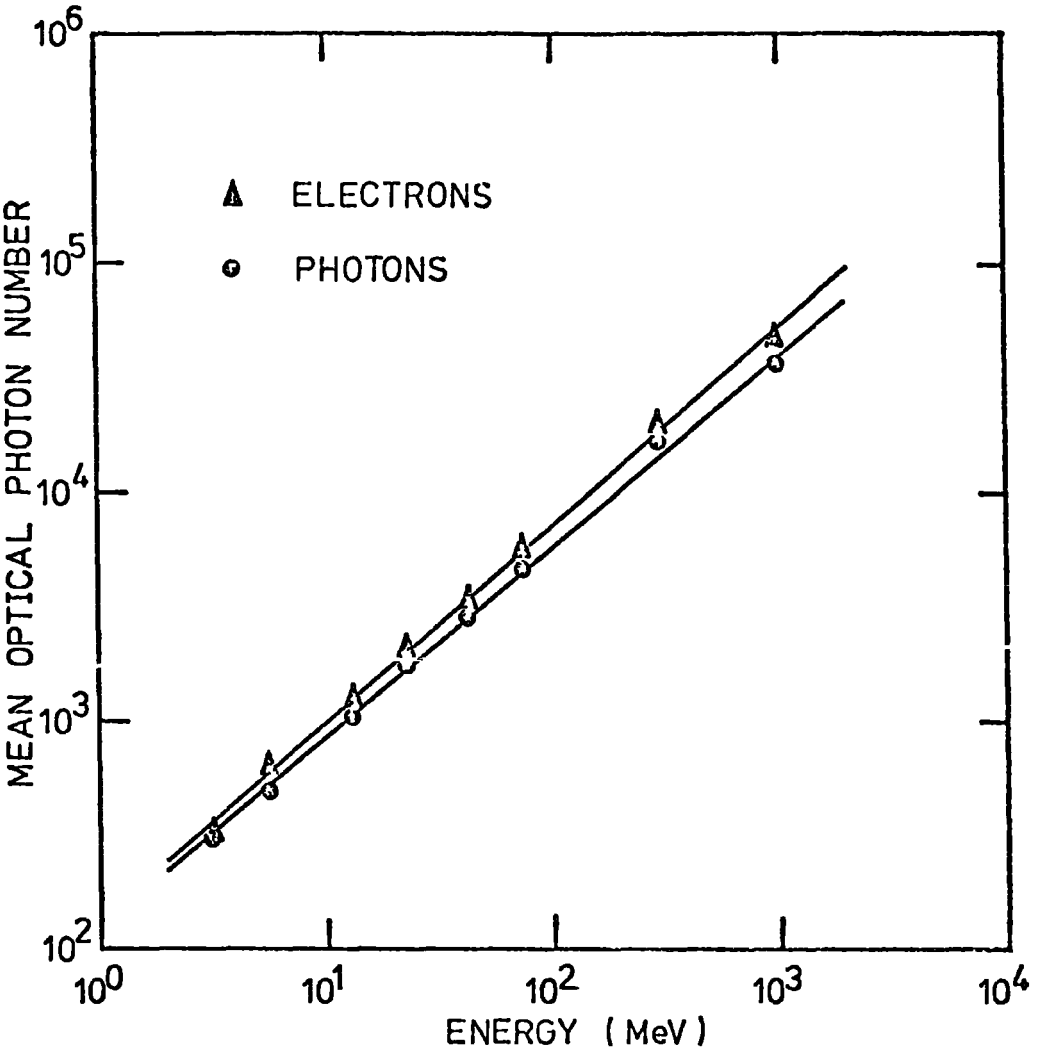

FIGURE 3-31 The mean optical photon yield of the Haverah Park water Cerenkov detectors as a function of incident electron and photon energy.

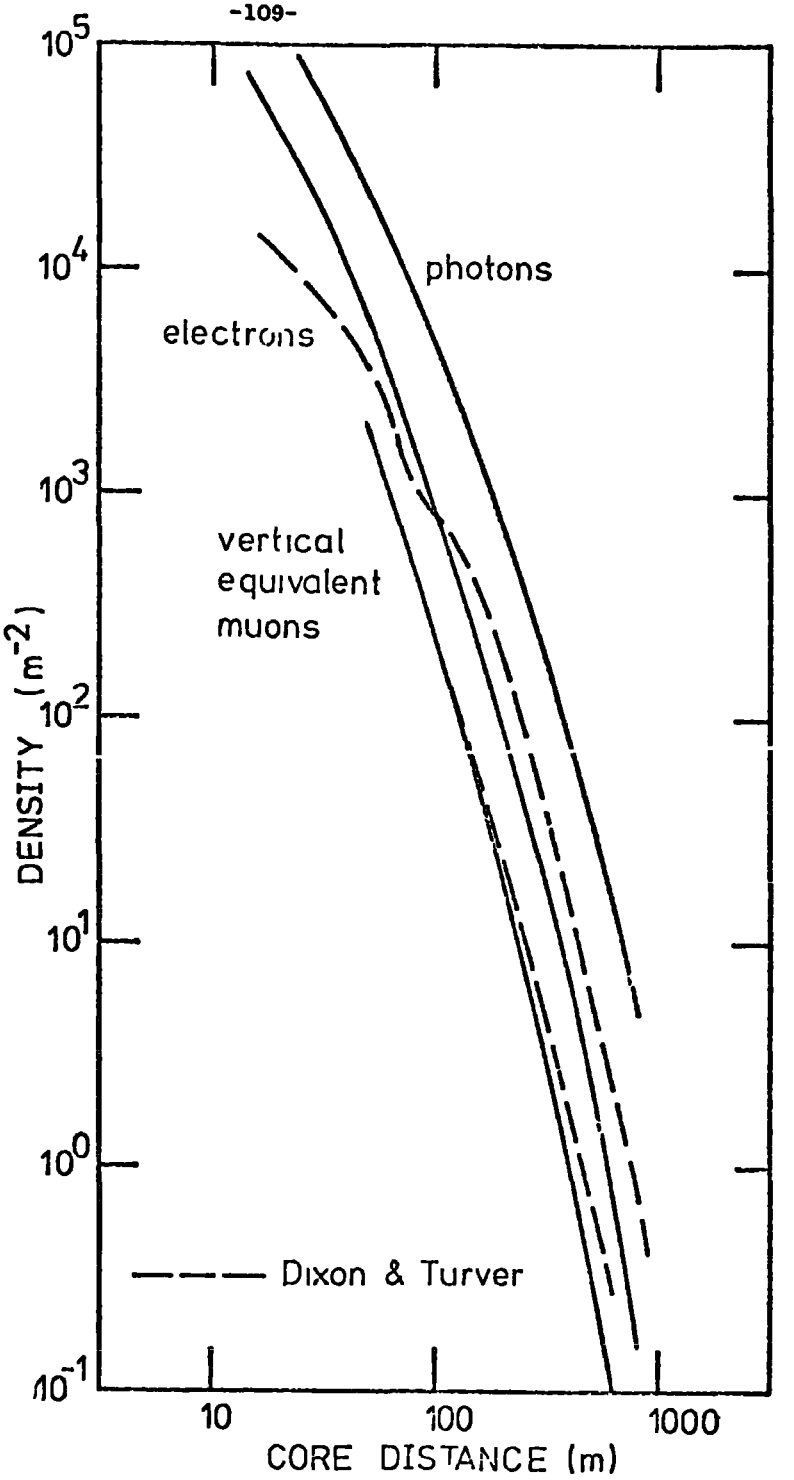

FIGURE 3-32 The Haverah Park detector response to the soft component, and the electron and photon lateral distributions from the present work are compared to those given by Dixon and Turver (1974) for the average 10^{18} eV CKP proton initiated shower.

CHAPTER FOUR

THE MUON COMPONENT OF COSMIC RAY SHOWERS

INTRODUCTION

Study of the muon component in conjunction with other components of large cosmic ray showers may give a valuable insight into the nature of high energy nuclear interactions. This is because the muon component, derived directly from the decay of the charged pion component, does not cascade but retains information about the parent pions. The stability of the muon component arises as the muon has a long mean lifetime ($\sim 2 \times 10^{-6}$ s), is weakly interacting and, due to its high mass (~ 0.106 GeV/c^2), has a low cross section for bremsstrahlung. This is in contrast to the electrons in large cosmic ray showers which may be as many as thirty interactions removed from their parent neutral pions.

In this chapter the main processes involved in the generation of the muon component from the charged pion production spectrum are described and the analytic approach to calculation of the lateral distribution of muons is discussed. Other important processes are described in detail and incorporated into the framework of a Monte Carlo computer simulation. Calculation of additional muons arising from photomeson production is desribed. Results are presented both of the muon component of large cosmic ray showers and the response of water Cerenkov detectors of the type deployed at the Haverah Park array to the muon and electron-photon components.

4-1 MAJOR PROCESSES AND THE ANALYTIC APPROACH TO CALCULATIONS OF THE MUON LATERAL DISTRIBUTION

Three processes have the largest effect in determining from the pion production spectrum the energy and spatial characteristics of muons

in large cosmic ray showers. These processes are: 1) the nuclear interactions in which pions obtain transverse momenta, 2) the competing processes of pion decay and nuclear interactions, and 3) the probability of muons reaching the observation level before decaying.

4-1.1 Transverse momentum of parent pions

The transverse momentum of pions produced in hadronic collisions was discussed in chapter 2. In the present work a distribution in transverse momentum of the form

$$f(p_t)\, dp_t = B^2\, p_t \exp(-Bp_t)\, dp_t , \qquad 1$$

where $B = 5\ (GeV/c)^{-1}$ was assumed. A pion with transverse momentum p_t (GeV/c) and energy E (GeV) was assumed to be travelling in a direction ϑ with respect to the shower core,

where

$$\vartheta = p_t c/E \quad \text{radians.} \qquad 2$$

The daughter muons are here considered as travelling in this direction since the energy of the muon in the rest system of the parent pion is small (see section 4-3.4).

4-1.2 Competing processes of pion decay and nuclear interaction

The mean lifetime of charged pions of energy E_π (GeV) is

$$\tau_\pi' = \gamma_\pi \tau_\pi \quad \text{s}, \qquad 3$$

where $\gamma_\pi = E_\pi/m_\pi c^2$, m_π is the mass of the charged pion (GeV/c^2) and τ_π (s) is the mean lifetime of charged pions at rest. In this time a pion will travel a distance, l_D, given by,

$$l_D = (\gamma_\pi \tau_\pi)\, \beta_\pi\, c \quad \text{m}, \qquad 4$$

where $\beta_\pi c$ (m s^{-1}) is the velocity of the pion. The interaction mean free path of pions, λ_π(g cm^{-2}), corresponds to a distance, l_I, given by,

$$l_I = \lambda_\pi/\rho \qquad \text{m}, \qquad 5$$

where ρ(g cm^{-2} m^{-1}) is the atmospheric density. The probabilities of interaction and decay in a small distance dl (m) are then respectively,

$$\left.\begin{aligned} P_I &= dl/l_I, \\ P_D &= dl/l_D . \end{aligned}\right\} \qquad 6$$

Then the probability of decaying before interaction is,

$$P_{\pi\mu}(h, E_\pi) = \frac{P_D}{P_D + P_I} = \lambda_\pi/(\lambda_\pi + \rho\gamma_\pi\tau_\pi\beta_\pi c). \qquad 7$$

This probability depends both on the pion energy and the atmospheric density (and hence altitude) and is plotted in figure 1 against pion energy for different heights of production where a value of 120 g cm^{-2} has been assumed for λ_π. It is noted that at a typical production altitude of 5 km, pion decay predominates over interaction at pion energies less than 30 GeV.

4-1.3 Muon survival probability

The probability of a muon with energy E_μ (GeV) surviving decay from an altitude of h (m) is

$$S(h, E_\mu) = \exp(-h/\gamma_\mu\beta_\mu c\tau_\mu) , \qquad 8$$

where $\gamma_\mu = E_\mu/m_\mu c^2$, m_μ is the mass of the muon (GeV/c^2), $\beta_\mu c$ is the velocity of the muon (m s^{-1}) and τ_μ is the mean lifetime of a muon at rest (s). The survival probability is plotted in figure 2 against muon energy for various production altitudes. It is noted that muons with energies above 1 GeV produced at 5 km have greater than a 45% probability of survival to sea level.

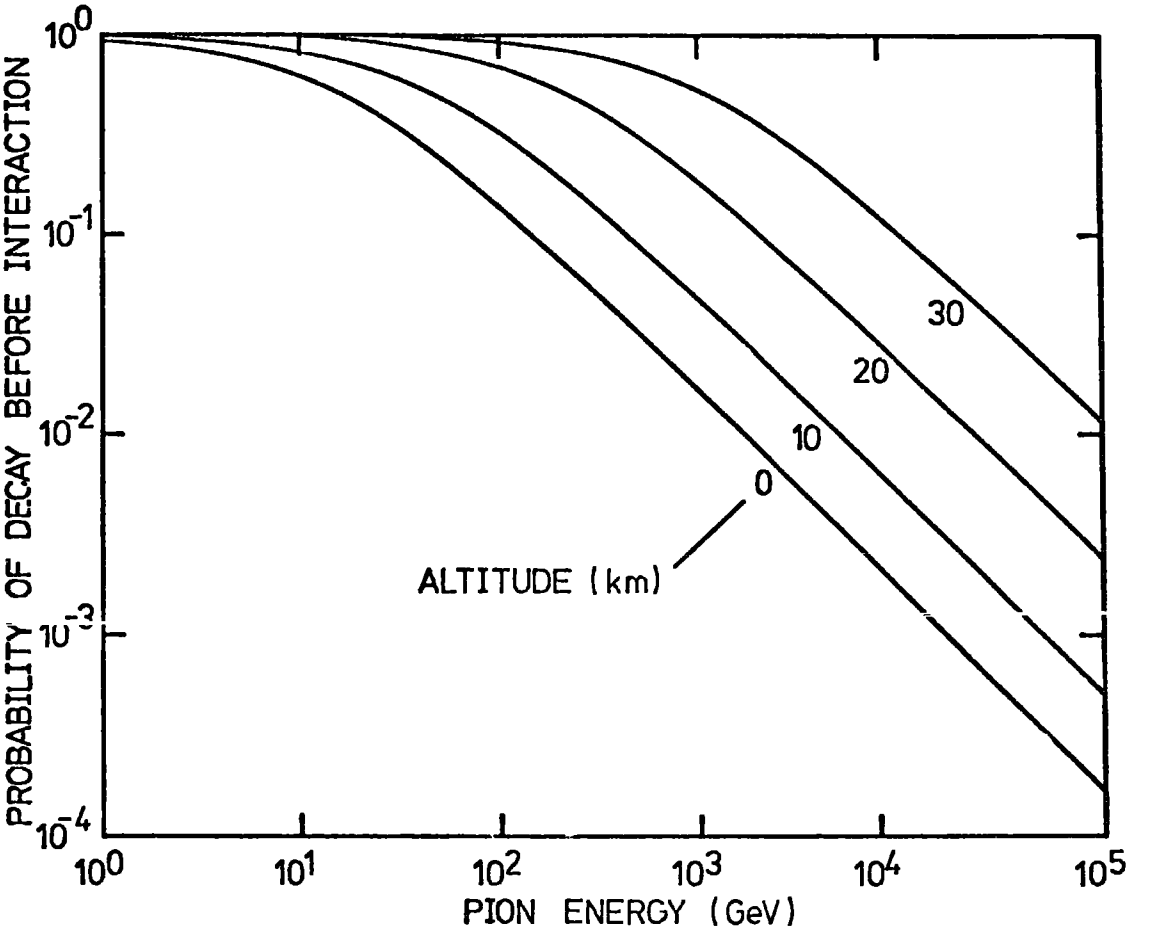

FIGURE 4-1 The probability of pion decay before interaction as a function of pion energy for atmospheric pressures corresponding to the altitudes shown.

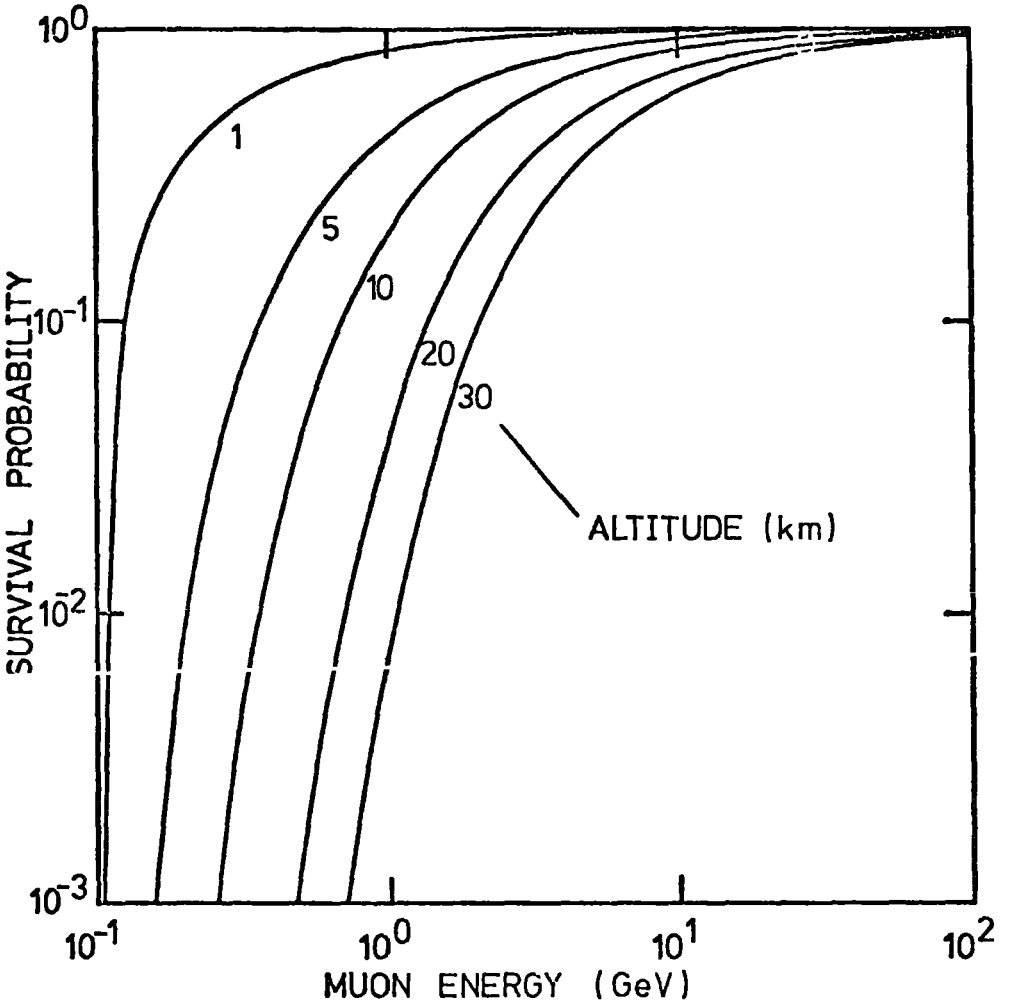

FIGURE 4-2 The probability of a muon surviving decay from various altitudes to sea level as a function of muon energy.

4-1.4 Analytic approach to calculations of the muon lateral distribution

It is possible to calculate by analytic means the approximate lateral distribution of muons in cosmic ray showers given the pion production spectrum. It is necessary however to make a number of approximations 1) muons travel in the same direction as their parent pions, 2) each muon has energy $C_{\pi\mu}E_\pi$ where $C_{\pi\mu} = (m_\pi^2 + m_\mu^2)/2m_\pi^2$, and 3) scattering and collision loss may be neglected.

From equation 2, a muon resulting from a pion produced at altitude h (m) will impact in the observation plane at a distance r (m) from the core given by

$$r = p_t c\, h/E_\pi \quad \text{m}. \tag{9}$$

Thus the probability of a muon impacting with core distance between r and (r + dr) is

$$P(r, E_\pi, h) = f(E_\pi r/h)\, \frac{E_\pi}{h}\, dr, \tag{10}$$

where $f(p_t)$ is the transverse momentum distribution of the parent pions. The muon density corresponding to this probability is simply,

$$d\rho\,(r, E_\pi, h) = \frac{f(E_\pi r/h)\, E_\pi/h}{2\pi r} \quad \text{m}^{-2}. \tag{11}$$

This function represents the muon lateral distribution resulting from a pion with energy E_π produced at altitude h which decayed into a muon which survived to the observation level. On using the transverse momentum distribution given in equation 1, this becomes

$$d\rho\,(r, E_\pi, h) = \frac{B^2}{2\pi}\, (E_\pi/h)^2 \exp(-Br\, E_\pi/h) \quad \text{m}^{-2} \tag{12}$$

and is plotted in figure 3 against core distance for several values of E_π/h. In order to obtain the lateral distribution of muons in a cosmic ray shower it is necessary to multiply $d\rho$ by the pion production spectrum, $\Phi_\pi(h, E_\pi)dhdE_\pi$ (the number of charged pions produced with energies between E_π and $(E_\pi + dE_\pi)$ between altitudes h and (h +dh)),

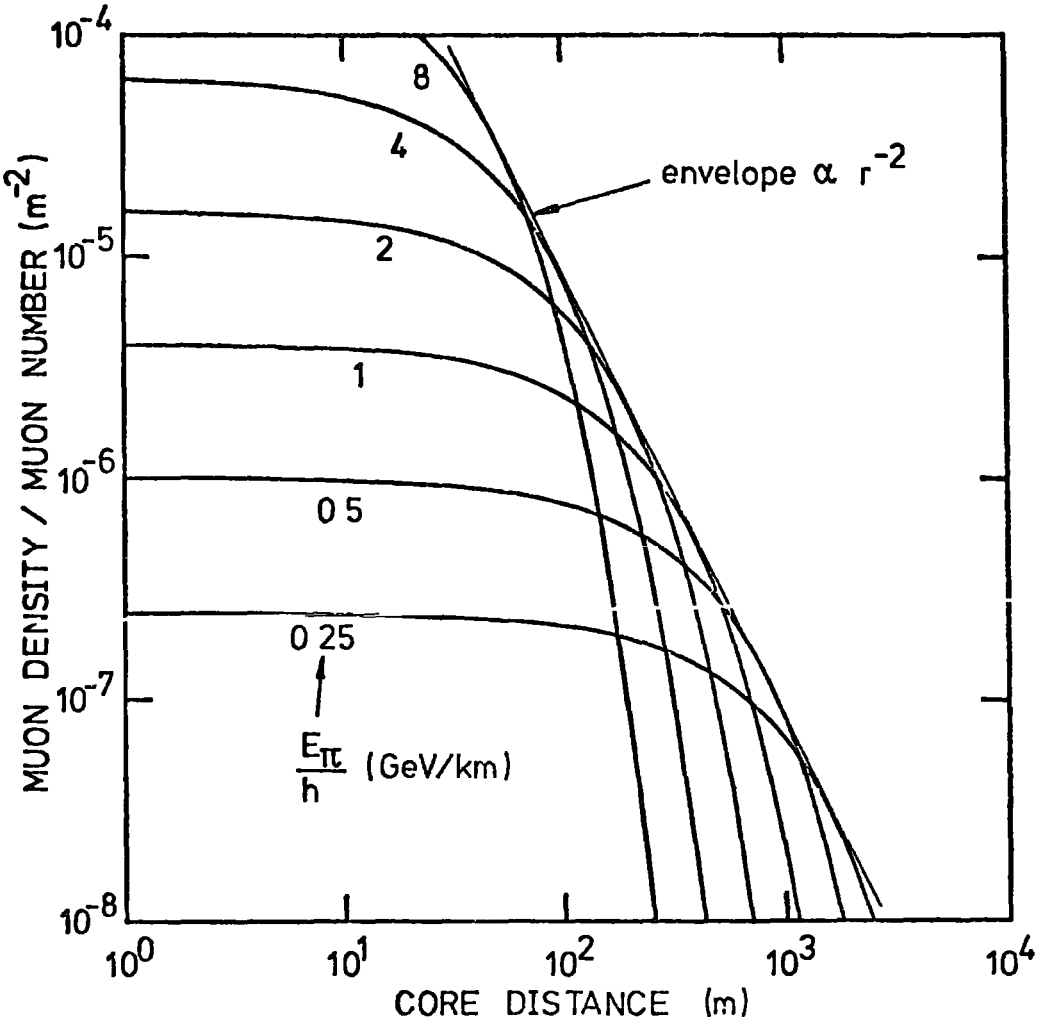

FIGURE 4-3 The muon lateral distribution resulting from a pion with energy E_π (GeV) produced at altitude h (km) as given by equation 12 for various values of E_π/h.

the probability of pion decay before interaction and the muon survival probability and then integrate the resulting function over all pion energies and production altitudes

$$\rho(>E_\mu, r) = \int_0^\infty \int_{\frac{E_\pi}{C_{\pi\mu}}}^\infty \frac{\Phi_\pi(h, E_\pi) P_{\pi\mu}(h, E_\pi) S(h, C_{\pi\mu} E_\pi) f(E_\pi r/h) E_\pi \, dE_\pi \, dh}{2\pi r \, h} \quad m^{-2}. \qquad 13$$

It is interesting to note that with scaling models for pion production,

$$\Phi_\pi(E_\pi, h) \sim \ln E_\pi \qquad 14$$

and for energies less than ~10 GeV inspection of figures 1 and 2 suggest that to a very crude approximation,

$$P_{\pi\mu}(h, E_\pi) S(h, C_{\pi\mu} E_\pi) \approx \text{constant}. \qquad 15$$

This means that the integral (equation 13) will look like the sum of the curves shown in figure 3 (spaced logarithmically in E_π), which is proportional to the envelope of these curves. Hence in general, very approximately,

$$\rho(r) \propto r^{-2}. \qquad 16$$

4-2 THE MONTE CARLO COMPUTER PROGRAM FOR MUON PROPAGATION

The present study, using a new computer program, was based on the work of Dixon et al (1974) and Turver (1975). As with the previous work, multiple Coulomb scattering and geomagnetic deflection of muons are considered. The program is fully three-dimensional and pion and muon decays are fully simulated.

4-2.1 The computational procedure

The computer program takes as input the charged pion production spectrum (PITOT) which was calculated as described in chapter 2. For economy of computing time, only a fraction of the pions are considered in detail (chosen so that~10^4 muons are fully simulated to ensure reasonable accuracy). Initially, each element of PITOT is reduced by this fraction and the final muon densities are increased accordingly.

Each element of PITOT (production height/energy) is treated in turn. If the number of pions in the element considered, n_π , is greater than one, n_π is reduced by one and the propogation of a pion with the appropriate mid-bin energy and production altitude is simulated. If nowever, n_π is less than one, a random number ($0<R<1$) is generated and if $R<n_\pi$ the propagation of a pion is simulated, otherwise this element of PITOT is treatod as empty and a new element is considered.

The lifetime of a pion, t_D (s), is then sampled from the distribution

$$f(t_D)dt_D = \frac{1}{\tau_\pi'} \exp(-t_D/\tau_\pi') \; dt_D \; , \qquad 17$$

where τ_π' is given by equation 3. The interaction length, x (g cm^{-2}), is chosen from

$$f(x)dx = \frac{1}{\lambda_\pi} \exp(x/\lambda_\pi) \; dx \; , \qquad 18$$

and the time after which the pion interacts is obtained

$$t_I = x/(\rho \beta_\pi c) \qquad s \; . \qquad 19$$

If $t_I < t_D$ the pion interacts and is not considered further as its progeny is already included in PITOT.

If the pion will subsequently decay into a muon, then the propagation of the pion and the muon to the observation level is simulated.

4-3 THE PROPAGATION OF PIONS AND MUONS THROUGH THE ATMOSPHERE

The propagation of the pion and muon component is considered in four dimensions. The spatial coordinate system used has the origin at the intersection of the shower core and sea level, the z-direction towards the centre of the Earth, the x-direction towards magnetic North and the y-direction towards magnetic East.

First, the transverse momentum of the pion is sampled from the distribution given in equation 1 and an azimuth angle is randomly selected. The initial velocity 3-vector, $\underline{v}$ (m s^{-1}), is then calculated and stored as are its initial position 3-vector, $\underline{x}$ (m), and energy E (GeV).

The propagation to sea level is considered over a number of small time intervals, t (s), in the following way 1) the new position, $\underline{x}'$, and velocity, $\underline{v}'$, after deflection in the geomagnetic field for time t are calculated neglecting collision loss and scattering, 2) the distance travelled is calculated and $\underline{x}'$, $\underline{v}'$ and t are corrected to account for Coulomb scattering within this element of track, and 3) the collision loss for this element of track is calculated and the energy is reduced accordingly. If the pion decay time has not been reached, then the whole process is repeated. If, on the other hand, the pion decay time has been exceeded, the pion "steps back" in time to the point of decay ($\underline{x}'$, $\underline{v}'$ and t being appropriately modified) and the decay to a muon is simulated. The lifetime of the muon is sampled from a distribution similar to the distribution of pion lifetimes given by equation 17 and the propagation of the muon is treated in the same way as the propagation of the pion as described above. When sea level is passed the muon "steps back" in time to the instant at which it was at sea level and its spatial information and energy are recorded together with its height of origin.

4-3.1 Geomagnetic deflection of charged particles

A magnetic field typical of Northern England has been chosen for the present calculation

$$\underline{B} = (1.66 \times 10^{-5},\ 0,\ 4.52 \times 10^{-5})\ \text{T}. \qquad 20$$

The force acting on a particle with velocity $\underline{v}$ (m s^{-1}) and charge q (C) is

$$\underline{F} = q\,\underline{v} \times \underline{B} \quad \text{N}. \qquad 21$$

As illustrated in figure 4 the motion of a charged particle in a uniform field is helical and the radius of the helix is,

$$R = \frac{\gamma m\ v \sin\varphi}{q\ B} \quad \text{m}, \qquad 22$$

where γm is the relativistic mass (kg) of the particle and φ is the angle between the velocity and field directions as shown in the figure. The projected angular deflection (see figure 4) is then obtained

$$\vartheta = \frac{q\ B\ t}{\gamma\ m} \quad \text{radians}, \qquad 23$$

and the displacement $\underline{dx} = (\underline{x}' - \underline{x})$ and change in velocity, $\underline{dv} = (\underline{v}' - \underline{v})$ may be calculated

$$\underline{dv} = (1 - \cos\vartheta)(\underline{v} \times \hat{\underline{B}}) \times \hat{\underline{B}} + \sin\vartheta\,(\underline{v} \times \hat{\underline{B}}) \quad \text{m}\ s^{-1}, \qquad 24$$

$$\underline{dx} = (\hat{\underline{B}} \cdot \underline{v})t\,\hat{\underline{B}} + \hat{\underline{B}} \times (\underline{v} \times \hat{\underline{B}})T\sin\vartheta + (\underline{v} \times \hat{\underline{B}})(1 - \cos\vartheta)T \quad \text{m}, \qquad 25$$

where $\hat{\underline{B}}$ is the unit vector in the direction of the magnetic field and $T = \gamma m/qB$ (s). Equations 23, 24 and 25 thus enable the new position and velocity of a particle to be calculated after a time t.

4-3.2 Multiple Coulomb scattering

Charged pions and muons will be elastically scattered by the Coulomb fields of air nuclei. Rossi and Greisen (1941) give the probability of a singly charged particle having a projected angular

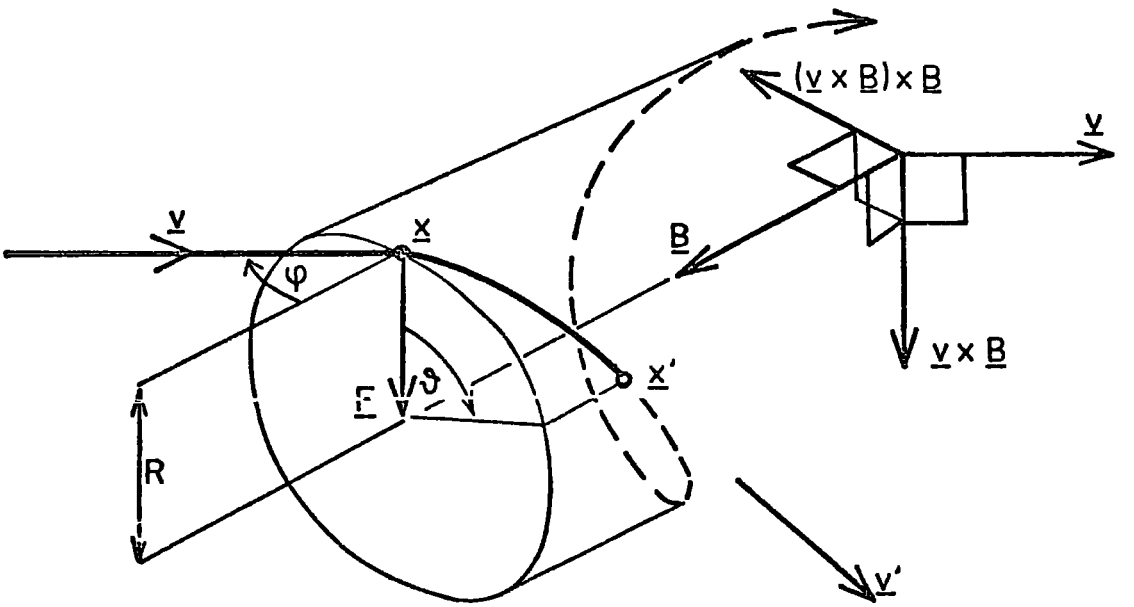

FIGURE 4-4 The deflection of a charged particle in a magnetic field. The meaning of the symbols is given in section 4-3.1.

deflection ϑ (radians) and a projected lateral displacement y (radiation lengths) after travelling small distance t (radiation lengths) based on the work of Williams (1939, 1940) as

$$F(t, y, \vartheta) \alpha \exp\left\{ \frac{-w^2}{t^3} \left(\vartheta^2 t^2 - 3y\vartheta t + 3y^2 \right) \right\}, \qquad 26$$

where $w = 2p\beta c/E_s$, p is the momentum (MeV/c), βc is the velocity and $E_s = 21$ MeV.

In the computer program, lateral and angular displacements were sampled using distributions based on equation 26 in two orthogonal planes whose line of intersection was in the direction of the velocity of the particle, v' (after geomagnetic deflection) and contained the position of the particle, x' . These additional displacements were then superimposed onto x' and v'.

The mean square projected lateral and angular displacements $\overline{y^2}$ and $\overline{\vartheta^2}$ are given by

$$\overline{y^2} = \frac{2t^3}{3w^2} = \frac{1}{3} t^2 \overline{\vartheta^2} \qquad , \qquad 27$$

and a very crude estimate of the additional distance travelled due to Coulomb scattering may be obtained by assuming the particle follows a trajectory of the form,

$$b = a\, l^{3/2} \qquad 28$$

where l (m) is the distance travelled in the original direction and b (m), the lateral displacement (a is obtained from the particular value of b sampled). Then the distance travelled is approximately,

$$l' \approx \int_0^l \sqrt{dl^2 + db^2} \approx l + \frac{9}{16} a^2 l^2 \qquad 29$$

with corresponding additional time delay of $\frac{9}{16} a^2 l^2/v$ (s).

4-3.3 Ionization loss

The energy loss due to ionization is calculated for each element of track assuming a constant value for the energy loss per g cm^{-2} of air calculated for the energy of the particle at the beginning of the track. The values used are based on those given by Sternheimer (1959) and are given in figure 5. Also shown in the figure is the energy loss per g cm^{-2} of barytes concrete shielding (the effect on the spatial characteristics of muons of barytes concrete shielding as used in a muon telescope described by Gibson (1976) has been investigated).

4-3.4 Pion decay

The decay of a pion into a muon and an anti-neutrino is a two-body decay with the result that the muon has a unique energy and momentum in the rest frame of the pion

$$E_\mu^* = \frac{m_\pi^2 + m_\mu^2}{2 m_\pi} c^2,$$
$$p_\mu^* = \frac{m_\pi^2 - m_\mu^2}{2 m_\pi} c . \qquad 30$$

The decay is isotropic in the rest frame of the pion so that the distribution of the component of momentum resolved along the direction of the pion velocity (or any arbitrary direction) is

$$f(p_l^*)\, dp_l^* = \frac{dp_l^*}{2p_\mu^*} . \qquad 31$$

The momentum is therefore sampled in the pion rest frame from equation 31 and Lorentz transformed to the LAB frame.

4-4 COMPARISON WITH OTHER WORK

Results of the present work have been compared with the predictions of Turver (1975) for the spatial characteristics of muons in the average proton initiated shower of primary energy 10^{18} eV

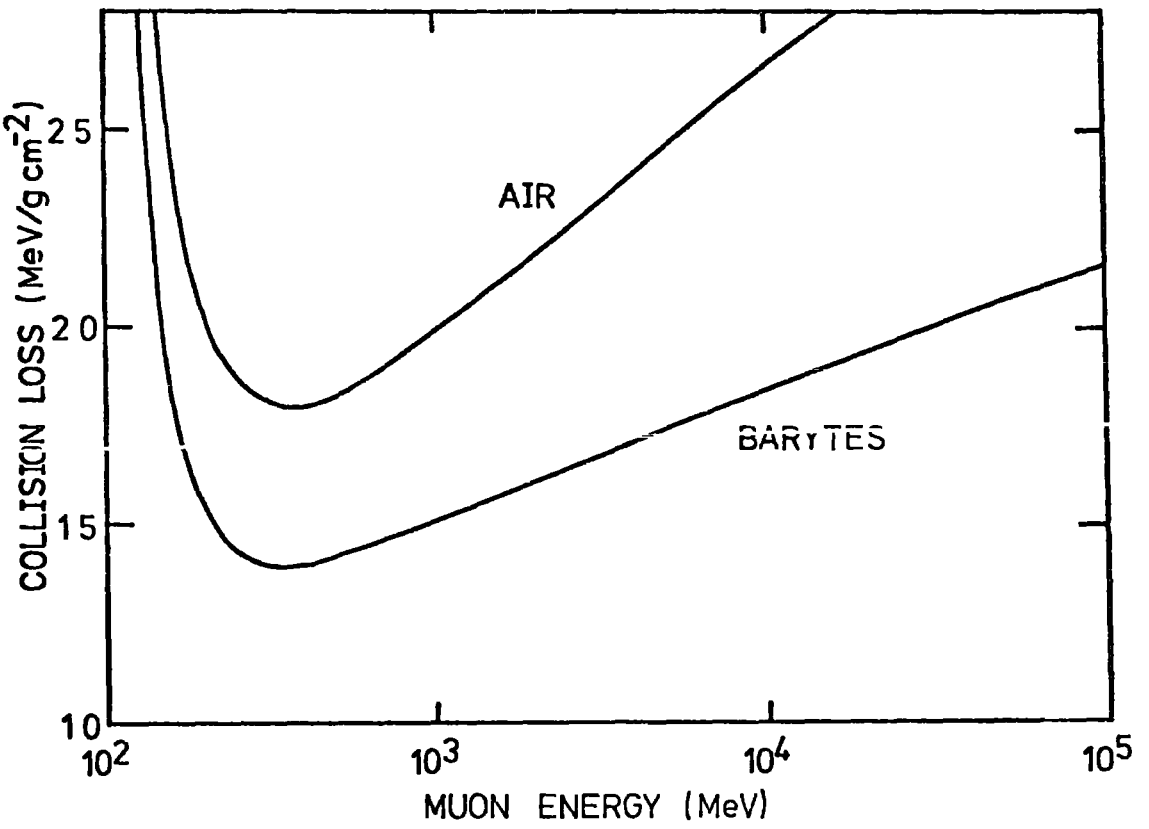

FIGURE 4-5 The energy loss per g cm^{-2} of air and barytes concrete for pions or muons due to ionization.

simulated using the CKP model (Cocconi et al (1961)) for pion production. In the present work the pion production spectrum (PITOT) as used by Turver was again used as input for the muon calculation in order to enable a direct comparison between the predictions of the two computer programs to be made. The result of this comparison is given in figure 6 which shows the lateral distribution of muons, figure 7 which shows the variation with core distance of the mean height of origin, figure 8 which shows the mean muon energy as a function of core distance, and figure 9 which shows the mean core angle as a function of core distance. From these figures it is seen that there is good overall agreement between the present results and the predictions of Turver.

It has been possible to compare the integral energy spectrum of muons calculated using the scaling model for primary protons with the work of Gaisser and Maurer (1972) and Grieder (1977a) who used similar models. This comparison is made in figure 10 where the results of the present work at primary energies of 10^{14}, 10^{15} and 10^{16} eV are compared with the results of Grieder at 10^{14} eV and 10^{15} eV and with the result of Gaisser and Maurer at 10^{16} eV. Grieder gives two spectra at 10^{14} eV corresponding to scaling models which include and neglect the production of leading pions in pion-nucleus interactions (in the present work the production of leading pions is included). There is reasonable overall agreement between the three calculations.

4-5 CALCULATION OF AN ADDITIONAL MUON COMPONENT ARISING FROM PHOTOMESON PRODUCTION

In chapter 3 it was pointed out that the treatment of photon-nucleus interactions might result in a significant increase in the muon component due to the photoproduction of charged pions. This additional component was generated first by calculating the production spectrum of charged pions resulting directly from photomeson production, then by using the analytic method described in appendix B to obtain

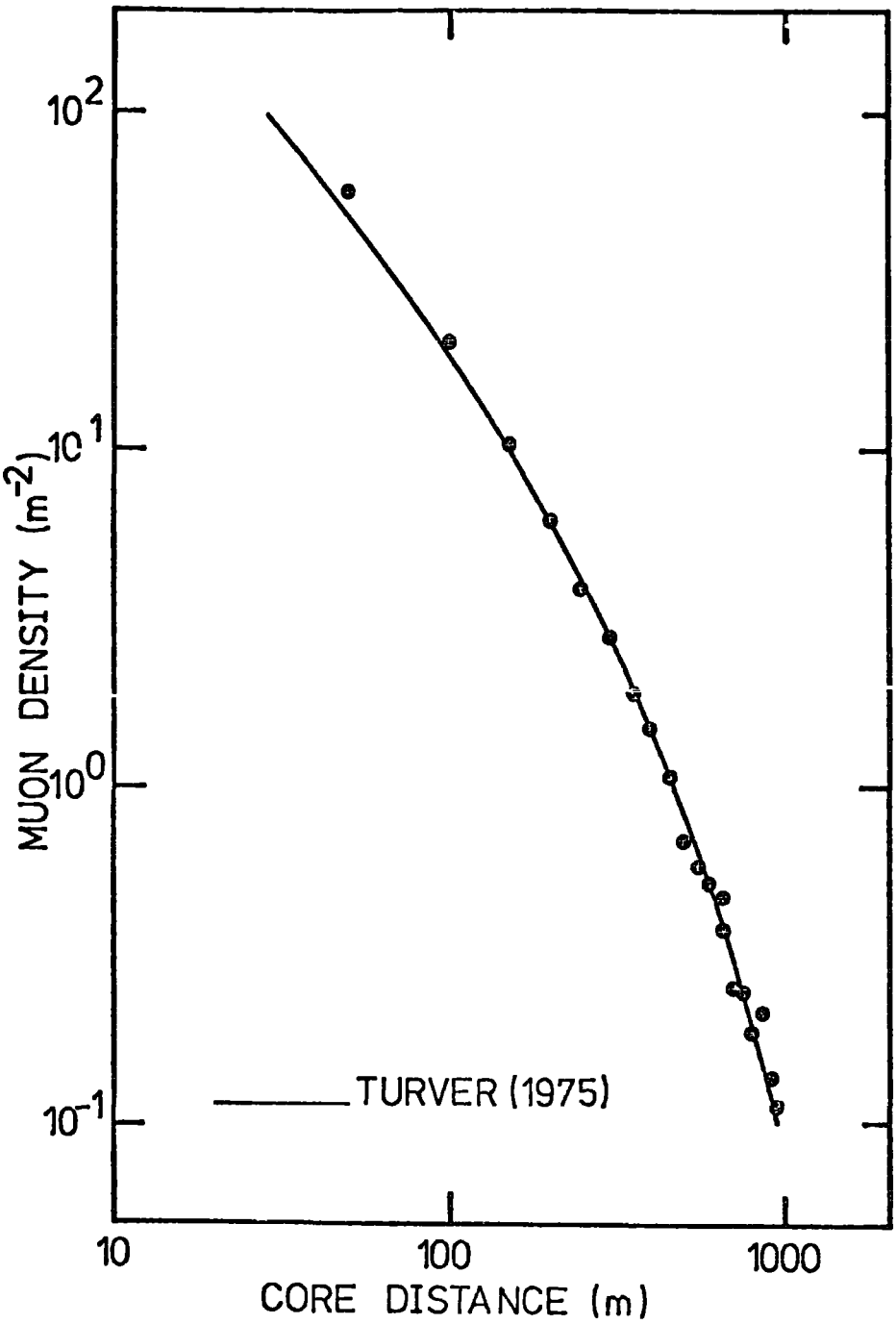

FIGURE 4-6 The lateral distribution from the present work is compared to that given by Turver (1975) for the average proton initiated 10^{18} eV shower (CKP model).

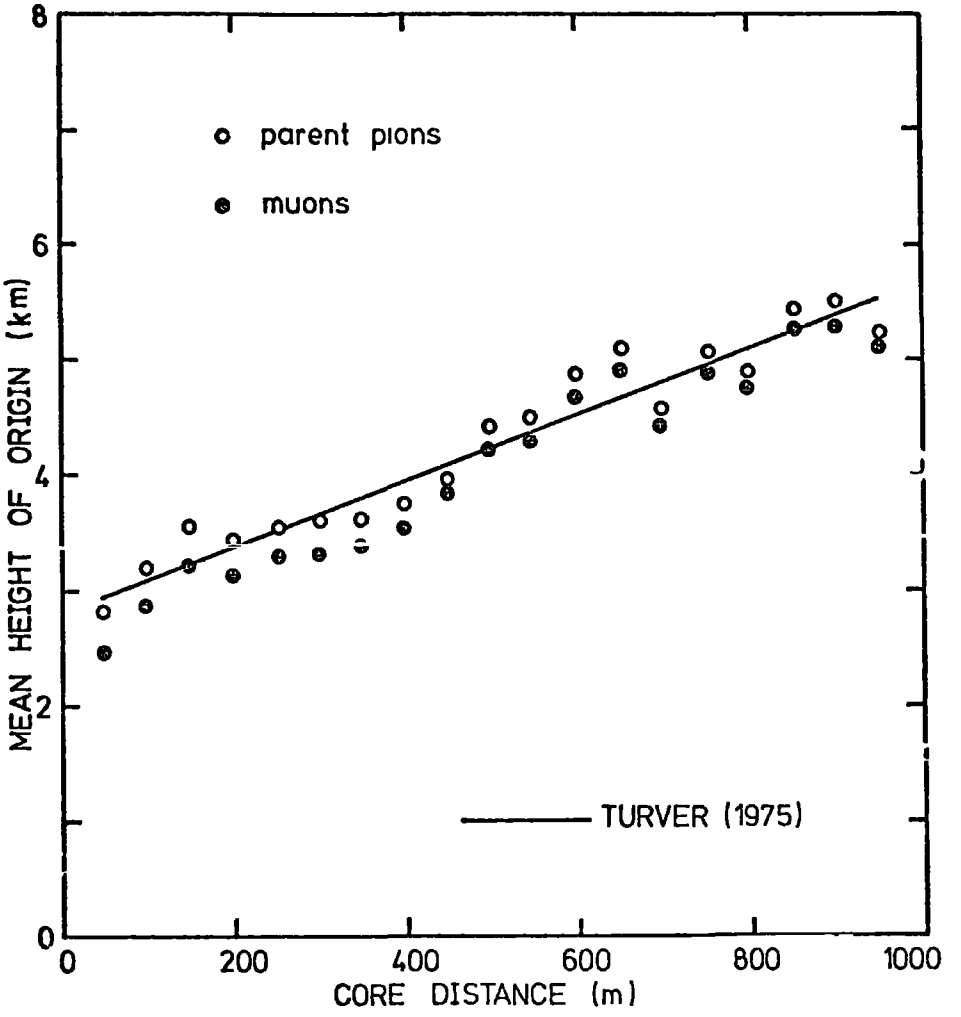

FIGURE 4-7 The mean height of origin of parent pions and muons as a function of core distance from the present work is compared to the mean height of origin of parent pions given by Turver (1975) for the average 10^{18} eV proton initiated shower (CKP model).

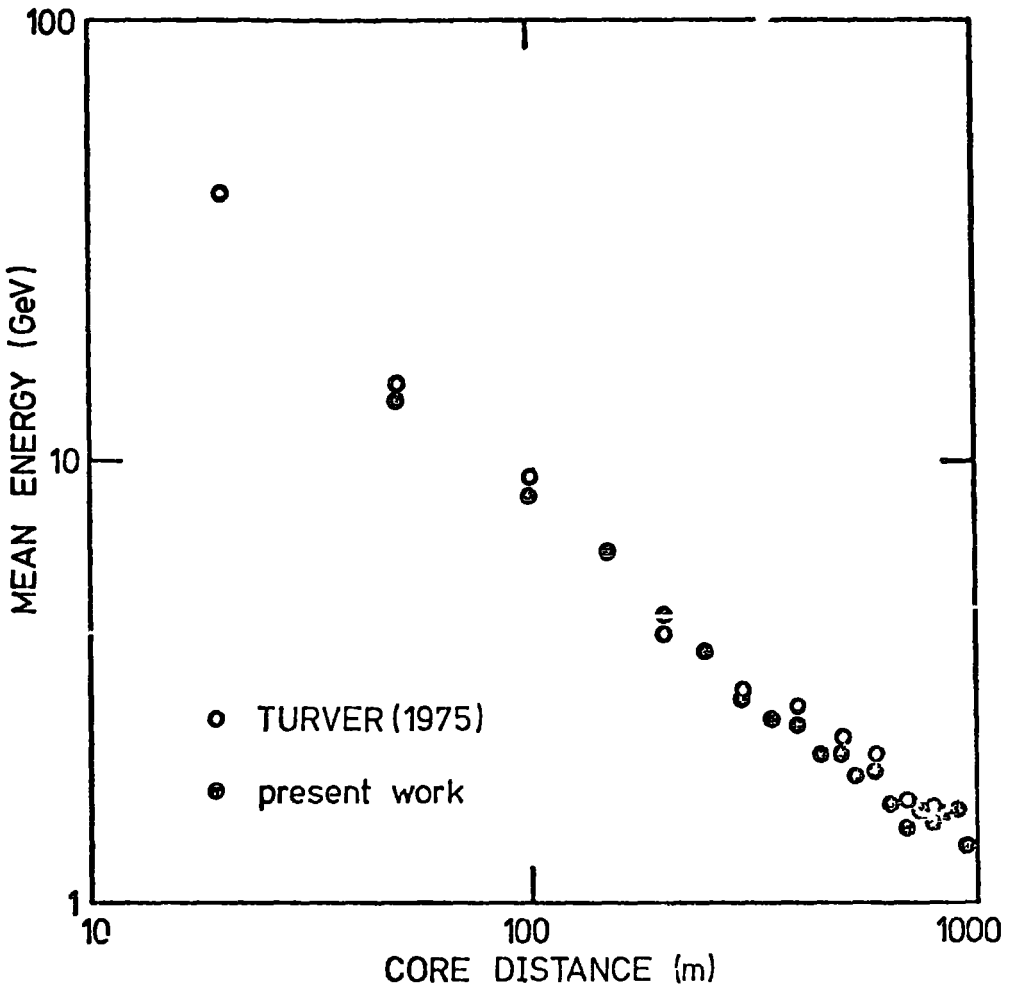

FIGURE 4-8 The mean muon energy as a function of core distance from the present work is compared to that given by Turver (1975) for the average 10^{18}eV proton initiated shower (CKP model).

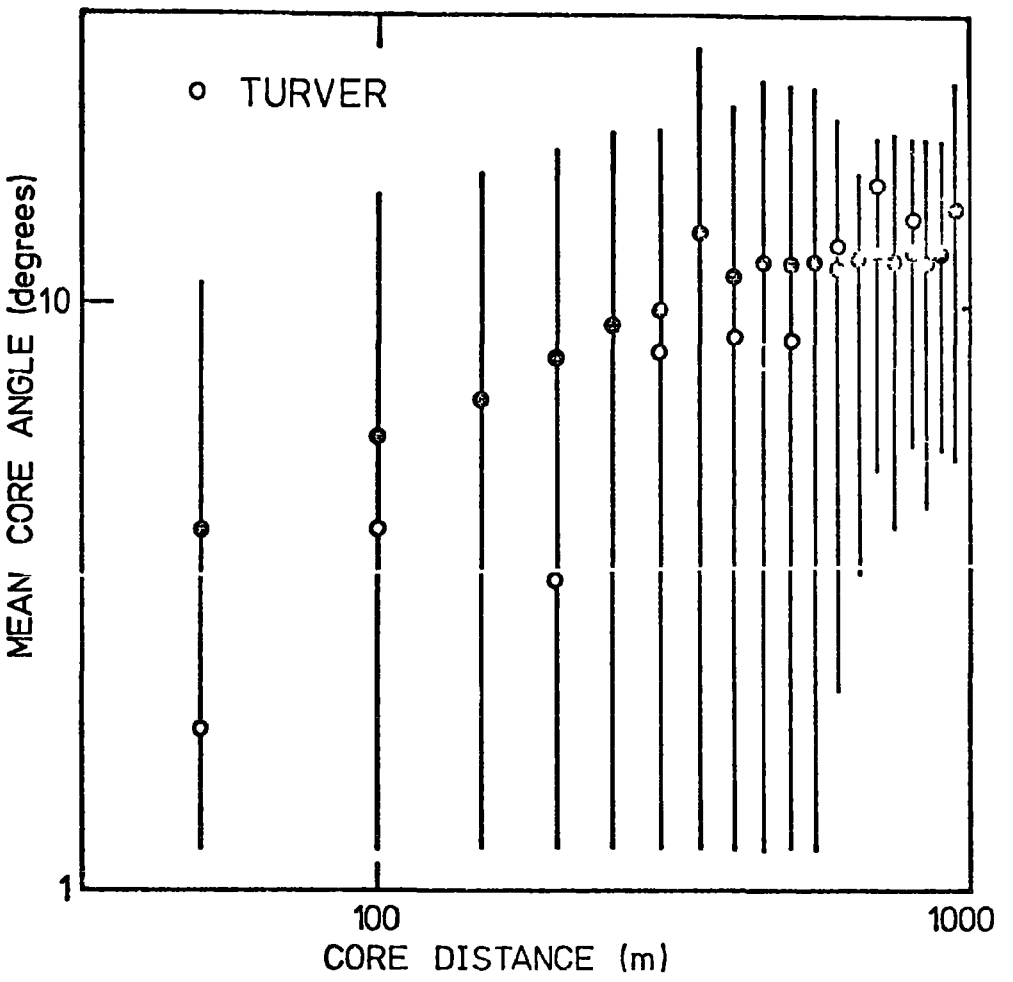

FIGURE 4-9 The mean core angle as a function of core distance from the present work is compared to that given by Turver (1975) for the average 10^{18}eV proton intiated shower (CKP model). The length of the error bar for the present work is one r.m.s. deviation and indicates the expected spread in core angle

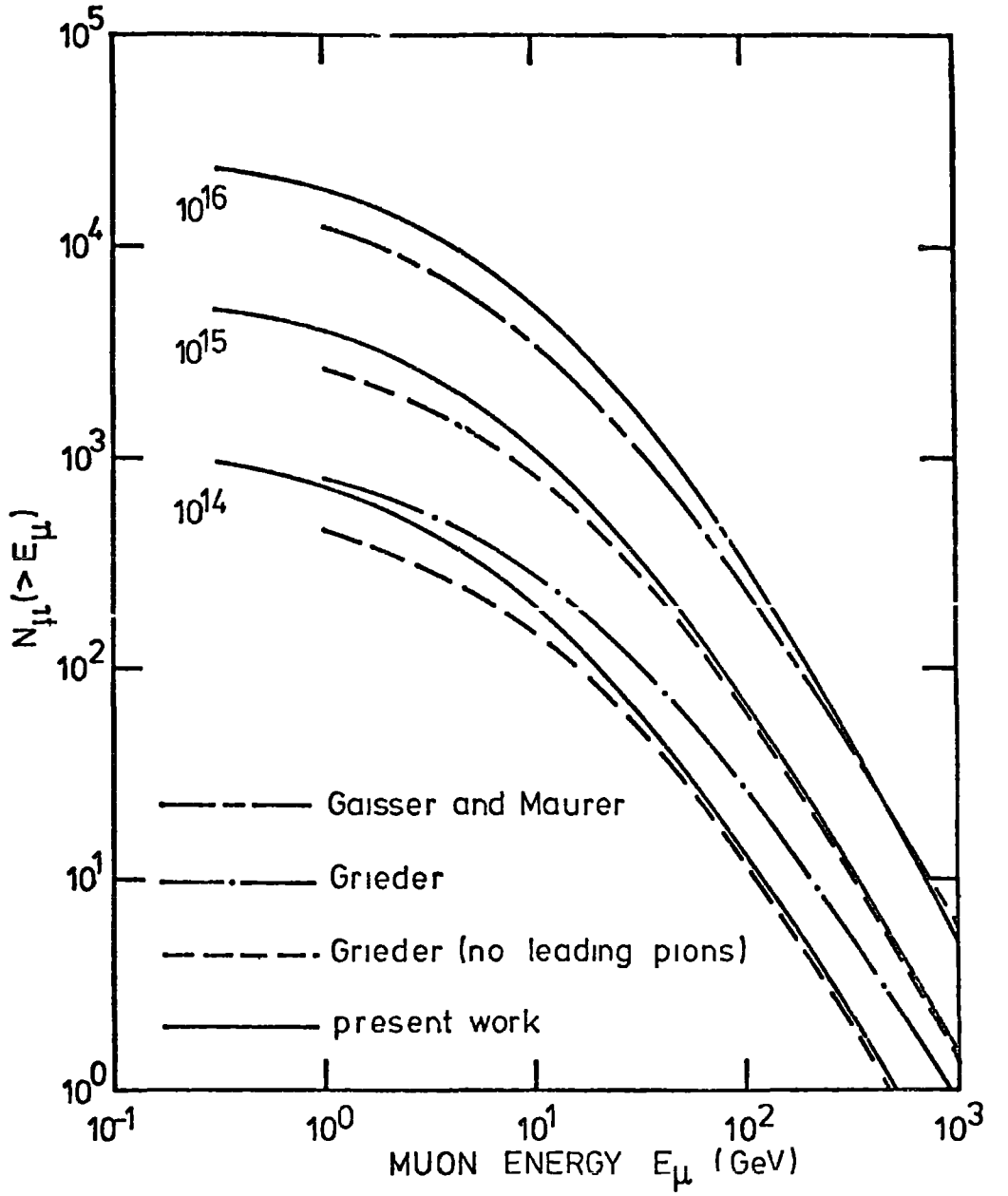

FIGURE 4-10 The integral muon energy spectrum from the present work for the scaling model and proton primaries is compared to the work of Gaisser and Maurer (1972) and Grieder (1977a). The numbers attached to the curves are the primary energies (eV) of the showers.

the production spectrum of all additional charged pions resulting (both directly and from the interaction of photoproduced pions) from photomeson production. Finally, the additional muon component was derived from the additional charged pion production spectrum as described in section 4-3.

The photoproduced pions were generated in the step-by-step electron-photon program described in chapter 3 in which the "step-by-step operators" were calculated under approximation A. An additional set of operators, "photoproduction operators" (based on the cross section for photomeson production given in equation 9 of chapter 3), were used to remove photons (which will undergo nuclear interaction) from the cascade to be treated separately. The step-by-step operators for pair production were reduced accordingly to conserve energy. The photons removed from the cascade were assumed to interact with air nuclei as if they were charged pions of the same energy and the production spectrum of charged pions resulting directly from photomeson production was then obtained from the spectrum of photons removed.

4-6 RESULTS OF THE PRESENT CALCULATIONS

In this section the average energy spectra, lateral distribution and spatial characteristics of muons at sea level obtained from the present calculations are presented. The results are for iron nucleus primaries ranging in energy from 10^{15} eV to 10^{18} eV (data presented outside this energy range are the result of extrapolation). Results for other primary nuclei may be obtained approximately from these data by use of the superposition model. The scaling model for pion production described in chapter 2 was used.

The effect of the incorporation of photomeson production (McComb, Protheroe and Turver (1977, in preparation)) is indicated throughout by

showing separately the total muon component (solid lines) and the muon component calculated neglecting photomeson production (dashed lines). Where appropriate, the effect is extrapolated to higher primary energies ($>10^{18}$eV). This source of extra muons, most important at ultra-high energies has customarily been neglected in air shower calculations. The consequences of this effect for ultra-high energy showers (in particular on the derived primary energy spectrum) will be considered in chapter 8. It should be emphasised that the muon component arising from photomeson production does not strongly depend on the model for nuclear interaction (as the mean interaction energy is low, due to the steep photon energy spectrum, it depends more on the photon component of the shower which depends mainly on primary energy) whereas the muon component arising from other normal processes does depend strongly on the nuclear interaction model. In consequence, the fractional increase in e.g. muon densities due to this additional component reported here may not be applied directly (as a correction factor) to muon calculations with differing primary mass or nuclear interaction model.

Results of the response of the Haverah Park water Cerenkov detectors to both the muon and the electron-photon components are given.

4-6.1 Energy spectra of muons

The total number of muons with energy greater than various prescribed threshold energies is given as a function of primary energy in figure 11. The integral energy spectra of all muons at sea level are shown in figure 12 for primary energies ranging from 10^{15} eV to 10^{18} eV. Figure 13 shows the integral energy spectra at various distances from the core of the average 10^{17} eV shower and the mean muon energy is plotted against core distance in figure 14 for the range of primary energy.

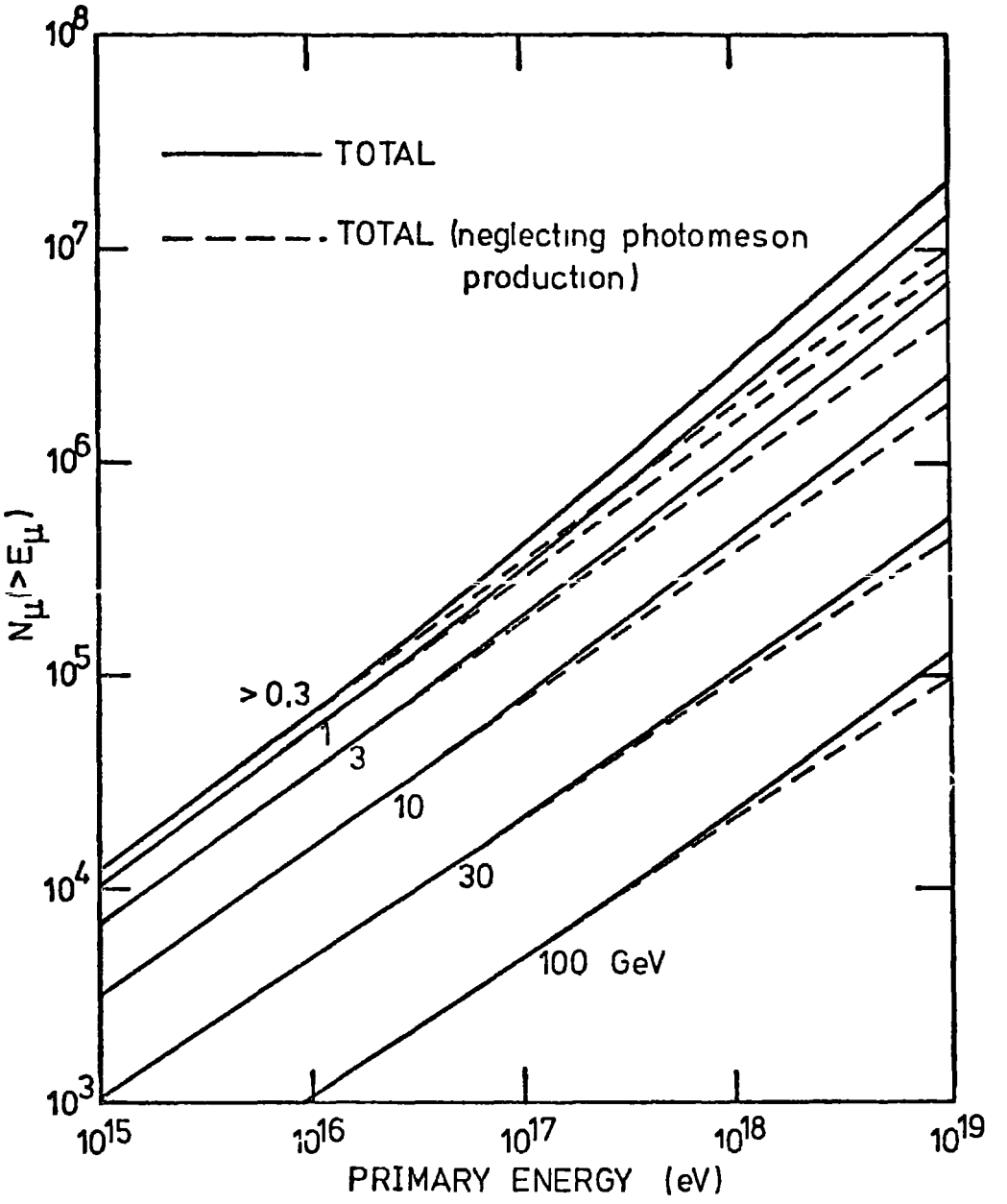

FIGURE 4-11 The total number of muons with energy greater than various prescribed energy thresholds (the numbers attached to the curves) as a function of primary energy.

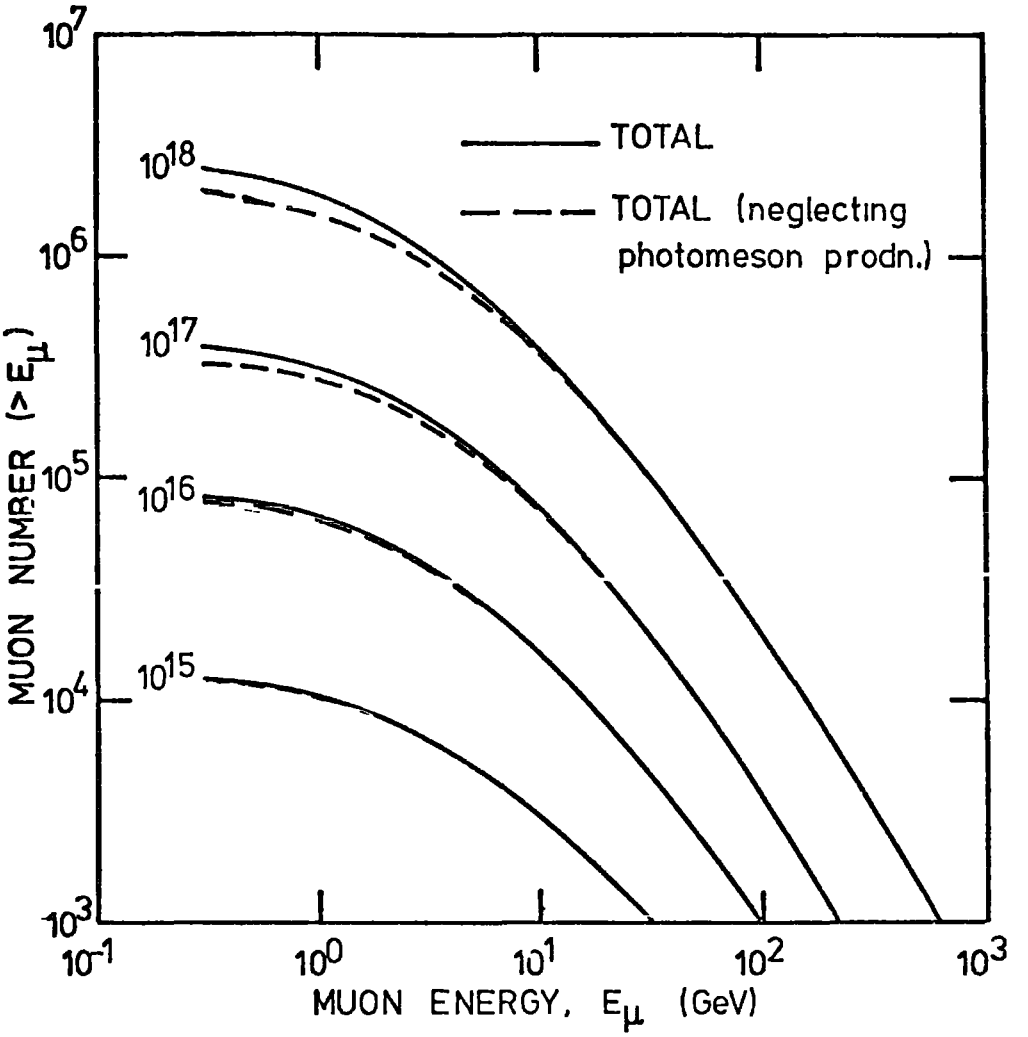

FIGURE 4-12 The integral energy spectrum of muons at sea level. The numbers attached to the curves are the primary energies (eV) of the showers.

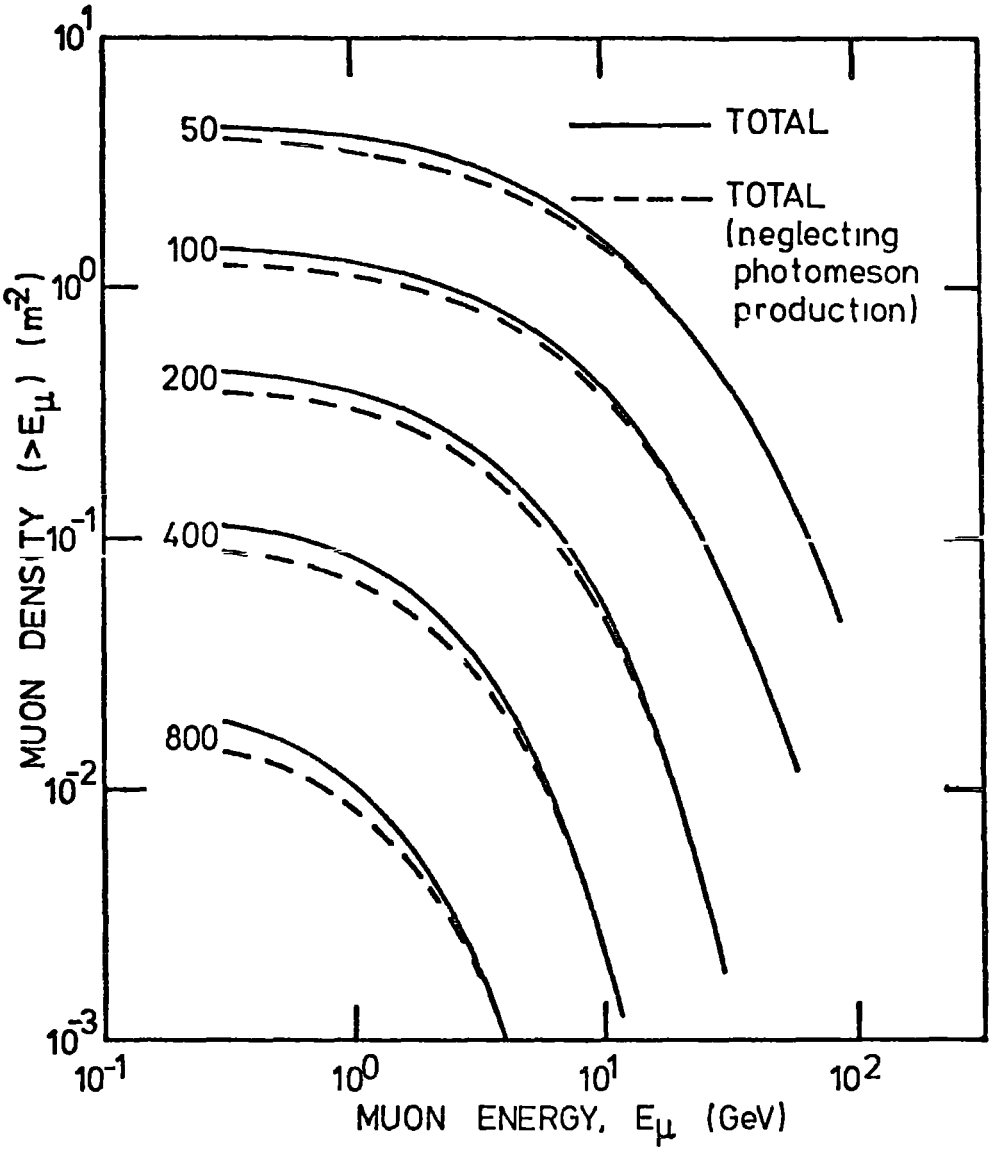

FIGURE 4-13 The integral energy spectra of muons at various distances from the core of the average 10^{17}eV shower The numbers attached to the curves are the core distances (m).

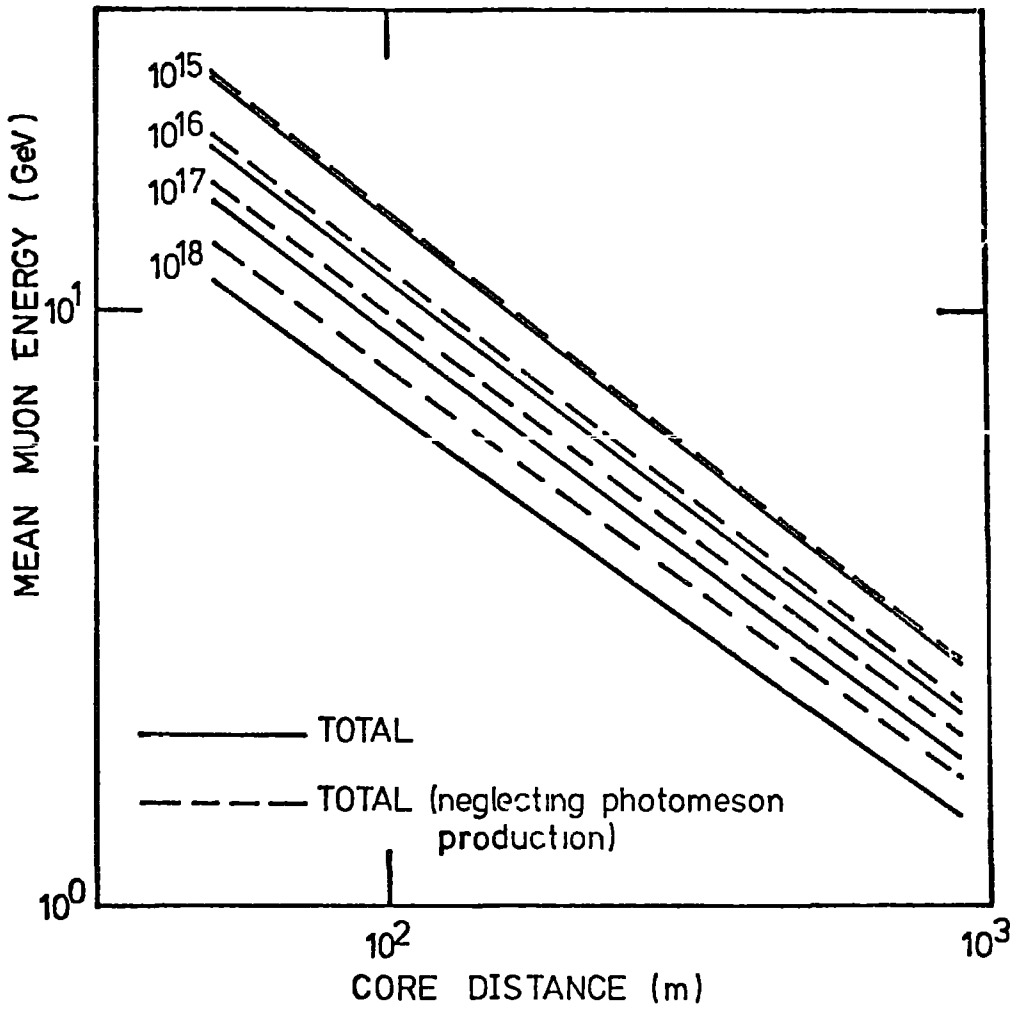

FIGURE 4-14 The mean muon energy as a function of core distance. The numbers attached to the curves are the primary energies (eV) of the showers.

4-6.2 Lateral distribution of muons

The lateral distribution of muons with energy greater than various prescribed threshold energies is shown in figure 15 for the average 10^{17}eV shower. Figure 16 shows the lateral distributions of muons with energy greater than 0.3 GeV (a typical detector threshold) for primary energies in the range 10^{15} eV to 10^{18}eV. The muon densities (E>0.3 GeV) given in figure 16 are extrapolated to higher primary energies (by summing the power law extrapolations of the two components) and plotted against primary energy for various core distances in figure 17. It is noted that at 10^{20} eV the muon density at 600 m from the core is expected to be about seven times that obtained when photomeson production is neglected!

4-6.3 Spatial characteristics of muons

The mean height of origin of muons (the mean production altitude of the parent pions) is given as a function of core distance in figure 18 for the range of primary energy. Also shown are the mean heights of origin of muons received by a detector situated beneath 0.6 m of barytes concrete shielding (density= 3.6×10^{3}kg m^{-3})as used in a muon telescope at Haverah Park by Gibson (1976). The effect of "filtering out" the low energy muons is clearly seen at large core distances.

The mean angle between muon directions and the core direction (projected into the core-detector plane) is plotted as a function of core distance in figure 19 for a range of primary energy. These results are for muons below the barytes absorber described above.

4-6.4 Response of Haverah Park water Cerenkov detectors

The response of the Haverah Park water Cerenkov detectors to the soft component of cosmic ray showers has been discussed in chapter 3. Here the response of these detectors to both the soft and hard

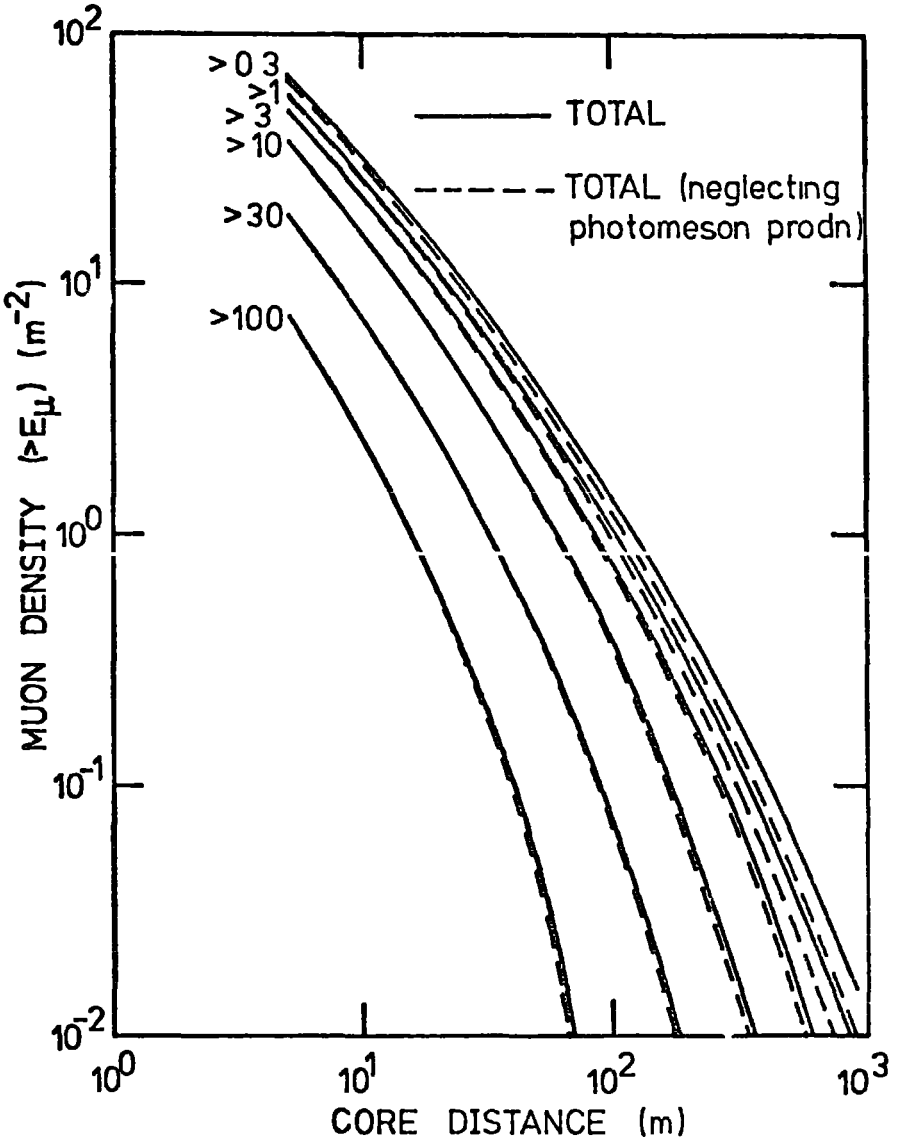

FIGURE 4-15 The lateral distribution of muons with energy greater than various prescribed threshold energies for the average 10^{17}eV shower. The numbers attached to the curves are the threshold energies (GeV).

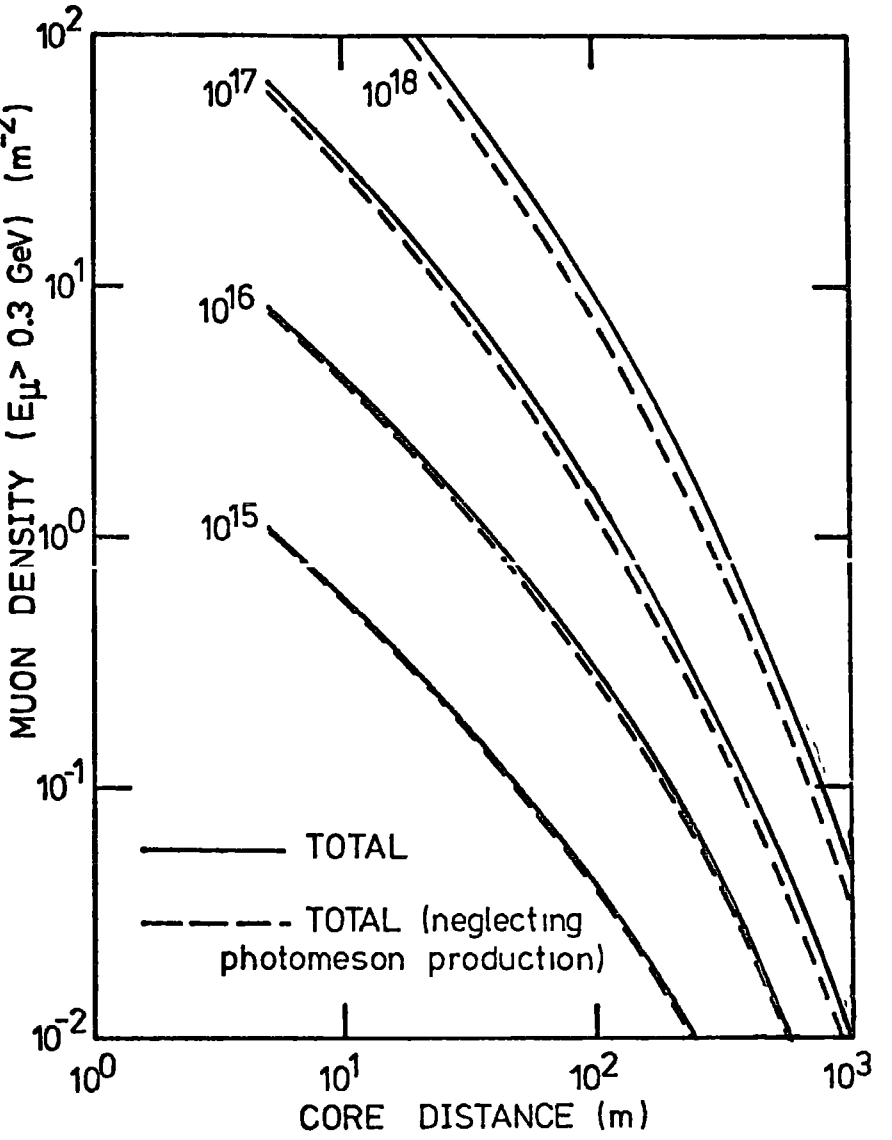

FIGURE 4-16 The lateral distribution of muons with energy greater than 0.3 GeV The numbers attached to the curves are the primary energies (eV) of the showers.

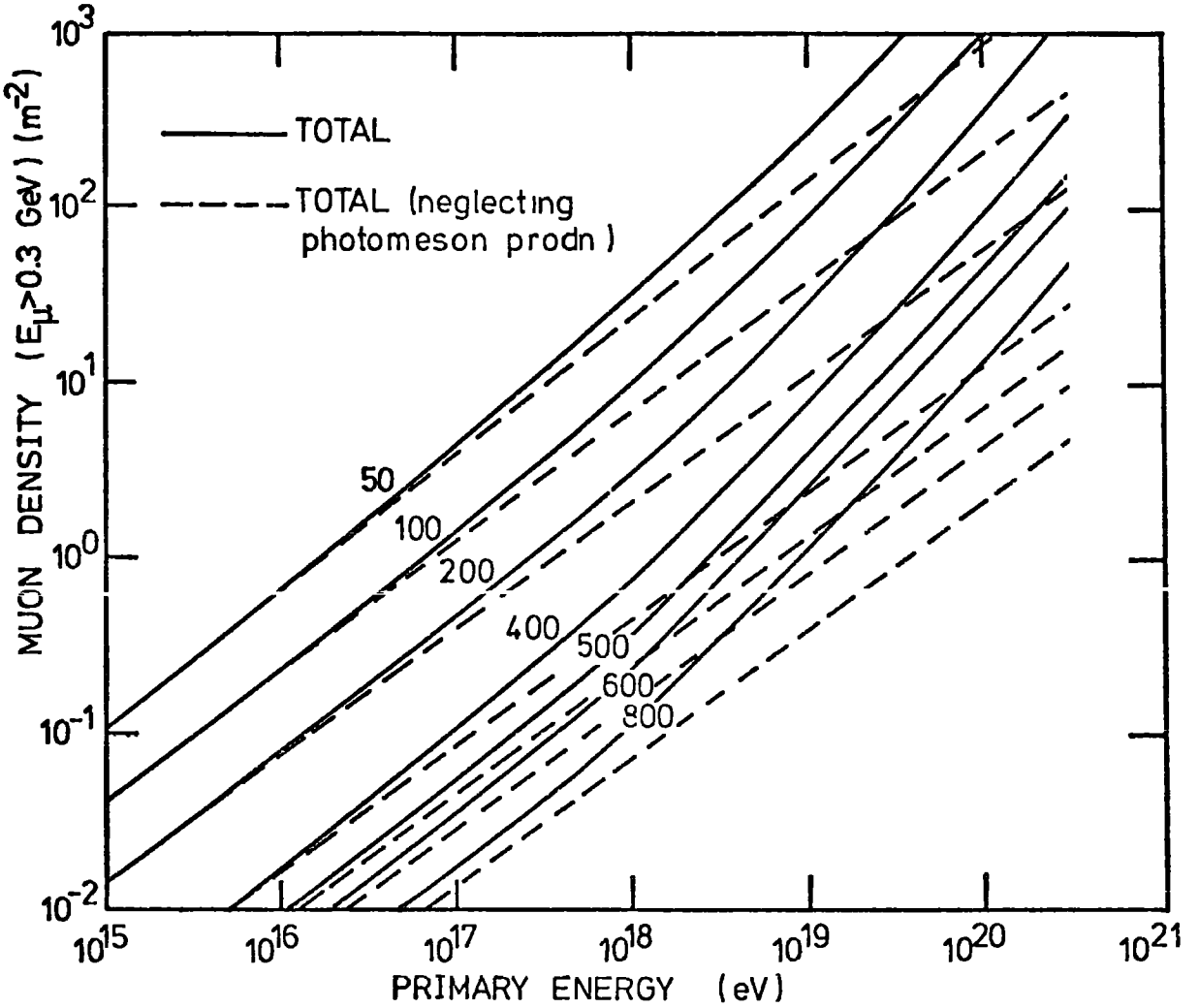

FIGURE 1-17 The muon densities at various core distances as a function of primary energy. The numbers attached to the curves are the core distances (m).

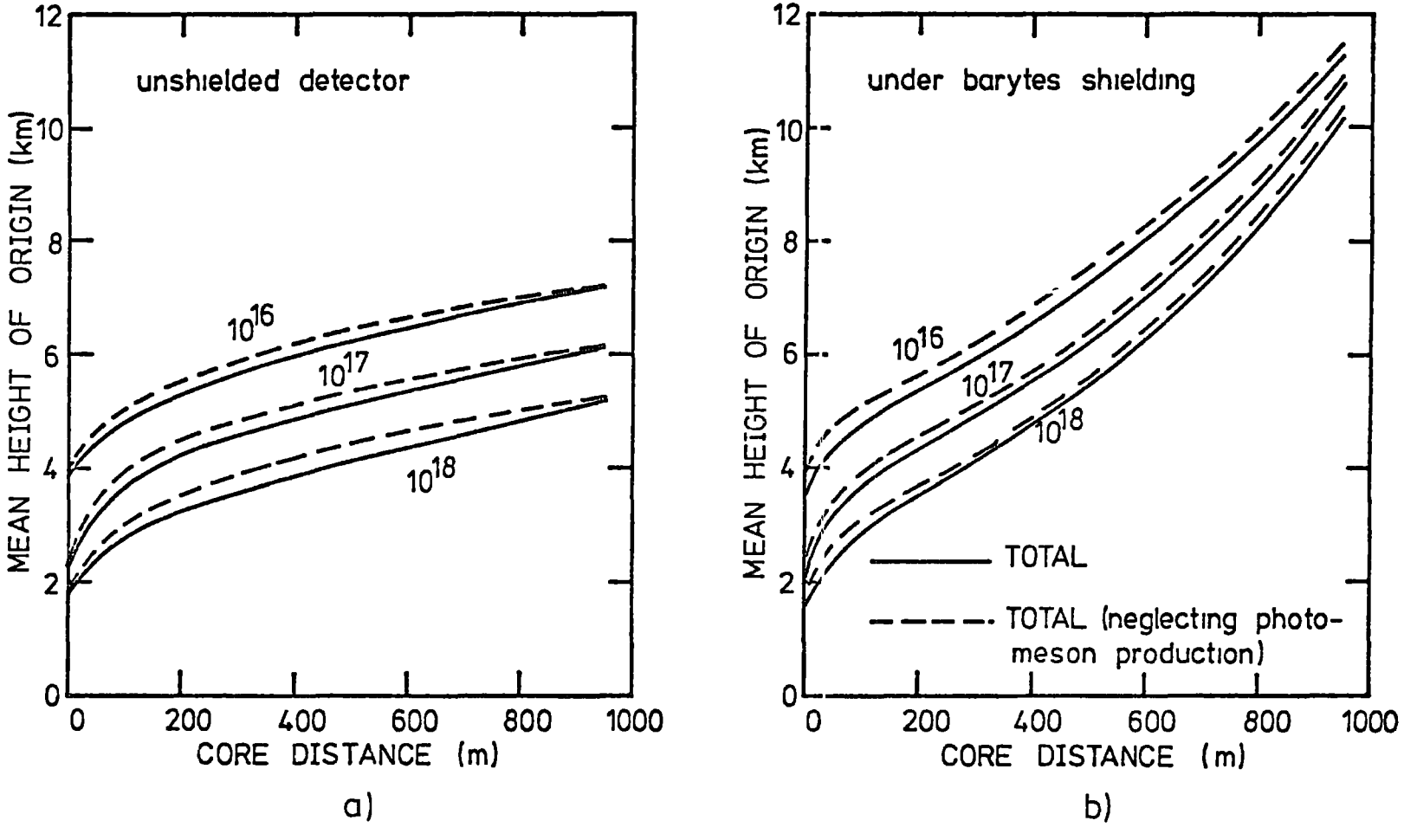

FIGURE 4-18 The mean height of origin as a function of core distance for a) an unshielded detector and b) a detector under 0.6 m of barytes concrete shielding. The numbers attached to the curves are the primary energies (eV) of the showers.

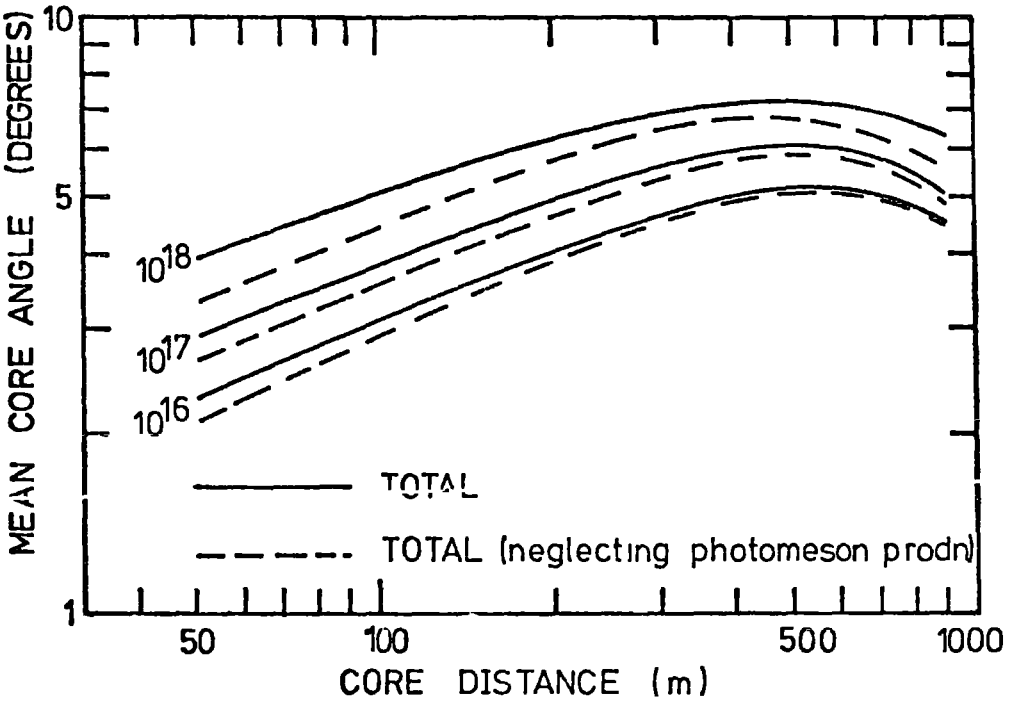

FIGURE 4-19 The mean core angle as a function of core distance for a detector situated under 0.6m of barytes concrete shielding The numbers attached to the curves are the primary energies (eV) of the showers.

components are presented. Figure 20 shows the lateral distribution of the soft component density combined with the muon density (E>0.3 GeV) for primary energies of 10^{16}, 10^{17} and 10^{18}eV. The response at 500 m and 600 m from the core (both of which are used as measurements of shower primary energy at the Haverah Park array) are plotted against primary energy in figure 21 where they are extrapolated to 10^{21}eV (by summing the power law extrapolations of the various components)

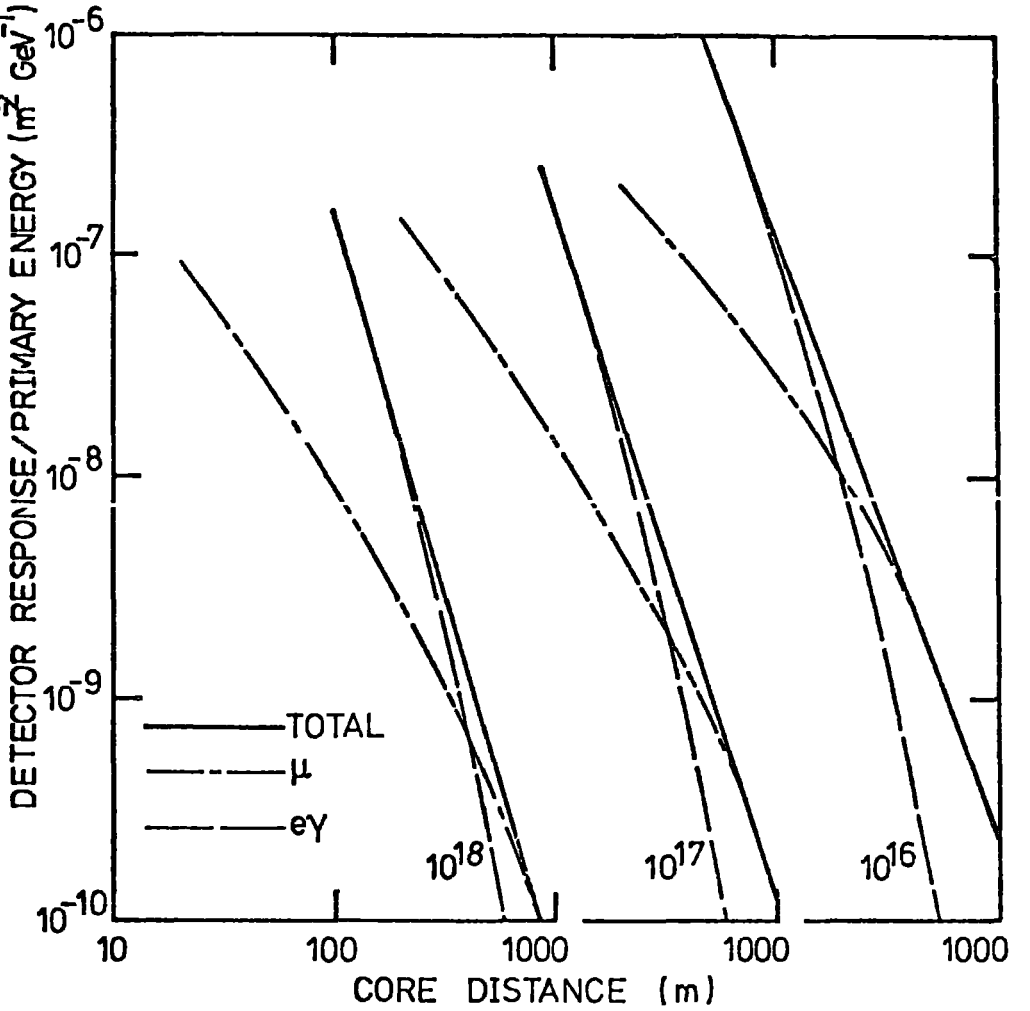

FIGURE 4-20 The lateral distribution of the Haverah Park water Cerenkov detector response (vertical equivalent muons m^{-2}), normalized to primary energy, showing the contributions from the muon component (μ) and the electron-photon component ($e\gamma$). The numbers attached to the curves are the primary energies (eV) of the showers.

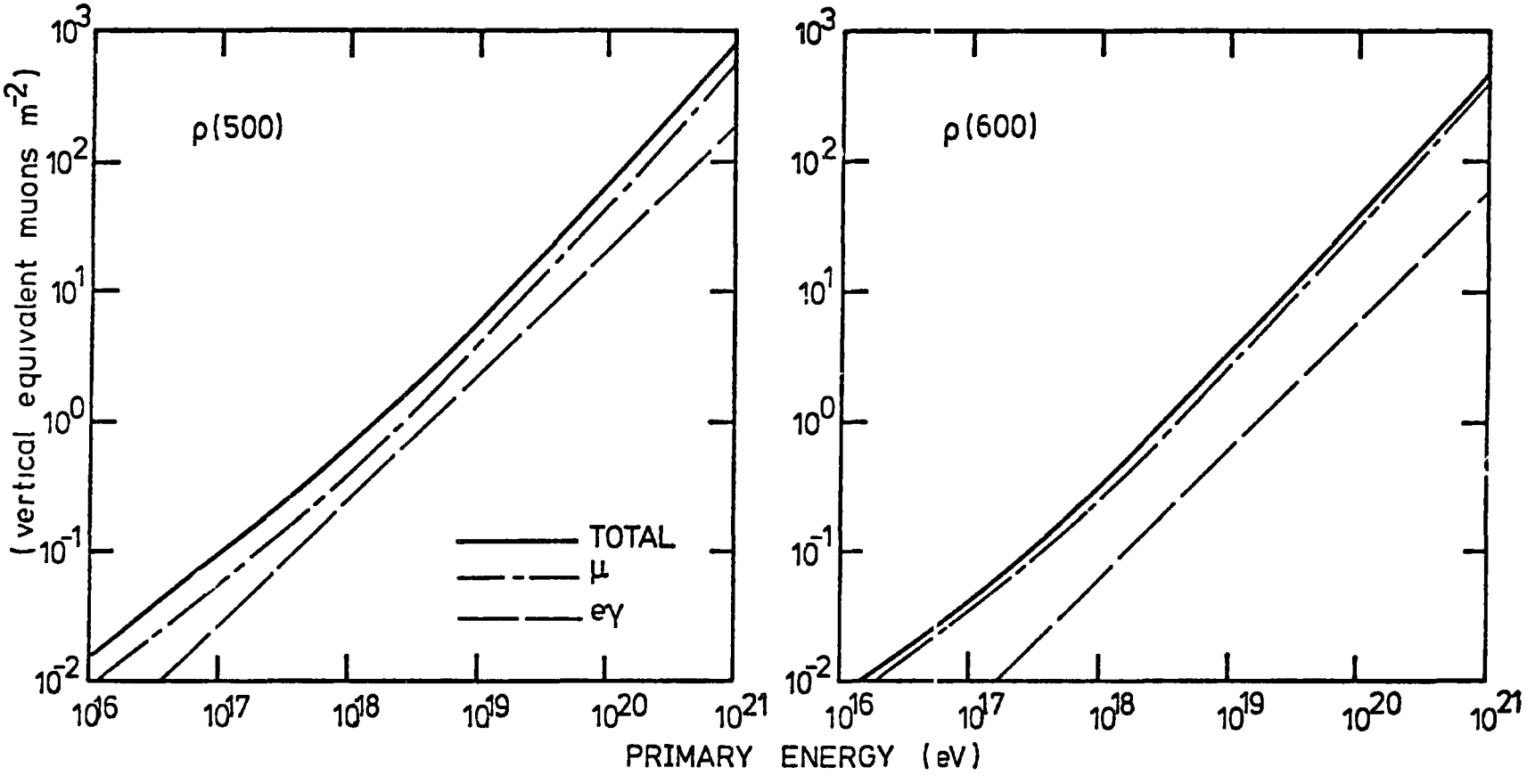

FIGURE 4-21 The Haverah Park water Cerenkov detector response at a distance of 500m, ρ(500), and 600 m, ρ(600), from the core as a function of primary energy showing the contributions from the muon component (μ) and electron-photon component (eγ).

CHAPTER FIVE

ATMOSPHERIC CERENKOV LIGHT FROM LARGE COSMIC RAY SHOWERS

INTRODUCTION

Since Galbraith and Jelley suggested in 1953 that it may be possible to detect Cerenkov light emitted in the atmosphere from the tracks of relativistic electrons in extensive air showers, there has been considerable effort devoted to both its measurement and simulation. Early calculations treated the electron cascade in one-dimension (ignoring the angular and lateral spread of electrons) and gave predictions of the lateral distribution of the light on the ground which were contradicted by experimental measurement. The importance of Coulomb scattering was soon realised and simulation techniques were improved.

More recently, there has been a resurgence of interest in studies of Cerenkov light in EAS as the development of fast electronics has enabled the time structure of the light pulses to be observed in detail. It was soon appreciated that the shape of the light pulses contained information about the development of the air shower and recent simulations, which are reported here, clearly show the relationship between pulse time structure and longitudinal cascade development. This has enabled recent measurements made by the Durham group to be analysed in a novel way enabling the longitudinal development of individual EAS to be inferred.

In this chapter, a survey of previous calculations of Cerenkov light in EAS is given together with a detailed description of the simulation techniques used for the present calculations. The importance of astmospheric attenuation and the scattering of Cerenkov light are discussed and results of the present calculations are given.

5-1 THE CERENKOV EFFECT

When a charged particle traverses a dielectric it polarizes the medium in the region of the track. If the velocity of the particle is greater than the phase velocity of light in the medium then the depolarization results in the emission of coherent radiation. This effect was first studied by Cerenkov (1934,1937).

5-1.1 Simple treatment and results of classical theory

In a simple picture, spherical wavelets of light are emitted from the particle track. If the velocity of the particle, v, is less than the phase velocity of light c/n (n is the refractive index of the medium), then the radiated wavelets will interfere destructively. If, however, $v > c/n$ wavelets from all portions of the track may be in phase with one another and constructively interfere to produce a conical wavefront travelling at an angle ϑ_c to the particle track as shown in the Huygen's construction of figure 1. Also shown in the figure is the construction for $v < c/n$ and the limiting case $v = c/n$.

From the above treatment the Cerenkov Relation is easily obtained

$$\cos \vartheta_c = \frac{c/n}{v} = (\beta n)^{-1} \qquad 1$$

A theoretical interpretation of the Cerenkov effect based on classical electromagetic theory has been given by Frank and Tamm (1937). Their result for the energy radiated, dW (J), at frequency ω in $d\omega$ (radians s^{-1}) from a length dl (m) of the track of a singly charged particle is

$$dW = \frac{e^2}{c^2}\left(1 - \frac{1}{\beta^2 n^2}\right)\omega\, d\omega\, dl \qquad 2$$

$$\therefore \quad dW = \frac{e^2}{c^2} \sin^2 \vartheta_c\, \omega\, d\omega\, dl$$

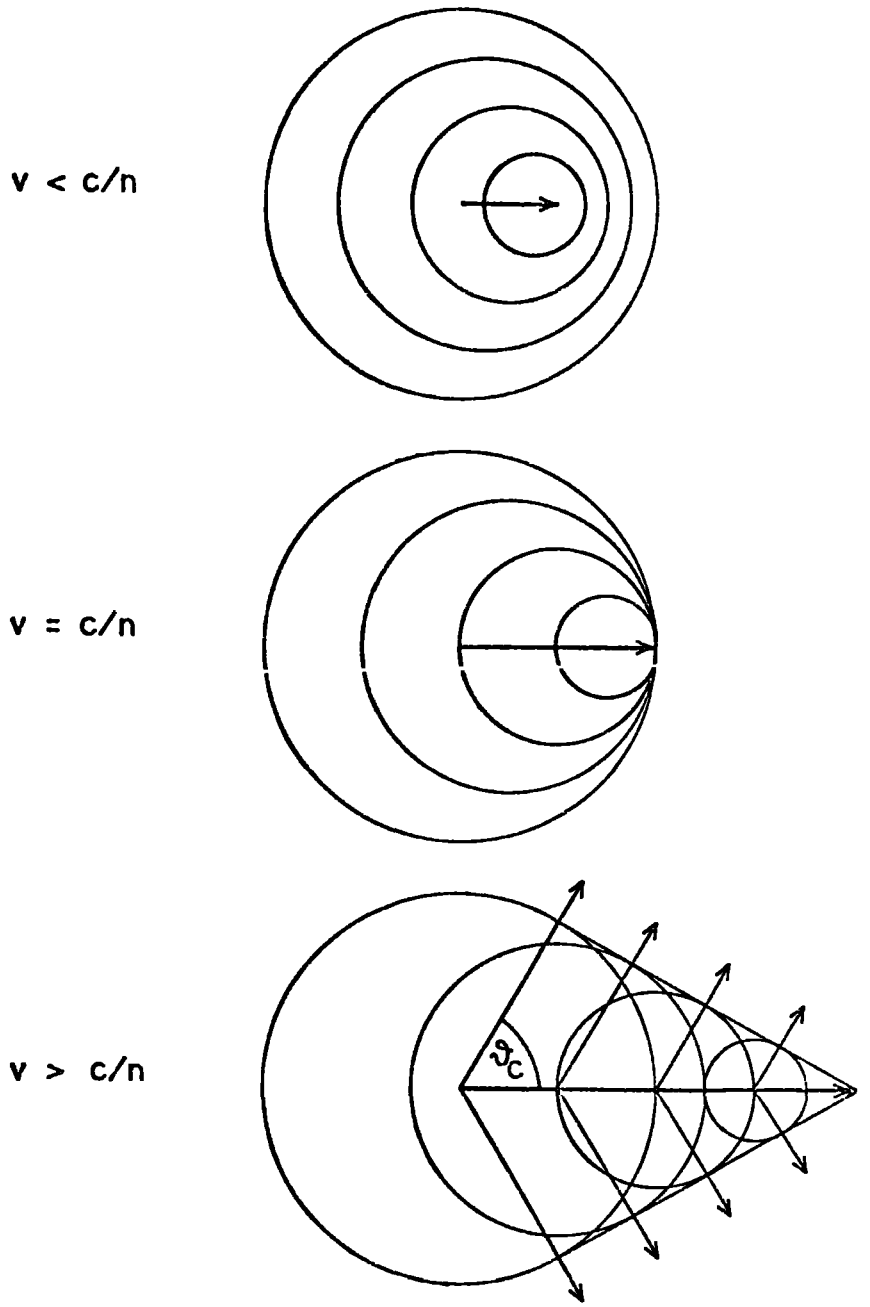

FIGURE 5-1 The Huygen's construction for Cerenkov light from a particle with velocity v in a medium with refractive index n.

It can be seen that the spectrum of Cerenkov light is proportional to $\omega d\omega$ (over the range of ω for which $\beta > \frac{1}{n}$) giving more radiation at higher frequencies.

Quantum treatments of the Cerenkov effect by Ginsburg (1940), Cox (1944) and others give essentially the same result and thus we can derive the number of photons, N, in wavelength range λ_1 to λ_2 (m) emitted from a length of track, l (m), using equation 2

$$dW = dN \hbar\omega$$

$$\therefore \quad N = \frac{e^2}{\hbar c^2} \sin^2 \vartheta_c \, (\omega_2 - \omega_1) \, l$$

$$\therefore \quad dN = 2\pi\alpha \sin^2 \vartheta_c \left(\frac{1}{\lambda_1} - \frac{1}{\lambda_2}\right) l \qquad 3$$

More generally, for a particle of charge ze, the above result is multiplied by z^2.

5-2 CERENKOV RADIATION FROM THE NIGHT SKY

In 1948 Blackett first drew attention to the possibility that Cerenkov radiation would be produced in a gas by the passage of fast charged particles. He was investigating the various sources of the general light of the night sky and concluded that Cerenkov light produced as cosmic rays pass through the atmosphere contributed about 0.01% of the total brightness of about 6.4×10^2 photons $m^{-2} ns^{-1} sr^{-1}$.

In 1953 Galbraith and Jelley suggested that it might be possible to detect Cerenkov light from EAS since the electrons arrive at the Earth's surface in a very short time interval ($\sim 10^{-8}$ s) and the Cerenkov photon density may exceed the night sky background during this period. In the same year they pioneered measurements of the Cerenkov light component of EAS by detecting these short light pulses in coincidence with EAS

5-2.1 Threhshold energy for emission of Cerenkov light in air

The refractive index of air is related to its density, ρ, through the Lorentz-Lorenz formula

$$\frac{n^2 - 1}{n^2 + 2} \cdot \frac{1}{\rho} = \text{const.} \qquad 4$$

An empirical formula for the refractive index as a function of pressure, p (mmHg), and temperature, t (^{o}C), is

$$(n_{t,p} - 1) = a\,(n_s - 1)p(1 + \beta_t p)/(1 + \alpha t) \qquad 5$$

(see Kaye and Laby (1966) for values of a, n_s, β_t and α).
The threshold energy for production of Cerenkov light by a particle of mass m (MeV/c^2) is

$$E_{min} = mc^2\,(1 - 1/n^2)^{-1/2}\ \text{MeV} \qquad 6$$

The threshold energy for electrons obtained in this way is plotted against altitude in figure 2.

5-2.2 Simple treatment of Cerenkov light in EAS

Although it has been shown by many authors that calculations based on a simple treatment of this effect give results far from reality, an appreciation of the important aspects of Cerenkov light in EAS may be obtained from simple arguments. For this reason, the production of Cerenkov light in an isothermal atmosphere by a one-dimensional cascade of ultra-relativistic electrons incident from the zenith will be considered here. For an isothermal atmosphere

$$x = x_o \exp(-h/H_o) \qquad 7$$

$$\eta = \eta_o \exp(-h/H_o) \qquad 8$$

where h is the altitude (m), H_o is the scale height (m), x is atmospheric depth (g cm^{-2}) and $\eta = (n-1)$ where n is the refractive index (the subscript

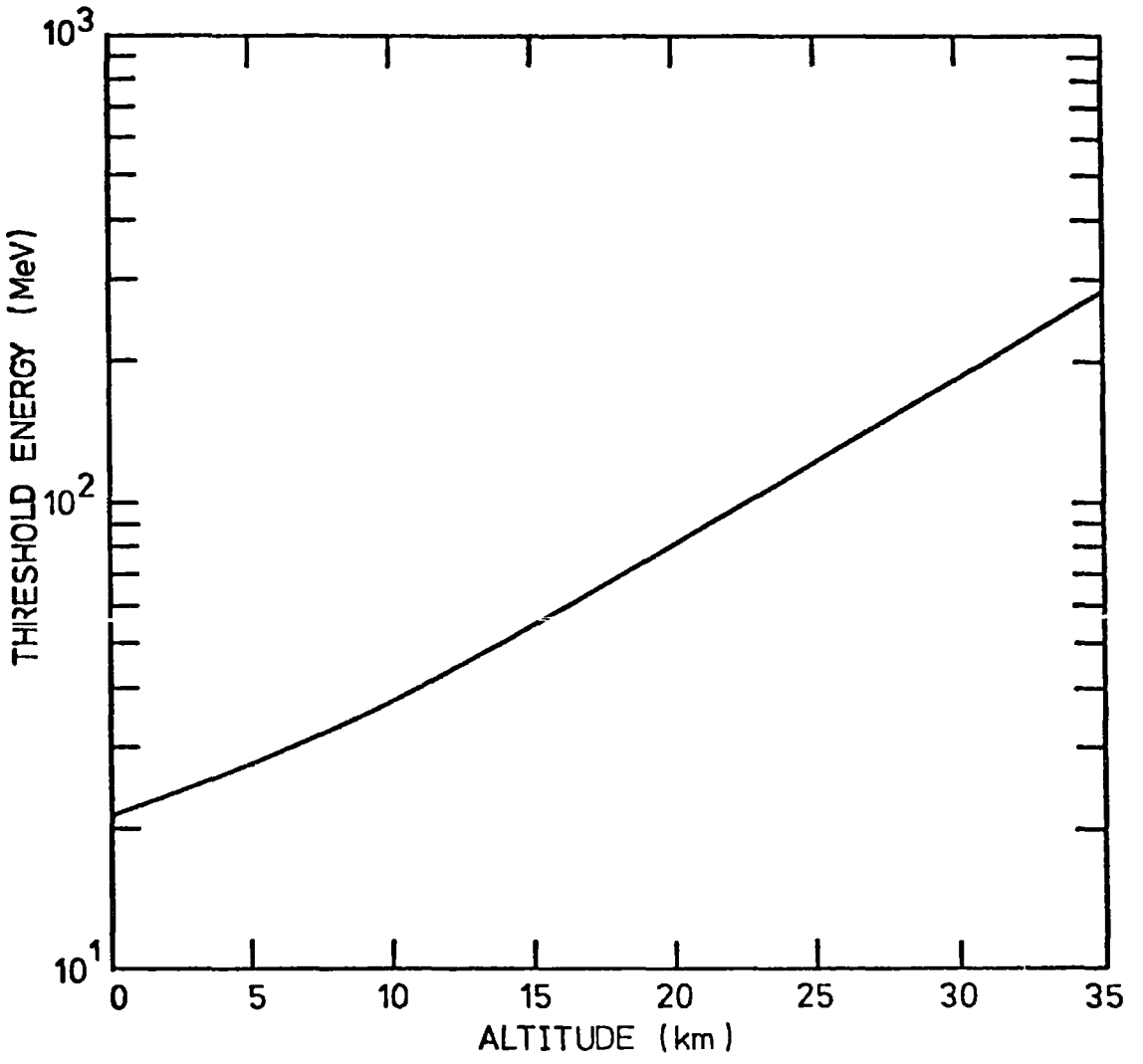

FIGURE 5-2 The threshold energy for the production of Cerenkov light by electrons in the atmosphere.

o refers to values at sea level x_o =1030 g cm^{-2}, η_o = 0.000292).

The Cerenkov angle at altitude h is (for $\beta \simeq 1$) given by

$$\cos \vartheta_c = (1 + \eta)^{-1} \qquad 9$$

Now ϑ_c is small and $\eta \ll 1$ for air so

$$1 - \vartheta_c^2/2 = 1 - \eta \qquad 10$$

$$\therefore \quad \vartheta_c = \sqrt{2\eta_o}\, \exp(-h/2H_o) \qquad 11$$

Now, under these assumptions, a Cerenkov photon emitted at altitude h (m) will arrive at sea level at a core distance r (m) given by

$$r = h\,\vartheta_c \qquad 12$$

$$\therefore \quad r = h\sqrt{2\eta_o}\, \exp(-h/2H_o) \qquad 13$$

from 7 $$h = H_o \ln(x_o/x) \qquad 14$$

$$\therefore \quad r = H_o\left[\frac{2\eta_o x}{x_o}\right]^{\frac{1}{2}} \ln(x_o/x) \qquad 15$$

Equation 15 represents a mapping between atmospheric depth of Cerenkov emission and core distance at sea level. This mapping (shown as the heavy line in figure 3) has two striking features first, at sea level no Cerenkov light is received at core distances greater than ~120 m, second, the mapping between core distance and atmospheric depth is not unique - each core distance can receive light from two depths.

Next, consider the photon yield per electron per element of atmospheric depth between wavelengths λ_1 and λ_2

$$\gamma(x)dx = 2\pi\alpha\left(\frac{1}{\lambda_2} - \frac{1}{\lambda_1}\right) \sin^2 \vartheta_c \, dh \qquad 16$$

where $$\sin^2 \vartheta_c \approx \vartheta_c^2 \approx 2\eta \approx \eta_o x/x_o \qquad 17$$

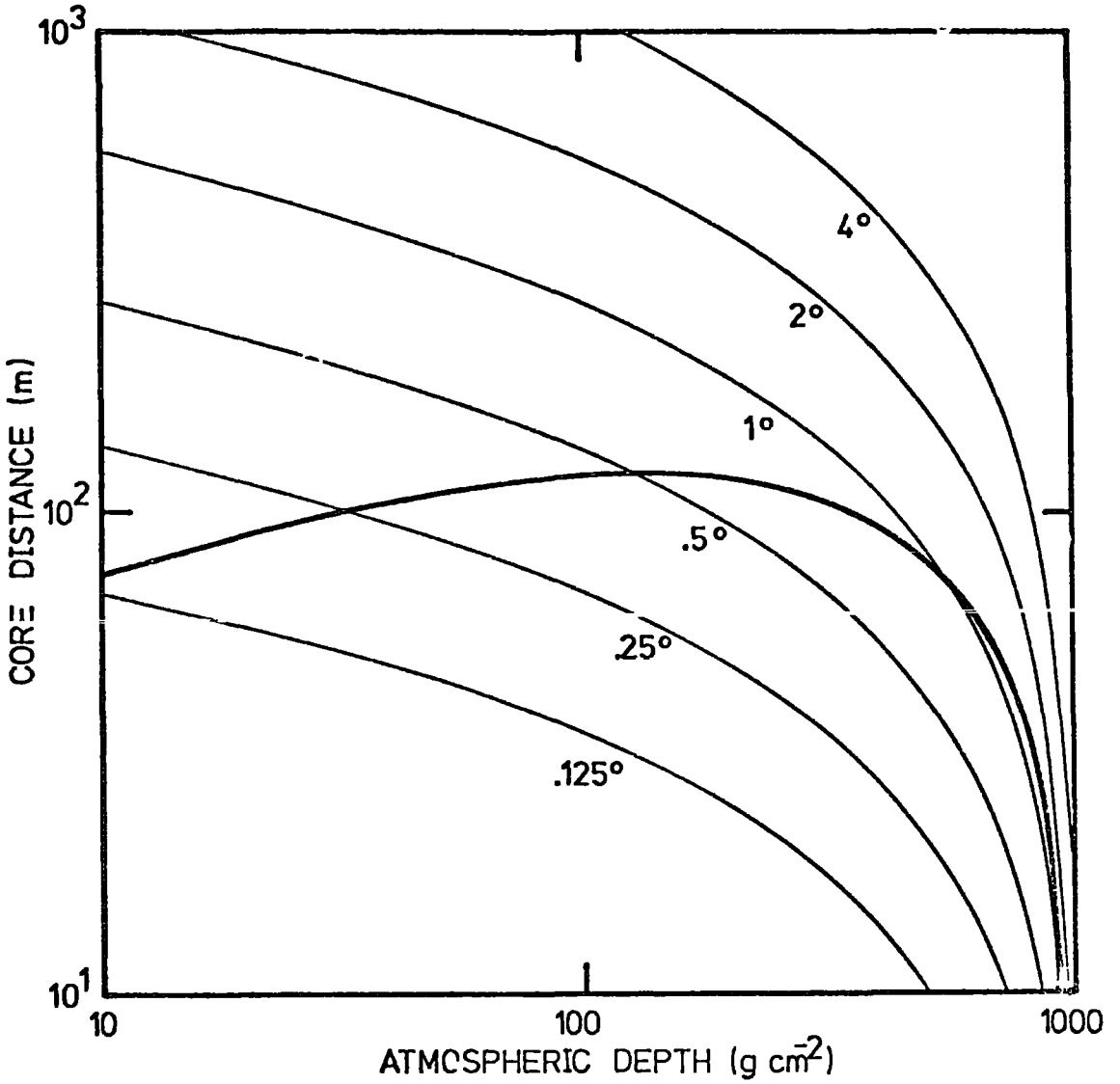

FIGURE 5-3 The mapping between atmospheric depth and core distance from equation 15 (solid line). Also shown are the curves for a constant angle of optical emission - the numbers attached to the curves are the angles of emission

and $$dh = -H_o dx/x \qquad 18$$

so $$\gamma(x)dx = 2\pi\alpha\left(\frac{1}{\lambda_2} - \frac{1}{\lambda_1}\right)\eta_o H_o \, dx/x_o \qquad 19$$

for $280 < \lambda < 600$ nm

$$\gamma(x) = \gamma_o = 317.4 \quad g^{-1}cm^2 \qquad 20$$

Hence a relativisitic electron will produce about 300 Cerenkov photons per g cm^{-2} irrespective of atmospheric depth.

All that remains to be done is to calculate the photon density as a function of core distance for a given electron cascade. This is simply,

$$\Phi(r) = \frac{N(x)\ \gamma_o\ dx}{2\pi r\ dr} \qquad 21$$

where N(x) is the number of electrons above the Cerenkov threshold at depth x.

from 15 $$\frac{dr}{dx} = -H_o\left\{\frac{2\eta_o}{x\ x_o}\right\}^{\frac{1}{2}}\left\{1 + \tfrac{1}{2}\ln(x/x_o)\right\} \qquad 22$$

$$\therefore \quad r\frac{dr}{dx} = H_o^2\frac{\eta_o}{x_o}\left\{2\ln(x/x_o) + \ln^2(x/x_o)\right\} \qquad 23$$

$$\therefore \quad \Phi(r) = N(x)\frac{\gamma_o\ x_o}{2\pi\eta_o H_o^2}\left\{2\ln(x/x_o) + \ln^2(x/x_o)\right\}^{-1} \qquad 24$$

The lateral distribution of Cerenkov light resulting from the electron cascade of a 10^7 GeV gamma-ray shower will be calculated in this way. For simplicity, the parameterization by Greisen (1956) of cascades derived under approximation B by Snyder will be used, and it is assumed that all electrons radiate Cerenkov light.

$$N(x) = \frac{.31}{\beta_o^{\frac{1}{2}}}\exp\left\{t(1 - 1.5\ln s)\right\} \qquad 25$$

where $t = x/X_o$ $(X_o \approx 37.7$ g cm^{-2} for air)

$\beta_o = \ln(E / \varepsilon_o)$ $(\varepsilon_o \approx 84$ MeV for air)

$$s = \frac{3t}{t + 2\beta_o}$$

For a 10^7 GeV gamma-ray equation 24 reduces to

$$\phi(r) = \frac{0.1478 \exp\left\{t(1 - 1.5 \ln s)\right\}}{2 \ln(x/x_o) + \ln^2(x/x_o)} \qquad 26$$

with $\beta_o = 18.595$. The resulting lateral distribution is shown as the heavy line in figure 4. Also shown in this figure is the calculation by Jelley and Galbraith (1955) of the lateral distribution of Cerenkov light from a proton initiated cascade of the same primary energy derived under essentially the same assumptions.

5-2.3 The importance of Coulomb scattering

In the above simple treatment and the calculations of Jelley and Galbraith (1955) no account was taken of the lateral spread and angular distribution of shower electrons. The importance of the angular distribution is seen by considering approximately the mean square angle of scatter of electrons using the formula given by Rossi and Greisen (1941). For short electron tracks, dx, the mean square angle of scatter is given approximately by

$$\langle \vartheta_s^2 \rangle = \left\{ \frac{E_s}{E} \right\}^2 \frac{dx}{X_o} \qquad 27$$

where $E_s \approx 21$ MeV. Now the Cerenkov threshold for electrons in air is approximately given by

$$E_{min} \approx \frac{m_e c^2}{\sqrt{2\eta}} \approx \frac{m_e c^2}{\vartheta_c} \qquad 28$$

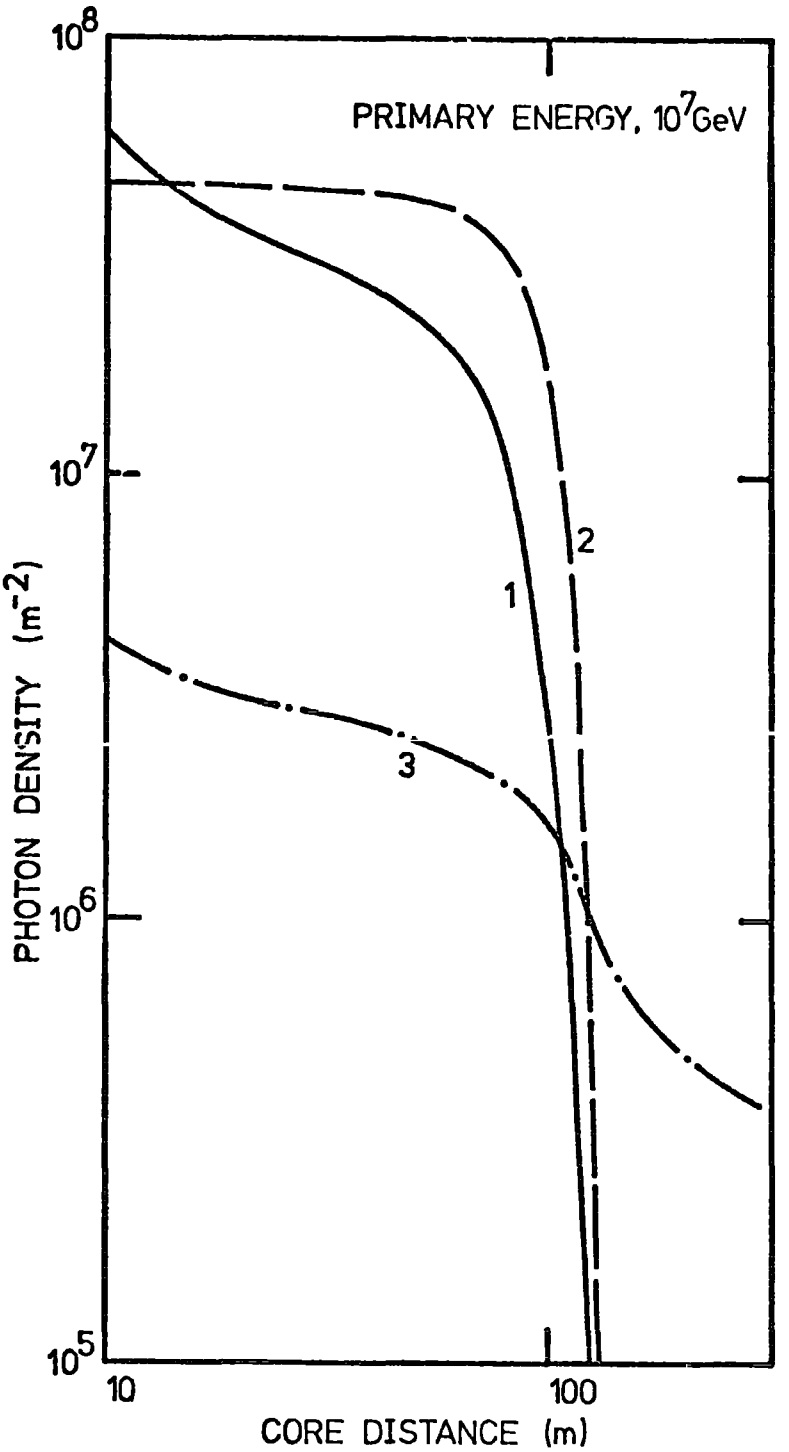

FIGURE 5-4 Lateral distribution of Cerenkov light
1- from equation 26.
2- Jelley and Galbraith (1955), proton.
3- Gol'danskii and Zhdanov (1954),

We are interested in all electrons above the threshold but the energy spectrum is approximately E^{-2} so we may consider the RMS angle of scatter of electrons at the Cerenkov threshold.

$$\vartheta_{s_{RMS}} = \frac{E_s}{E_{min}} \left\{\frac{dx}{X_o}\right\}^{\frac{1}{2}} \qquad 29$$

$$\therefore \quad \vartheta_{s_{RMS}} = \frac{E_s}{m_e c^2} \left\{\frac{dx}{X_o}\right\}^{\frac{1}{2}} \vartheta_c \qquad 30$$

Thus for $dx \geq 0.00057\ X_o$ the RMS angle of scatter is greater than the Cerenkov angle.

This inadequacy in simple treatments of Cerenkov light production in the atmosphere was clearly indicated when Barclay and Jelley (1956) observed a substantial proportion of the Cerenkov light from EAS at core distances greater than 126 m. In the calculations of Gol'danskii and Zhdanov (1954) a crude attempt was made to include the effects of Coulomb scattering. Their result is included in figure 4 for comparison.

5-3 ATMOSPHERIC ATTENUATION OF LIGHT

Light is attenuated in the atmosphere at different rates depending on wavelength and altitude. This attenuation is primarily due to Rayleigh scattering, aerosol scattering and ozone absorption. Rayleigh (molecular) scattering of light depends only on the molecule number density. Scattering by aerosols (small particles, 1 - 10 μm in size) depends on their size distribution and number density, is most important near ground level and is highly fluctuating. Ozone absorption is a major factor only at wavelenghts $\leq$ 290 nm.

5-3.1 The model of atmospheric attenuation

A description and model of atmospheric attenuation of light was given by Elterman (1968) and has been adopted throughout the present

work. In this model, the attenuation coefficients at an altitude h (km) for Rayleigh scattering, aerosol scattering and ozone absorption are defined as

$$\beta_r(h) = \sigma_r n_r(h) \times 10^3 \quad km^{-1} \qquad 31$$

$$\beta_p(h) = \beta_p(0) n_p(h)/n_p(0) \quad km^{-1} \qquad 32$$

$$\beta_3(h) = A_v \times D_3(h) \quad km^{-1} \qquad 33$$

where: σ_r is the Rayleigh scattering cross section (m^2),

n_r is the atmospheric number density (m^{-3}),

n_p is the aerosol number density (m^{-3}),

A_v is the Vigroux coefficient (cm^{-1}),

D_3 is the ozone concentration (cm km^{-1}).

The attenuation coefficients at a wavelength of 360 nm are plotted against altitude for the three processes in figure 5 together with their sum, the extinction coefficient defined by

$$\beta_t(h) = \beta_r(h) + \beta_p(h) + \beta_3(h) \quad km^{-1} \qquad 34$$

It is seen that at this wavelength aerosol scattering is most important at ground level but Rayleigh scattering predominates above ~2 km.

When considering the attenuation of light transmitted from one altitude to another, it is useful to define four optical thickness parameters $\tau_r(h)$, $\tau_p(h)$, $\tau_3(h)$ and $\tau_t(h)$ in terms of the attenuation coefficients

$$\tau(h) = \int_0^h \beta(h)dh \qquad 35$$

Then the fraction of light surviving attenuation from altitude h_2 to altitude h_1 ($<h_2$) over a slant path with zenith angle ϑ is

$$T = \exp\left\{-(\tau(h_2) - \tau(h_1))\sec\vartheta\right\} \qquad 36$$

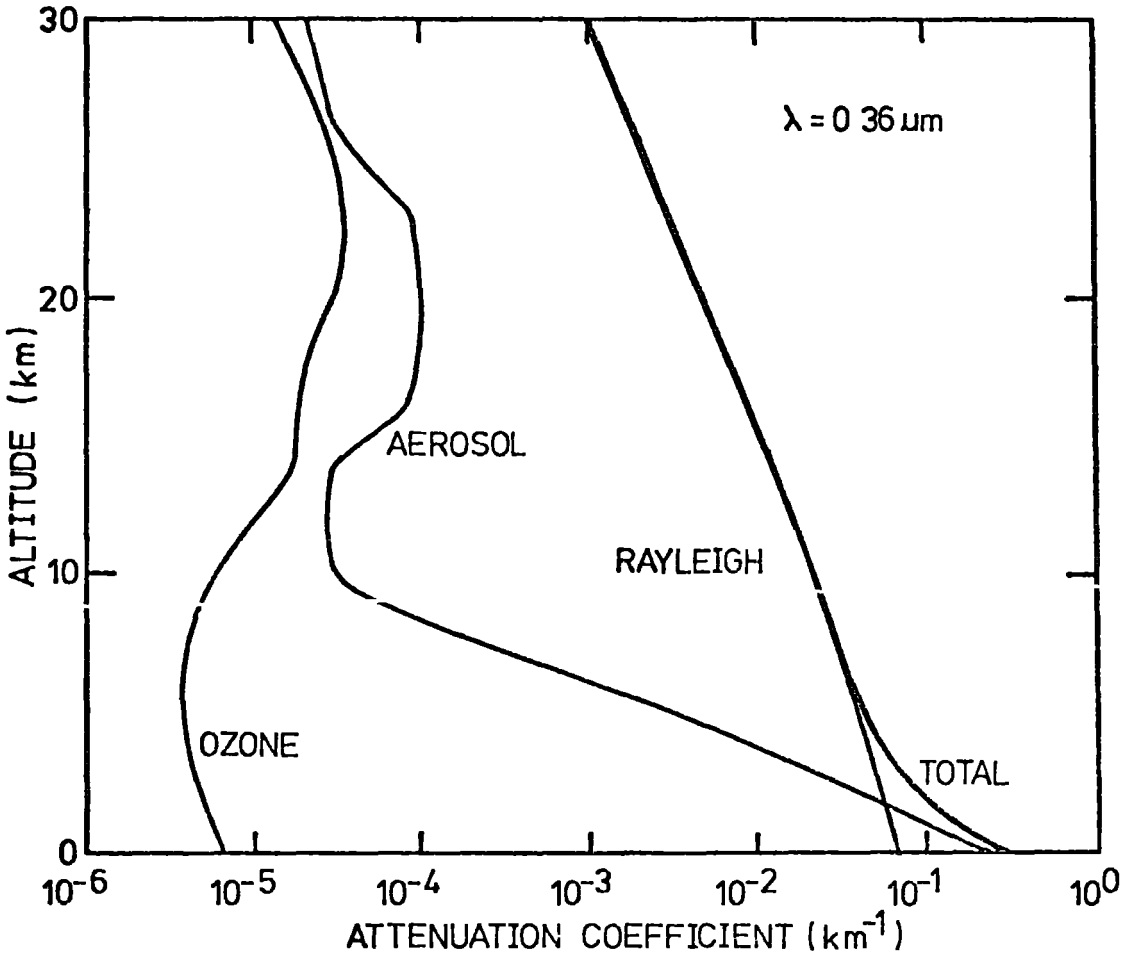

FIGURE 5-5 The atmospheric attenuation coefficients as a function of altitude at a wavelength of 0.36 μm.

The fraction of light surviving from altitude h to sea level over a vertical path is given by

$$T = \exp\left\{-\tau_t(h)\right\} \qquad 37$$

which is plotted in figure 6 against altitude for a range of wavelenths.

5-3.2 Atmospheric attenuation of Cerenkov light from EAS

The wavelength spectrum of Cerenkov light is proportional to λ^{-2} on emission but after attenuation the spectrum is distorted due to strong attenuation at short wavelengths. The spectra of Cerenkov light observed at sea level from gamma-ray cascades (calculated here under approximation B) of primary energies 10^3 - 10^9 GeV are shown in figure 7 where they are compared to the spectra of light emitted (each curve has been normalised by dividing by the number of photons emitted). The attenuation is increasingly important for low energy showers maximizing high in the atmosphere resulting also in the peak in the observed spectrum moving from blue towards red.

The photon number (wavelengths, 280 - 600 nm) is plotted against atmospheric depth for gamma-ray cascades of primary energies 10^2 - 10^6 GeV in figure 8. Also shown are the photon number curves calculated neglecting atmospheric attenuation. The ratio of the photon number at sea level to that calculated neglecting attenuation is plotted against depth of maximum in figure 9 for gamma-ray cascades of primary energies 10^0 -10^9 GeV. Also shown is the fraction of Cerenkov light surviving to sea level plotted against the depth of emission.

5-4 SURVEY OF PREVIOUS CALCULATIONS

Soon after the possibility of detection of Cerenkov light in cosmic ray showers had been suggested by Galbraith and Jelley (1953) calculations of this component were initiated by Gol'danskii and

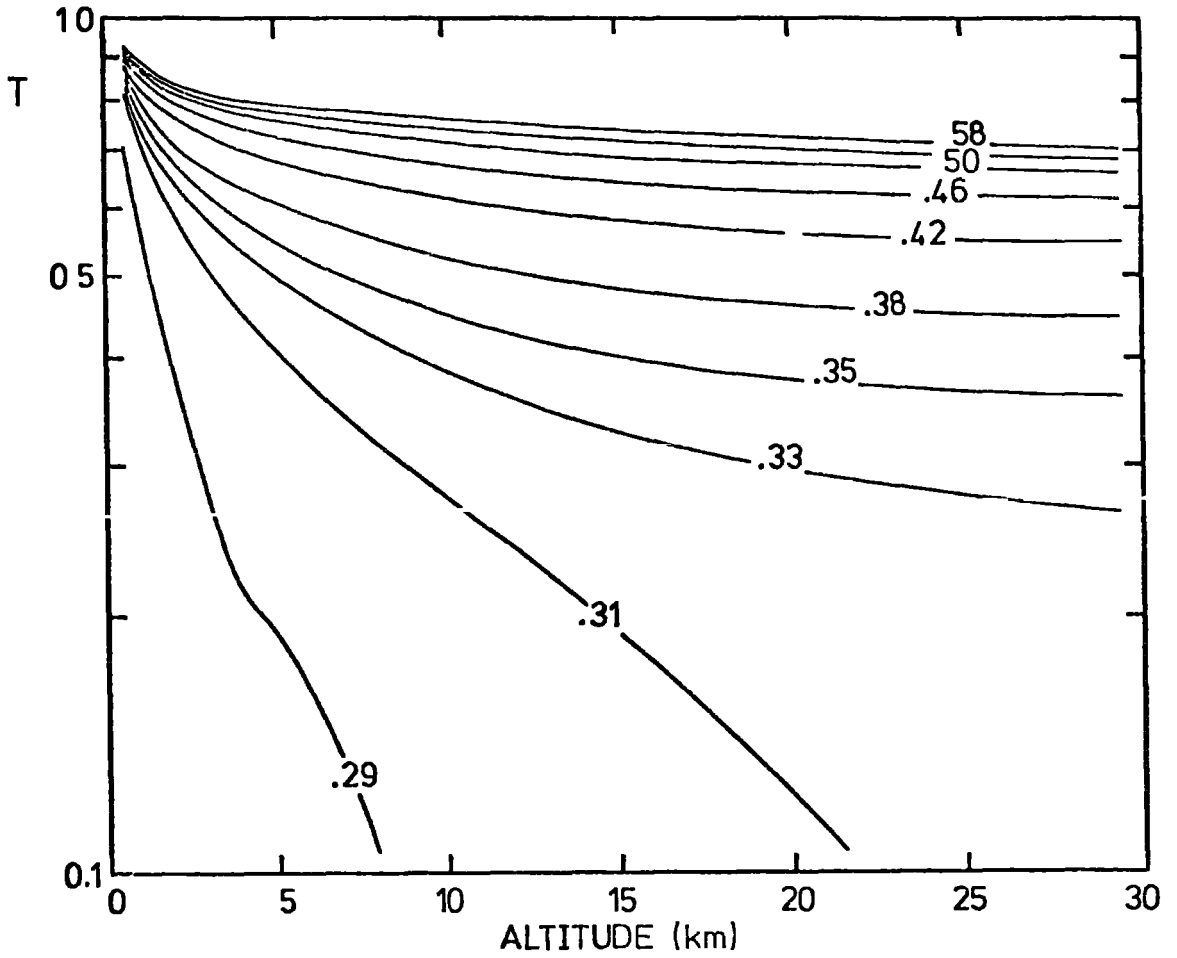

FIGURE 5-6 The fraction of light surviving from a given altitude to sea level over a vertical path - the numbers attached to the curves are the wavelengths (μm) of light considered.

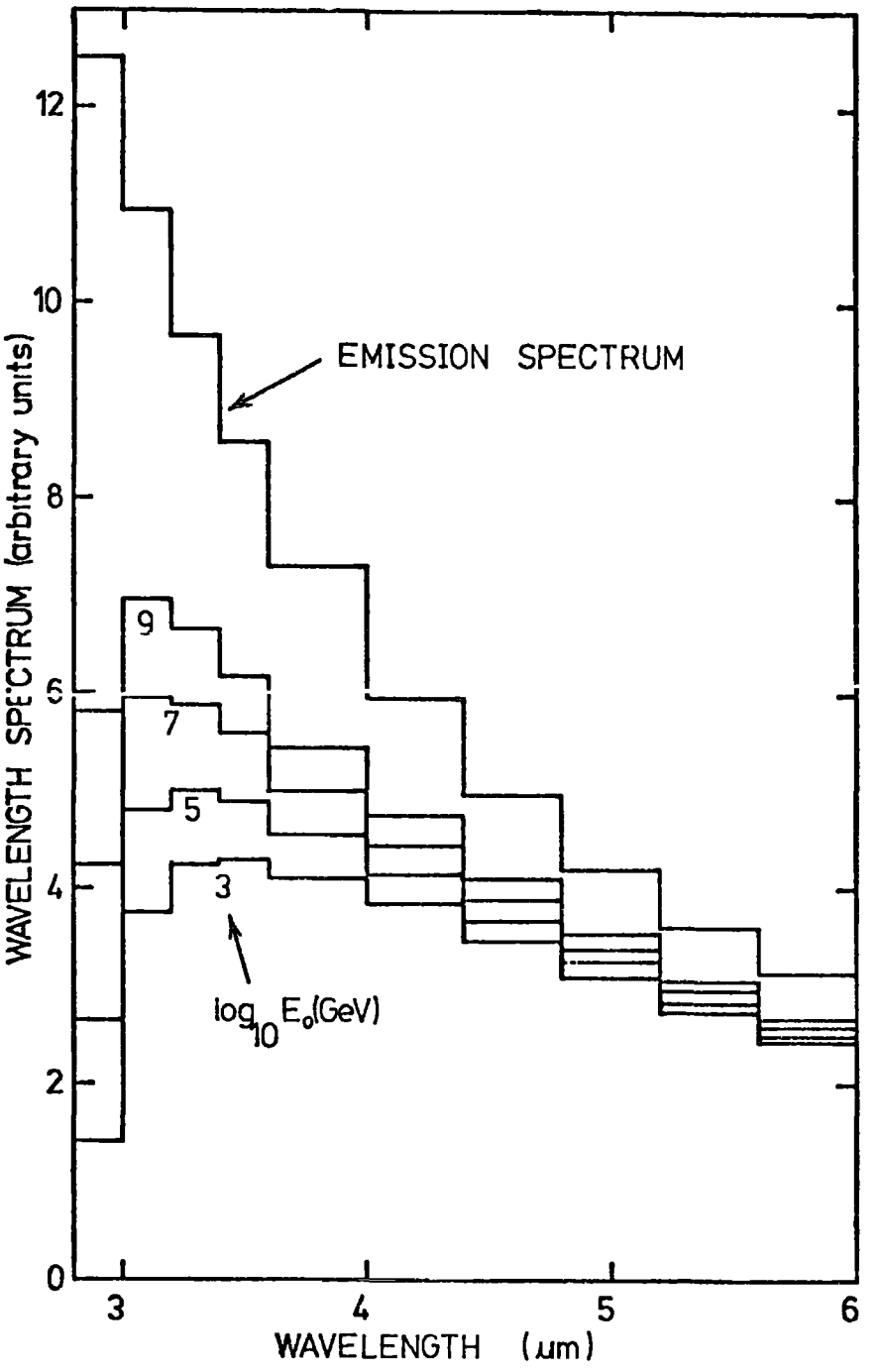

FIGURE 5-7 The spectra of light observed at sea level from a gamma-ray shower of primary energy E_o.

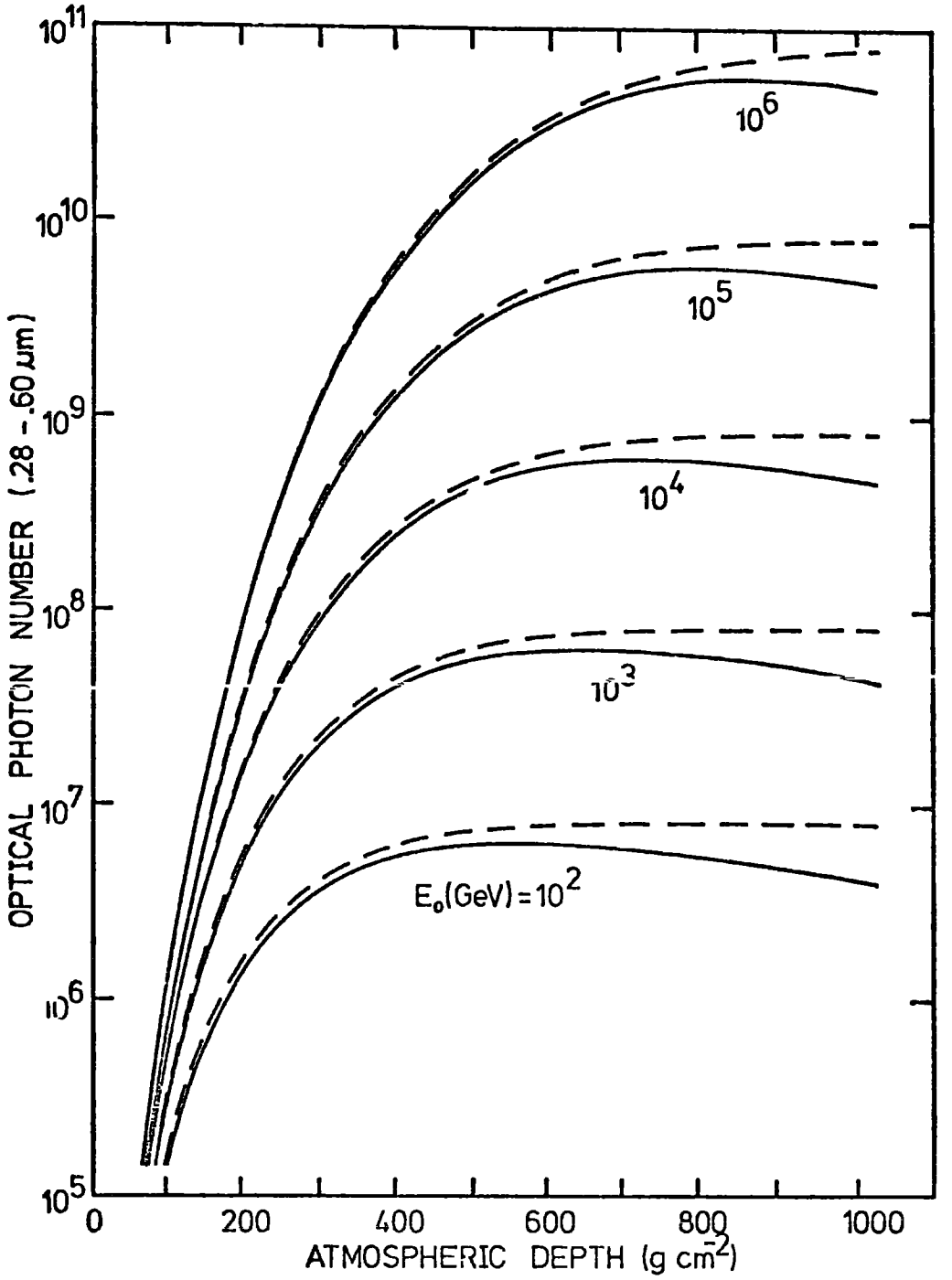

FIGURE 5-3 The photon number longitudinal development neglecting attenuation (dashed lines) and including attenuation (solid lines) for gamma-ray showers of primary energy E_o.

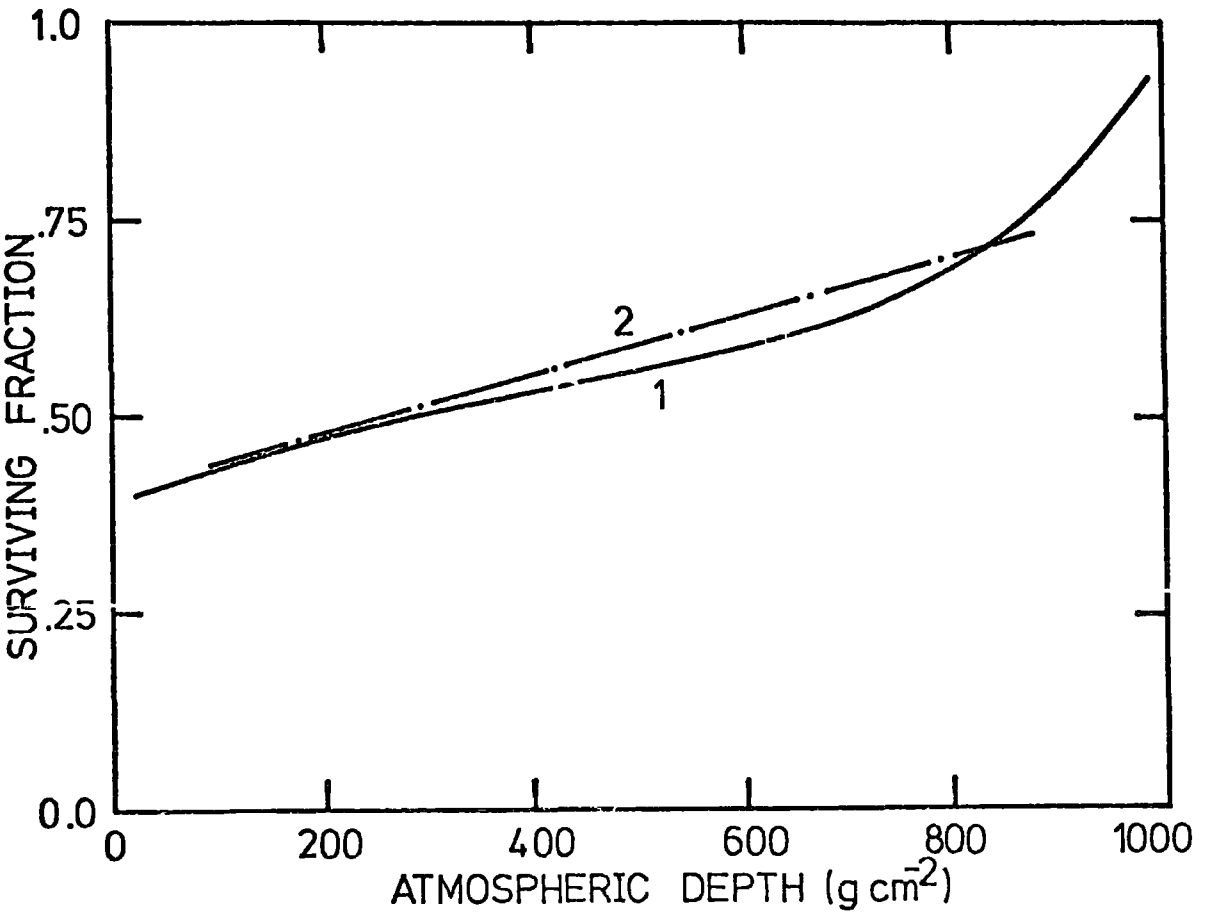

FIGURE 5-9 The fraction of Cerenkov light surviving to sea level from gamma-ray cascades maximizing at the atmospheric depth shown (curve 2) and the fraction surviving to sea level emitted by an electron at the atmospheric depth shown (curve 1).

Zhdanov (1954) and Jelley and Galbraith (1955). Jelley and Galbraith neglected Coulomb scattering and Gol'danskii and Zhdanov made crude approximations. These calculations were followed by those of Zatsepin and Chudakov (1962) and Sitte (1962) using more realistic Coulomb scattering. Sitte's calculations were for non-vertical showers and detectors of finite acceptance angle. He also calculated the relative contributions to the total light from various heights. Similar results on the heights of origin of the light were given by Brennan et al (1958) and developed by Malos et al (1962).

The calculations of Castagnoli et al (1967), Sitte (1969) and Rieke (1969) included predictions of pulse time structure. Boley (1964) suggested that the time dependence of the received light would greatly supplement the shower development information obtained from lateral distributions. Fomin and Khristiansen (1971) suggested how the time structure depended on the longitudinal development of the shower and Bosia et al (1972) investigated the dependence of pulse shape on shower age. Castagnoli et al (1972) reported simulations of the temporal development of isophotes.

Many calculations followed for a variety of observation altitudes, primary energies and masses. Smith and Turver (1973) used a detailed model for the atmospheric attenuation of light and Browning and Turver (1977) were the first to consider geomagnetic deflection of electrons in the context of full scale simulations.

An inexhaustive survey of these calculations is given in table 1.

5-5 DETAILED SIMULATION OF CERENKOV LIGHT FROM EAS

The present work is a development of the simulations of Smith and Turver (1973) and extends the simulation study of Cerenkov light in gamma-ray showers by Browning and Turver (1977) to EAS energies.

REFERENCE	DATE	PRIMARY MASS	RANGE OF PRIMARY ENERGY (eV)	PRIMARY ZENITH ANGLE (°)	RANGE OF OBSERVATION ALTITUDES (m)	ATTENUATION	GEOMAG DEFLECTION	LATERAL DISTRIBUTION	ANGULAR DISTRIBUTION	PULSE TIME STRUCTURE	SUGGEST IMAGING
Gol'danskii et al	1954			0				*			
Jelley et al	1955	0,1	10^{12-16}	0	0,2860			*			
Brennan et al	1958										*
Sitte	1962			25-20				*	*		*
Zatsepin et al	1962	0,1	10^{11}-4.5×10^{15}	0	0,3860			*			
Malos et al	1962										*
Castagnoli et al	1967	0	10^{12-14}	0	0,3500, 6500			*		*	
Krieger et al	1969	1	10^{15-17}	0	5200			*			
Sitte	1969									*	
Rieke	1969	0	10^{11}	0-60	2320			*	*	*	
Fomin et al	1971	1-50	10^{17}	0	0					*	*
Bosia et al	1972	0	10^{11-14}	10	0,3500				*	*	*
Castagnoli	1972	0	10^{11-12}	0	2320			*	*	*	
Smith et al	1973	1	10^{15-18}	0	0	*		*			
Dyakonov et al	1973		10^{16-18}	0	0	*					
Efimov et al	1973		10^{17}	0	0					*	
Grindlay	1974	≥ 1	$\geq 10^{12}$	0	2300			*	*		
Guzhavin et al	1975	1	10^{12-16}	0	0,3860			*		*	
Kalmykov et al	1975a	1-52	10^{17}	0	0					*	
Protheroe et al	1975	1,56	10^{17}	0	0	*		*	*	*	
Ivanenko et al	1976	0	10^{12-17}	0	0			*		*	
Browning et al	1977	0	10^{10}-3×10^{11}	0	0,2380	*	*	*	*	*	
Protheroe et al	1977	1-56	10^{16-18}	0	0,1800	*	*	*	*	*	*

TABLE 5-1 A brief survey of previous calculations

The Cerenkov light from gamma-ray showers with primary energies of 1, 1.77, 3.16, 5.62, 10.0, 17.7, 31.6 and 56.2 GeV (averaged over 50, 30, 20, 10, 6, 3, 3 and 3 showers respectively) injected at 40 atmospheric depths was calculated and stored on magnetic tape. The π^o production spectrum was calculated at the 40 levels as described in chapter 2. The electron-photon cascade derived from the π^o production spectrum was followed using a step-by-step method under approximation A (as described in detail in chapter 3) with particles extracted from the cascade as their energies fell below 75.0 GeV. This spectrum of particles with energies below 75.0 GeV (produced by particles with energies above 75.0 GeV) was reduced to the standard format (quarter decade energy bins at 40 atmospheric depths) and used to weight the Cerenkov light information for gamma-ray showers (stored on the magnetic tape) to give the Cerenkov light produced by the high energy EAS.

5-5.1 The framework for simulation

The computer program used for these simulations was identical with the detailed electron-photon program described in chapter 3 except for the addition of routines to calculate the production and propagation of Cerenkov light.

In this program the tracks of all electrons and positrons above the Cerenkov threshold were split into a number of straight segments approximating to their curved trajectories in the geomagnetic field. The problem is thus to calculate at the observation level the photon density, wavelength spectrum, arrival direction and arrival time distribution of the light resulting from an arbitrary electron track extending from (x_1, y_1, z_1) at time t_1 to (x_2, y_2, z_2) at time t_2. The coordinate system used in these simulations was a left handed set with the origin at the point of injection of the primary gamma-ray.

The x direction was defined as the direction of magnetic East, the y direction as magnetic North and the z direction as towards the centre of the Earth with all distances measured in metres. All times were measured in ns with respect to a plane parallel to the x-yplane moving in the z direction with velocity c starting from the origin at the time of injection of the primary.

5-5.2 Storage of photon information at the observation level

The information which was stored in the program was of necessity a compromise based on the potential interest of the information, since the amount of storage space available was limited by the amount available on the computer and the requirements of the main electron-photon program. For this reason directional and wavelength information were binned independently of timing information. The photon density was simultaneously binned in core distance (8 radial bins), zenith angle (10 bins) and wavelength (10 bins) in a three dimensional matrix as indicated in table 2. In addition, photon density was binned simultaneously in core distance and time (irrespective of zenith angle and wavelength) in a two dimensional matrix. 300 time bins were used per core distance as indicated in table 3. The effect of the spectral response of a typical photomultiplier on the pulse time structure was considered and the response of a photomultiplier was also binned simultaneously in core distance and time.

5-5.3 The method of simulation

The Cerenkov light produced by the electron track from (x_1, y_1, z_1) to (x_2, y_2, z_2) was considered to originate from the midpoint of the track: (y_0, y_0, z_0). The Cerenkov cone angle ϑ_c was calculated from equation 1 enabling the Cerenkov cone to be projected onto the observation level ($z = z_3$) where the intersection of the cone and the

number of bin	range of core distance (m)	range of zenith angle (degrees)	range of wavelength (nm)
1	0 - 1	0.0 - 0.5	280 - 300
2	49 - 51	0.5 - 1.0	300 - 320
3	99 - 101	1.0 - 1.5	320 - 340
4	199 - 201	1.5 - 2.0	340 - 360
5	349 - 351	2.0 - 3.0	360 - 400
6	499 - 501	3.0 - 4.0	400 - 440
7	699 - 701	4.0 - 5.0	440 - 480
8	899 - 901	5.0 - 10.0	480 - 520
9		10.0 - 30.0	520 - 560
10		30.0 - 90.0	560 - 600

TABLE 5-2. The core distance, zenith angle and wavelength bins used in the computer program.

number of bin	range of tangent plane delay (ns) core distance bins 1 - 4	core distance bins 5 - 8
1	0 - 1	0 - 4
2	1 - 2	4 - 8
3	2 - 3	8 - 12
4	3 - 4	12 - 16
5	4 - 5	16 - 20
.	.	.
.	.	.
.	.	.
300	299 - 300	1196 - 1200

TABLE 5-3 The time bins used in the computer program.

observation plane formed an ellipse as shown in figure 10.

The semi-major and semi-minor axes b and a of the ellipse were calculated as follows

$$d = \left\{(x_3 - x_0)^2 + (y_3 - y_0)^2 + (z_3 - z_0)^2 \right\}^{\frac{1}{2}} \tan \vartheta_c$$

$$s = d \cos \vartheta_c \sec (\theta - \vartheta_c)$$

$$t = d \cos \vartheta_c \sec (\theta + \vartheta_c)$$

$$\therefore \quad b = (s + t)/2 \qquad 38$$

for the ellipse,

$$\frac{d^2}{a^2} + \frac{(b-s)^2}{b^2} = 1$$

$$\therefore \quad a = \frac{db}{\sqrt{st}} \qquad 39$$

Any point on the ellipse (given in the primed coordinate system shown in figure 10) satisfies

$$\frac{x'^2}{a^2} + \frac{y'^2}{b^2} = 1 \qquad 40$$

and may be easily transformed to the main coordinate system.

The number of photons produced by the electron track in each of the ten wavelength bins was calculated from equation 3. These photons were considered to progagate along 180 rays in the surface of the cone originating from (x_0, y_0, z_0) and terminating in the observation plane at 180 points around the ellipse given (in the primed coordinate system) by

$$x' = a \cos \alpha$$

$$y' = b \sin \alpha \quad , \alpha = 2, 4, 6 \ldots 360^{\circ} \qquad 41$$

The number of photons arriving at each of the 180 points on the ellipse was obtained for each wavelength bin by multiplying the number produced

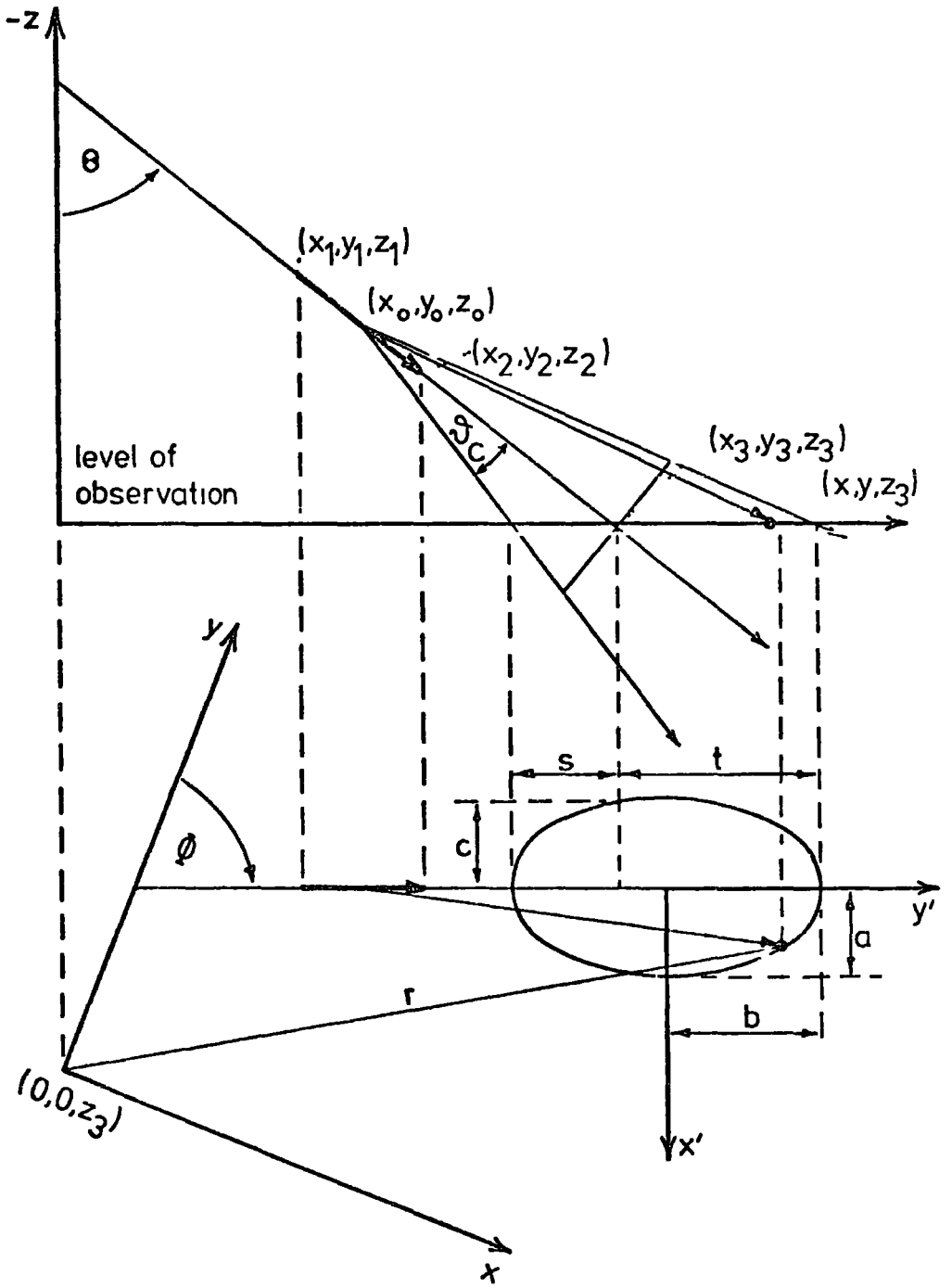

FIGURE 5-10 Two orthogonal views showing the Cerenkov cone and ellipse in the observation plane.

(divided by 180) by the atmospheric transmission factor calculated from equation 36.

The time of arrival of the ray behind the tangent plane, t_3, was calculated from

$$t_3 = t_0 + \frac{\sec\vartheta_R}{c} \int_{z_0}^{z_3} \{ 1 + \eta(z) \} dz - \frac{z_3 - z_0}{c} \qquad 42$$

where t_0 is the tangent plane delay of the electron at (x_0, y_0, z_0),

ϑ_R is the zenith angle of the ray,

$(1 + \eta(z))$ is the refractive index of air at an altitude corresponding to z.

If the ray under consideration intersected the observation plane within the limits of one of the 8 radial bins then its temporal, spatial and wavelength information was binned. The photon density (obtained by dividing the number of photons in the ray at the observation level by the area of the radial bin) was added to the appropriate element of the radial-time matrix. The photon densities corresponding to each wavelength band were added to the appropriate element of the radial-zenith angle-wavelength matrix The effect of the spectral response of an RCA type 4522 5" photomultiplier (shown, reduced to the same wavelength bins of this calculation, in figure 11) on the pulse time structure was accounted for by adding the sum over wavelength bins of the partial photon densities multiplied by the spectral response of the photomultiplier to the appropriate element of the radial-time matrix.

This procedure was adopted for each electron track enabling information about Cerenkov light produced by the whole shower to be built up.

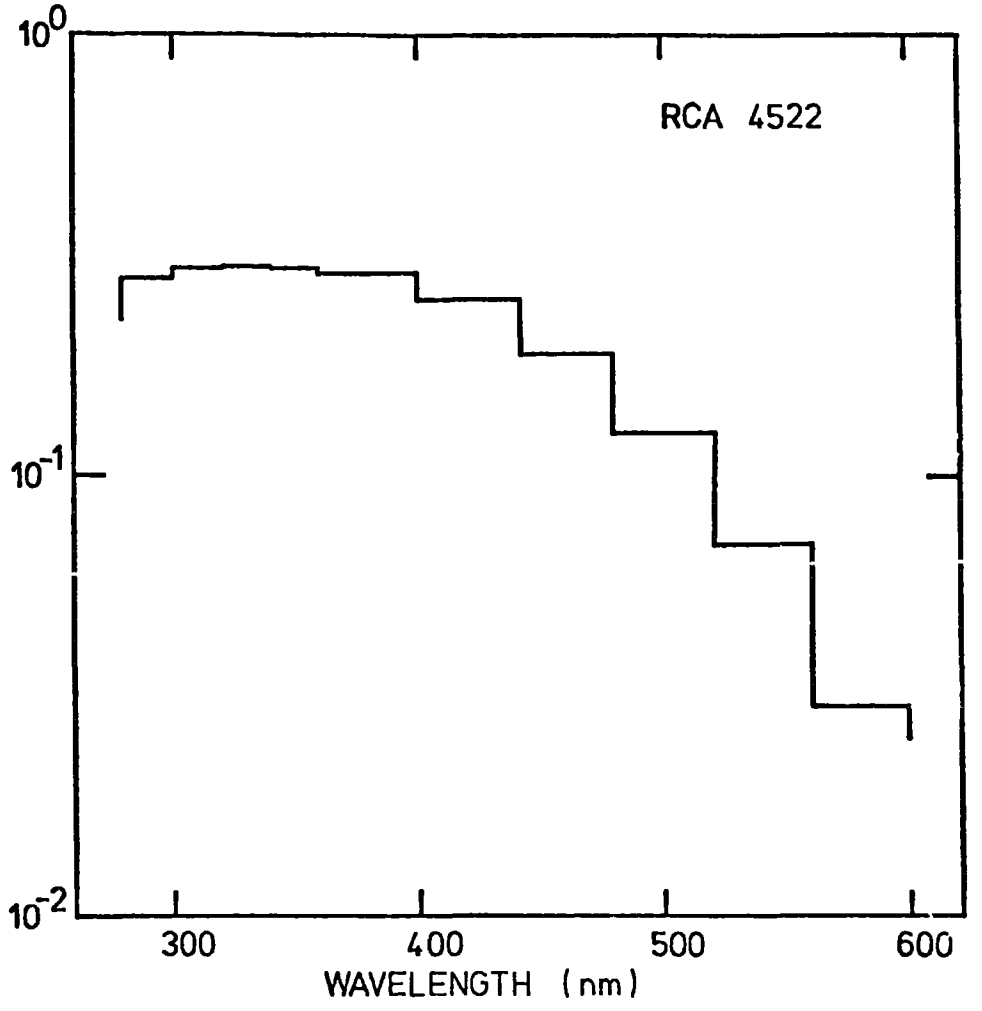

FIGURE 5-11 The spectral response of a RCA type 4522 photomultiplier - typical of those used in measurements of atmospheric Cerenkov light.

5-6 REDISTRIBUTION OF SCATTERED LIGHT

The Rayleigh moleuclar law of scattering is

$$\beta_{\varphi\lambda} = \frac{2^2}{N\lambda^4} (\mu_\lambda - 1)^2 (1 + \cos^2\varphi) \qquad 43$$

where λ is wavelength (m),

μ_λ is refractive index at wavelength λ,

N is the molecular number density (m^{-3}),

φ is the angle of scatter,

such that the intensity of the scattered beam $i_{\varphi\lambda}$ is

$$i_{\varphi\lambda} = \beta_{\varphi\lambda}\, i_\lambda \qquad 44$$

where i_λ is the intensity of the unscattered beam. The total intensity scattered is

$$i_\lambda' = \beta_\lambda\, i_\lambda = N\sigma_R\, i_\lambda \qquad 45$$

where σ_R is the Rayleigh scattering cross section.

$$\sigma_R = \frac{\beta_\lambda}{N} = \frac{1}{N}\int \beta_{\varphi\lambda}\, d\Omega \qquad 46$$

hence $$\sigma_R = \frac{32\pi^3(\mu_\lambda - 1)^2}{3N^2\lambda^4} \quad m^2 \qquad 47$$

It can be seen from equation 43 that the scattered light is approximately isotropic. Scattered light makes an important contribution to the total light seen in experiments where optical detectors are not looking at direct Cerenkov light, as discussed in chapter 6.

In previous calculations of Cerenkov light in EAS scattering was considered as an absorption process and for the present study it was considered desirable to justify this assumption.

5-6.1 The simulation method for scattering

In the simulation of direct Cerenkov light the hypothetical detector considered was an annular ring centered on the shower core. The detector

used here consisted of 8 detectors with total area equal to the area of the anular ring, positioned uniformly around the ring. Each ray of Cerenkov light, generated as described previously, was divided into 8 equal segments and considered as being scattered from a point midway along the segment. A pencil of light of intensity calculated using the Rayleigh molecular law was then shone onto each hyptothetical detector in turn, as shown in figure 12.

The light received, $\Delta J'$, in the hypothetical detector is given by,

$$\Delta J' = \Delta J \exp\left\{-(\tau_t(h) - \tau_t(h_{obs}))\sec\vartheta\right\} \qquad 48$$

where ΔJ, the light scattered from the Cerenkov beam into $\Delta\Omega$ is attenuated in the atmosphere. Double Rayleigh scattering (i.e. scattering of scattered light) has been considered as absorption. ΔJ is related to the total light scattered from the Cerenkov beam segment J by,

$$\Delta J = J \frac{3}{16\pi}(1 + \cos^2\varphi_R)\,\Delta\Omega \qquad 49$$

where $$\Delta\Omega = \frac{a\cos\vartheta}{(h\sec\vartheta)^2} .$$

Consider a Cerenkov beam segment of length $\Delta h \sec\vartheta_B$. If the intensity of the beam emitted from the particle track at altitude h_o is $i(h_o)$, the intensity at altitude $h + \frac{1}{2}\Delta h$ is,

$$i(h + \tfrac{1}{2}\Delta h) = i(h_o)\exp\left\{-(\tau_t(h_o) - \tau_t(h+\tfrac{1}{2}\Delta h))\sec\vartheta_B\right\} \qquad 50$$

If the intensity changes little over Δh then

$$J \simeq i(h+\tfrac{1}{2}\Delta h)\left[1 - \exp\left\{-(\tau_R(h+\tfrac{1}{2}\Delta h) - \tau_R(h-\tfrac{1}{2}\Delta h))\sec\vartheta_B\right\}\right] \qquad 51$$

where $\tau_R(h)$ is the Rayleigh optical thickness at altitude h. So the additional flux and arrival direction are found and the arrival time is

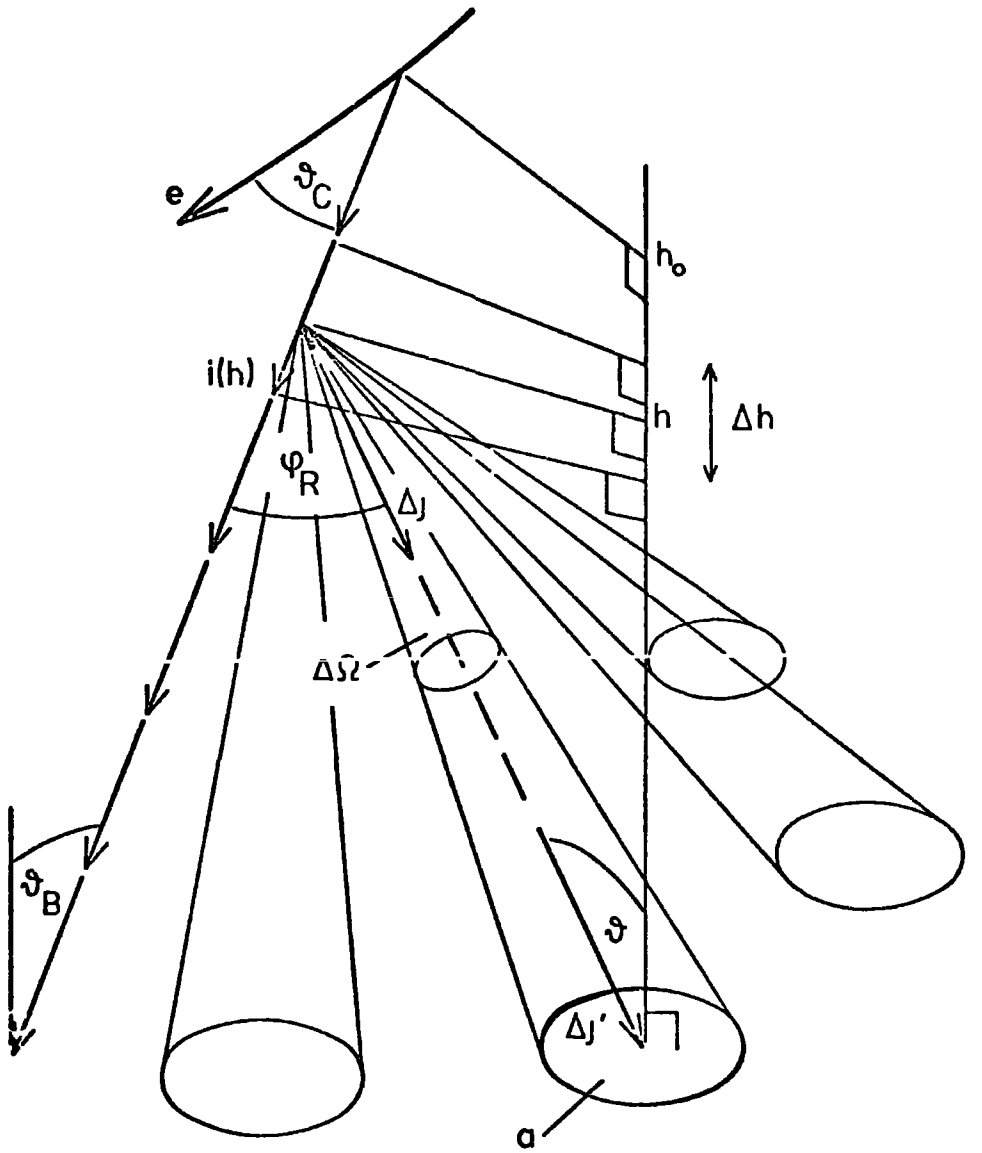

FIGURE 5-12 Pencils of scattered Cerenkov light as seen by the hypothetical detectors.

calculated in the usual way. This procedure was adopted for both aerosol and Rayleigh scattering of all rays generated in the program and in each case the scattering cross section appropriate to the wavelength of the ray was used.

5-6.2 Results of simulations with scattering

The lateral distribution of scattered light has been calculated at sea level for a gamma-ray primary of energy 100 GeV (i.e. an individual shower) and is shown in figure 13 where it is compared to that of direct Cerenkov light in the same shower. Clearly, in the region where most measurements are made (100-500 m from the core) scattered light may be neglected. The angular distribution of direct and scattered Cerenkov light at 900 m from the core are compared in figure 14.

5-7 COMPARISON OF PRESENT WORK WITH OTHER CALCULATIONS

The diverse methods of calculation of Cerenkov light from electron-photon cascades employed by different authors together with the different ranges of primary energy, primary particle and depth of observation (see table 1) make comparison of the present work with other calculations difficult. Also, many authors have used analytic approximations for the lateral and angular distributions of electrons and neglected atmospheric attenuation of light. Despite these difficulties, a comparison of average lateral distributions for photon densities at 2380 m above sea level in showers initiated by 100 GeV gamma-rays has been made by Browning and Turver (1977) with the work of Zatsepin and Chudakov (1962) and Rieke (1969) and is reproduced here in figure 15. The present calculations were made using a computer program based on that used by Browning and Turver and the comparisons made in figure 15 are applicable here.

A similar comparison is made at sea level between the lateral distribution of an individual 100 GeV shower from the present work

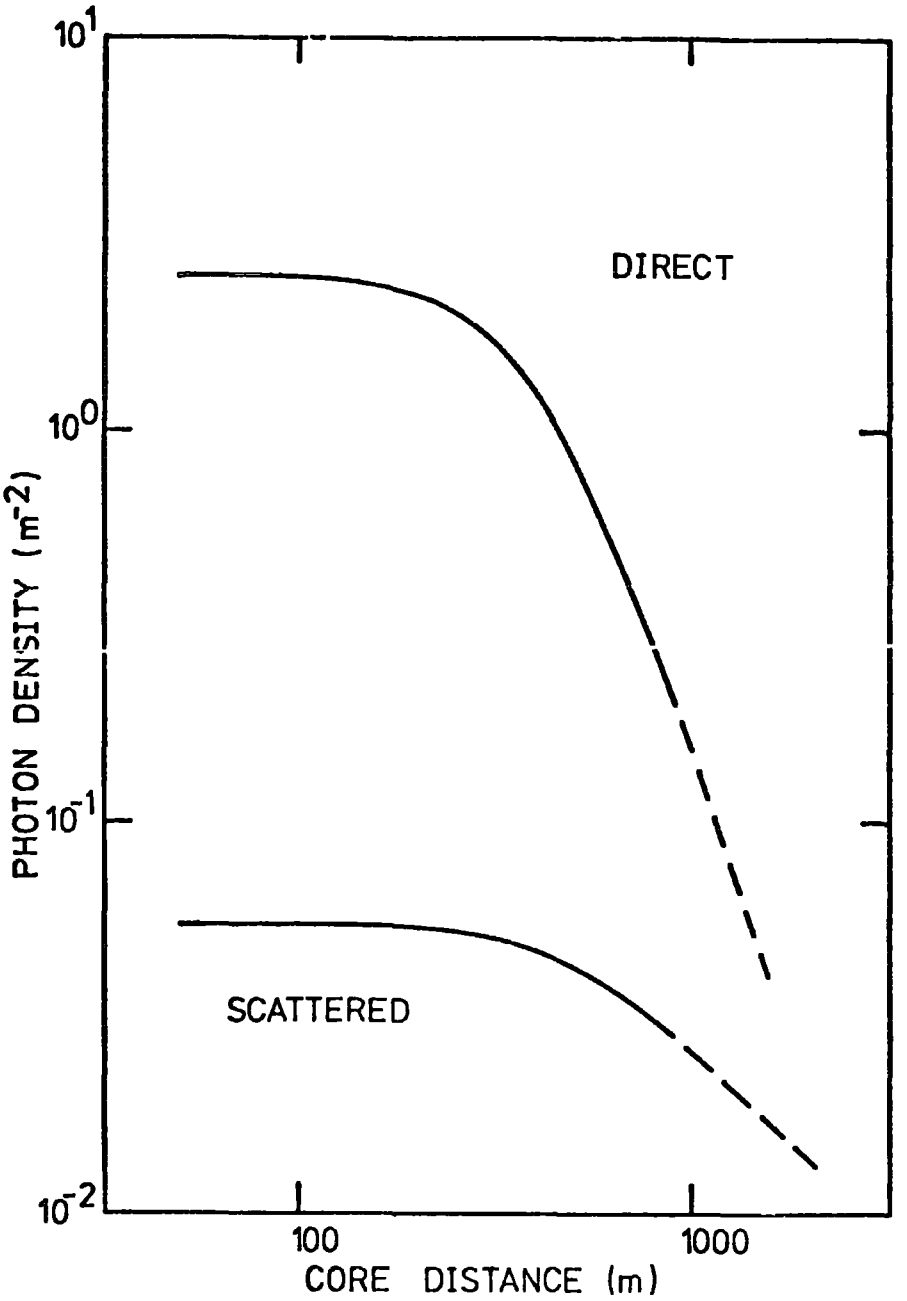

FIGURE 5-13. The lateral distribution of direct and scattered Cerenkov light in the same shower

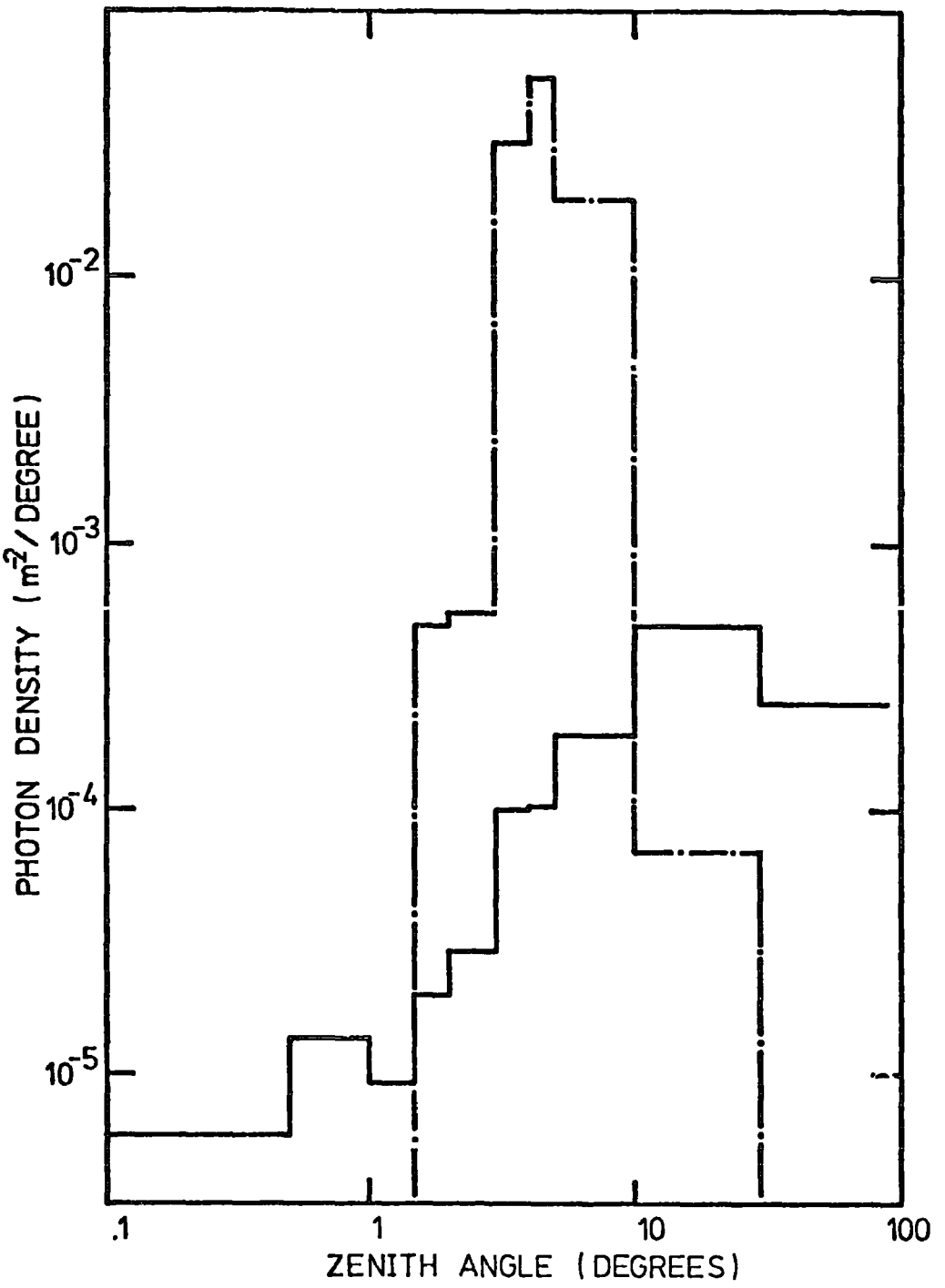

FIGURE 5-14 The angular distribution of direct (dot-dash line) and scattered (solid line) Cerenkov light at 900 m from the core of the same shower.

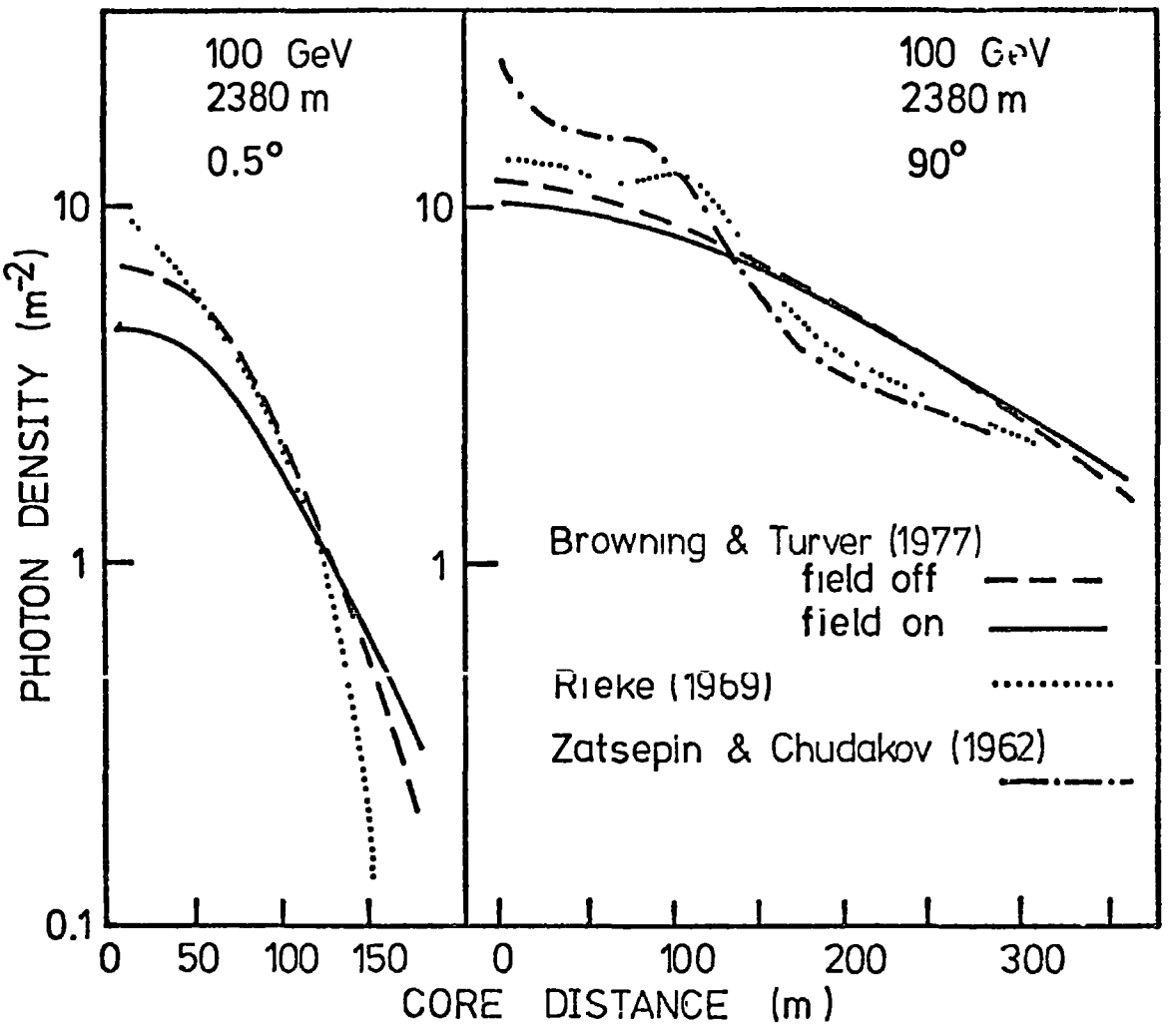

FIGURE 5-15 Comparison of lateral distributions calculated by Browning and Turver (1977), Rieke (1969) and Zatsepin and Chudakov (1962) in gamma-ray showers of primary energy 100 GeV.

maximizing at 280 g cm^{-2} (developing slightly below average) and the lateral distribution given by Zatsepin and Chudakov in figure 16.

5-7.1 Comparison with results of Ivanenko et al (1976)

Many recent calculations of Cerenkov light in large cosmic ray showers at sea level have been based on the results of analytical calculations made by Ivanenko et al (1976) for gamma-ray showers with primary energies in the range 10^{12} - 10^{17} eV. The results of these calculations (which use approximations A and B for the electron-photon cascades) were adjusted for various models of nuclear interactions and applied to showers with primary nuclei (by selecting gamma-ray showers with similar depths of electron cascade maxima). These results have also been adjusted for atmospheric conditions (see Kalmykov et al (1976) who have corrected for the mean winter temperature of the Yakutsk array of -30°C). Because of the uncertain nature of these adjustments the present work has been compared with that of Ivanenko et al (1976) for gamma-ray primaries of energy 10^{16} eV. The data of Ivanenko et al considered here is that referring to the cascade maximising at 18.6 radiation lengths, which is average under approximation B.

In the present work, the average electron-photon cascade was considered under approximation A for energies greater than 75 GeV and its development at lower energies was obtained using the results of detailed Monte Carlo calculations as described in chapter 3. The lateral distributions of photon density are compared in figure 17, the rise time (t_R) and full width at half maximum (FWHM), both divided by the square of core distance, are compared in figures 18 and 19 respectively. Considering the entirely different approach to the problem the results are in reasonable agreement. The discrepancies

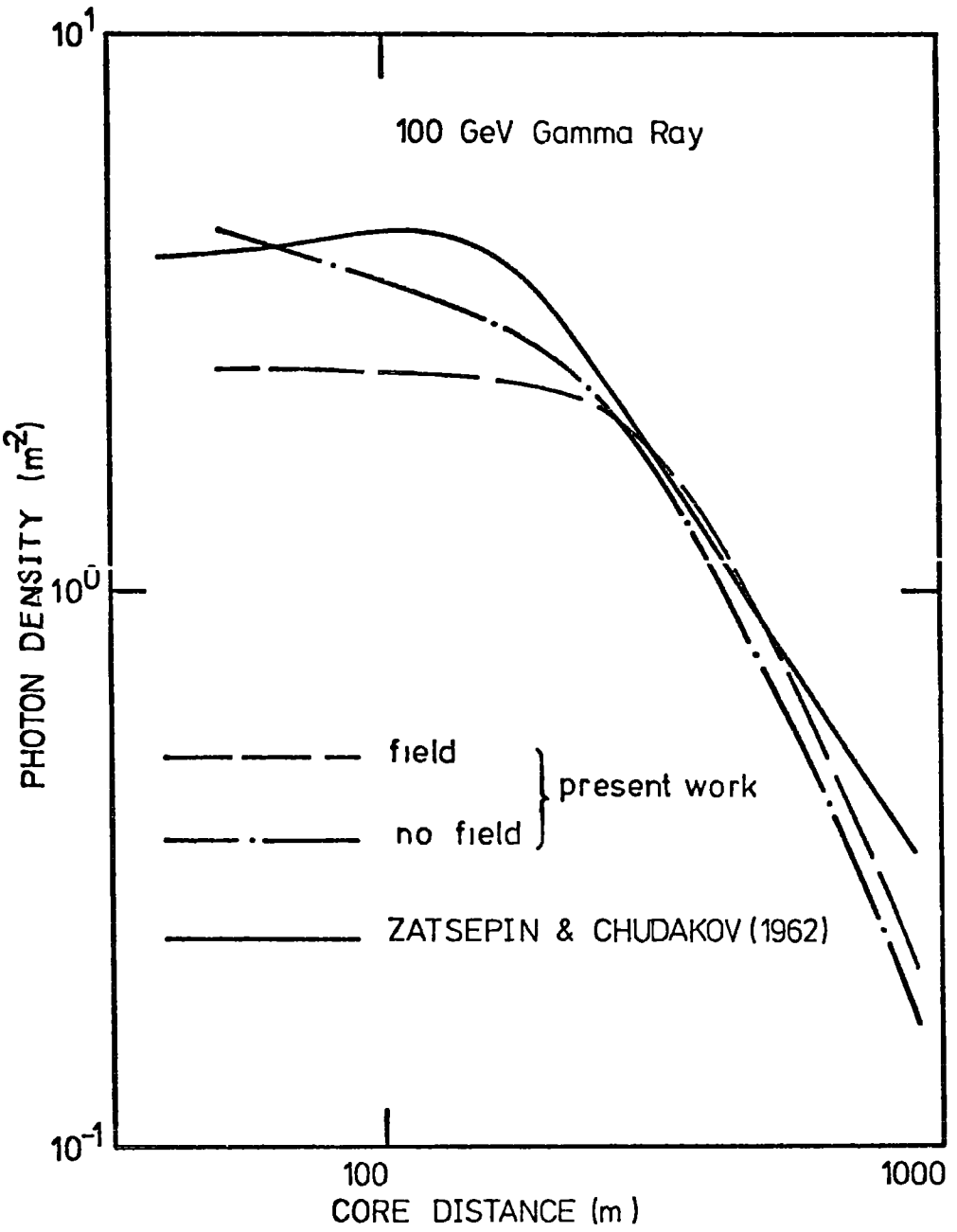

FIGURE 5-16 Comparison of the lateral distributions from the present work with that calculated by Zatsepin and Chudakov (1962).

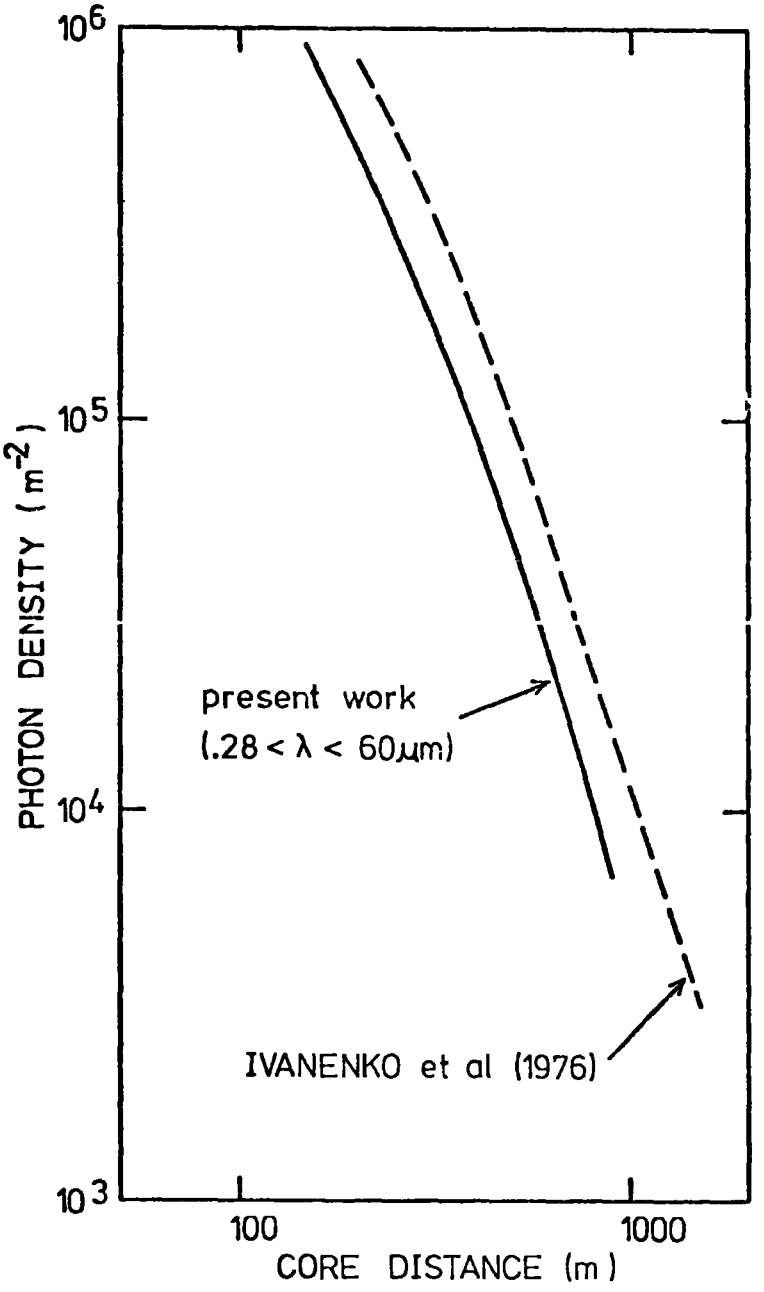

FIGURE 5-17 Comparison of the lateral distribution from the present work with that calculated by Ivanenko et al (1976).

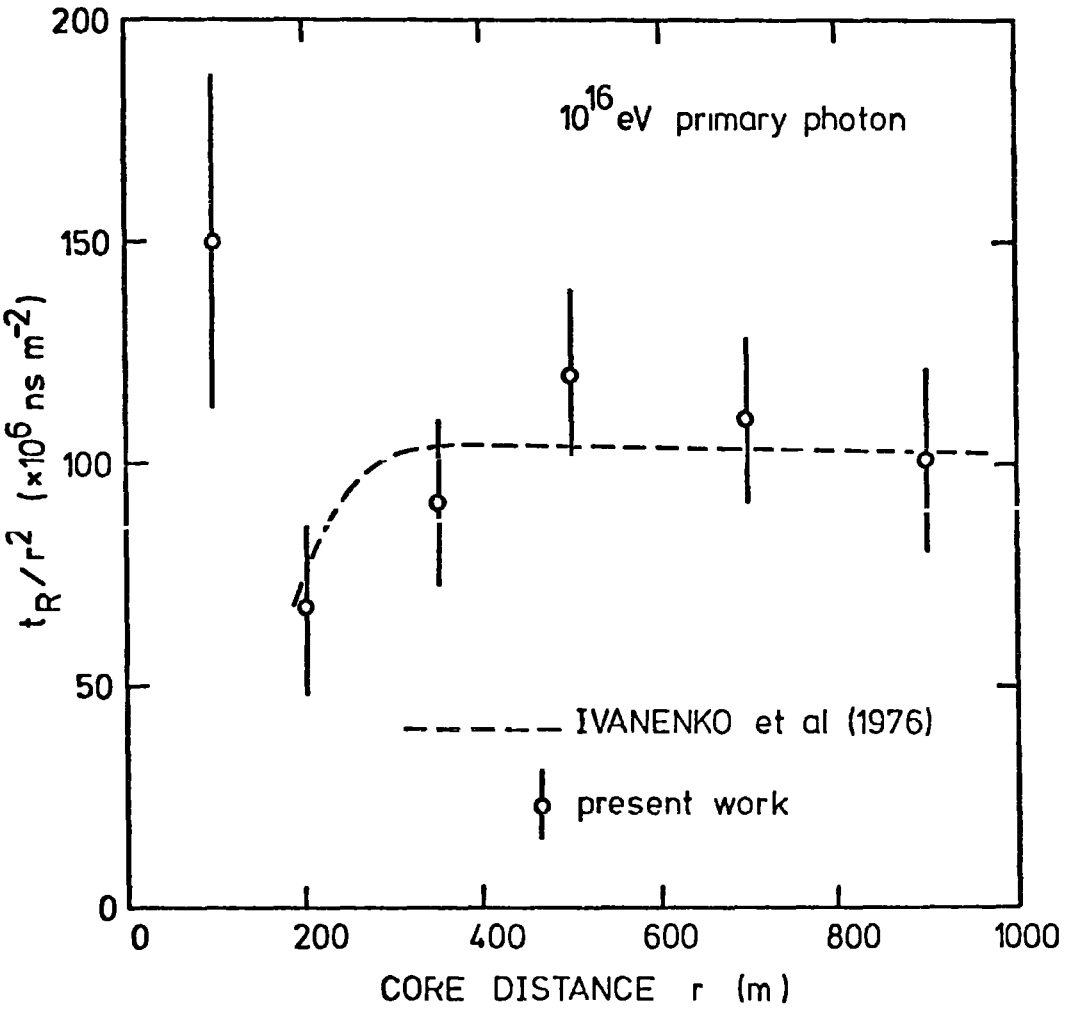

FIGURE 5-18 Comparison of rise times (t_R) from the present work with those of Ivanenko et al (1976)

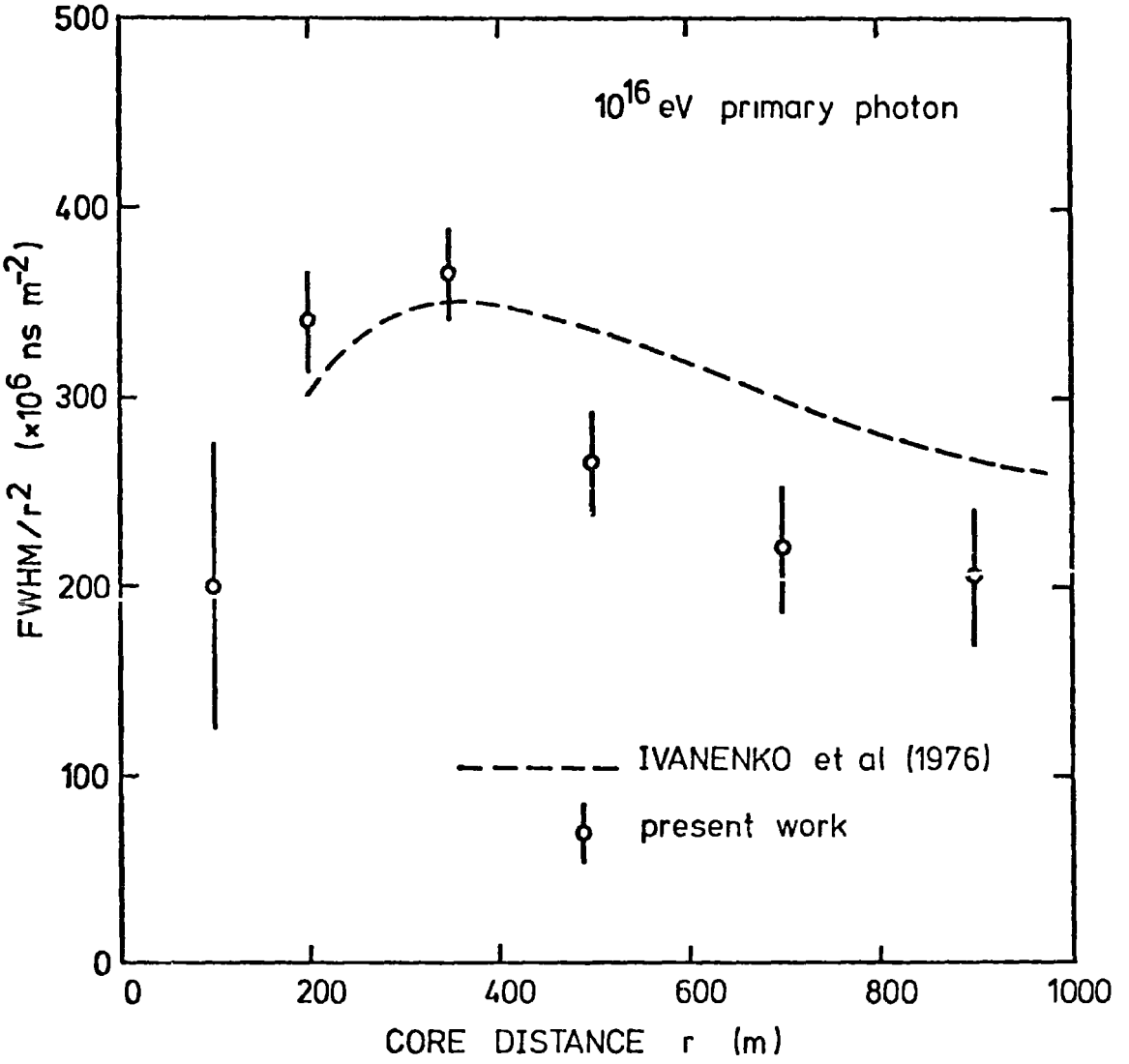

FIGURE 5-19 Comparison of the FWHM from the present work with those of Ivanenko et al (1976).

are thought to originate in the limitations of the model employed by Ivanenko et al (eg neglect of atmospheric attenuation and geomagentic deflection of electrons).

5-8 CERENKOV LIGHT FROM AVERAGE SHOWERS, 10^{16}-10^{18}eV

Simulations of the Cerenkov light component at sea level and at an altitude of 1.8 km have been made for average showers of primary mass 1, 4 and 56 and primary energies 10^{16}, 10^{17} and 10^{18} eV using the scaling model described in chapter 2 for the nuclear interactions. In each case the electron cascades are averaged over 50 showers.

5-8.1 Cascade development and photon lateral distribution

The longitudinal electron cascades (E_e>20 MeV) are shown in figure 20 for the nine average showers. The lateral distributions of the total light density in these average showers are shown in figure 21 at two observation altitudes. The broader light pools of the heavier primary initiated showers are clearly seen at both altitudes and the distance at which the photon density is independent of primary mass varies with primary energy and observation altitude. For core distances, r, in the range 100 - 500 m the lateral distribution is well represented by a power law of the form,

$$\phi(r) = C\, r^{-\gamma} \qquad 52$$

The power law exponent, γ, represents the "steepness" of the structure function and is shown to be a strong measure of shower development in figure 22 where it is plotted against the depths of electron cascade maximum for the average showers irrespective of primary energy and mass.

5-8.2 Angular and wavelength distribution of light

The angular distribution of light at sea level is given in figure 23 for the average 10^{17}eV proton initiated shower and shows

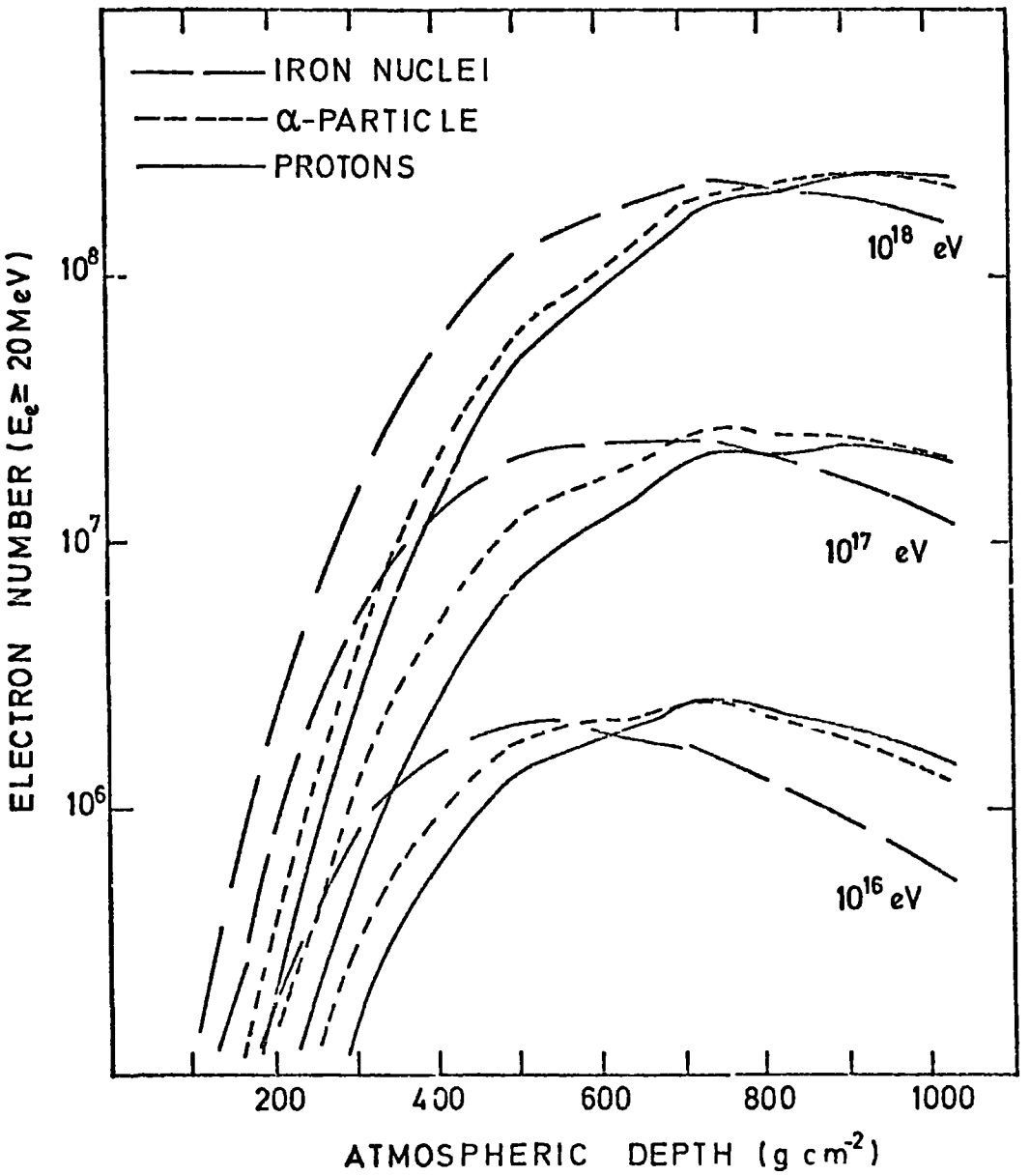

FIGURE 5-20 The electron cascade development for average showers.

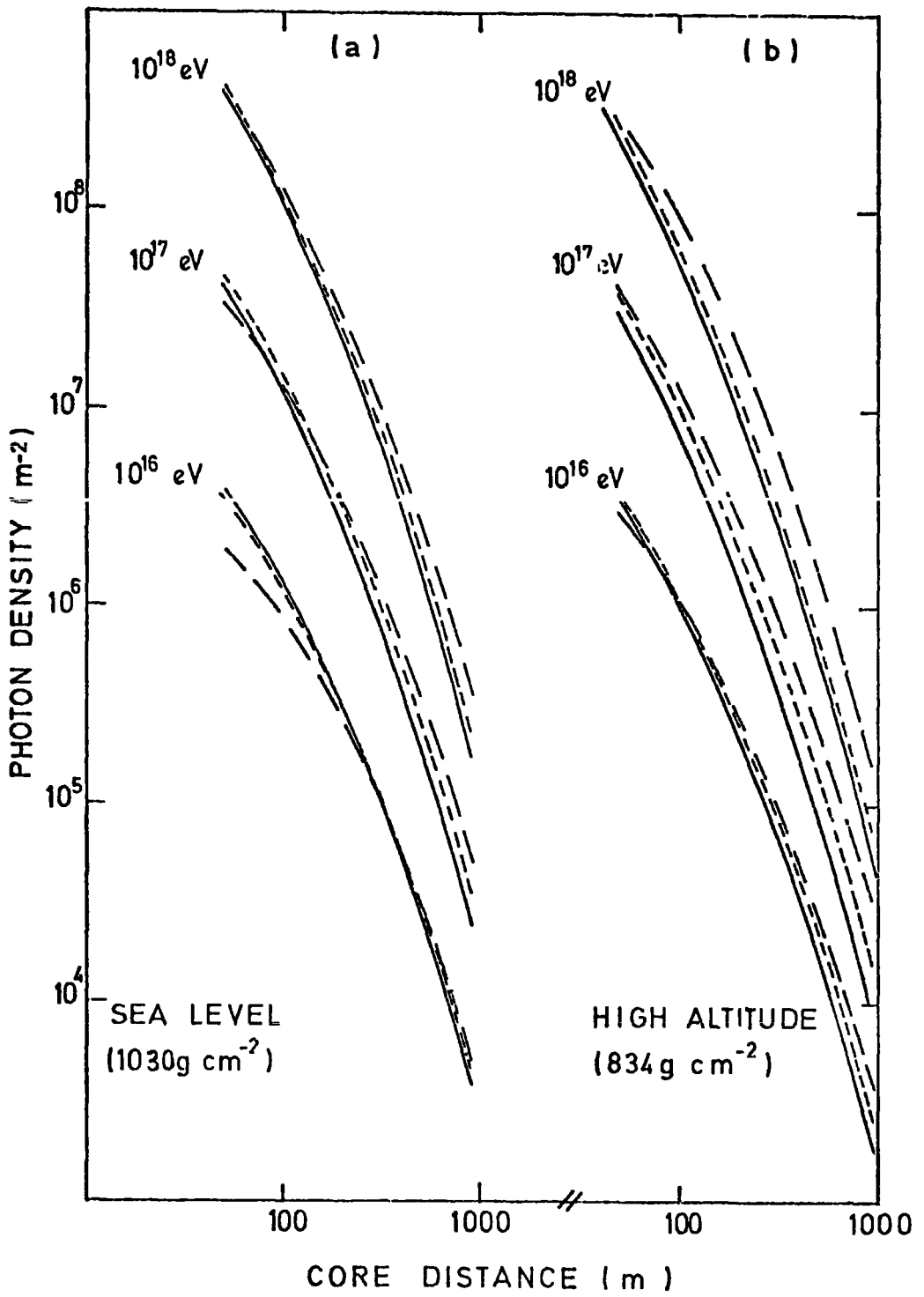

FIGURE 5-21 The lateral distribution of photon density for average showers at two atmospheric depths.

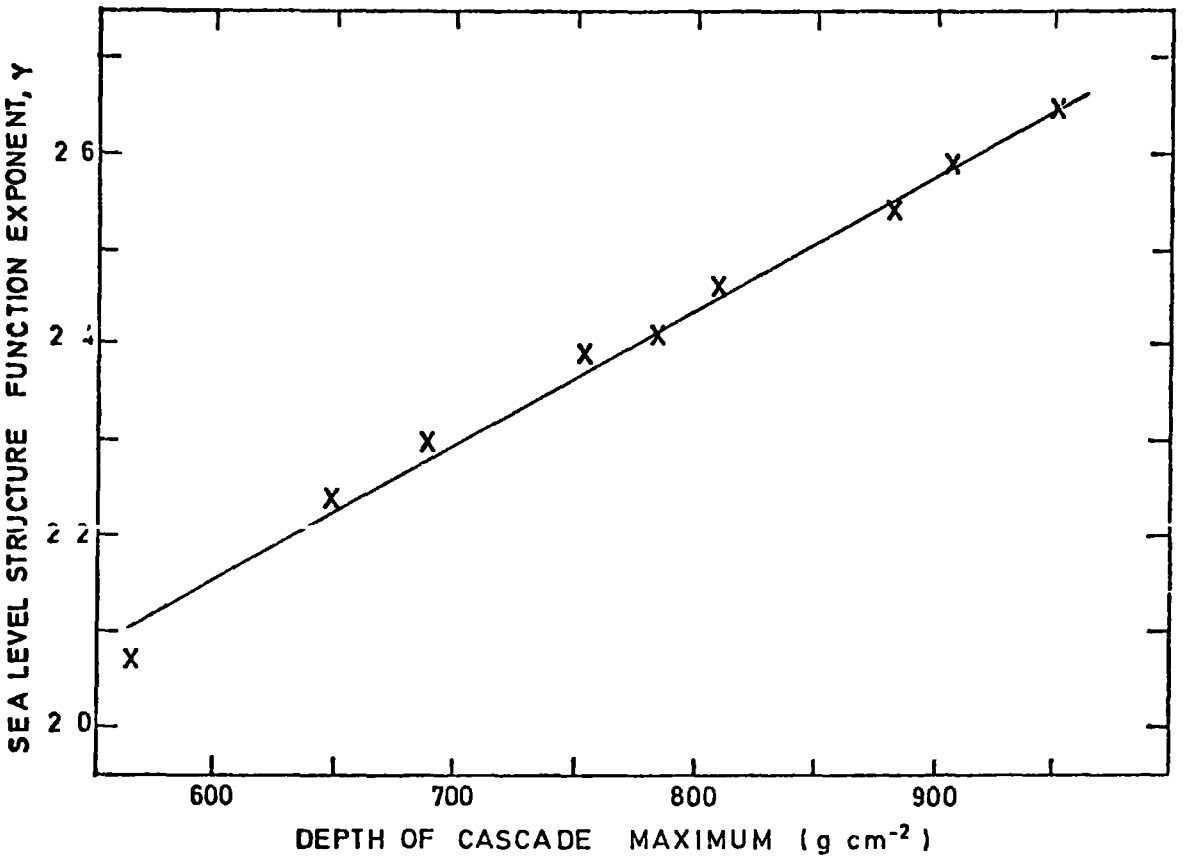

FIGURE 5-22 Lateral distribution structure function exponent plotted against depth of electron cascade maximum irrespective of primary mass or energy.

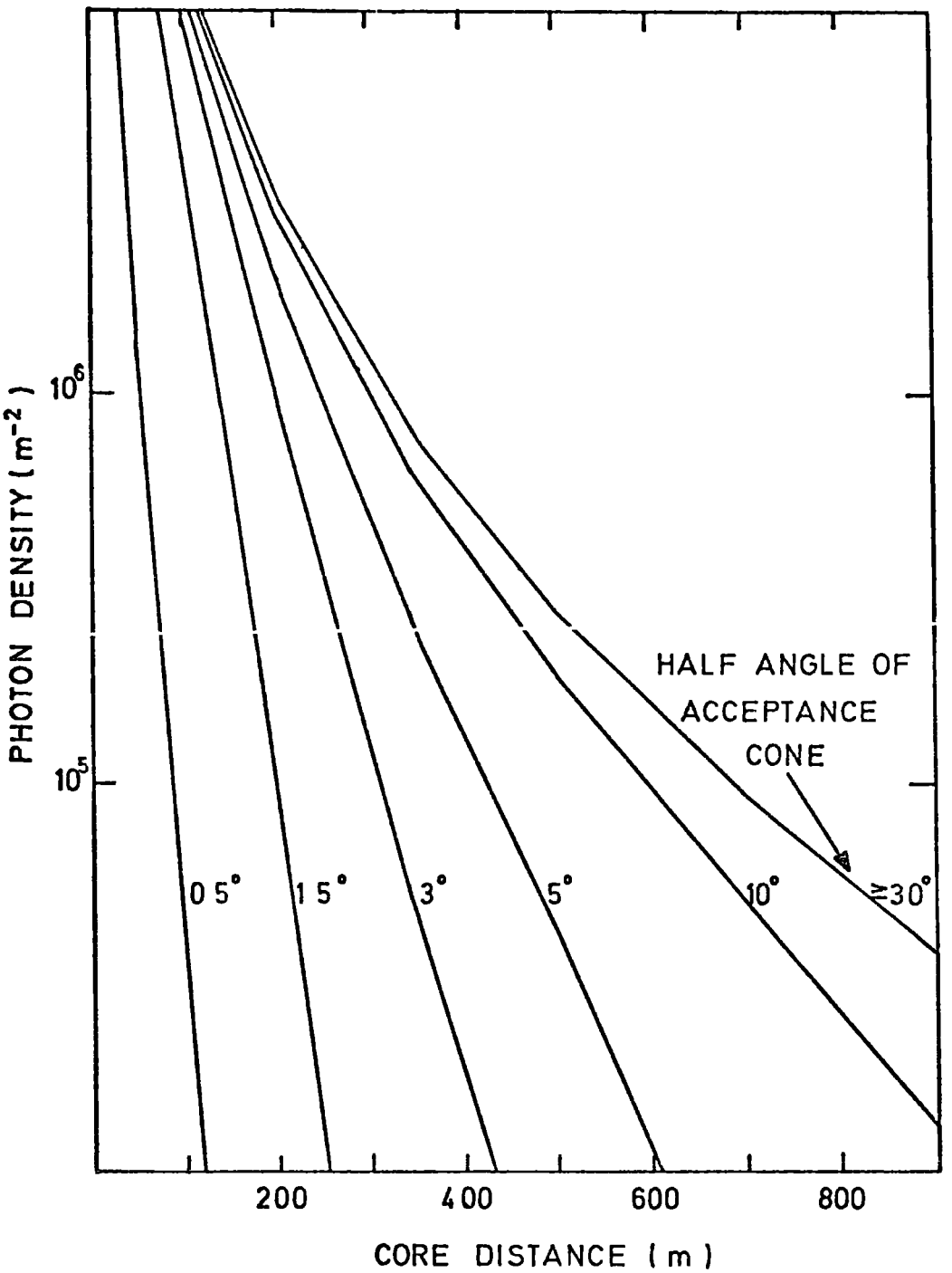

FIGURE 5-23 Angular distribution of light in the average 10^{17} eV proton initiated shower.

the lateral distribution of photon densities as "seen" by detectors with a range of acceptance angle.

The wavelength distribution of light in the same shower is shown in figure 24 at various core distances and the distorting effect of atmospheric attenuation on the shape of the spectrum is clearly seen, particularly at large core distances.

5-8.3 Cerenkov light pulse time structure

Light pulse time measurements now play an important role in the analysis of Cerenkov light data and, as independent measures within the shower, complement photon density measurements. One may expect to obtain two independent quantities from measurements of light pulse profiles, eg. rise time and fall time (these times are shown for a typical pulse in figure 25a). Showers may thus be analysed using up to three independent sets of data (densities and timing information) to find, for example, three estimates of the position of the shower core with subsequent improvement in core location (see Hammond et al 1977 a)). In the present simulations it was considered important therefore to attempt to reproduce the temporal response of the detectors employed by Hammond et al at the Haverah Park array. These detectors respond to a narrow pulse of light (~1 ns) with a pulse shape characterised by a rise time of 9 ns and a FWHM of 18 ns as shown in figure 25b. The time pulses in the present simulations have thus been convoluted with this response.

The dependences of the rise time, FWHM, and fall time on core distance for the average showers are shown in figures 26a, b and c respectively which also indicate the effect of making measurements at a different altitude and the effect of a perfect time response detector. The rise times, FWHM, widths of the top of the pulse (90-90%) and fall times at core distances of 200 m, 350 m, 500 m and 700 m have

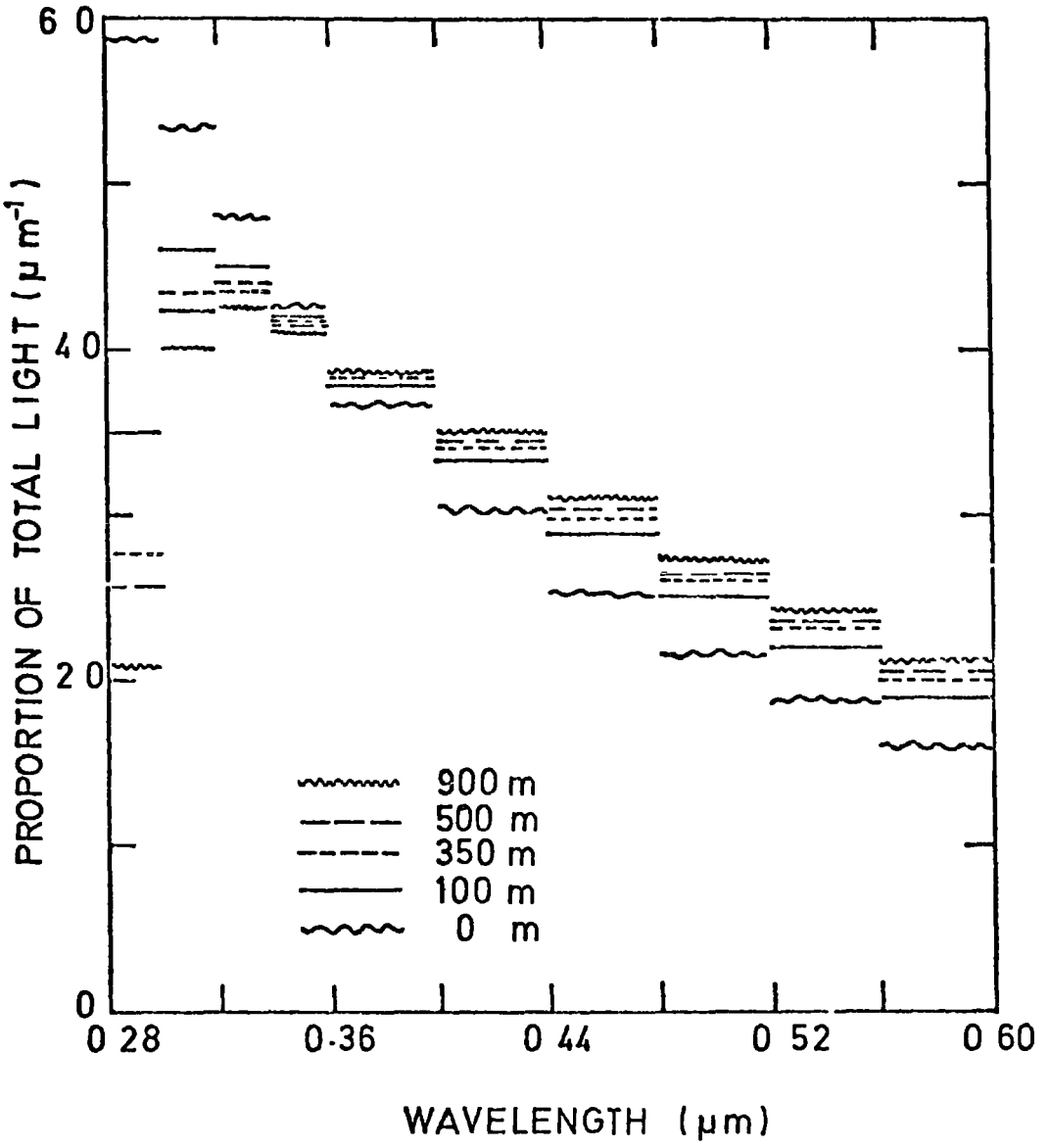

FIGURE 5-24 The wavelength spectrum of light in the average 10^{17} eV proton initiated shower at various distances from the core.

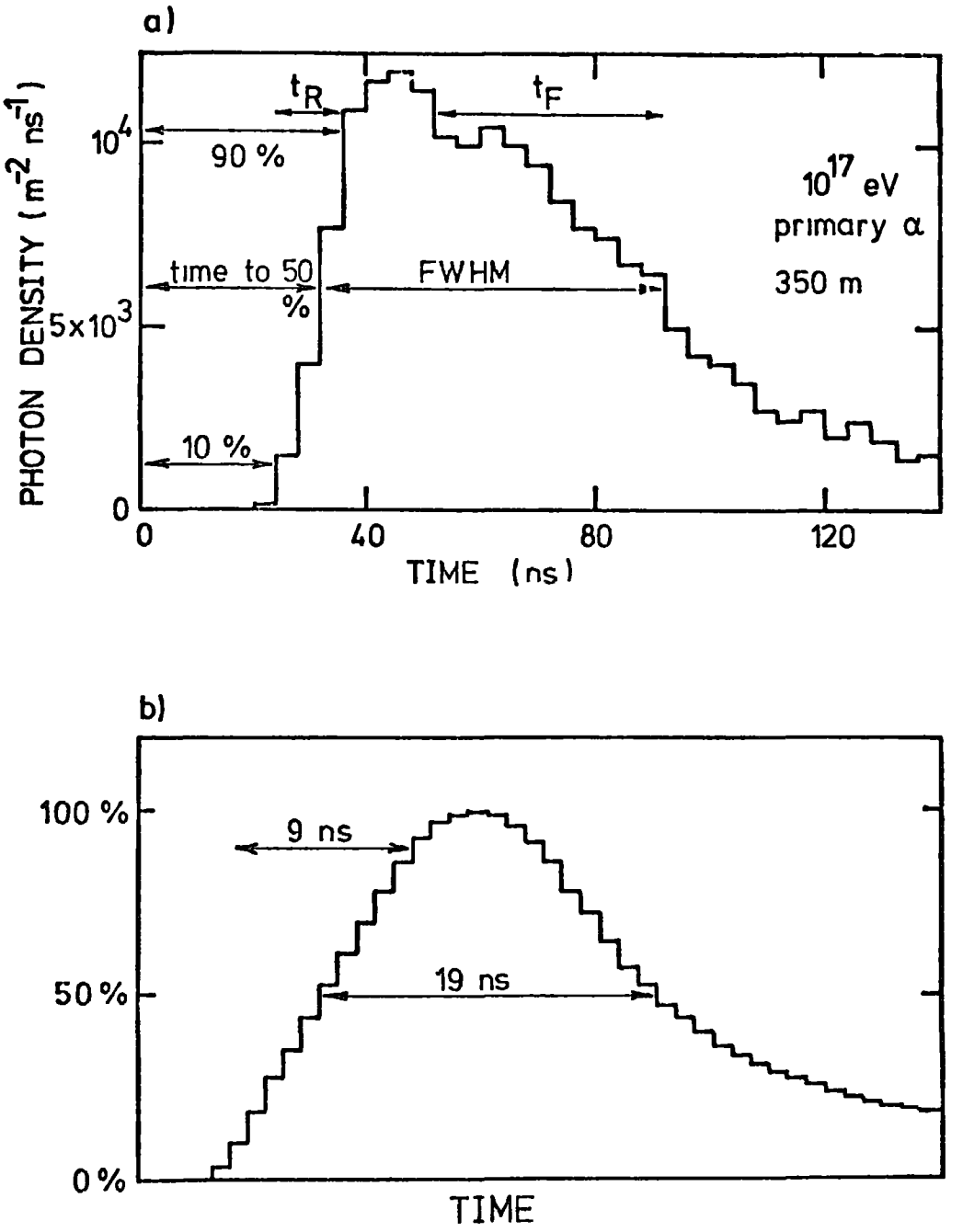

FIGURE 5-25(a) Time structure of a typical light pulse

FICURE 5-25(b) Response of detectors of the type deployed at Haverah Park to a narrow light pulse (~1 ns).

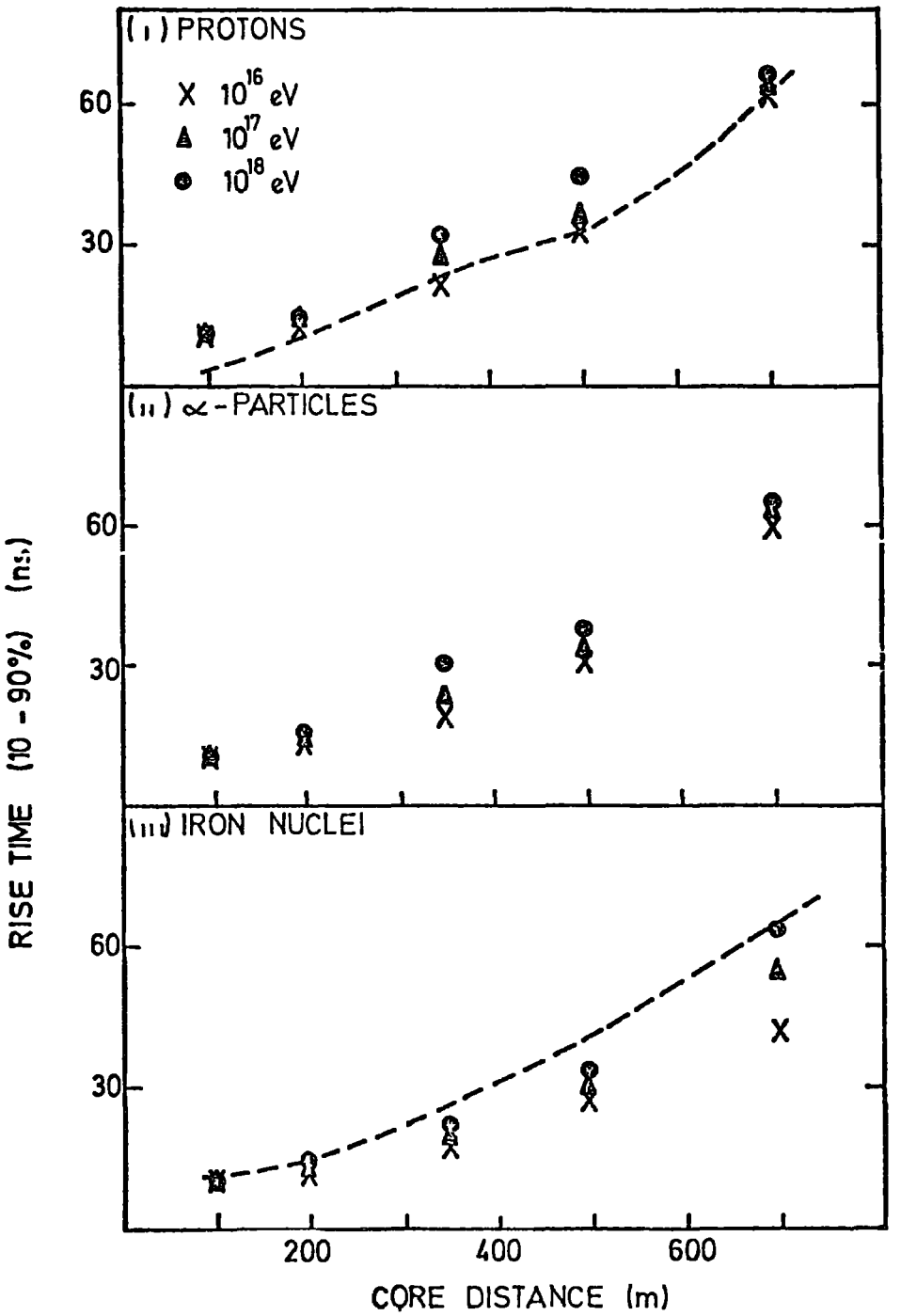

FIGURE 26a The variation with core distance of the rise time for average showers at sea level The broken lines in (i) and (iii) indicate the effect of perfect time response and an observation depth of 835 g cm^{-2} respectively, both at 10^{17} eV.

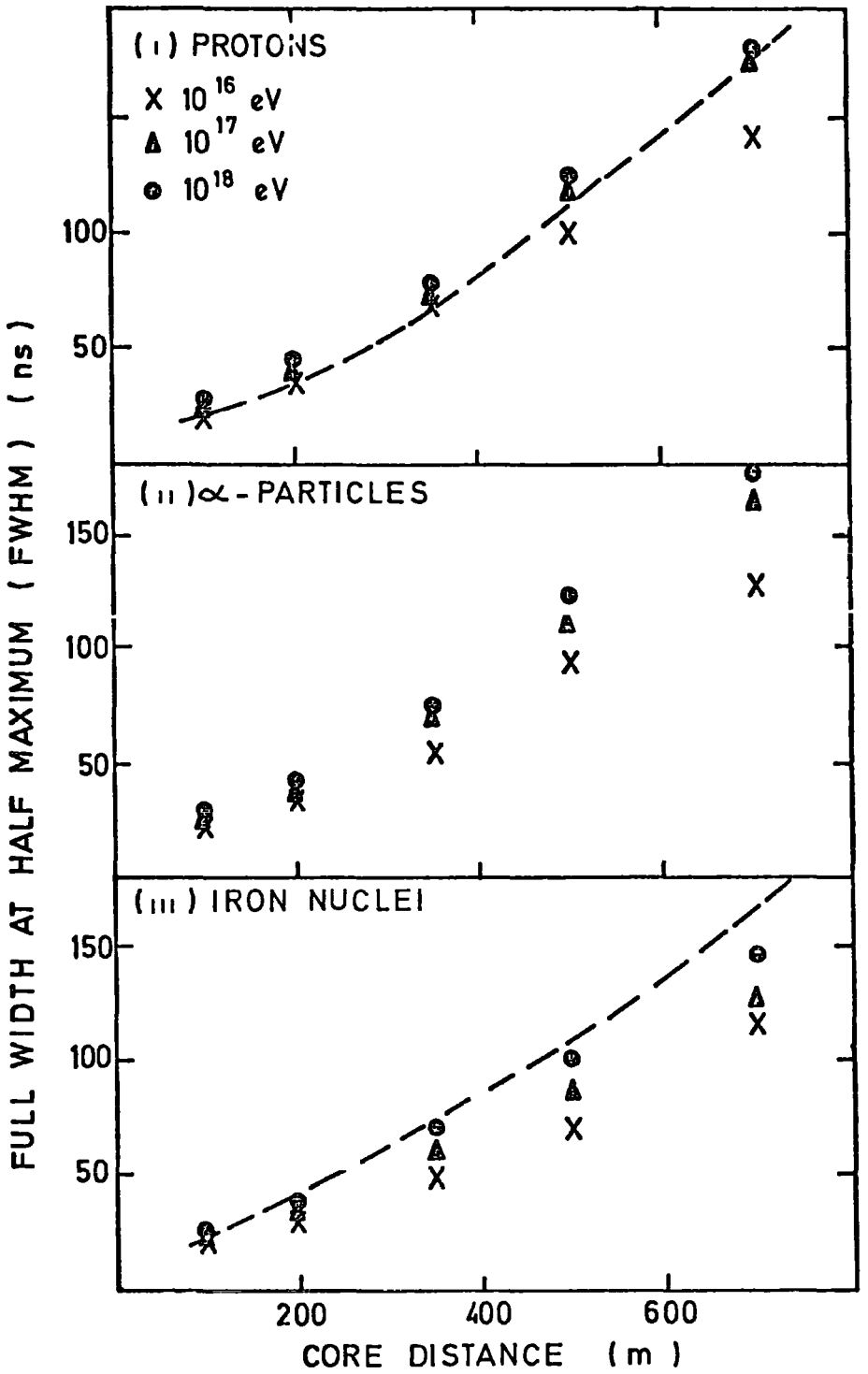

FIGURE 5-26b The variation with core distance of the FWHM for average showers at sea level. Broken lines are as in figure 26a.

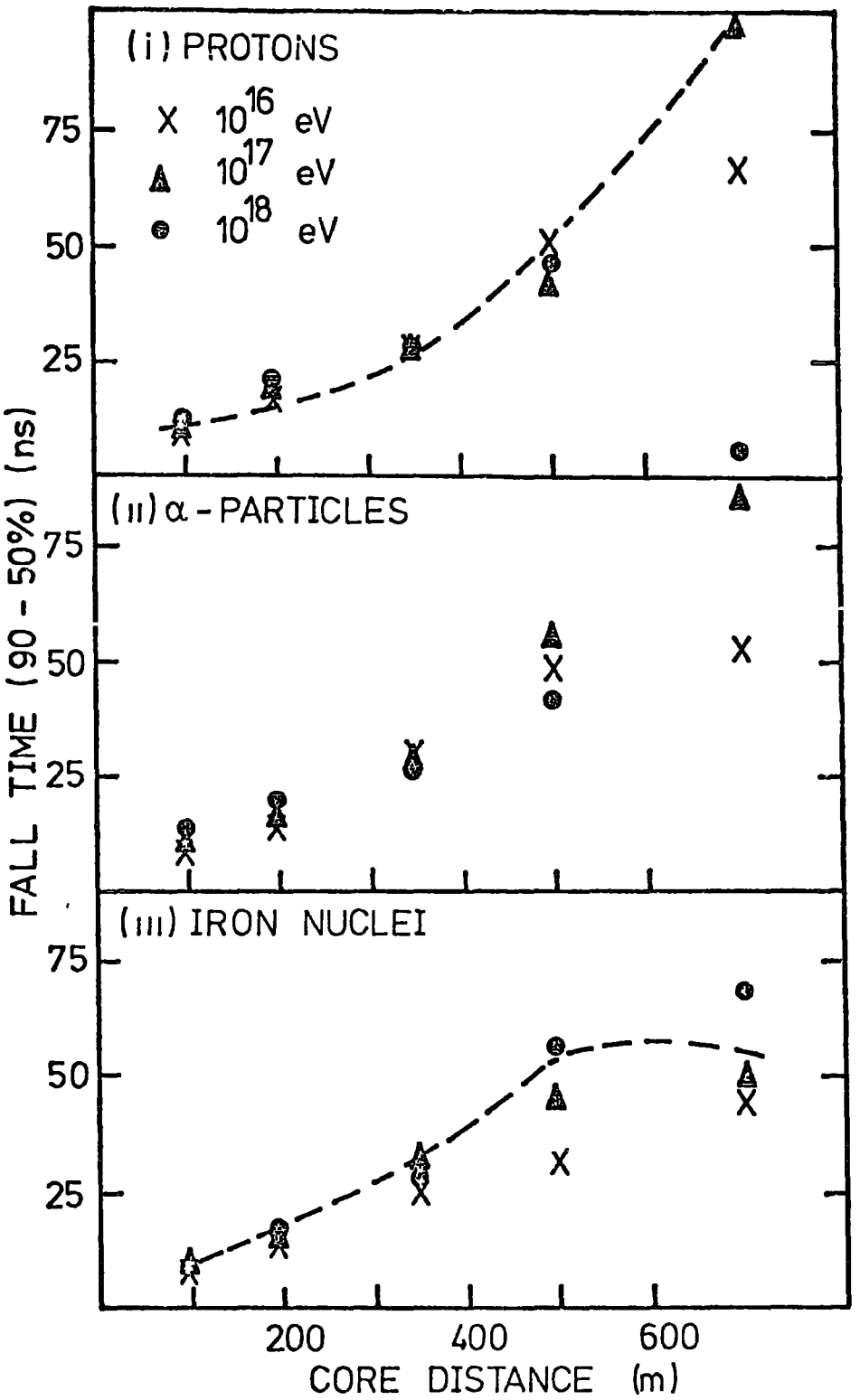

FIGURE 5-26c The variation with core distance of the fall time for average showers at sea level. Broken lines are as in figure 26a.

been plotted against the depths of electron cascade maxima irrespective of the primary energy or mass in figures 27a - d where it is seen that the differences in pulse time measurements between showers of different primary energy and mass arise mainly from differences in cascade development.

5-9 IMAGING THE CASCADE IN CERENKOV LIGHT

It has been suggested by Fomin and Khristiansen (1971) and Efimov et al (1973) that the FWHM of the Cerenkov light pulses may depend on the longitudinal development of the shower. Later, Protheroe et al (1975) indicated that other measures of pulse time structure may be more sensitive to cascade development and that the radius of curvature of the light front correlated strongly with the depth of maximum of the electron-photon cascade. They also showed that the radius of curvature corresponding to different percentage levels of the pulse (eg. 10%, 50% and 95% levels on the rising edge and 95% and 10% on the falling edge) ranked monotonically with percentage level and also correlated strongly with depth of shower maximum.

These developments have stimulated an interest in identifying which sections of the electron cascade were responsible for light arriving at a given time in the pulse.

5-9.1 Simulations to identify the origin of the light

Computer simulations have clarified the relation between the pulse time structure and the electron cascade. The average 10^{17} eV proton initiated shower has been segmented by considering separately the electron cascades and the Cerenkov light resulting from π^o's produced in 8 equal sections of atmospheric depth. The 8 subshowers are shown in figure 28 together with the total electron cascade. The

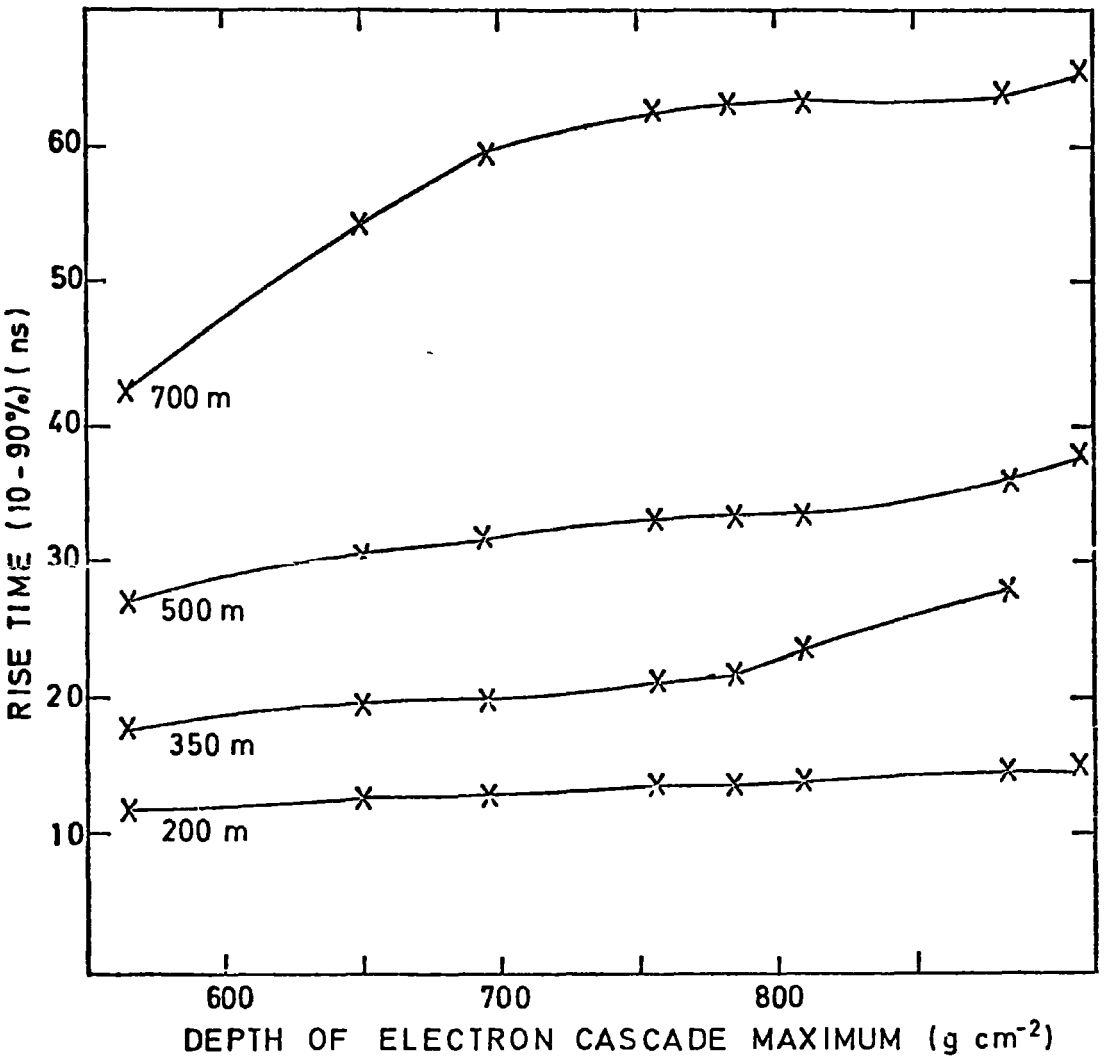

FIGURE 5-27a The variation of rise time at specified core distances with depth of election cascade maximum.

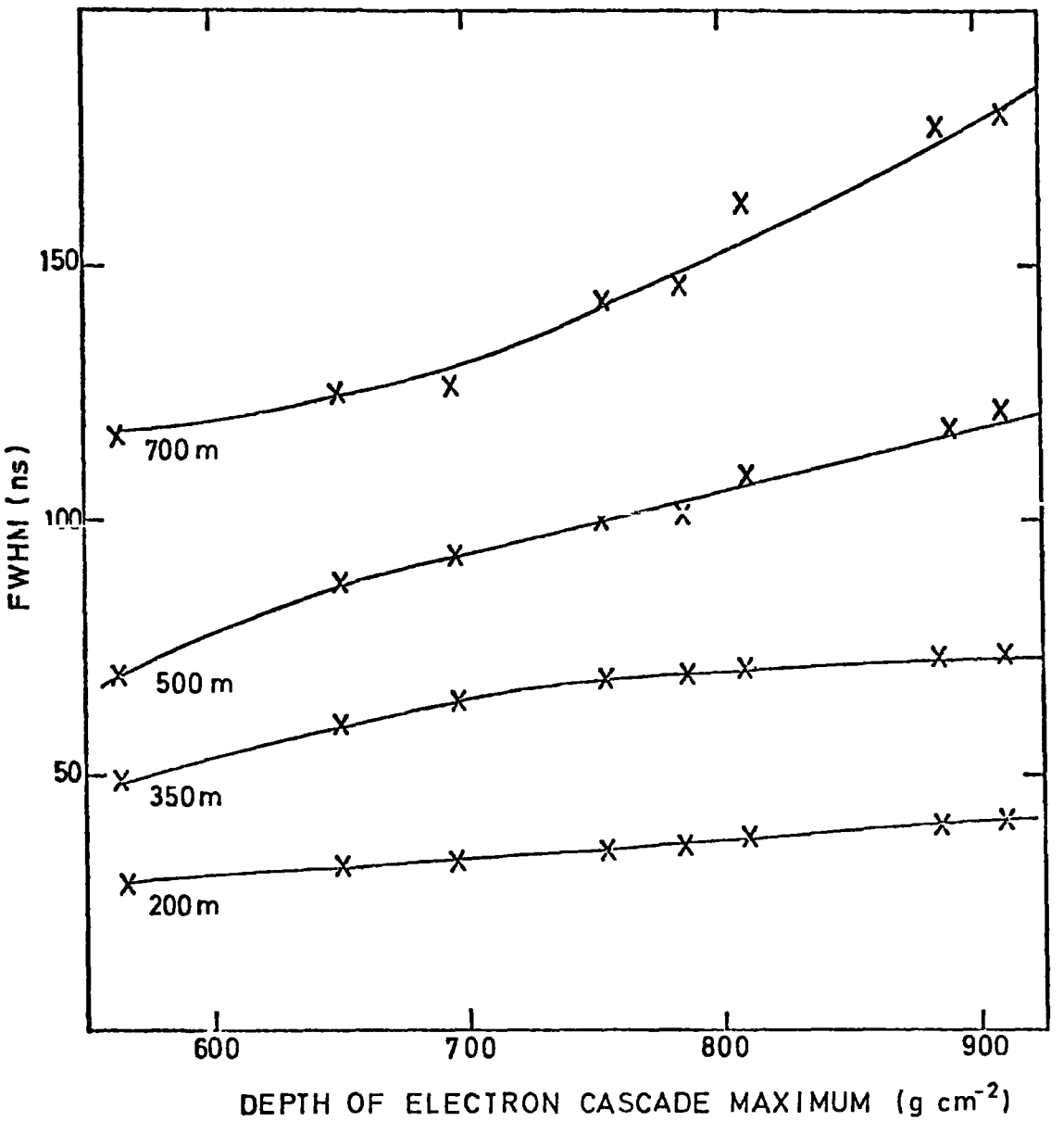

FIGURE 5-27b The variation of FWHM at specified core distances with depth of electron cascade maximum.

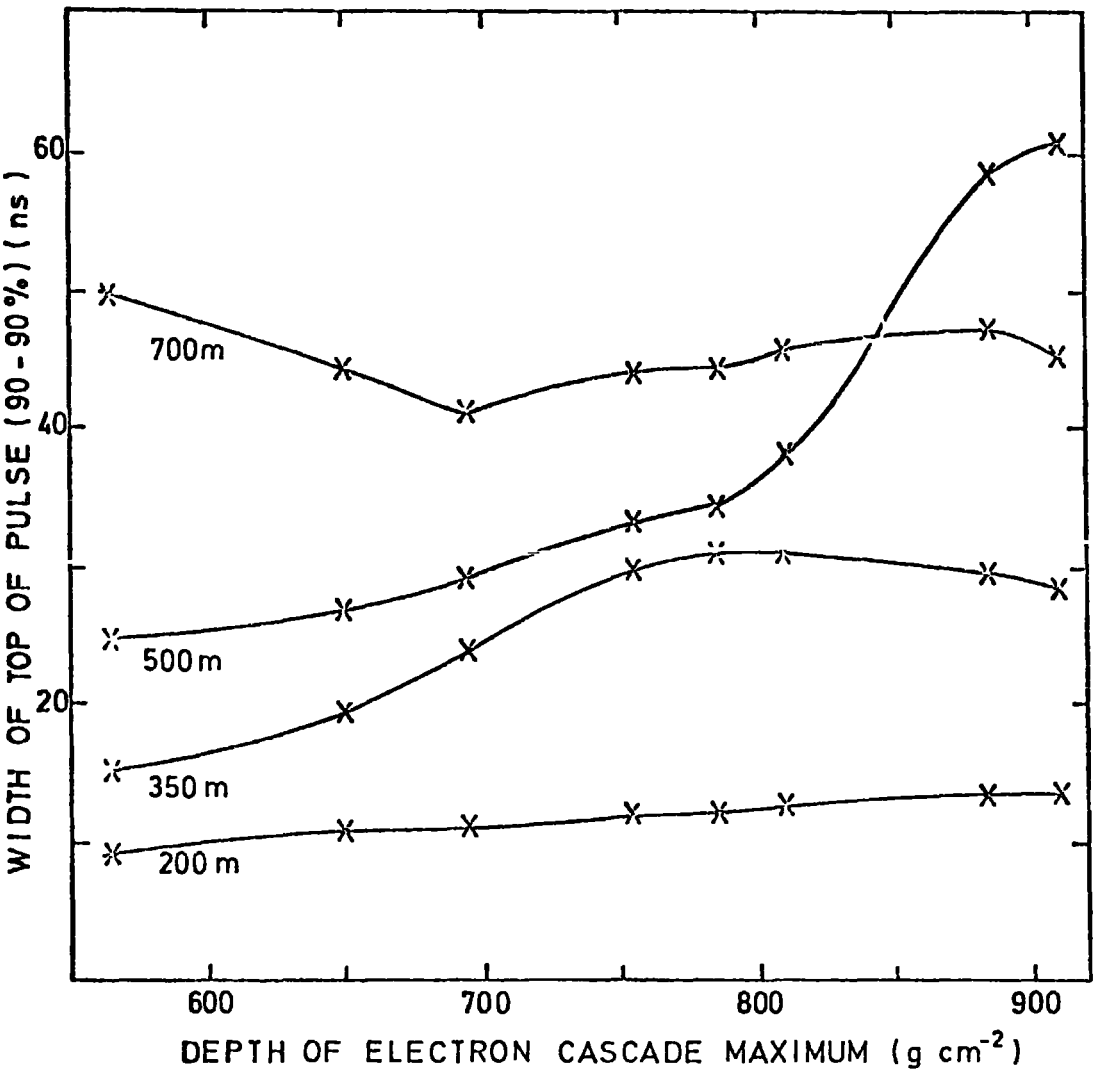

FIGURE 5-27c The variation of the width of the top of the pulse at specified core distances with depth of electron cascade maximum.

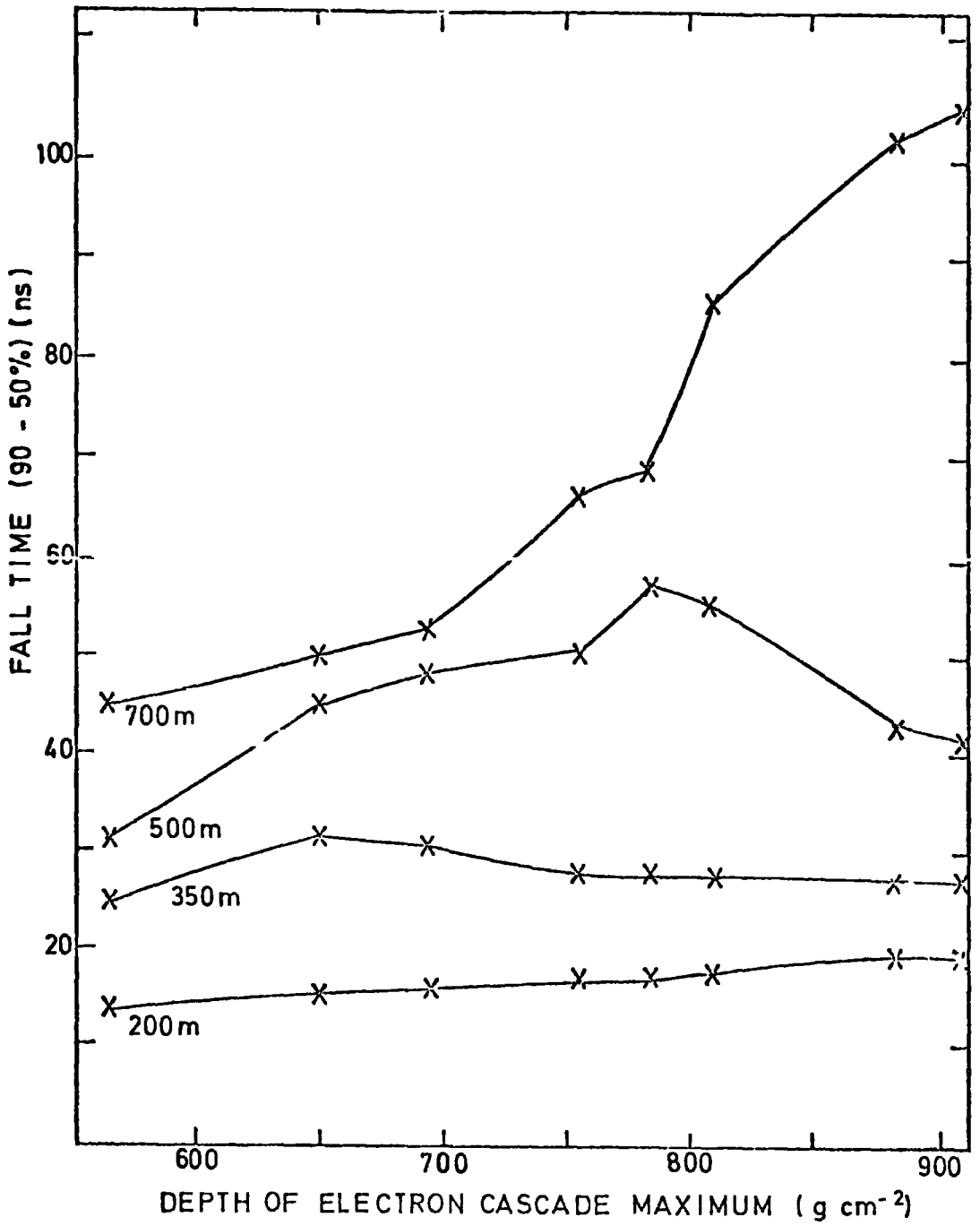

FIGURE 5-27d The variation of the fall time at specified core distances with depth of electron cascade maximum.

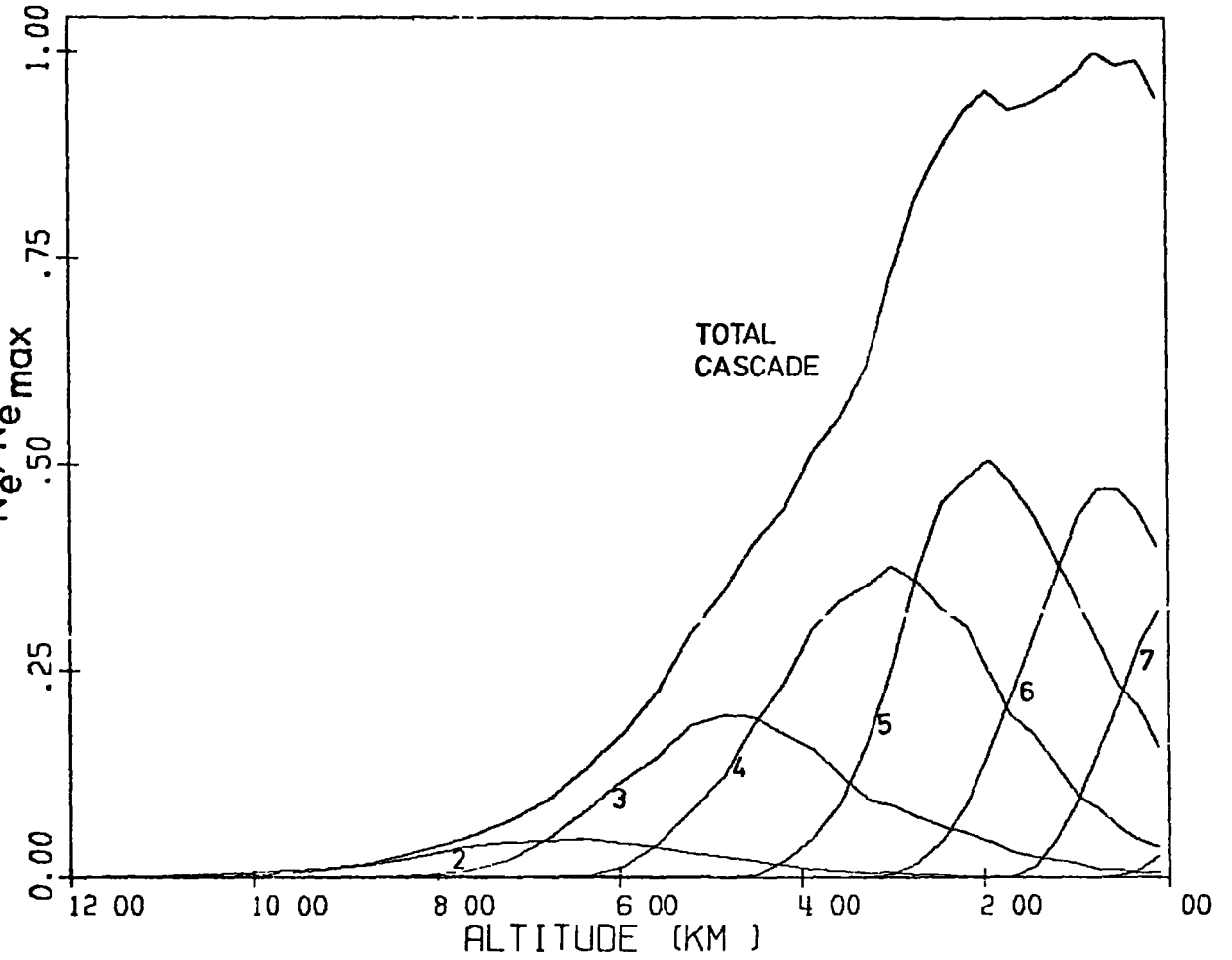

FIGURE 5-28 The electron cascade of the average 10^{17} eV proton initiated shower shown segmented into 8 subshowers.

contributions of each individual subshower to the total photon density (lateral distribution) and pulse time structure are shown in figures 29 and 30 respectively. The contributions of the 8 subshowers of figure 28 to the wavelength distributions of light at the core and at 350 m from the core are shown in figure 31 where distortion in the shape of the spectrum due to atmospheric attenuation is most evident for light originating high in the atmosphere.

It is clear from figure 29 that most of the light close to the core originates low in the atmosphere (as concluded from earlier work reviewed by Jelley (1968)). At large core distances ($\gtrsim$100 m, the region of interest in large air shower work) the majority of light can be seen to originate from higher in the atmosphere. Furthermore it is clear fron figure 30 that at these large core distances ($\gtrsim$ 100 m) there is a direct link between the pulse shape and electron cascade shape. This suggests that the rising edge of the electron cascade may be interpreted from pulse shape measurements. It is also seen that near the core ($\lesssim$50 m) the time sequence of sub pulses is reversed, the first light arriving from low down in the shower.

The connection between height of origin and arrival time is also suggested by simple arguments. A photon emitted at an angle ϑ to the vertical at an altitude h from the core of a vertical shower will arrive at ground level at a time t behind the tangent plane where,

$$t = \frac{\sec \vartheta}{c} \int_0^h \mu \, dh - h/c \qquad 53$$

where μ is the refractive index of air at altitude h. For an atmosphere of scale height H this becomes,

$$t = \frac{\sqrt{h^2 + r^2} - h}{c} + \frac{H(\mu_o - 1)\sqrt{h^2 + r^2}}{h\,c}\left\{1 - e^{-h/H}\right\} \qquad 54$$

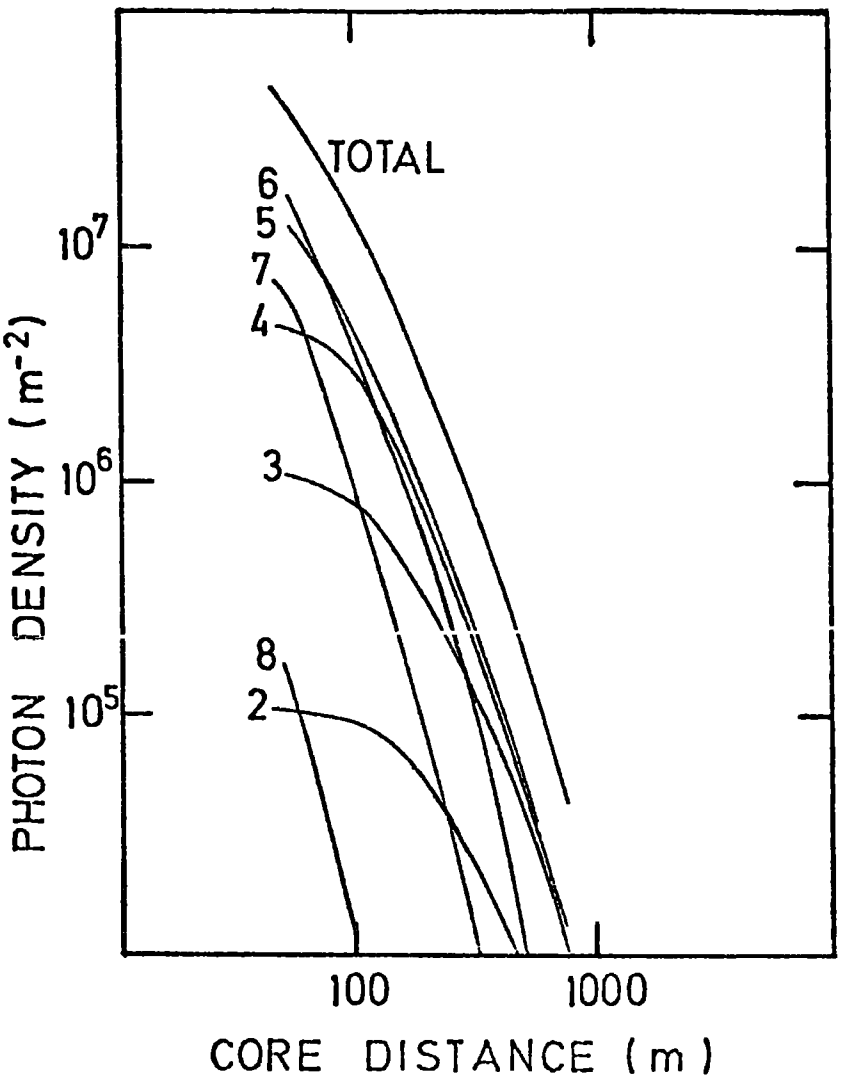

FIGURE 5-29 The lateral distribution of photon density in the average 10^{17}ev proton initiated shower showing the contributions from the 8 subshowers of figure 28.

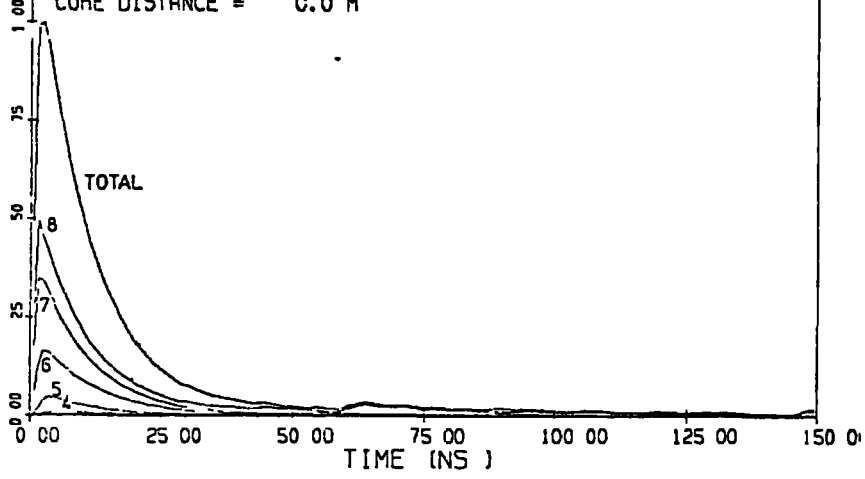

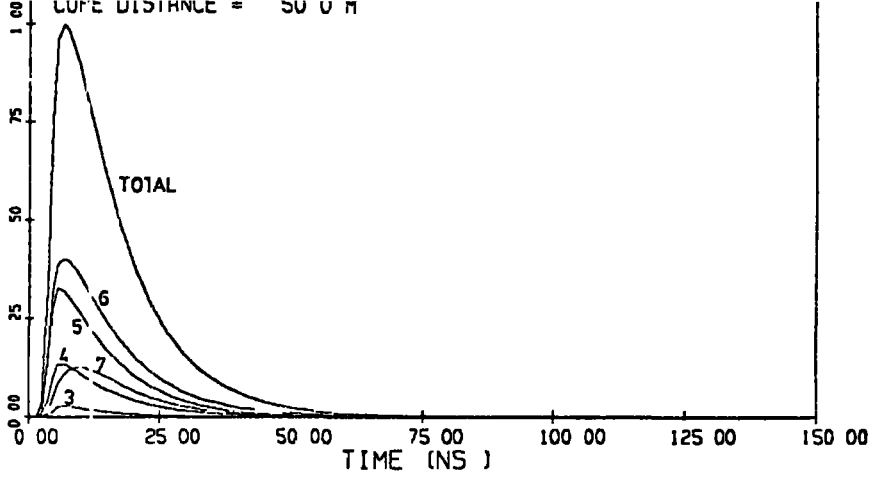

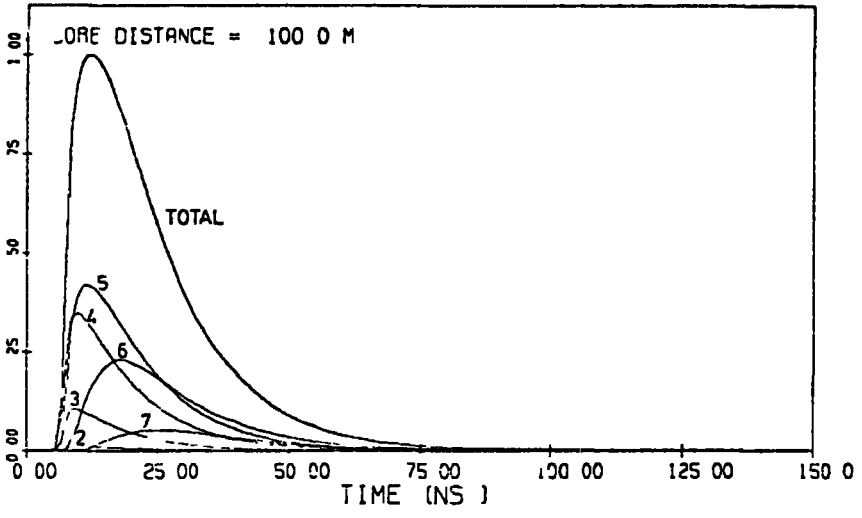

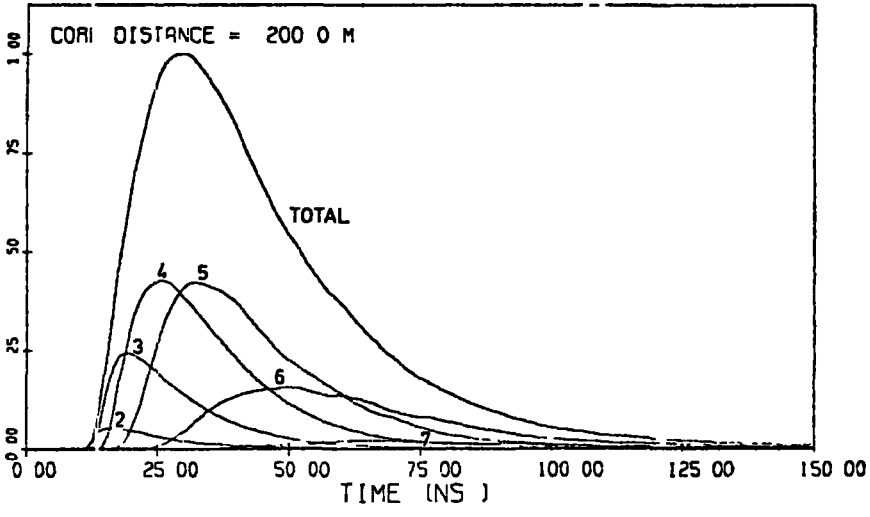

FIGURE 5-30 The contributions to the light pulse resulting from the 8 subshowers shown in figure 5-28 are given at various core distances.

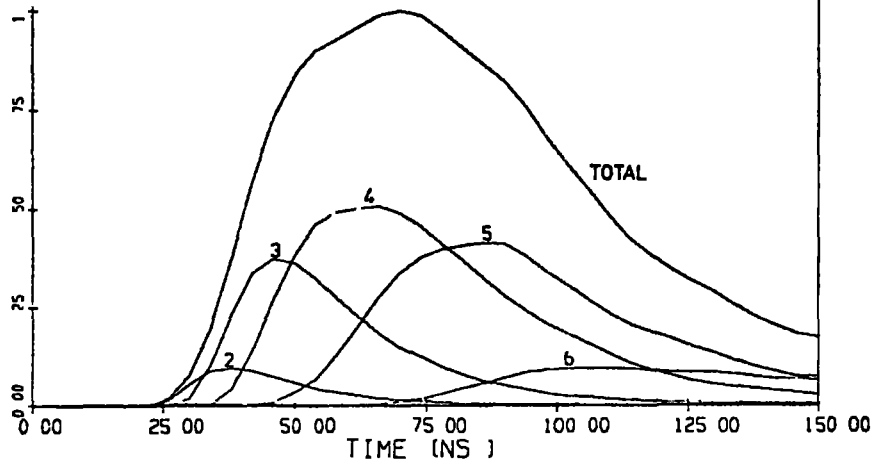

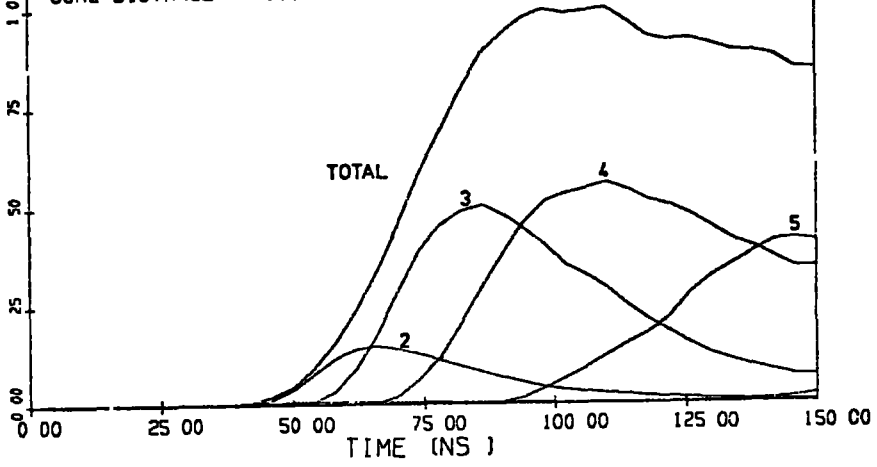

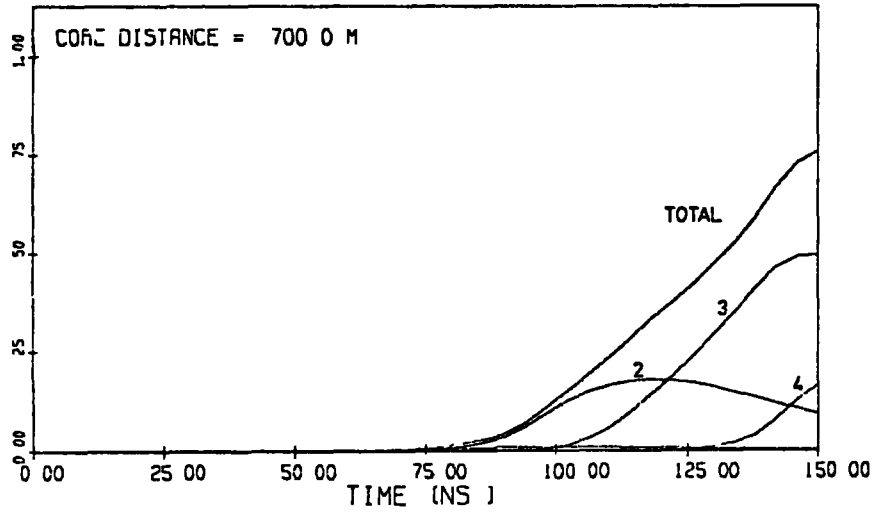

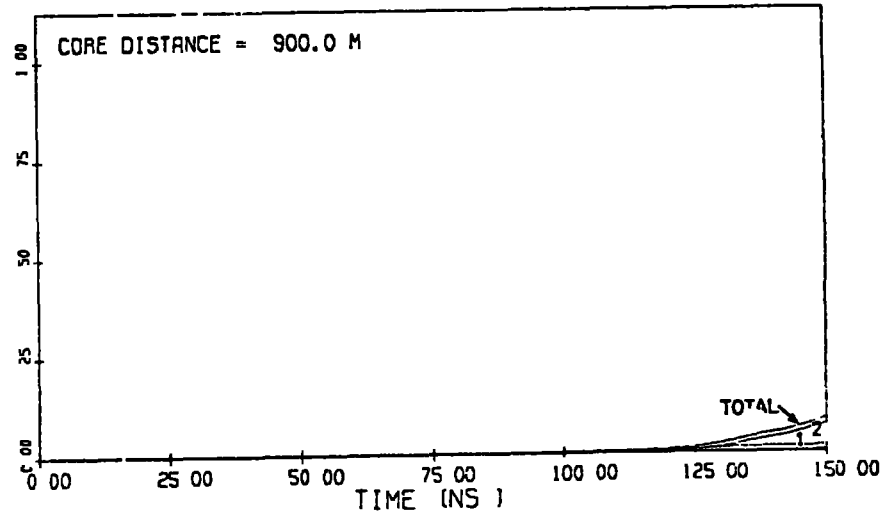

FIGURE 5-30 (continued)

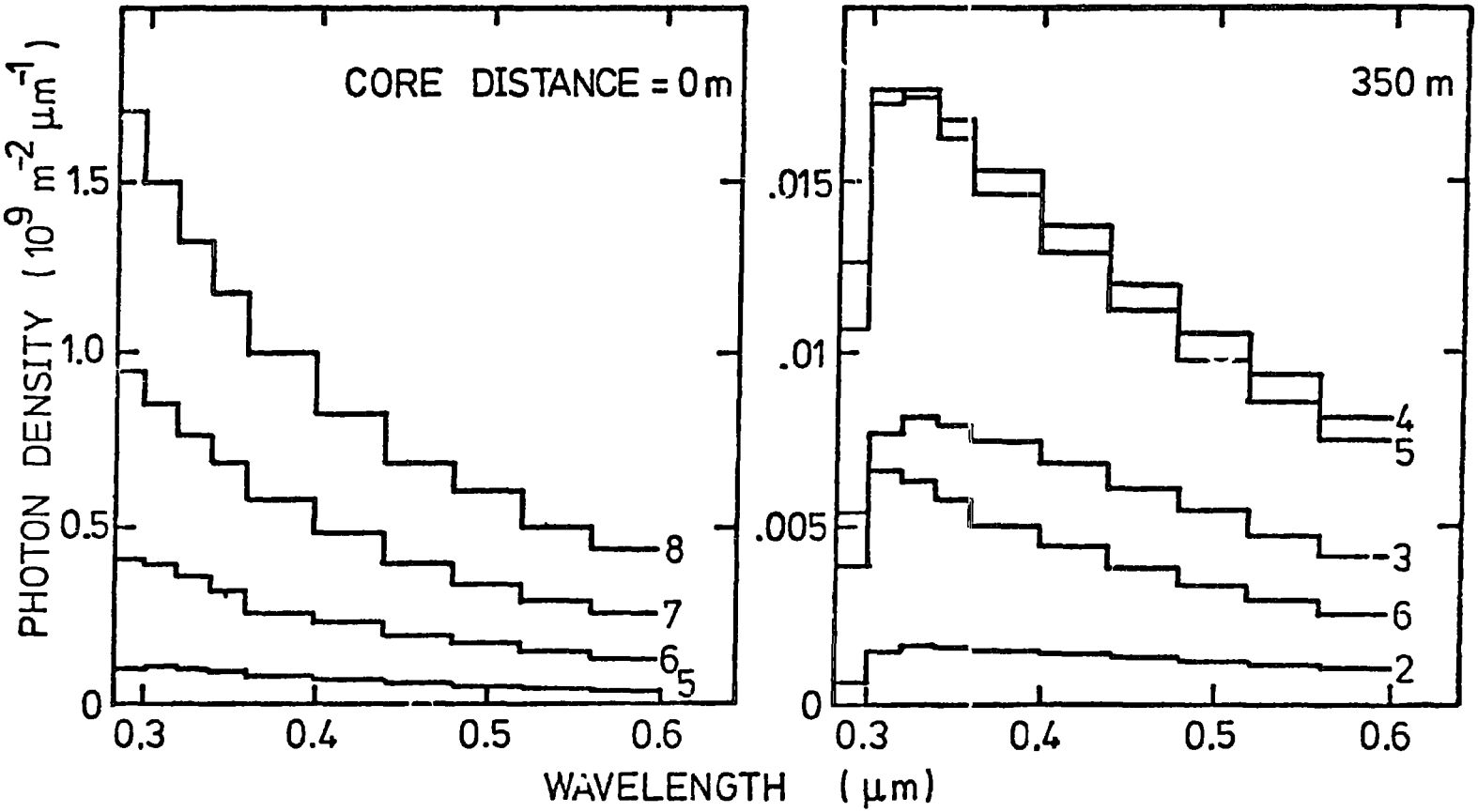

FIGURE 5-31: The wavelength spectrum of light in the core and at 350 m from the core showing the contributions from the 8 subshowers of figure 28.

where μ_o is the refractive index of air at ground level. Figure 32 (Hammond et al (1977, in preparation)) shows the time delay of a photon reaching the ground at a core distance r from an altitude of 1 km with respect to a photon arriving from altitude h km assuming the shower propagates with velocity c.

5-9.2 Imaging the cascade from curvature measurements

Measurements of the curvature of the light front have been made by Boley et al (1961) and Bosia et al (1973) in showers of primary energy $\gtrsim 10^{15}$ eV but most of these measurements were close to the core where interpretation is difficult. More recently, Tornabene (1976 private communication) has measured the radius of curvature with a larger array for showers of primary energy 10^{12}-10^{15} eV and finds typical values of 6 - 8 km.

A new technique for imaging the shower through curvature measurements has been developed by the Durham group using an array of eight Cerenkov light detectors as reported by Orford and Turver (1976). Their novel method of shower analysis is to consider the times, t, to a given level in the pulse (e.g. 50% on the rising edge) and ascribe to them their corresponding distances, ct. They then attach these distances to their appropriate detectors and proceed to fit a sphere to the ends of these lines such that the lines are normals of the sphere. The centre of the sphere is defined as the origin at (in this case) 50% light intensity. The origins at 10%, 50% and 90% on the rising edge and 90%, 50% and 10% on the falling edge of the pulses are found to define a line in space (the trajectory of the shower core) as shown in figure 33.

Two advantages of this approach are immediately apparent first, it is unnecessary to know the location of the core (although it is

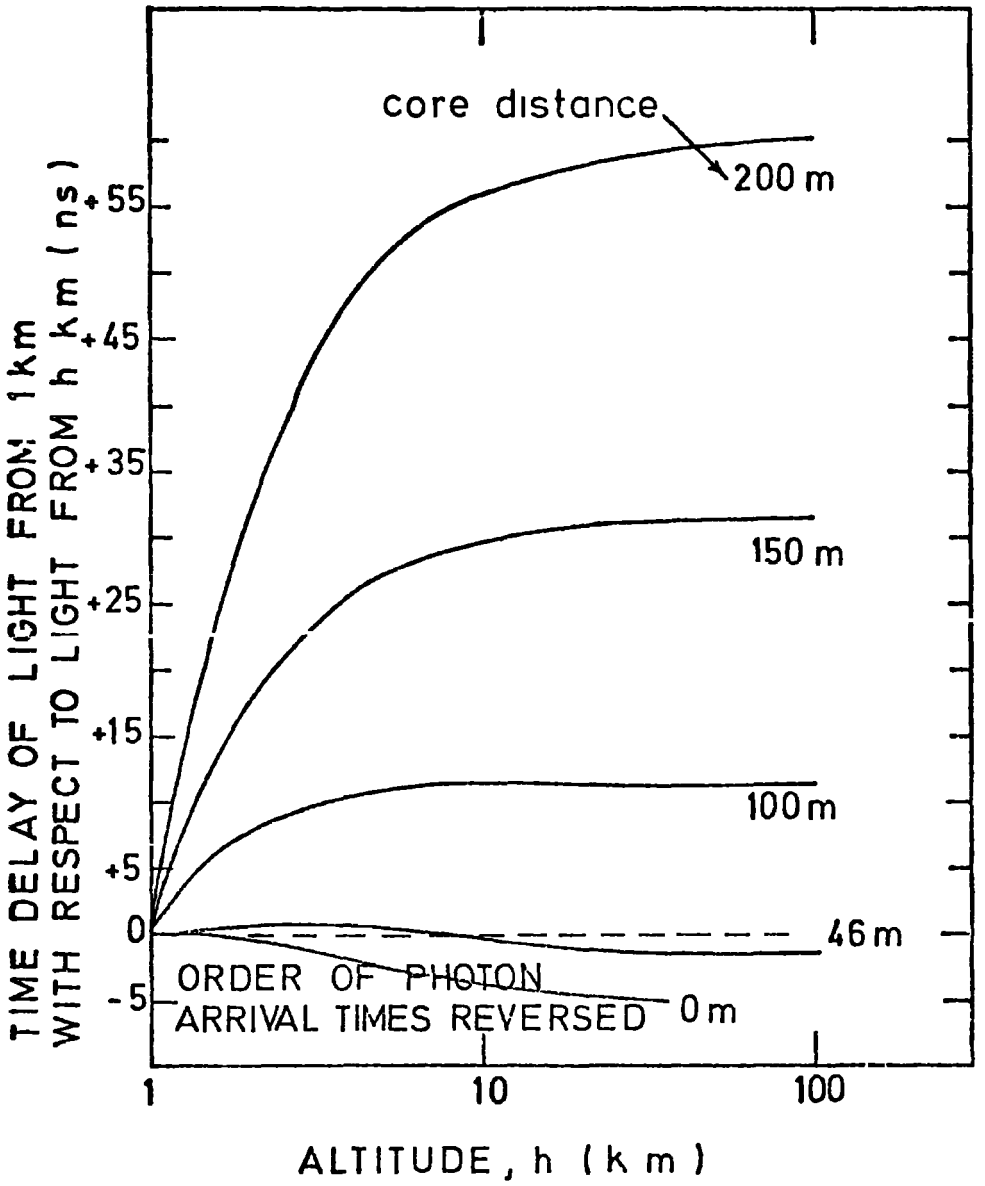

FIGURE 5-32 The time delay of light originating at an altitude of 1 km with respect to that originating at h km as a function of h (from Hammond et al (1977)).

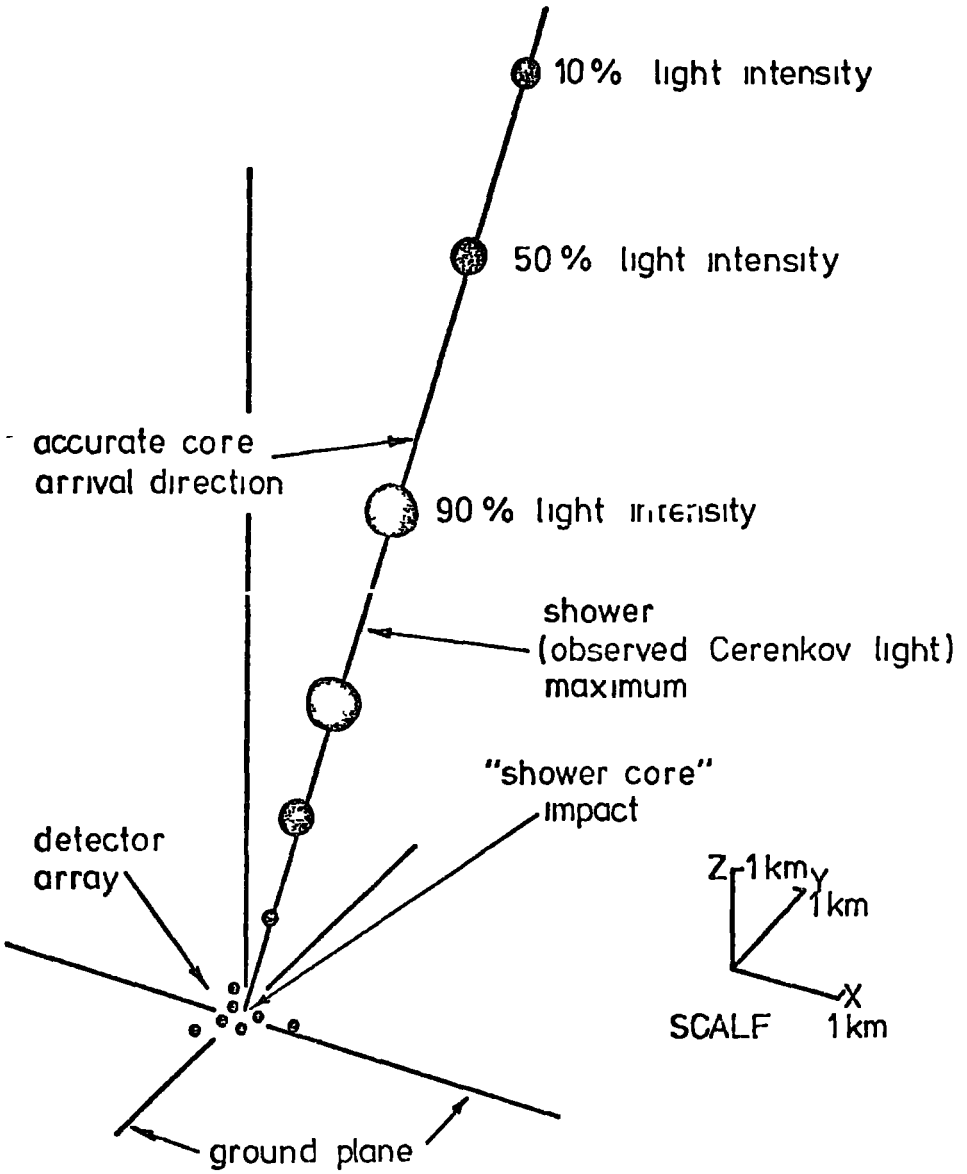

FIGURE 5-33 Summary of the information available in individual showers using the technique described by Orford and Turver (1976).

easily obtained as the intersection of the trajectory with the ground plane if desired) and second, an image of the cascade development in individual showers is obtained in a straight-forward way from arrival time data. Useful measures of shower development determined from this image are the atmospheric depths corresponding to the origin of light at various percentage levels (eg D_{50} is the depth corresponding to the origin at the 50% level) and the atmospheric thickness for the growth (10-90%), D_{rise}, thickness at maximum (90-90%), D_{top}, and decay of the cascade image (90-50%), D_{fall}. The image of the average 10^{17} eV α-particle initiated shower simulated in this way is shown in figure 34.

Calculated values of D_{10}, D_{90}, D_{-90}, and D_{-10} (- indicates falling edge of pulse) based on simulated pulses between 100 m and 500 m from the core are plotted in figure 35 against depth of electron cascade maximum for the average showers described in section 5-9 and are found to correlate well with depth of maximum. This is in contrast to the relative insensitivity of D_{rise}, D_{top} and D_{fall} to the depth of cascade maximum shown in figure 36. This is due to the similar shapes of the electron cascades when plotted against atmospheric depth. The deviation from this rule for late developing showers is due to the fact that only the cascade above the ground may be imaged.

5-10 CERENKOV LIGHT FROM FLUCTUATING SHOWERS, 5×10^{17} eV

Measurements of the quantities described in sections 5-8 and 5-9 may form part of experiments to identify the primary mass through cascade development. Depth of development alone is not sufficient to determine primary mass as interpretations depend on models for nuclear interactions. Measurements of fluctuations and the correlation between observables may

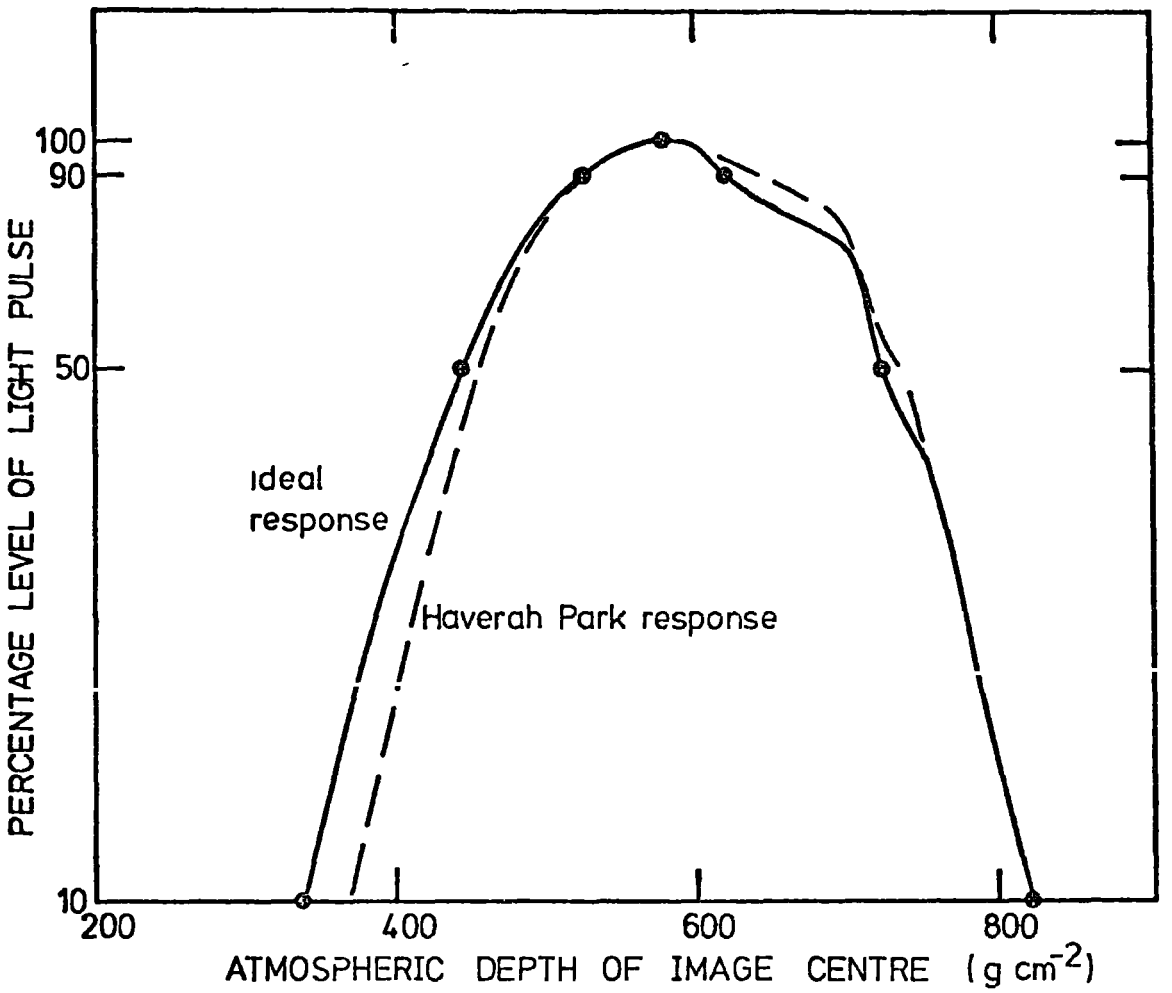

FIGURE 5-34 The image of the average 10^{17} eV α-particle initiated shower simulating the technique described by Orford and Turver (1976).

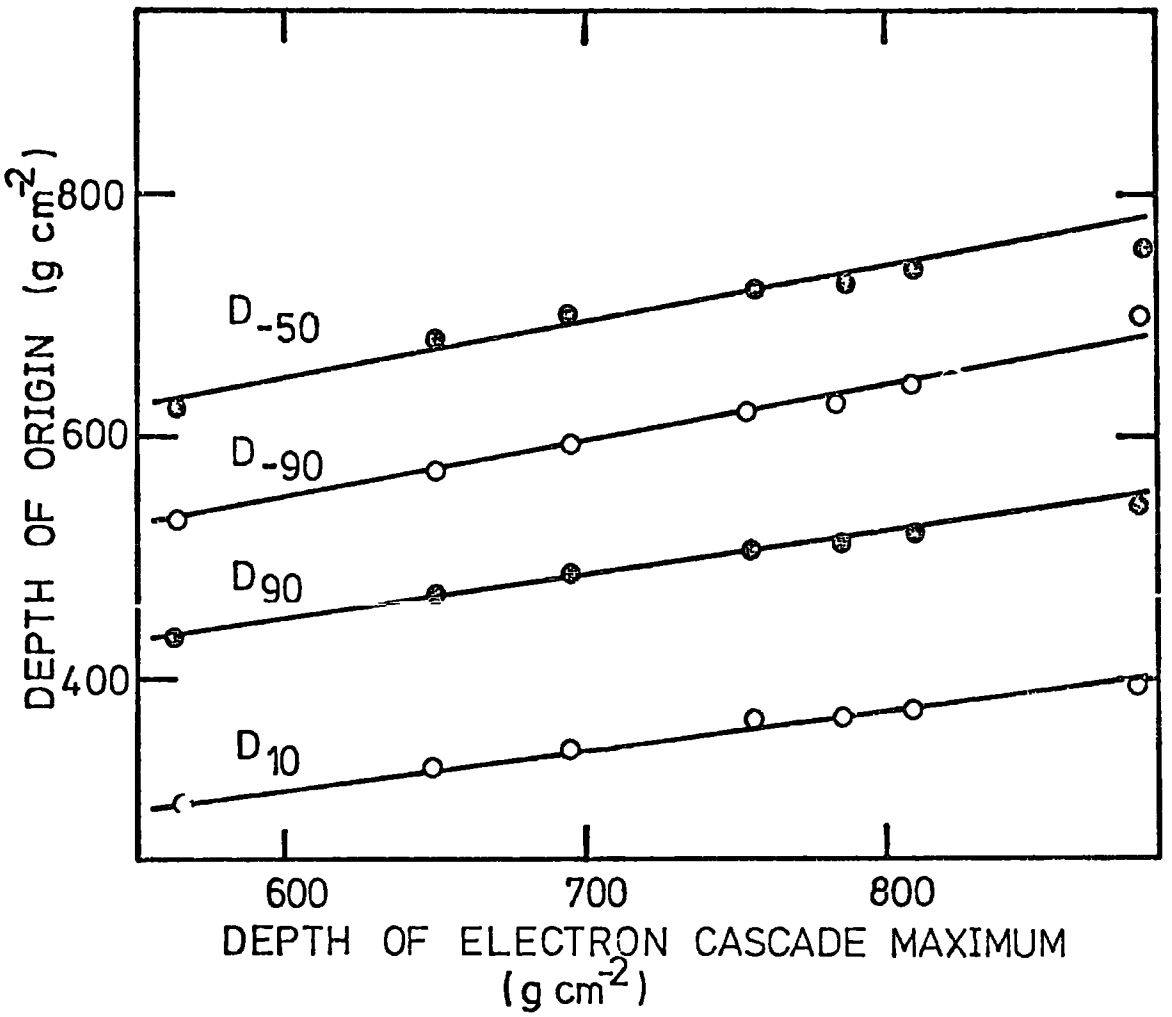

FIGURE 5-35 Values of D_{10}, D_{90}, D_{-90}, and D_{-50} plotted against depth of electron cascade maximum for the average showers.

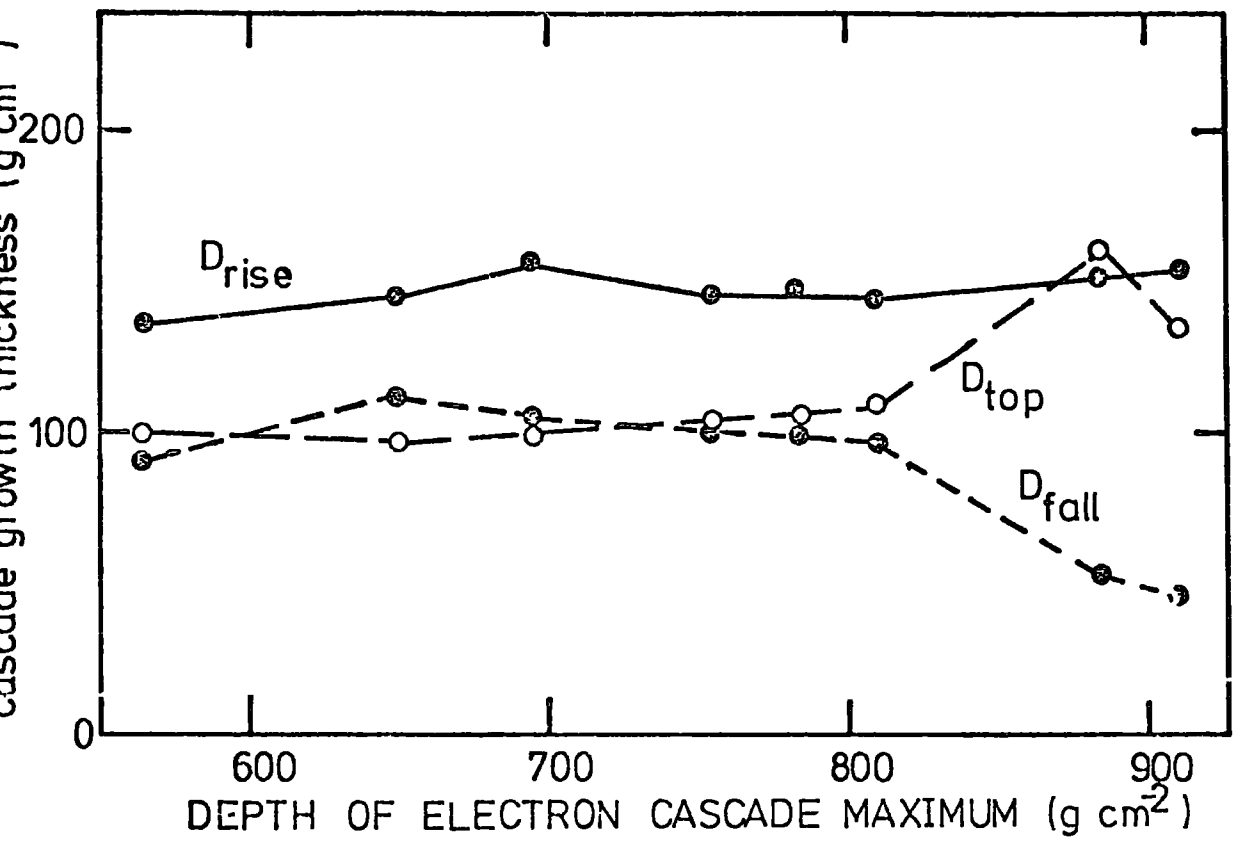

FIGURE 5-36 Values of D_{rise}, D_{top}, and D_{fall} plotted against depth of electron cascade maximum for the average showers.

reinforce hints as to the primary mass given by measurements of average development.

The Cerenkov light component has been calculated for a sample of 20 proton initiated showers and 10 iron nucleus showers with a primary energy of 5×10^{17} eV. The sensitivity of the lateral structure function exponent, γ, and various measures derived from the light pulse shape to the early (10%) and maximum (100%) development of the electron cascade are shown in figures 37, 38 and 39. Correlation coefficients have been calculated between selected measures of the light pulse and cascade development and are shown in table 4. γ is also considered here as a measure of cascade development.

It is noted that γ, D_{10} and D_{100} correlate particularly strongly with cascade development and that generally light pulse measures that reflect the start of the pulse correlate better with the depth for 10% of electron cascade maximum, x_{10}, than the depth of electron cascade maximum, x_{max}, i.e. they are related to the start of the electron cascade. It is also noted that correlation coefficients are often higher for the iron nucleus showers than for the proton showers reflecting a wider spread in shape of electron cascades for proton initiated showers with this model.

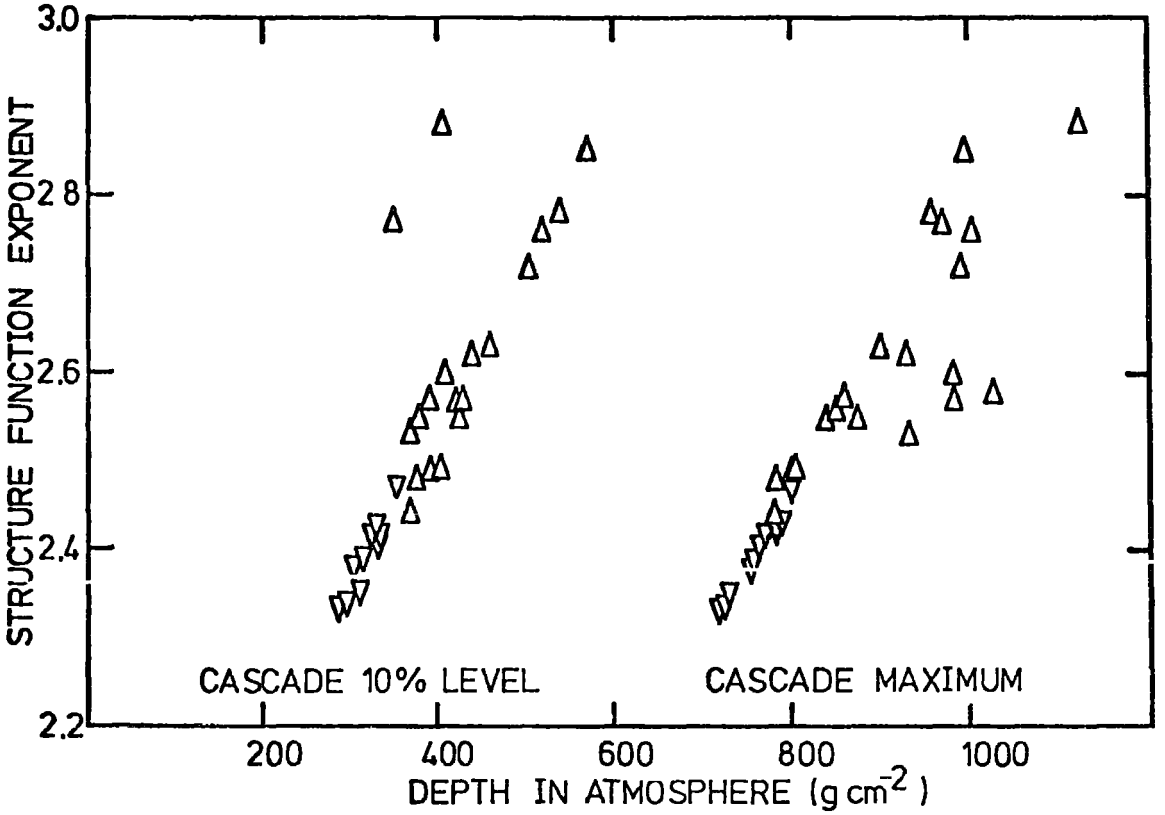

FIGURE 5-37 Values of lateral distribution structure function exponent in individual proton (Δ) and iron nucleus (∇) initiated showers plotted against the depths for 10% and 100% of electron cascade maximum.

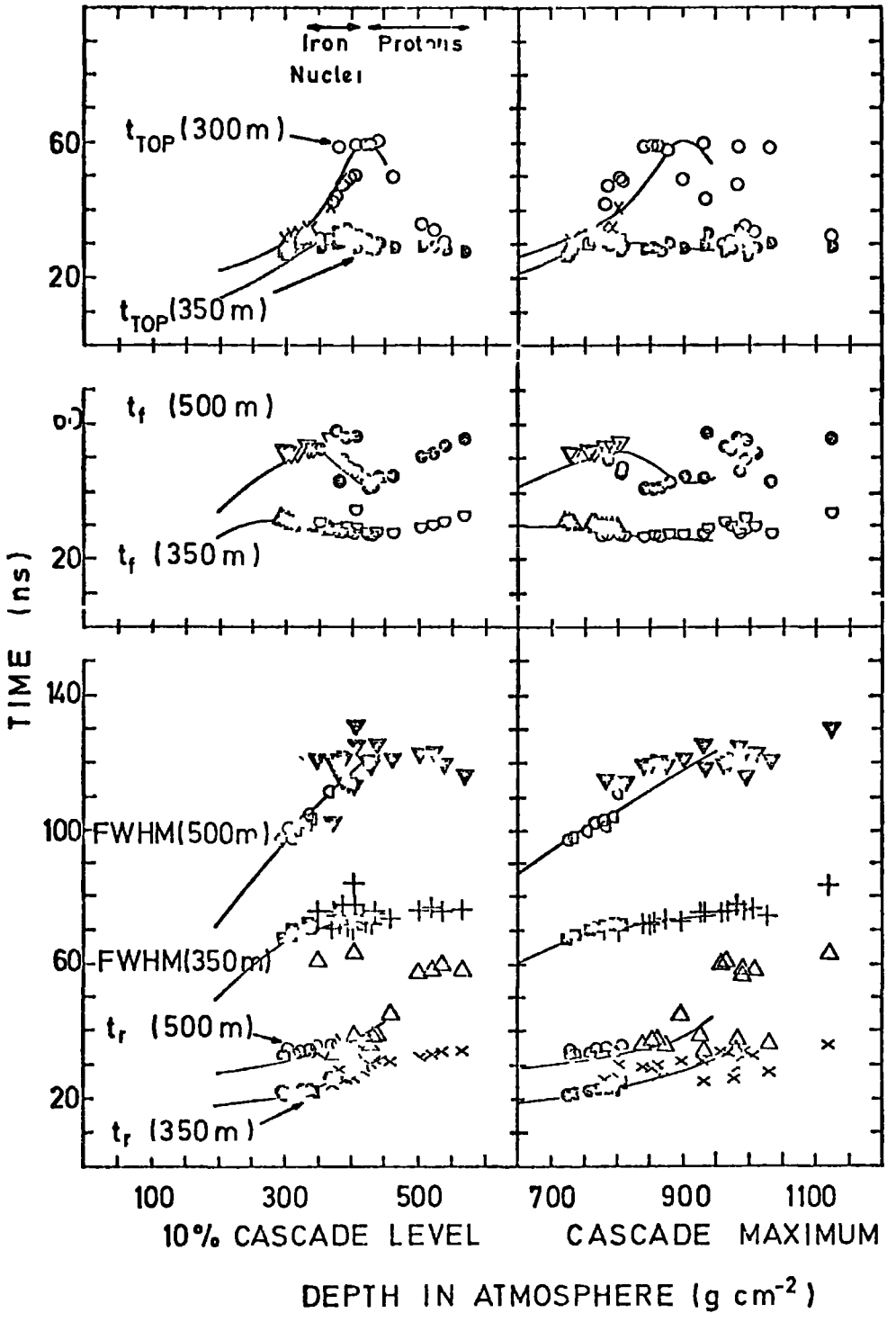

FIGURE 5-38 Measures of pulse shape at 350 m and 500 m from the core in individual showers plotted against measures of cascade development.

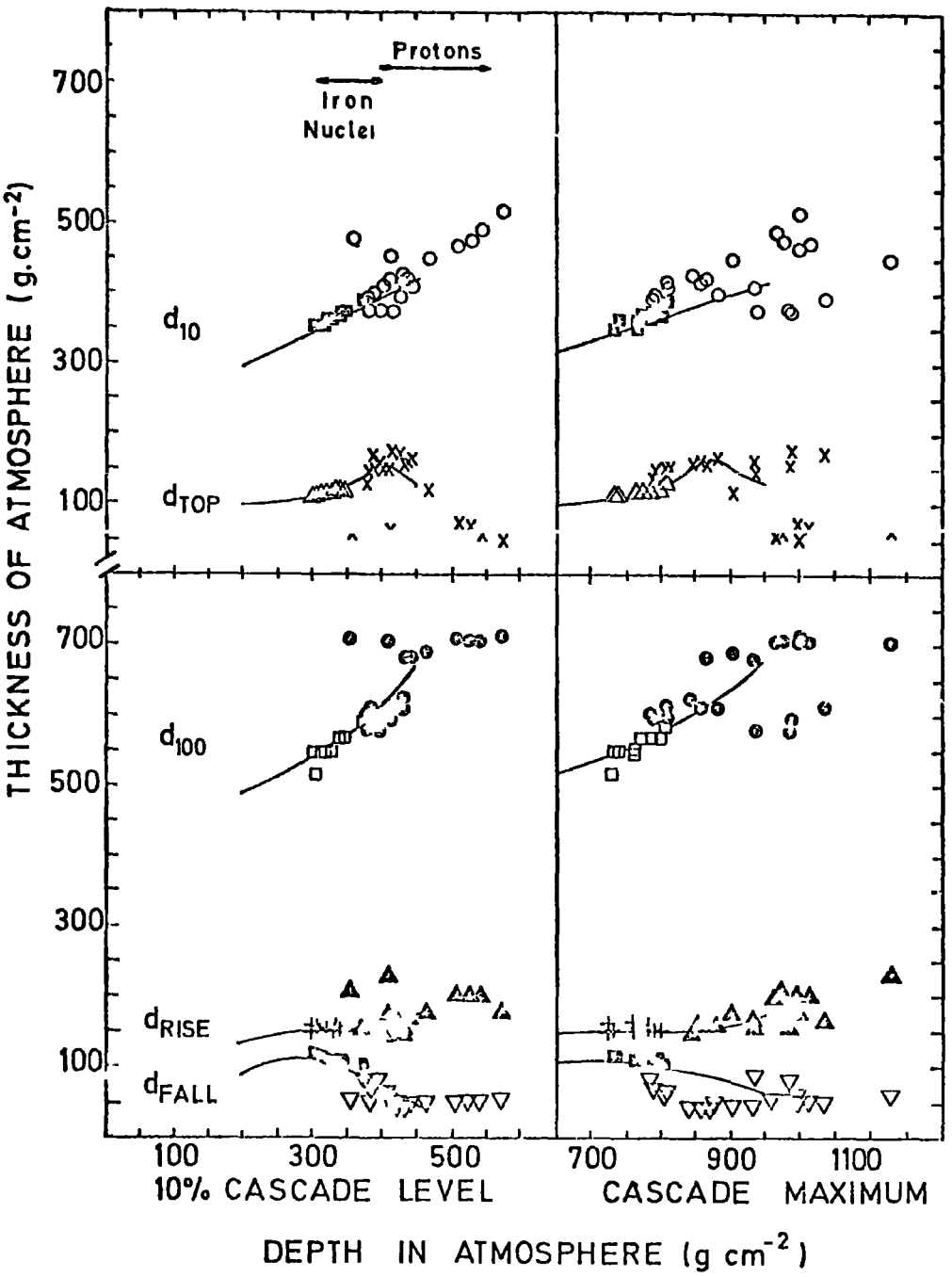

FIGURE 5-39 Measures of development of the Cerenkov light image in individual showers plotted against measures of cascade development.

		PRIMARY PROTONS				PRIMARY IRON NUCLEI			
		x_1	x_{10}	x_{max}	γ	I_F	x_{10}	x_{max}	γ
Lateral Distribution Structure Function Exponent	γ	0.687	0.607	0.804	-	0.965	0.964	0 986	-
Pulse Rise Time (ns)	$t_r(350)$	0 626	0.576	0 637	0 911	0.957	0 976	0.897	0.954
	$t_r(500)$	0 688	0 573	0 668	0.948	0 912	0 885	0 873	0 913
Pulse Top Time (ns)	$t_{top}(350)$	-0.483	-0.520	0 186	-0.337	0.812	0.777	0 912	0 875
	$t_{top}(500)$	-0.587	-0.421	-0.416	-0 690	0 941	0 968	0 886	0.942
Pulse FWHM (ns)	$t_{\frac{1}{2}}(350)$	0.307	0 197	0 924	0.763	0 913	0 873	0 986	0 962
	$t_{\frac{1}{2}}(500)$	0 189	0.190	0 743	0 581	0.939	0.954	0 891	0 939
Pulse Fall Time (ns)	$t_F(350)$	0.563	0.406	0 781	0 891	-0 948	-0 967	-0 906	-0 948
	$t_F(500)$	0 270	0 118	0 432	0 442	0 935	0 914	0 921	0 938
Image Depths ($g\ cm^{-2}$) at 10% level	d_{10}	0 776	0 733	0 343	0 803	0 920	0 983	0.841	0 905
at 100% level	d_{100}	0 653	0 657	0 487	0 840	0 840	0 876	0 862	0.882
10% to 90% level	d_{rise}	0 522	0 390	0 733	0.898	-0 367	-0.490	-0.304	-0 343
90% to 90% levels	d_{top}	-0 702	-0 574	-0 513	-0.853	0 926	0 944	0 864	0 918
90% to 50% levels	d_{fall}	-0 256	-0.358	-0 125	-0 287	-0 939	-0 969	-0.890	-0 948

TABLE 5-4 The correlation between selected measures of the light pulse and longitudinal development.

CHAPTER SIX

THE SIMULATED RESPONSE OF "FLY'S EYE" TYPE IMAGING SYSTEMS TO THE OPTICAL EMISSION FROM LARGE COSMIC RAY SHOWERS

INTRODUCTION

A detailed knowledge of the energy spectrum and composition of the primary cosmic radiation up to energies of $\sim 10^{21}$ eV is necessary to advance our understanding of astrophysics. At these very high energies the spectrum of the primary radiation is measured indirectly because of its low flux. The conventional approach has been to detect extensive air showers with an array of ground based particle detectors (Tennent (1967)). This approach is not suitable for the detailed study of the energy spectrum above 10^{20} eV as an array of detectors defining a sensitive area of about 10 km^2 would be required to obtain a rate of one shower of primary energy greater than 10^{20} eV per year.

An alternative approach pioneered by Greisen (1966) is to use the atmosphere as a scintillator and detect the fluorescence light emitted isotropically from electron tracks The shower electrons excite nitrogen molecules which subsequently emit light on de-excitation - the optical yield, which is approximately independent of pressure (Bunner (1967)), is about 4 photons per metre of electron track. Further attempts to use this technique (Porter et al (1970), Hara et al (1969) and Tanahashi et al (1975)) met with limited success.

In 1975 the University of Utah group reported their proposal to build a "Fly's Eye" detector on a site in Western Utah blessed with favourable atmospheric visibility using a system consisting of 79 detector units (Bergeson et al (1975)). Each proposed detector unit consisted of 12 photomultiplier tubes with hexagonal light funnels clustered above a 1.5 m diameter f/1.0 mirror so that the photomultiplier

tubes viewed adjacent hexagonal areas of the sky, each subtending a solid angle of 0.006 steradians. In this way, with the collection of detector units (called the "Fly's Eye"), 94% of the sky could be covered and remote air showers would be recorded by their optical emission as shown in figure 1. The direction and location of the air shower core trajectory would be obtained from the timing information on the light samples as the shower swept past the detector. The electron cascade development would then be inferred from the photon densities recorded by the photomultipliers. With such a system, the sensitive volume for large air showers would be enormous and the event rate would be high (a pessimistic estimate given by Bergeson et al (1975) is about 20 showers with primary energy greater than 10^{20} eV per year and Cassiday et al (1977a) expect to map the primary energy spectrum from 10^{16} eV to 10^{21} eV with a rate of 10^{6} events per year).

A Fly's Eye consisting of three detector units was successfully operated during 1976/77 in coincidence with the Volcano Ranch scintillation counter array (Mason et al (1977), Cassiday et al (1977)) and a full Fly's Eye is being constructed at Dugway, Utah (Bergeson et al (1977)). The experiment proved the viability of imaging air showers by their isotropic optical emission. By observing showers recorded by the scintillation counter array from a site 1.5 km away, the response of the Fly's Eye to shower particles near ground level could be calibrated. It was found that more light was detected by the Fly's Eye than expected from the scintillation counter array response and this excess was attributed to atmospheric scattering of the Cerenkov light emitted by the air shower (Elbert et al (1977)). Furthermore, as expected, the Fly's Eye detectors which were looking at small angles to the core observed large photon densities due to direct Cerenkov light.

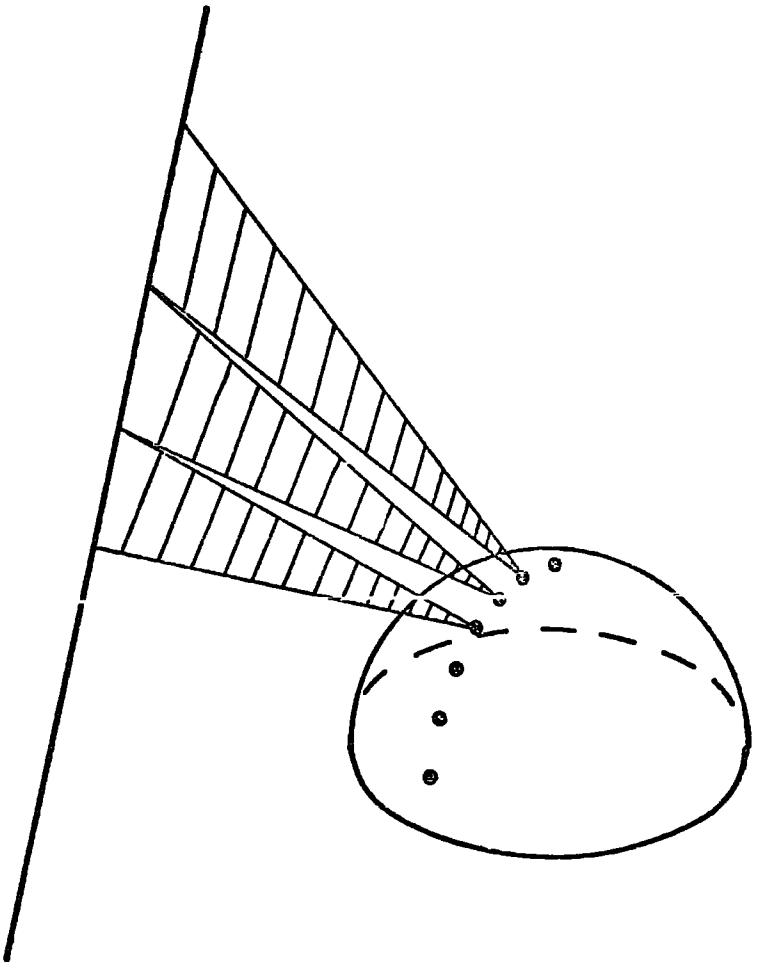

FIGURE 6-1 Segments of a high energy cosmic ray shower as seen by three phototubes of the Fly's Eye detector (from Bergeson et al (1975)).

The detailed study of the origin of the isotropic radiation forms an important part of this new technique (Elbert et al (1977)). In this chapter computer simulations of Cerenkov light have been extended to investigate the important problem of the spatial and temporal response of a Fly's Eye imaging system to the fluorescence light, direct Cerenkov light and scattered Cerenkov light from air showers.

6-1 DETAILED COMPUTER SIMULATION

A detailed Monte Carlo calculation has been made of the response of a Fly's Eye type imaging system situated at an altitude of 1.6 km (the altitude of the proposed University of Utah Fly's Eye) to fluorescence light, direct Cerenkov light and scattered Cerenkov light from an electron cascade. The electron cascade shown in figure 2 was initiated by a vertically incident gamma-ray of energy 2×10^{11} eV. The point of initiation of the shower was chosen to be low in the atmosphere so that the electron cascade would maximize at a depth similar to that of a shower initiated by a primary particle of energy $\sim 10^{17}$ eV. In this way the simulated distribution of electrons was appropriate to large cosmic ray showers but the computation was economic.

The calculation of the electron-photon cascade and the direct Cerenkov light component follows that described in chapters 3 and 5. For example, the wavelength dependent atmospheric attenuation of light was considered using the model described by Elterman (1968). The Rayleigh Law of Scattering has been introduced to allow for both molecular and aerosol scattering of Cerenkov light as described in chapter 5. A fluorescence yield of 4 photons per metre of electron track has been adopted and the attenuation of fluorescence light has been allowed for assuming that all the fluorescence light was produced at a wavelenth of 360 nm.

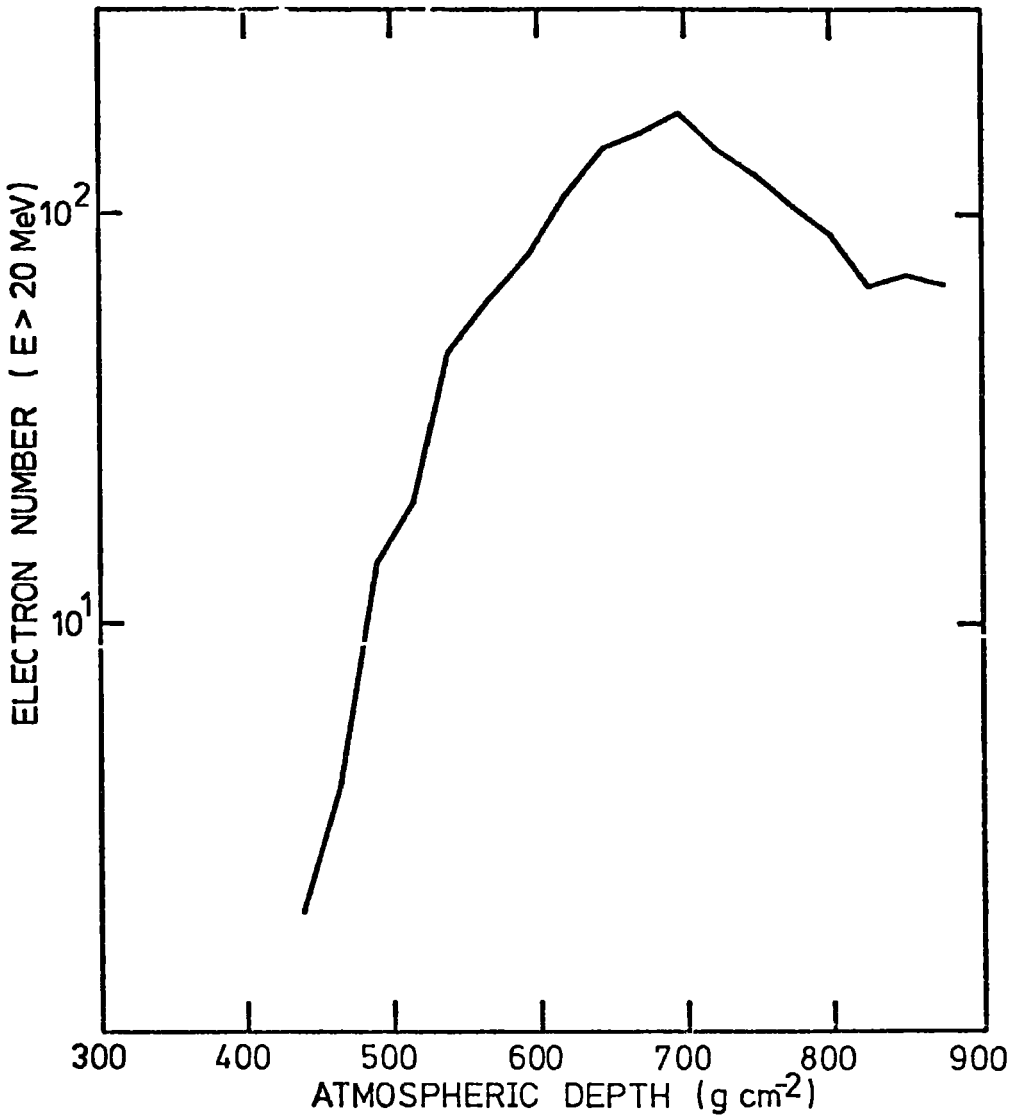

FIGURE 6-2 The longitudinal electron cascade of a 2×10^{11} eV gamma-ray initiated shower developing low in the atmosphere.

6-2 SPATIAL CHARACTERISTICS OF THE OPTICAL IMAGE

The images in fluorescence light, direct and scattered Cerenkov light received by an imaging system consisting of detectors with an acceptance solid angle of 0.006 steradians pointing towards the shower core trajectory from locations with impact parameters of 0.5 km, 1 km, 2 km, 4 km, 8 km and 16 km are shown in figure 3. It is noted that when the imaging system is located near the core (impact parameter $\leq$1 km) the first half of the image (from the zenith to $\sim 45^{\circ}$ from the zenith) is dominated by direct Cerenkov light, whereas the second half of the image ($\sim 45^{\circ}$ to the zenith to 90° to the zenith, i.e. when the shower is viewed from the side) is dominated by scattered Cerenkov light. The image in fluorescence light is seen to grow, maximize and decay reflecting directly the growth, maximization and decay of the electron cascade. In constrast, the image in scattered Cerenkov light continues to brighten at ever increasing angles to the zenith. At large impact parameters fluorescence light is seen to dominate the image, scattered Cerenkov light making an important contribution only to the light seen by detectors looking at large zenith angles (i.e. when the shower is viewed from the side).

The above analysis may be compared to the results of calculations by J.W. Elbert (1977, private communication) who has mapped out regions of emission angle - emission altitude space where direct Cerenkov light, scattered Cerenkov light and fluorescence light predominate as shown in figure 4. The trajectory of the shower core as viewed by the imaging system has been added to this figure for the impact parameters used in the present work. The predominant light component is indicated at each point along the trajectory and is found to be in good agreement with that given by Elbert.

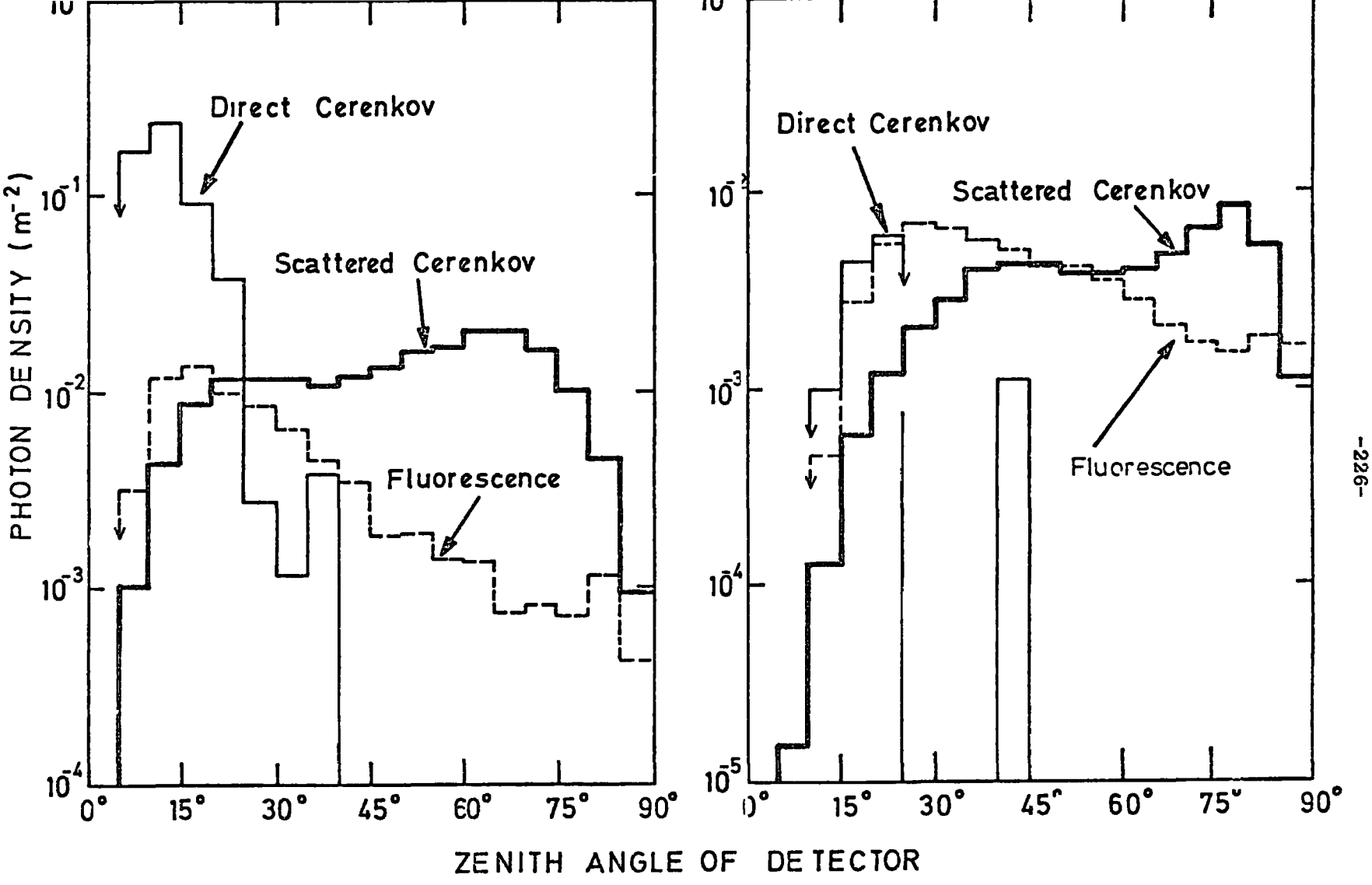

FIGURE 6-3. The images in fluorescence light, direct Cerenkov light and scattered Cerenkov light received by a Fly's Eye detector at various impact parameters (the absence of direct Cerenkov light received between 30° and 40° of the zenith at an impact parameter of 2 km is not significant).

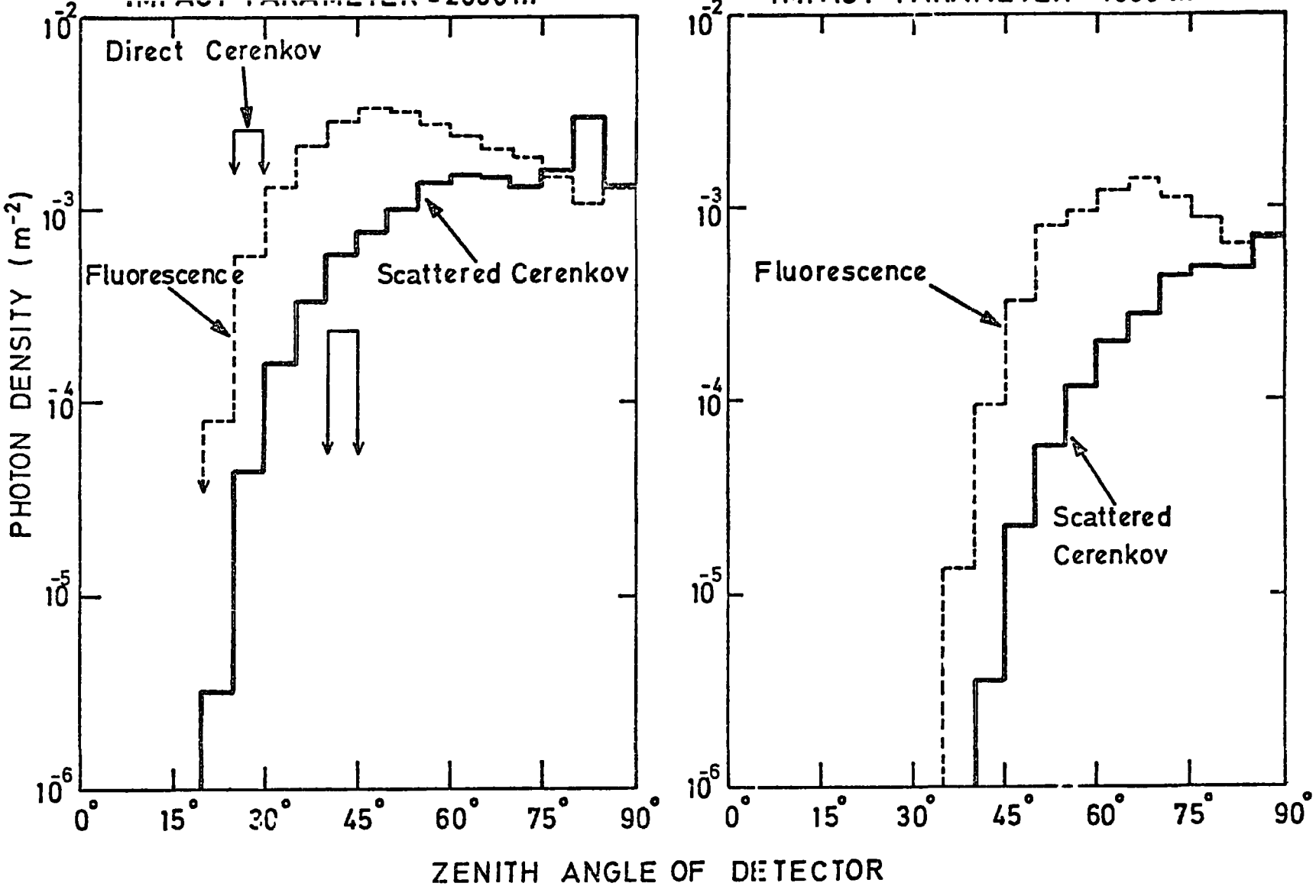

FIGURE 6-3 (continued)

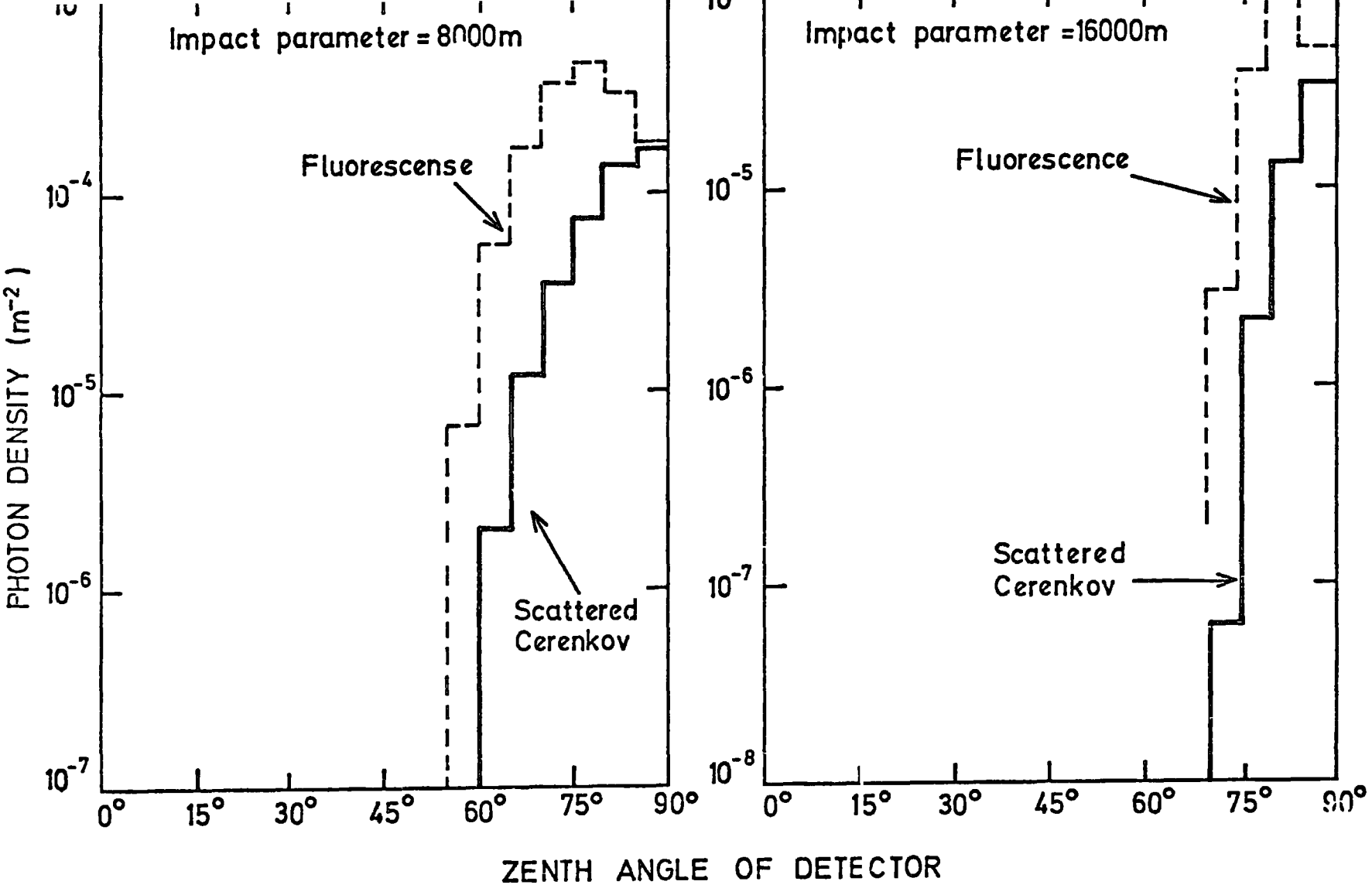

FIGURE 6-3 (Continued)

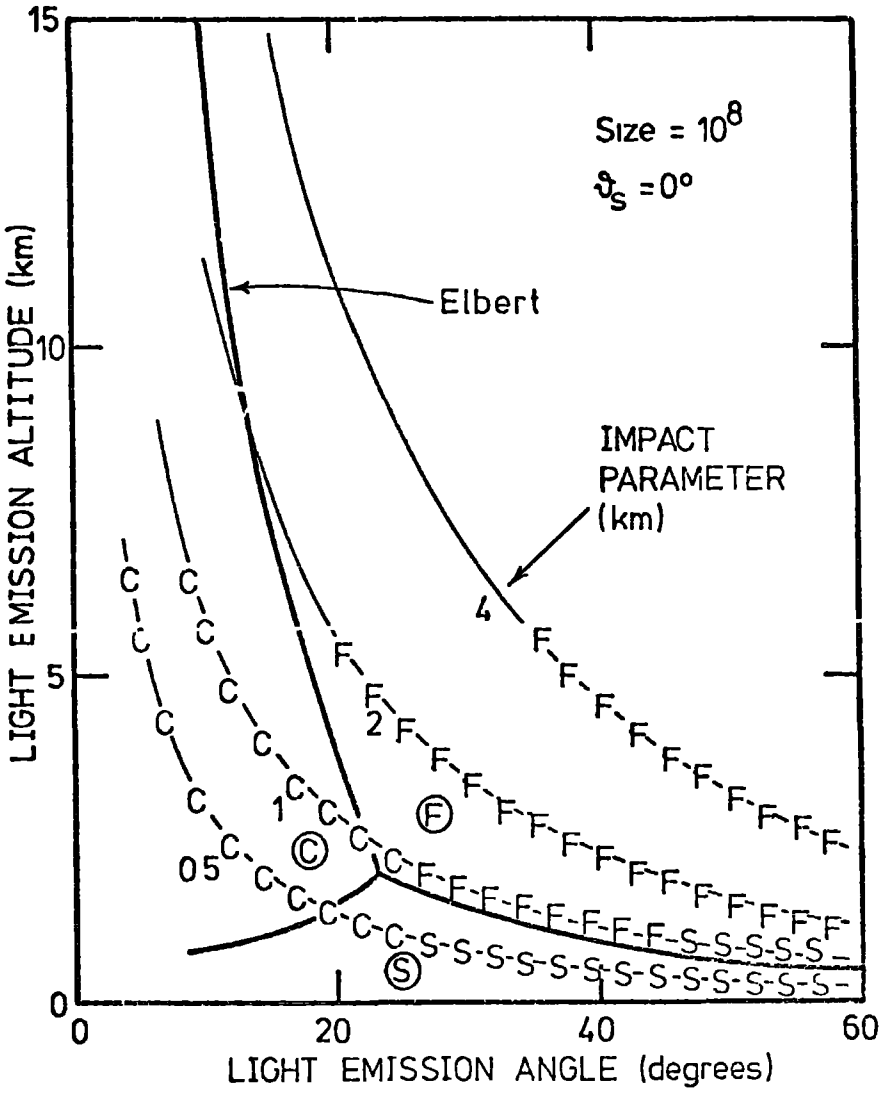

FIGURE 6-4 The regions of emission angle - emission altitude space where, according to Elbert (1977, private communication), direct Cerenkov light, scattered Cerenkov light and fluorescence light predominate. The trajectory of the shower core as viewed by the imaging system for the impact parameters used in the present work are also shown and the predominant light is indicated at each point on the trajectory C - direct Cerenkov, S - scattered Cerenkov, F - fluorescence.

6-3 TEMPORAL CHARACTERISTICS OF THE OPTICAL IMAGE

The time structure of the light pulses received by an imaging system located at 1 km from the shower core has been investigated in detail. This distance is typical of the impact parameters of showers recorded by the University of Utah imaging system during its operation at Volcano Ranch but larger distances will be appropriate to the final imaging system at Dugway. In these simulations the timing origin at any given point in space is defined as the time at which that point is coincident with a plane which has the core direction as a normal and is moving with velocity c in the direction of the primary gamma-ray, starting at its first interaction.

The light pulses showing the total light and the contribution from atmospheric fluorescence received by detectors of tne imaging system looking at the shower core trajectory are shown in figure 5. The detectors are looking at different angles to the zenith and observe the shower in various stages of development. As the shower sweeps through the field of view of each detector in turn, the pulses are seen to increase in duration. The first pulses are dominated by a very fast, intense direct Cerenkov light component. It is seen that the pulses due to scattered Cerenkov light and fluorescence light are approximately symmetric about the same mean arrival time and that the scattered Cerenkov light pulse is much broader than the fluorescence light pulse.

The above results are consistent with the shower electron density (the source of fluorescence light) falling off much more rapidly with core distance than theCerenkov photon density (the source of scattered Cerenkov light). In consequence, the volume of space from which the fluorescence light component originates, the "electron volume", is much

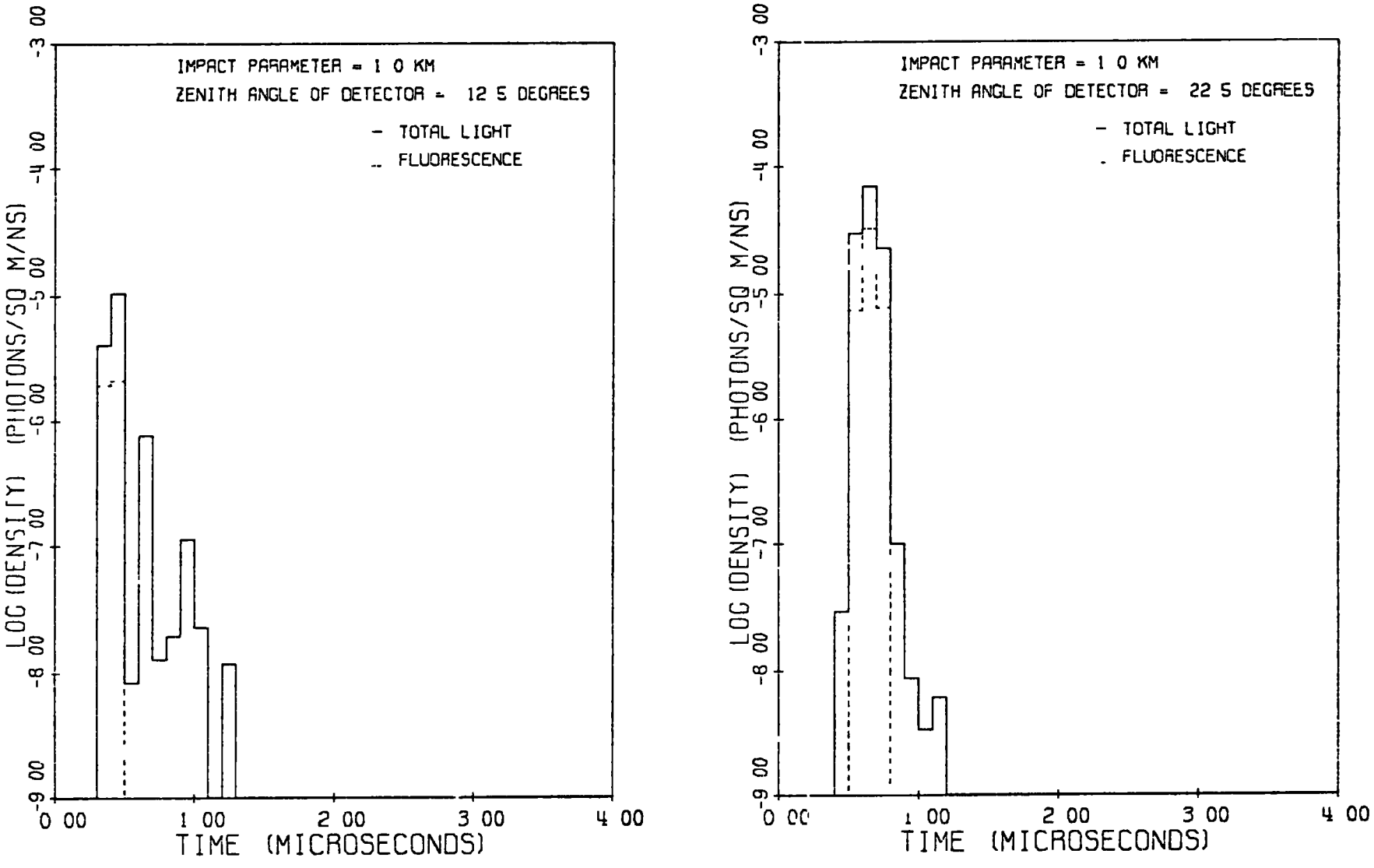

FIGURE 6-5. The light pulses received by detectors of a Fly's Eye type imaging system pointed in various directions showing the contribution from the fluorescence light component.

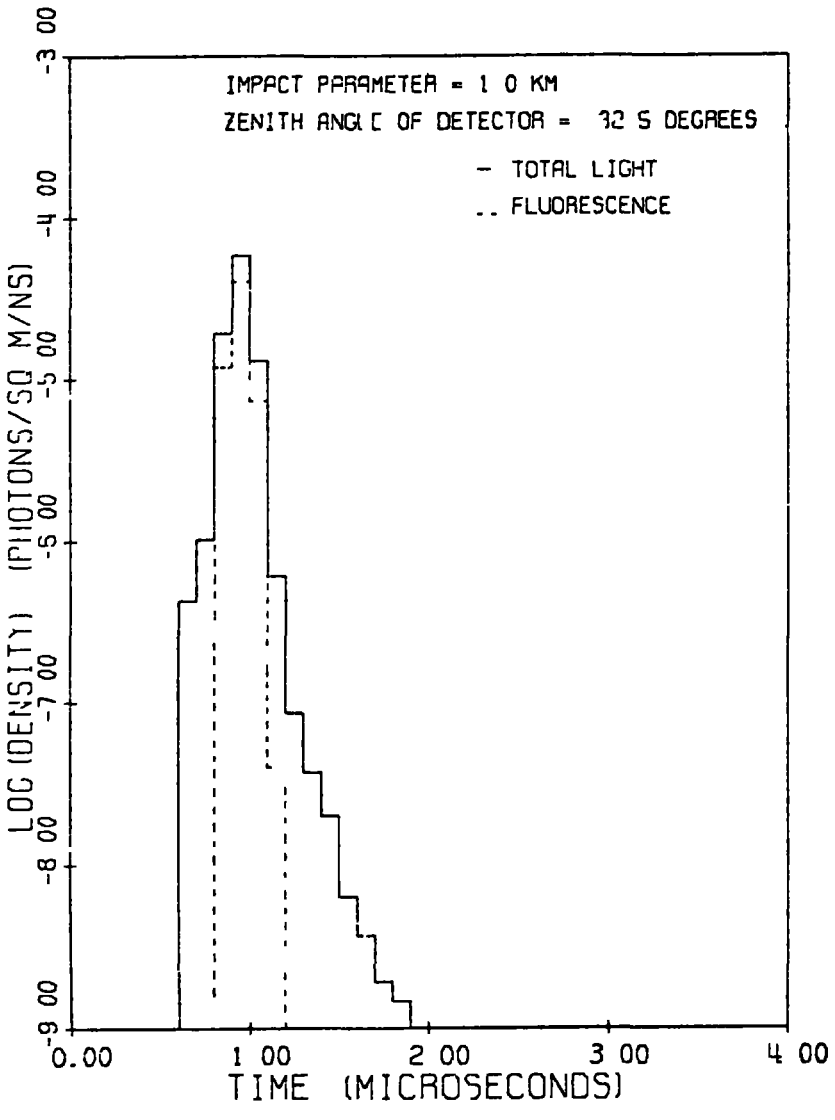

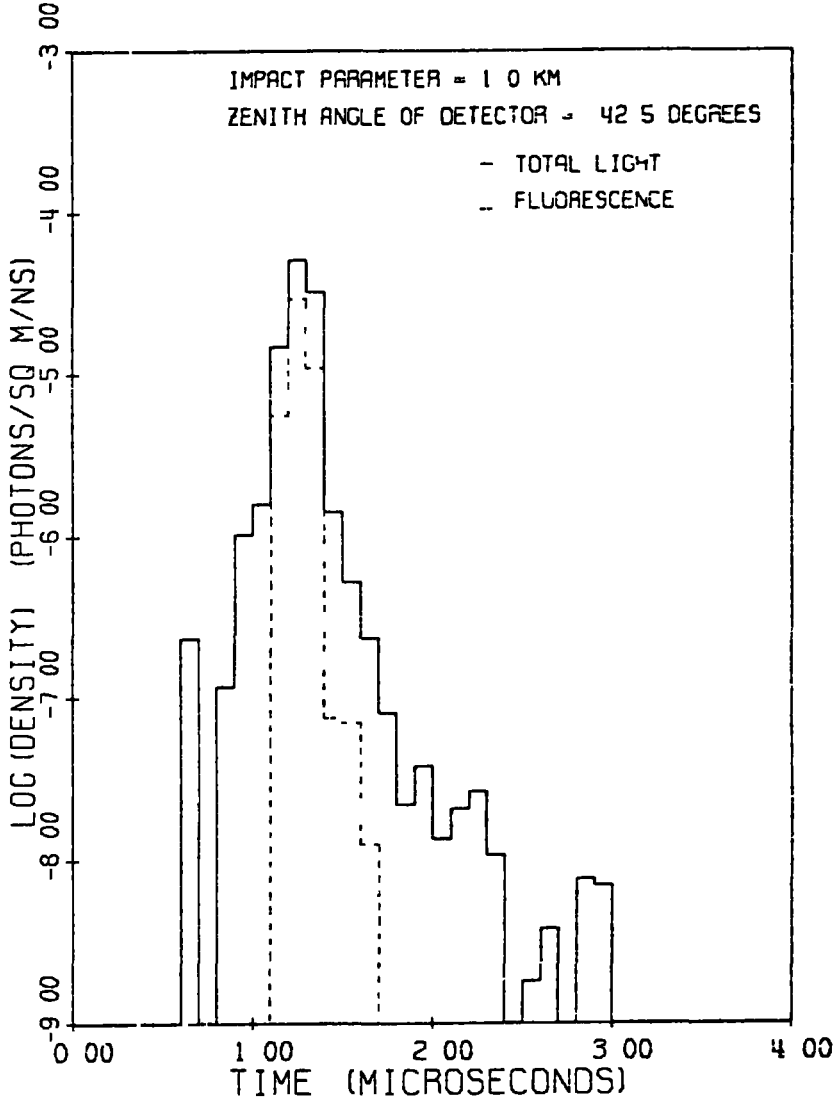

FIGURE 6-5. (continued)

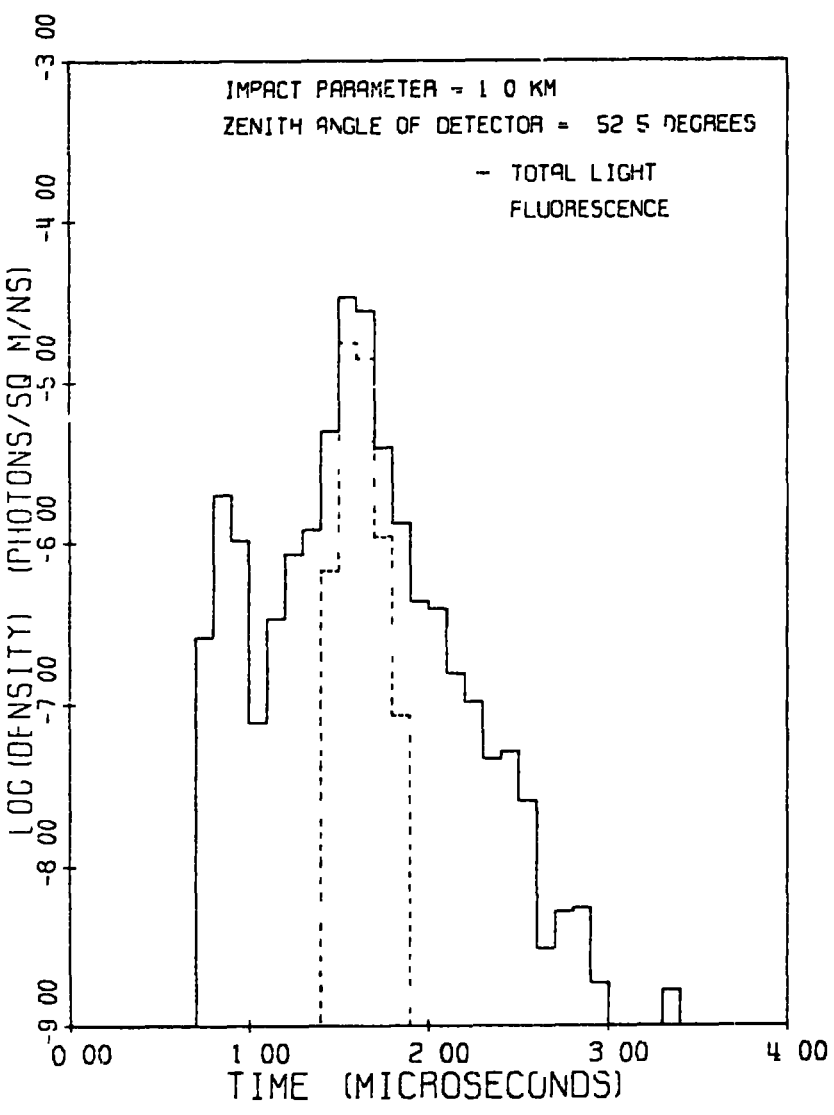

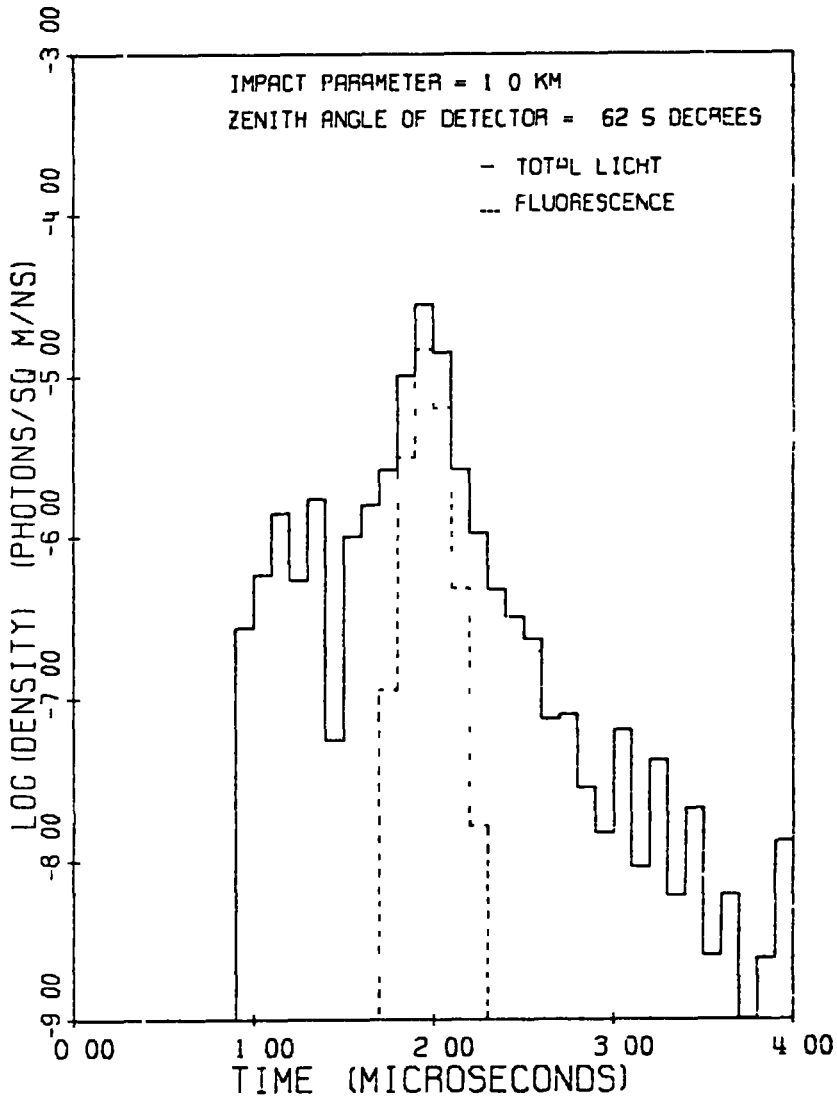

FIGURE 6-5 (continued)

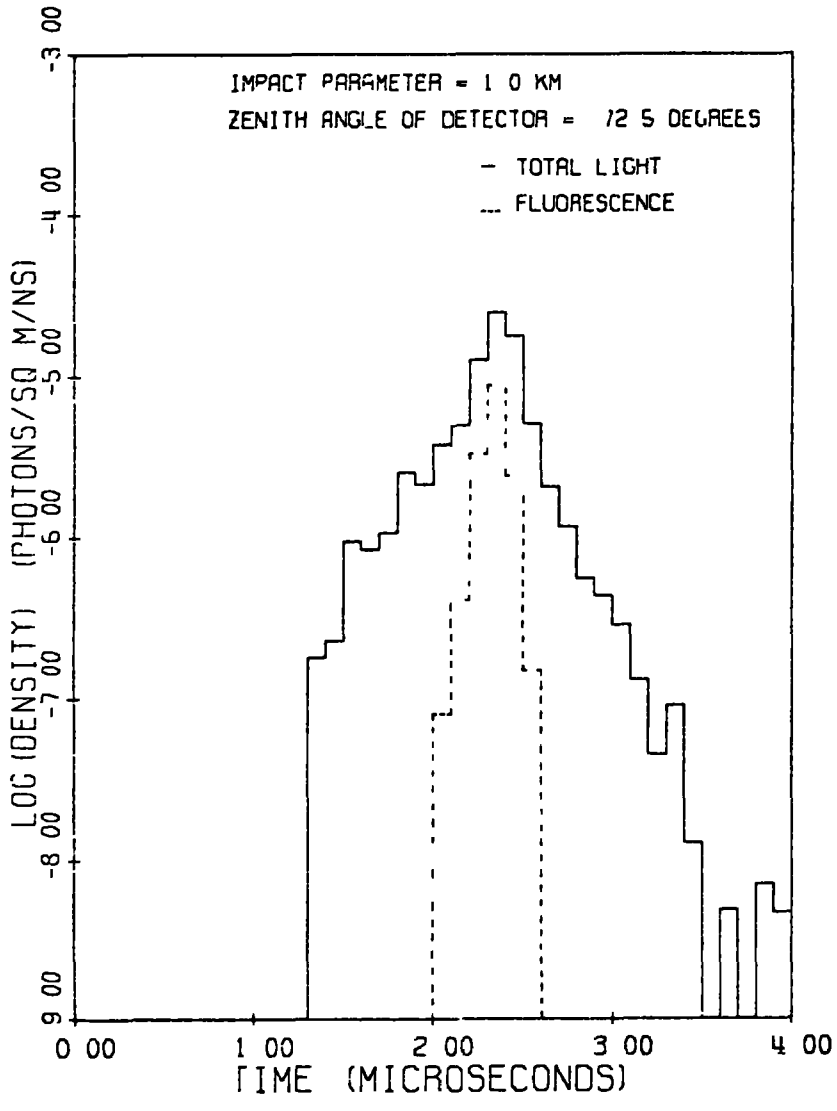

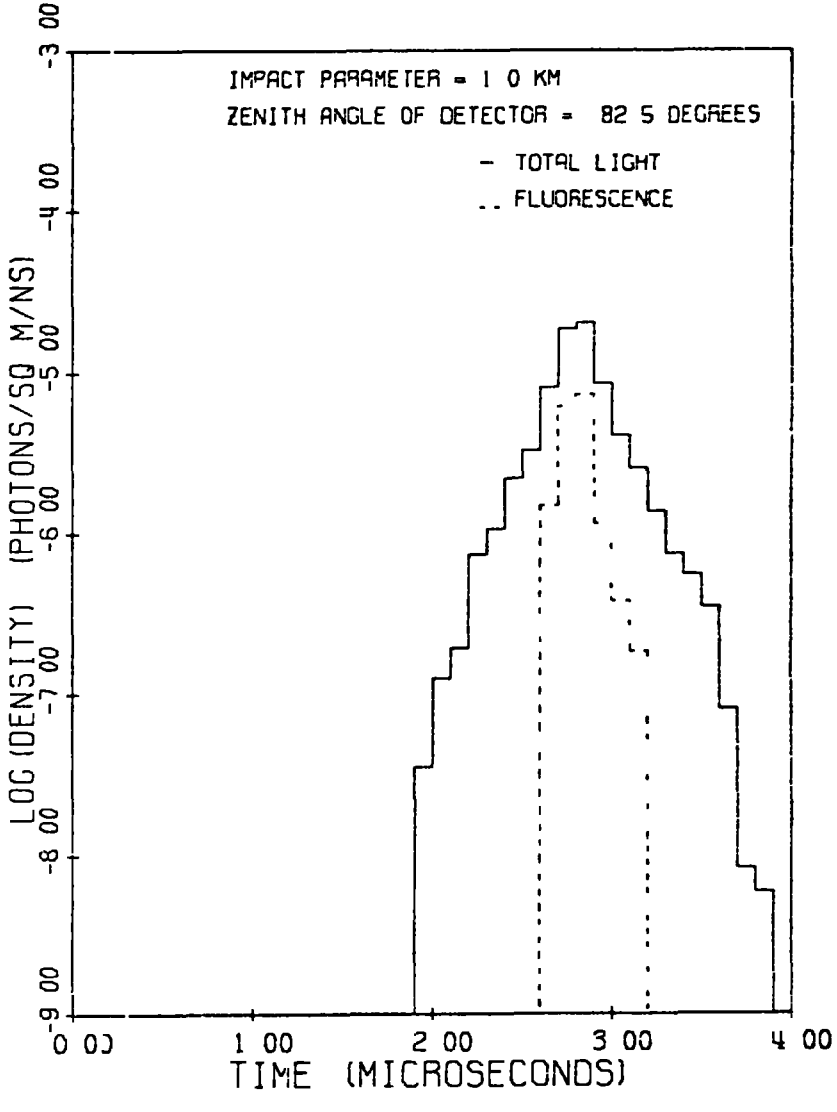

FIGURE 6-5· (continued)

smaller than the volume in space from which the scattered Cerenkov light originates, the "Cerenkov volume" as shown schematically in figure 6. This results in a larger spread in arrival times for the scattered Cerenkov light component than for the fluorescence light component (this is most marked at small impact parameters) as illustrated in figures 7 and 8. These figures show the pulse widths for scattered Cerenkov and fluorescence light respectively (defined here as the r.m.s. deviation in photon arrival time $\approx$ FWHM/3) as a function of zenith angle of the detector for various impact parameters. In either case the source of light is most dense at the shower core and one would therefore expect the scattered Cerenkov and fluorescence light pulses to peak at about the same time. This is substantiated in figure 9 which shows the mean arrival times of these two components as a function of zenith angle of the detector for various impact parameters of the Fly's Eye.

6-4 CONCLUSION

Detailed computer simulation of the response of a Fly's Eye type imaging system to the optical emission from an electron cascade in the atmosphere has been made and this confirms the observation by Elbert et al (1977) that direct and scattered Cerenkov light may make an important contribution to the image of cosmic ray showers recorded by such a system, particularly for showers with impact parameters less than $\sim$2 km. Elbert et al give the ratio of the apparent optical shower size to the Volcano Ranch array shower size as a function of light emission angle (irrespective of impact parameter and shower size) and as a function of shower size (iresspective of impact parameter and light emission angle). The present simulations are not directly comparable to these results but indicate the relative importance of the three optical components at different impact parameters and light

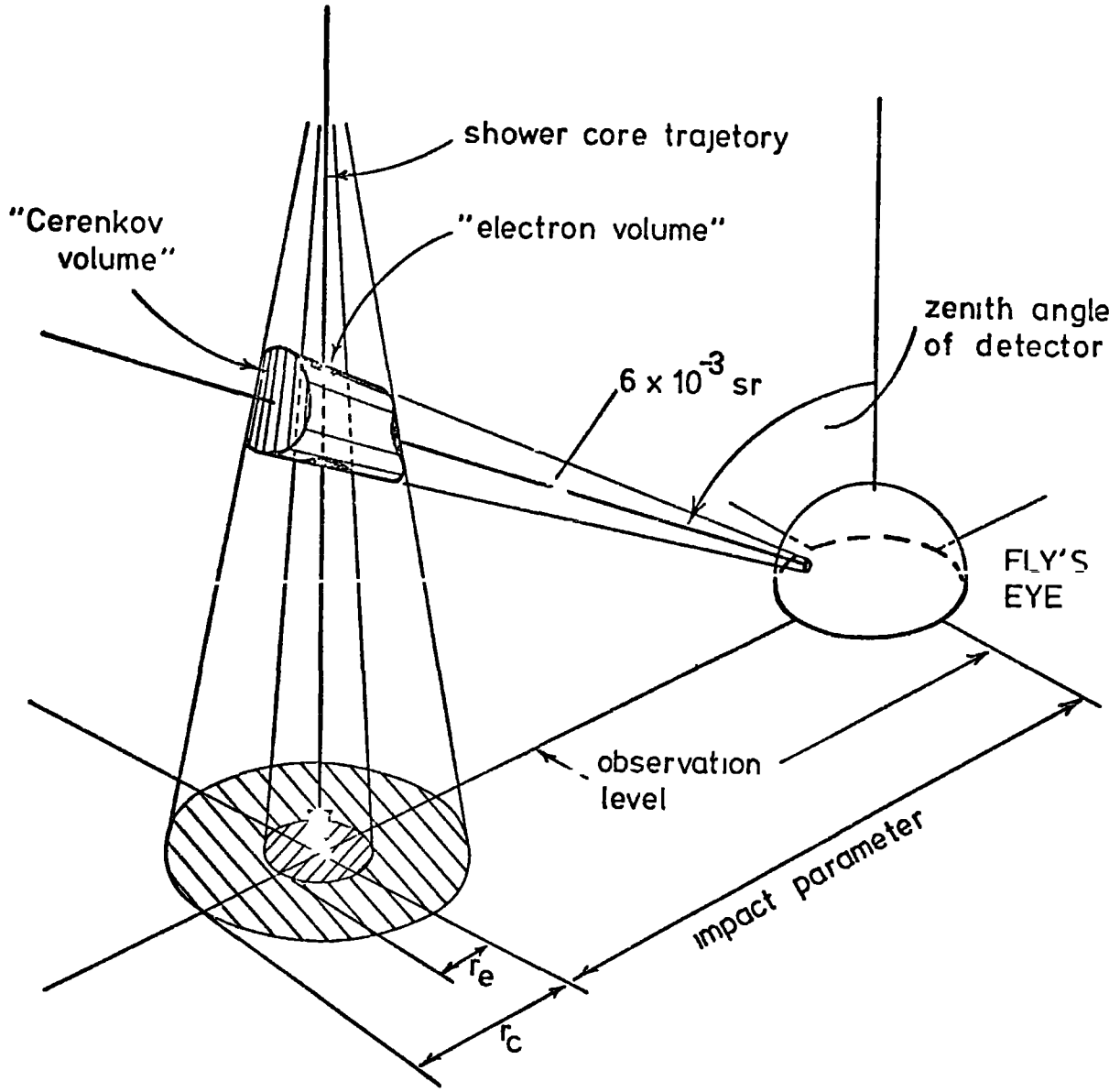

FIGURE 6-6 The volumes in space from which most fluorescence light received by a detector originates ("electron volume"), and from which most scattered Cerenkov light originates ("Cerenkov volume") are shown schematically. r_e and r_c represent the median electron and Cerenkov photon radii.

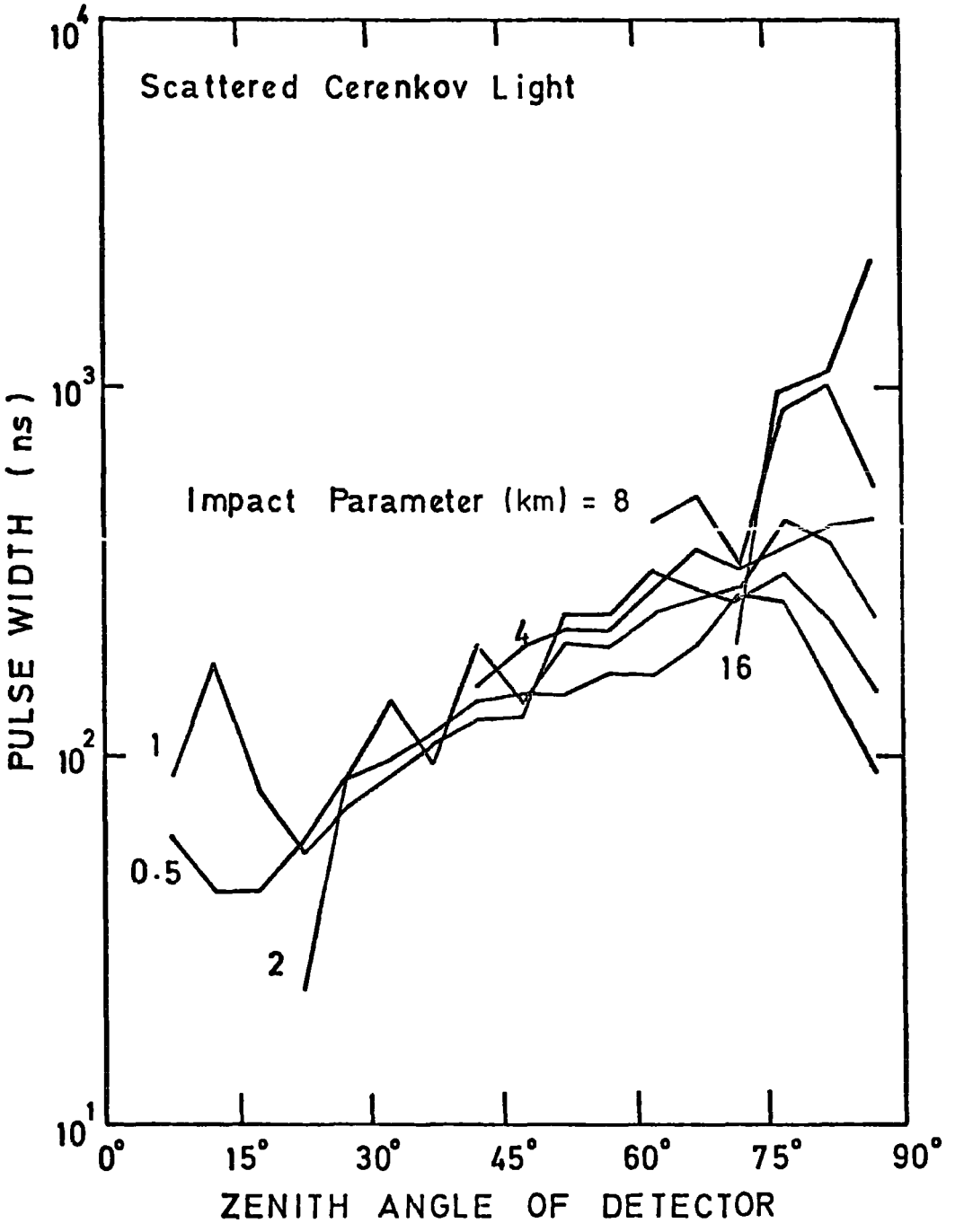

FIGURE 6-7 The width of the scattered Cerenkov light pulse as a function of zenith angle of the detector for various impact parameters.

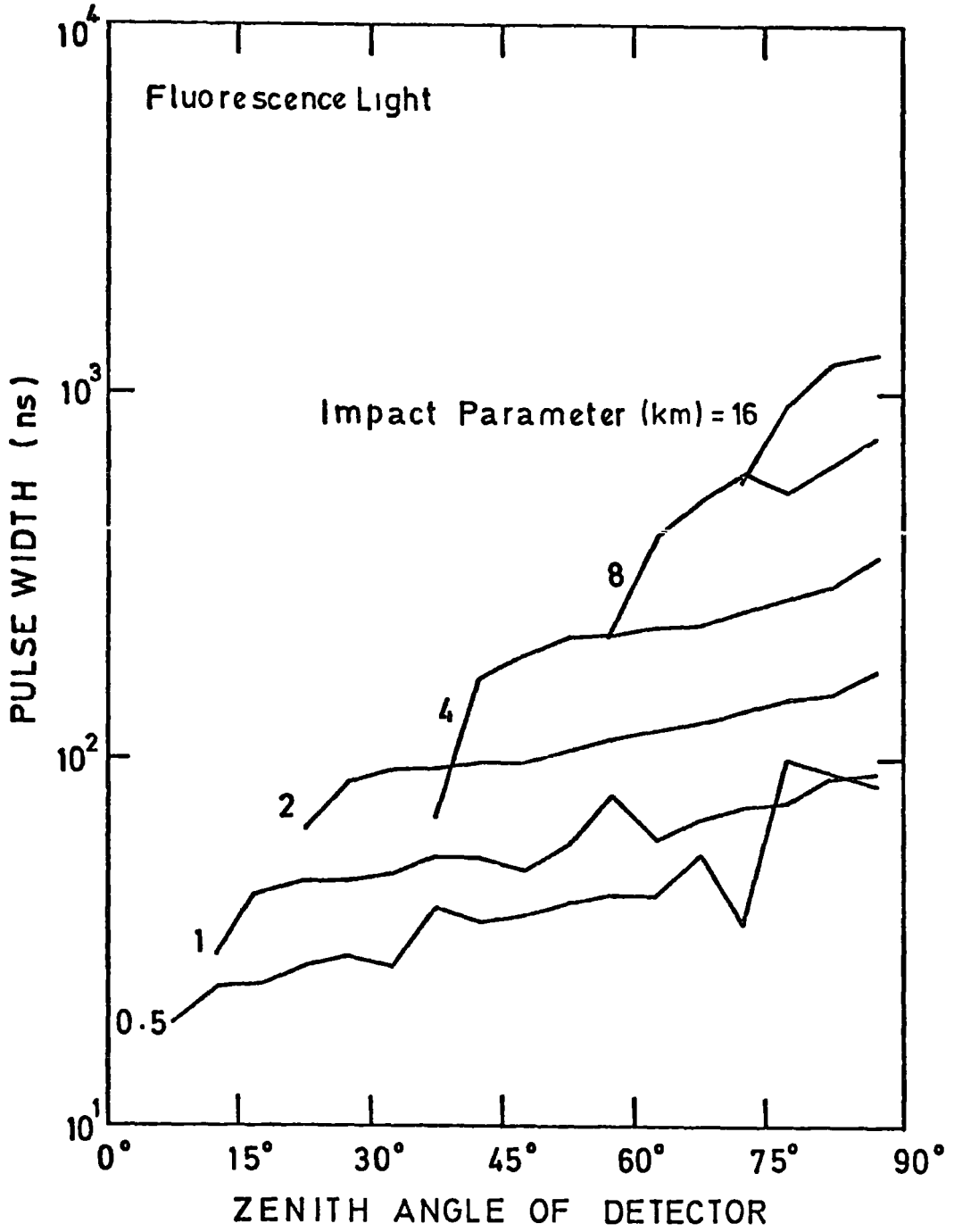

FIGURE 6-8 The width of the fluorescence light pulse as a function of zenith angle of the detector for various impact parameters

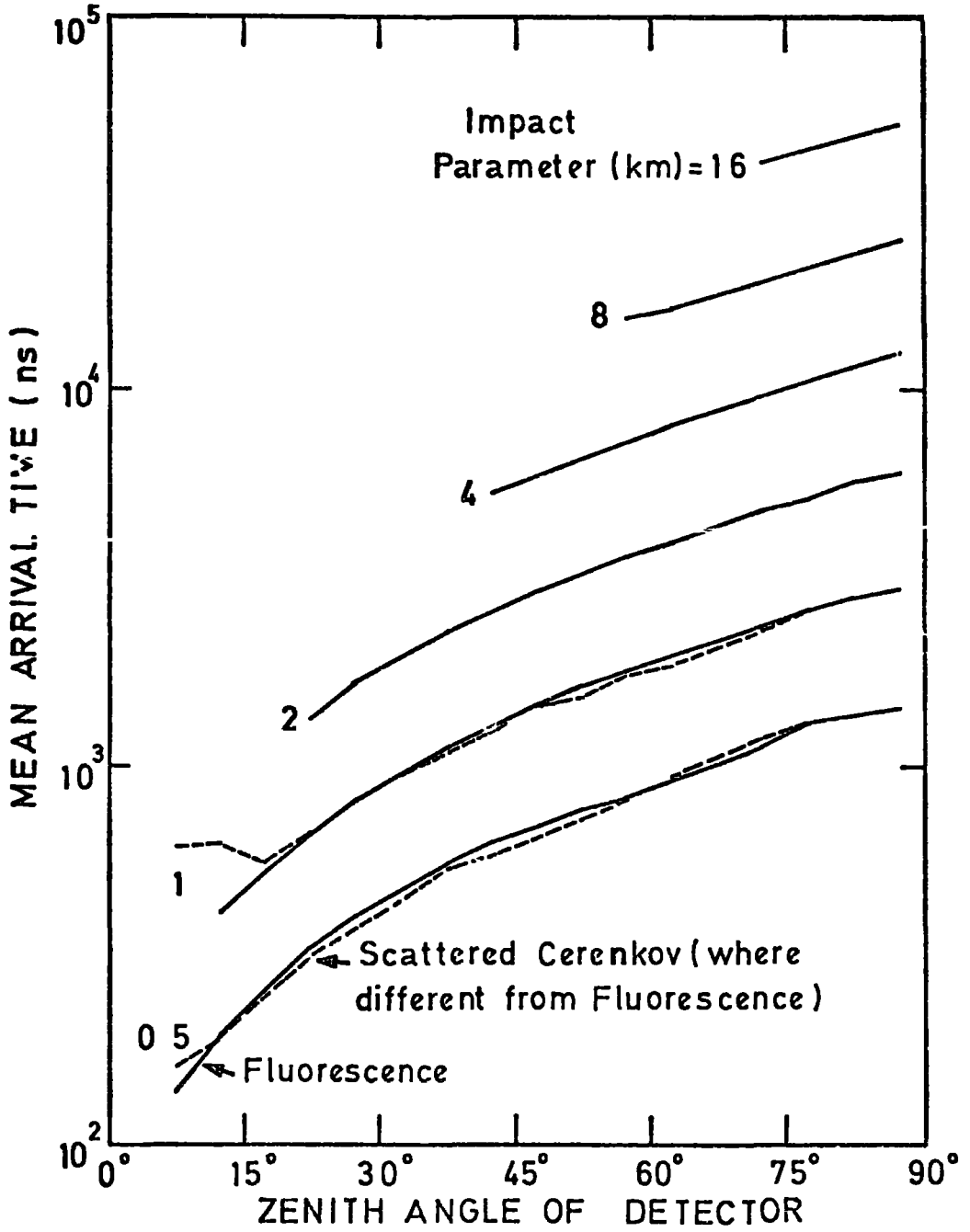

FIGURE 6-9 The mean arrival time of the fluoresence light component and the scattered Cerenkov light component as a function of the zenith angle of the detector for various impact parameters.

emission angles, in good agreement with the calculations of Elbert (1977, private communication).

The analysis of timing information from a Fly's Eye type imaging system to obtain the shower core trajectory should not be impaired by the presence of a Cerenkov light component since the mean arrival time of this component is similar to that of the fluorescence light component. The lateral distribution of the electron component of cosmic ray showers is difficult to study using a conventional ground based array of detectors as the median electron radius is small. Examination of the detailed time structure of pulses from a Fly's Eye type imaging system for showers with large impact parameters (so that fluorescence light dominates the pulse) may form the basis of a new technique to study the lateral spread of the electron component at various stages of development, a subject of contemporary interest (see Hillas and Lapikens (1977) and references therein).

CHAPTER SEVEN

COMPARISON OF AIR SHOWER SIMULATIONS WITH EXPERIMENTAL DATA

INTRODUCTION

The most populous particles in cosmic ray air showers are the electrons, and the growth of the electron cascade is a fundamental characteristic of the air shower. This cascade development depends primarily upon the momentum distribution of the secondary π^o's in energetic N-air and π-air interactions. The cascade shows a growth maximization and decay as the energy of the shower is degraded. The single most useful measure of cascade development is the depth of maximum development of the cascade in the atmosphere. Although the depth of maximum is difficult to observe with most existing experiments, it can be shown to be well correlated with several other shower observables (Dixon and Turver (1974)) and is readily calculable.

The value of the muon content of a shower gives an indication of the energy degradation and the sharing of energy between charged and neutral pions in a cascade. In contrast to the electron cascade, the muon cascade grows and maximizes, but decays only slowly, as a result of the stability of the muon and its small cross section for radiation and pair production. The ratio of muon number to electron number is thus an indication of overall shower development. The data of Kalmykov et al (1975) on $N_\mu - N_e$ dependences have frequently been interpreted as strong evidence against the validity of the scaling concept if a beam of primary protons is assumed, as illustrated by figure 1. Here the calculations refer to showers of fixed primary energy, whereas the measurements are for showers of fixed size. A consequence of this is that the calculated N_μ values are upper limits. As will be explained later, the correct calculation for proton primaries, will be even further from the data, while the curve for iron nucleus primaries will be essentially unaffected. This is demonstrated by the calculation of Vernov et al

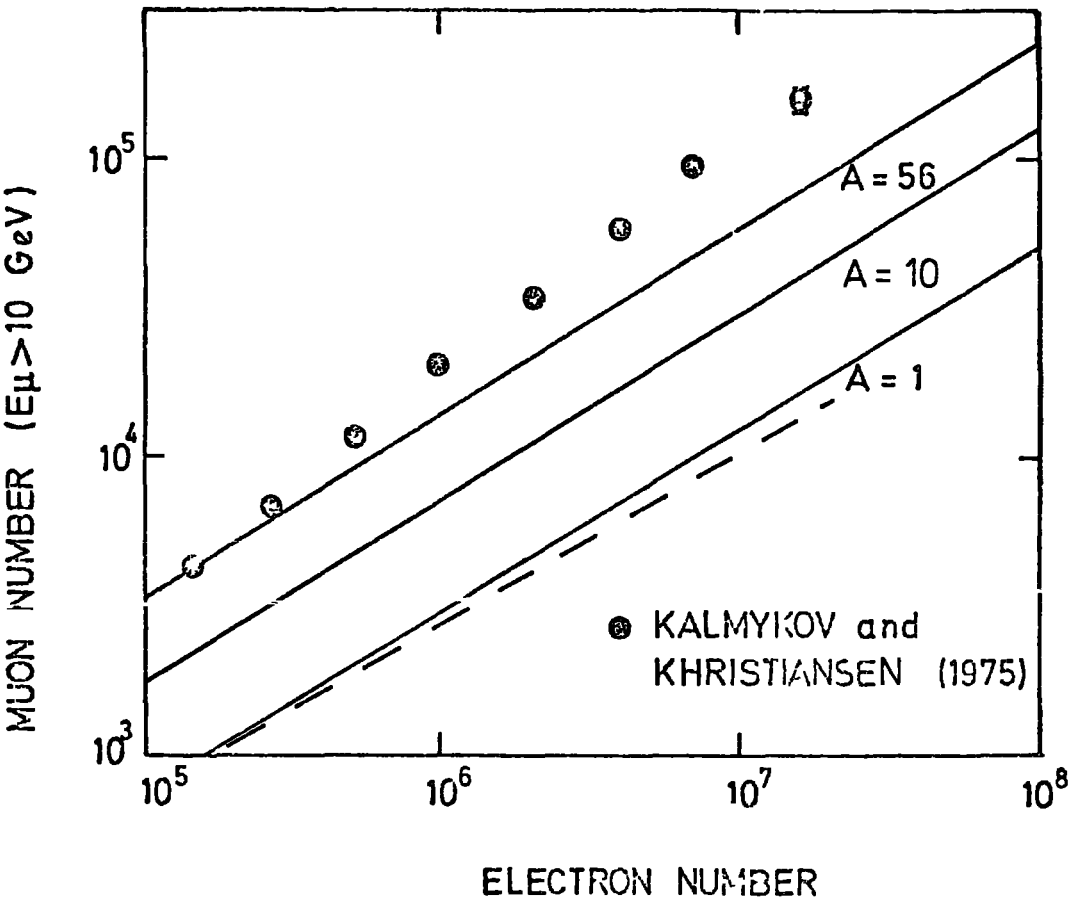

FIGURE 7-1 The experimental variation of muon number (E_μ>10 GeV) with shower size from Kalmykov and Khristiansen (1975) is compared to the results of the present simulations at fixed primary energy for A=1, 10 and 56 as the primary mass number The calculations of Vernov et al (1977) at fixed shower size are also shown for proton primaries (dashed line)

(1974), which is shown by the dashed line in figure 1. This calculation is for scaling and proton primaries, taking into account the fact that the measurements are for showers of fixed N_e rather than for fixed primary energy.

Interpretations to date (e.g., Wdowczyk and Wolfendale (1972), Gaisser and Maurer (1972), Gaisser, Protheroe and Turver (1977)), suggest that the cascades develop with their maxima significantly higher in the atmosphere than can readily be accounted for if the primary particles are protons and the momentum distribution of secondaries follows scaling. This conclusion is illustrated by figure 2 which shows data for depth of maximum compared to the scaling calculations for A=1, A=10 and A=56 as the primary mass number.

We note that these discrepancies may be alleviated by many changes in assumed primary particle mass and/or interaction models which result in a decrease in the depth of maximum of electron cascade of $\backsim$100 g cm^{-2} and many authors (e.g. Wdowczyk and Wolfendale (1972), Barrett et al (1975), Kalmykov et al (1975), Olejniczak et al (1977), Grieder (1977), etc.) have argued that these difficulties are symptomatic of a fundamental change or threshold in the particle physics somewhere between the highest accelerator energies ($\backsim$2 TeV) and EAS energies ($\gtrsim 10^{15}$ eV)

As is illustrated in figures 1 and 2, one such possibility is the assumption of a beam of heavy nuclei as primaries. Thus a fundamental problem with the interpretation of EAS data is to disentangle astrophysical aspects (e.g., composition of cosmic rays) from the particle physics aspects.

It should also be emphasised, however, that neither the average depth of maximum of showers of fixed primary energy, nor the muon content (N_μ/N_e) is a directly measured quantity. Both are inferred from measurements of densities of particles in showers with significant fluctuations from shower to shower in primary energy, in depth of first (and subsequent)

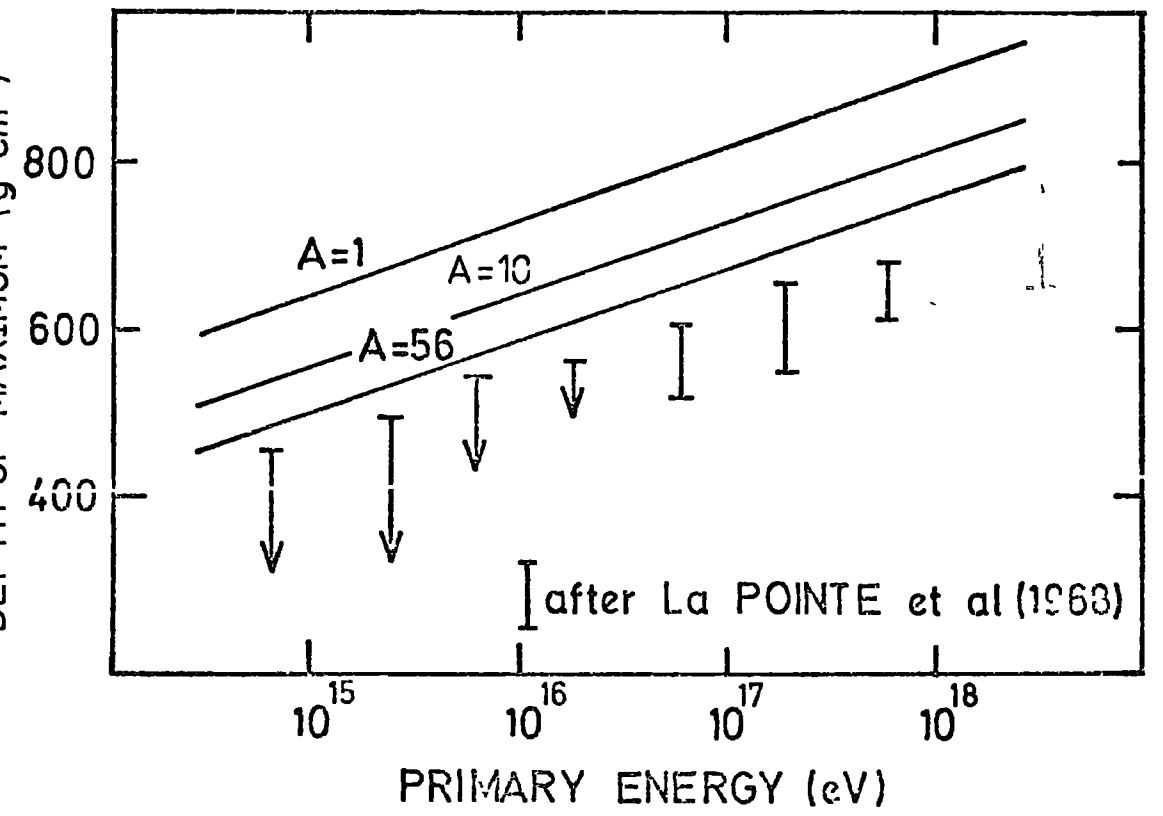

FIGURE 7-2 The variation of the depth of electron cascade maximum with primary energy as estimated from the electron cascade development curves given by La Pointe et al (1968).

interaction, in location of the core relative to the detectors, etc. In these circumstances, the possibility of systematic effects cannot always be ruled out. Such possibilities motivate the attempt here to produce detailed simulation results which are directly comparable to the measured quantities. In this chapter therefore, detailed comparison is made between a broad range of air shower data and the results of computer simulations for proton and iron-nucleus primaries using the scaling model and the constant inelastic cross sections described in chapter 2. Iron is chosen as the nominal heavy nucleus for calculation because it has the highest binding energy per nucleon. Other heavy primaries would lead to similar showers characterised by small fluctuations and early development. Simulation results for A=1 and A=56 are compared with experimental data in the remainder of this chapter since a pure proton composition and a pure iron composition represent two extremes of a feasible primary mass composition.

7-1 INTERPRETATION OF 10^{17} - 10^{18} eV DATA

The first application of the simulations described in previous chapters is to the large showers with primary energy 10^{17} - 10^{18} eV An important characteristic of the data considered, which have been obtained at the Haverah Park air shower experiment, is the consistent estimate of the primary energy which is available for each shower from this well-established array.

7-1.1 The Detection and Recording of Large Showers

The requirement when recording showers for astrophysical studies (e.g. measurements of the primary energy spectra, arrival directions) or energetic interaction studies (e.g. measurements of cascade longitudinal development)is to obtain a sample of the times of arrival and particle densities across the shower front in individual showers. At Haverah

Park this is done using an array of a relatively small number (7) of large area (34 m^2) water Cerenkov detectors (Tennant (1967)). This is in contrast to the procedure e.g. at the Volcano Ranch array (Linsley (1973)) where a large number (79) of small area (1 m^2) scintillation detectors are employed. In the measurements at Haverah Park the arrival direction of the shower is assumed to be the normal to a plane fitted to the arrival times of the signals at widely spaced ($\sim$800 m) detectors. The centre of symmetry (the core) of the shower is found using computer optimization techniques from an assumption that the variation of detector response with distance from the core, the lateral distribution, is monotonic.

The measures of primary energy adopted at the Haverah Park array are the ground parameters $\rho(500)$ and $\rho(600)$, the response of a water Cerenkov detector to shower particles of 500 m and 600 m from the air shower core respectively, and have been described by Edge et al (1973). Since these detectors are sensitive to both the electromagnetic component and the muon component they are calibrated by their response to single muons and $\rho(500)$ and $\rho(600)$ are therefore measured in units of vertical equivalent muons per square metre. The essential reason (first suggested by Hillas et al (1971)) that $\rho(500)$ and $\rho(600)$ are well correlated with primary energy on a shower-by-shower basis (despite fluctuations in the development of individual showers) is that at $\sim$500 m from the core the detector response arises from approximately equal contributions from the electron-photon and muon components. Furthermore, changes in longitudinal cascade development lead to anti-correlated changes in the muon and electromagnetic components.

Some data reported here, e.g. the shape of the water Cerenkov detector structure function, were obtained with the large area detectors

which form the main shower detection facility.

Other data have been recorded by additional types of detector exposed in the "beam" of well measured showers available from the main facility. These additional detectors have included a large area magnet spectrograph for the measurement of the momentum distributions of muons, various muon number density detectors (currently a total sensitive area of 50 m^2 is available) and in recent years an array of 8 air Cerenkov detectors.

The Cerenkov light produced by electron cascades and by muons within the water Cerenkov detectors has been calculated, in order to assign values for $\rho(500)$ and $\rho(600)$ to simulated showers.

The simulations have been tailored to reproduce the conditions appropriate to each observation considered, thus reducing the uncertainties which arise when simulations of a more general nature are compared with specific measurements.

7-1.2 The Muon Component

Measurements have been made at Haverah Park of the lateral distribution of muons of energy greater than 0.3 GeV and 1.0 GeV by Strutt (1976) and Dixon et al (1974) respectively. The measurements were made in showers incident from within 30° of the zenith and of known $\rho(500)$. The data are reduced to refer to showers from the zenith. In the experiments, consideration was given to the effects of detector saturation (occurring when the detector is close to the core) and in the simulations the effects of core mislocation have been considered. Both of these features are known to cause distortion of the structure function. The data from these experiments are shown in figures 3 and 4, where they are compared with the results of the simulations. A satisfactory representation is given both of the structure function shape and the absolute muon densities particularly at core distances

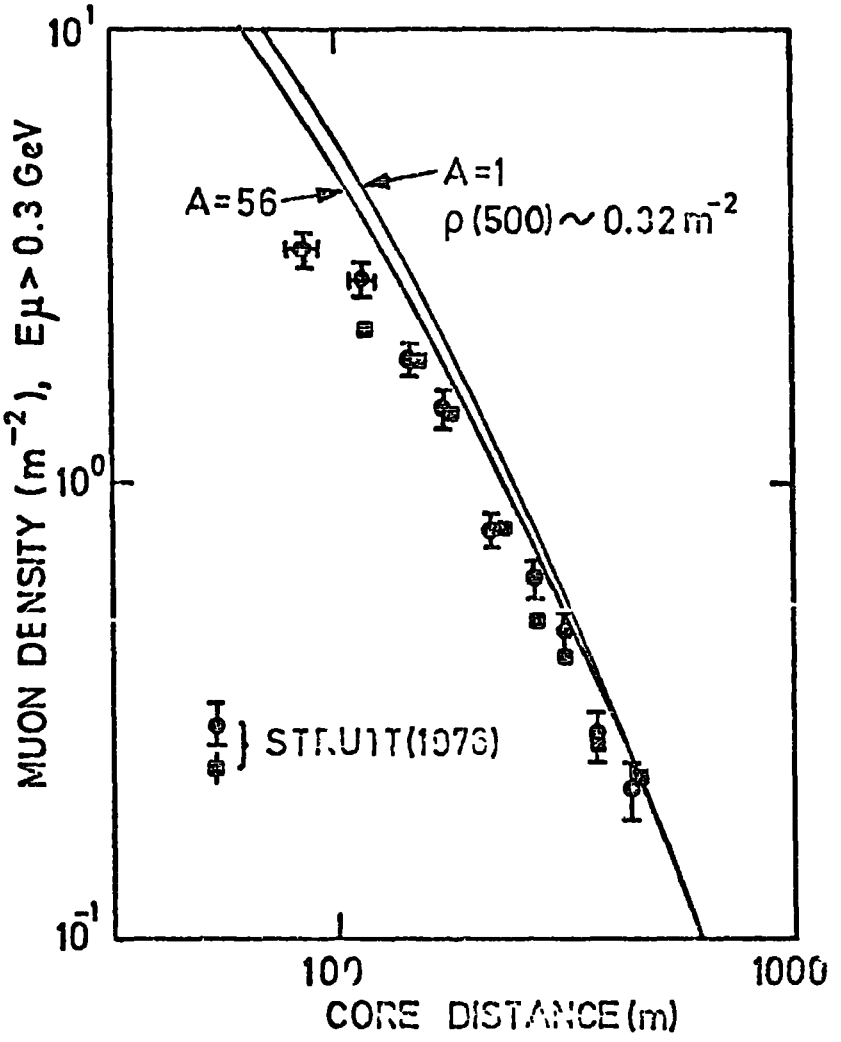

Figure 7-3 The measured lateral distribution of muons with energy greater than 0.3 GeV is compared to the results of simulations at a primary energy corresponding to $\rho(500) = 0.32\ m^{-2}$.

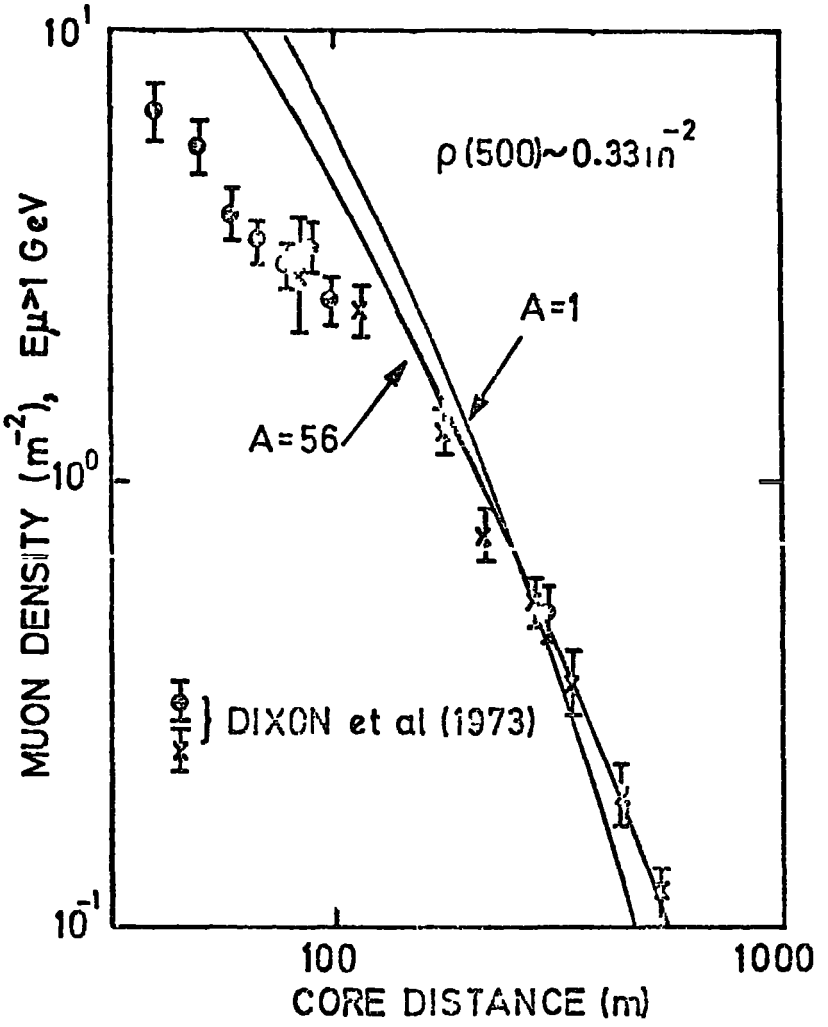

FIGURE 7-4· The measured lateral distribution of muons with energy greater than 1 GeV is compared to the results of simulations at a primary energy corresponding to $\rho(500) = 0.33\ m^{-2}$.

greater than 100 m by the scaling model with proton and iron nucleus primaries. Other models of particle physics give similar representations of the data. No marked sensitivity to primary mass is observed, although if the scaling model is accepted then the broader lateral distribution resulting from heavy primary nuclei is preferred. At core distances less than 100 m, the fit of the simulated structure function to the observations is less satisfactory. This may be a consequence of inadequate allowance for core mislocation effects (which have their maximum effect flattening the structure function near the core) or, in the case of the 1 GeV threshold data, of inaccurate normalization of measurements (data at distances less than and greater than 100 m were obtained in separate experiments). This difficulty at small core distances is shared with other models.

The differential momentum spectra of muons at 300 m and 500 m from the shower core have been measured using a magnet spectrograph by Dixon et al (1974). The spectra measured in showers incident at less than 30^{o} from the zenith are shown in figure 5 and are compared with the results of the present simulations using the scaling model with proton and iron nucleus primaries for vertical showers. In particular, greater significance should be attached to the shape of the spectrum as the absolute densities are based directly on the measurements already discussed above. The measurements in non-vertical showers will account for some of the deficiency in low momentum muons. The shape at both core distances predicted for proton primaries is, however, much too steep.

The heights of origin of muons (reduced to a common detector momentum threshold of 0 3 GeV/c) in large showers have been summarised by Earnshaw et al (1973). These heights, which were derived from the spatial and temporal distribution of muons and the geomagnetic distortion

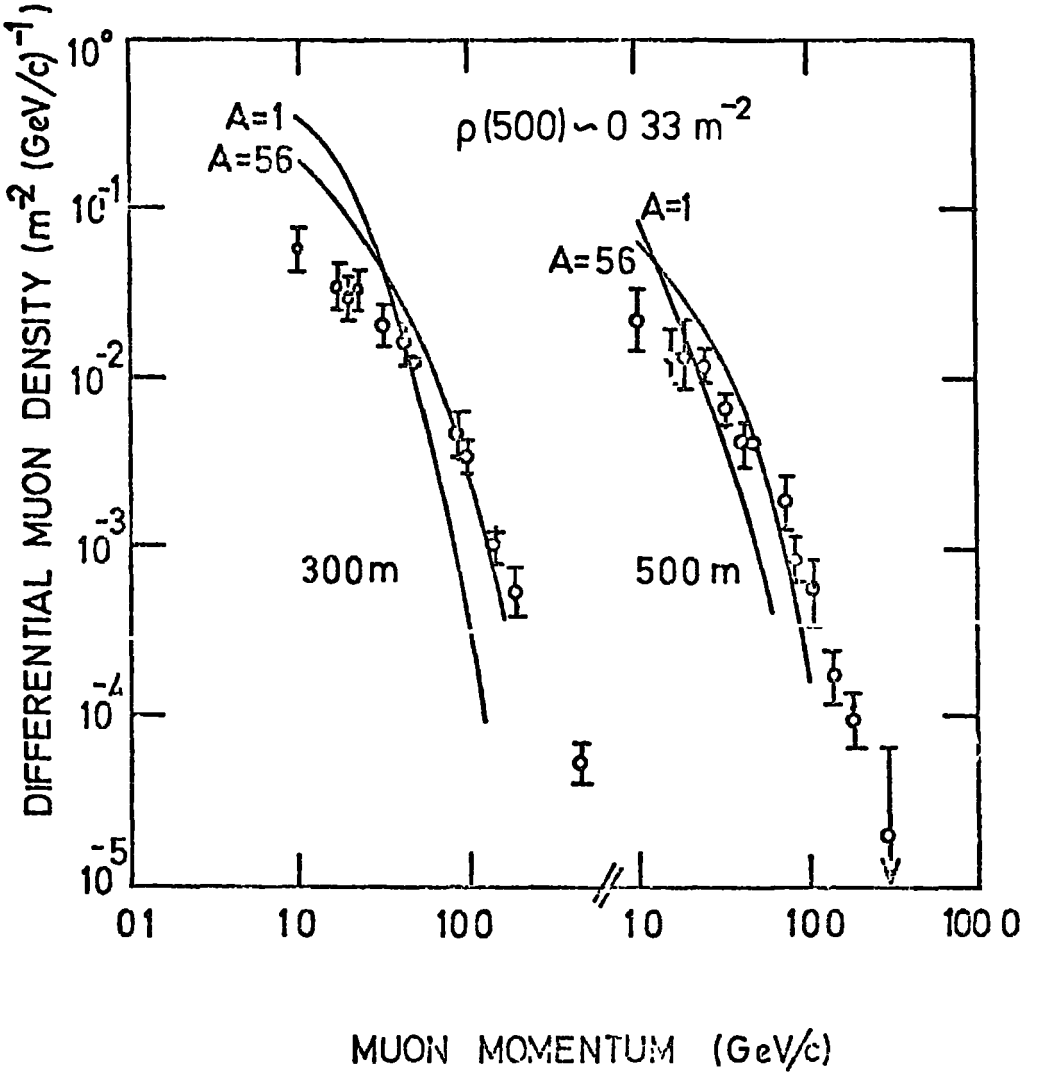

FIGURE 7-5. The momentum spectrum of muons at 300 m and 500 m from the core given by Dixon et al (1974) are compared to the results of simulations at a primary energy corresponding to $\rho(500) = 0.33\ m^{-2}$.

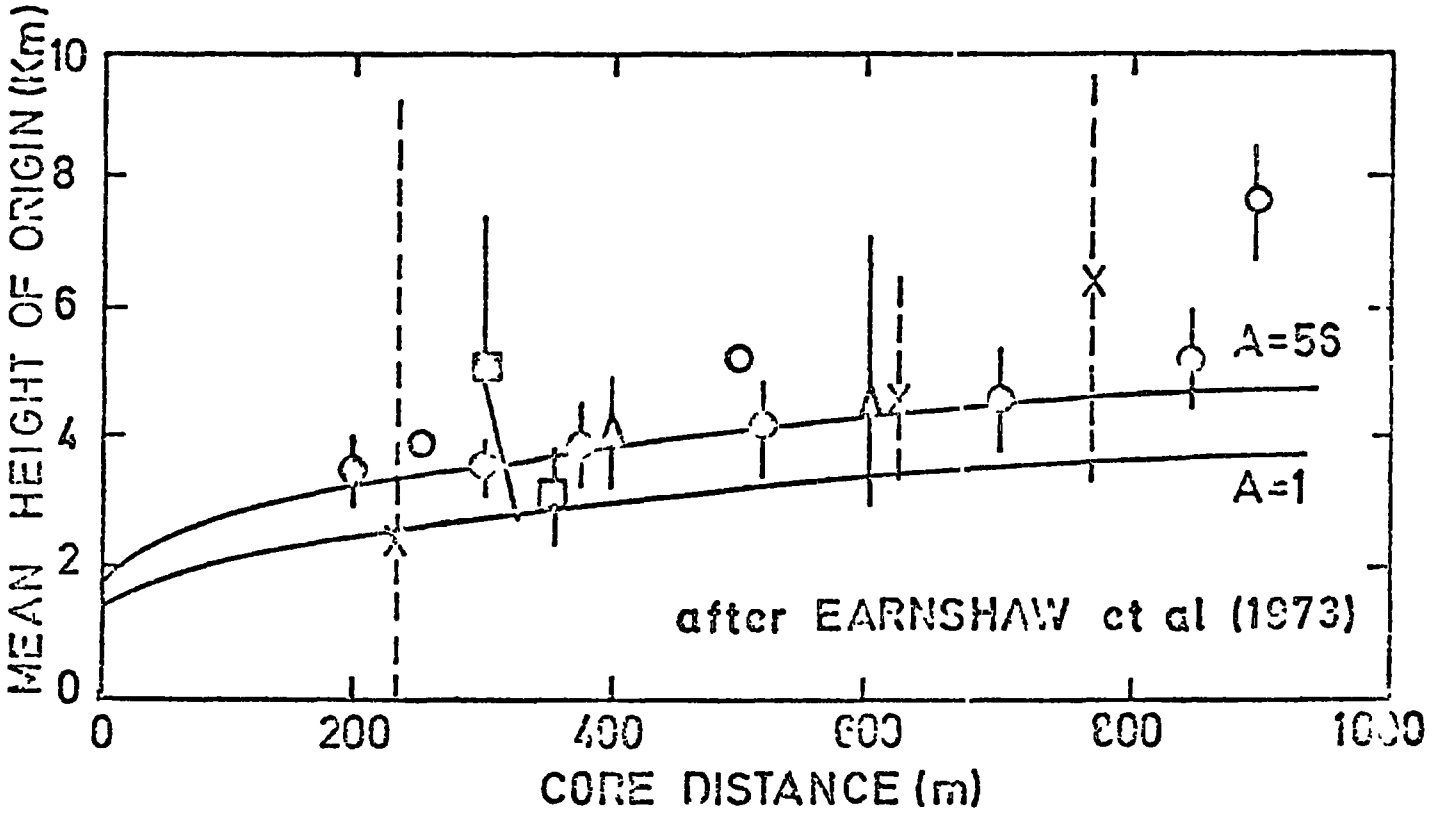

FIGURE 7-6 The mean height of origin of muons of momenta greater than 0.3 GeV/c in showers of primary energy $\sim 10^{17}$ eV as a function of core distance from Earnshaw et al (1973) are compared to the results of the present simulations.

of the muon charge ratio in a number of experiments, are shown in figure 6. The simulation results using scaling with iron nucleus primaries are found to be in good agreement with the data.

7-1.3 Atmospheric Cerenkov radiation

A large proportion of the electrons in showers are sufficiently energetic to emit visible Cerenkov radiation in the air and recently, measurement of the photon flux at large core distances in high energy showers has become popular. Such visibile photons, primarily from atmospheric Cerenkov radiation, are the most numerous component at all core distances in large showers. The information carried by these photons is derived from all electrons in the shower, thus the signal relates to the primary energy and mirrors the development of the shower (see chapter 5).

The lateral distribution of the total Cerenkov light signal in near vertical showers of known primary energy estimate $\rho(500)$ has been measured by Hammond et al (1977). The measurement and calculation of the absolute photon flux is demanding, and greater significance should be given to the shape of the function than to absolute fluxes. A comparison is made in figure 7 between the data of Hammond et al and the present work which is normalized to the lower energy shower data at 200 m from the core.

The potential of the light pulse shape as an indicator of cascade development was suggested by Boley (1964) and measurements were initiated by Efimov et al (1973) and have been fully exploited by Hammond et al (1977a). The average pulse shape can be representated by the rise and fall times and the FWHM at known core distances, which are shown in figures 8, 9 and 10. The response of the detectors of the type used by Hammond et al has been allowed for in the calculations, and again the

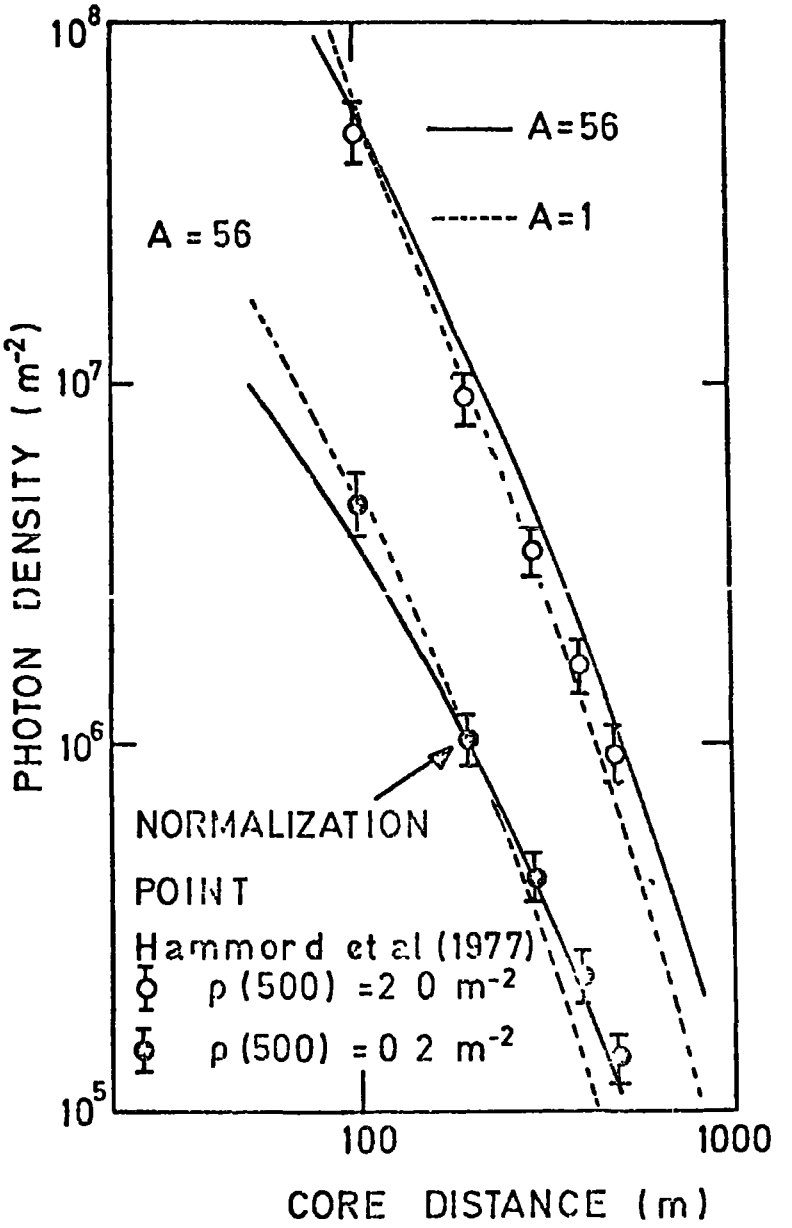

FIGURE 7-7 The average lateral distribution function for air Cerenkov radiation in showers having values of the Haverah Park ground parameter 0.2 and 2.0 m^{-2}.

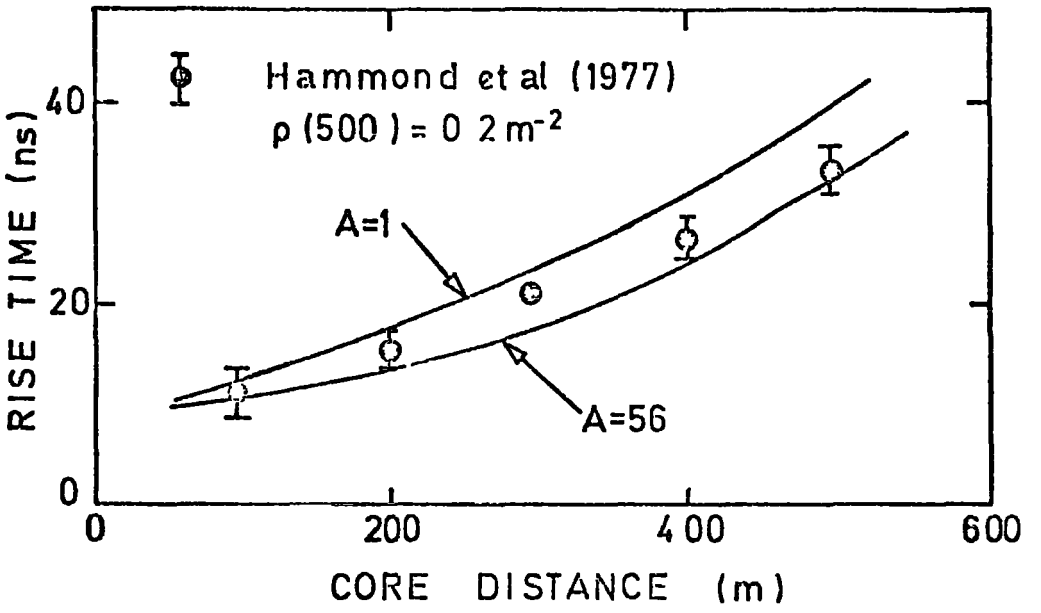

FIGURE 7-8 The average rise time of the air Cerenkov pulses recorded at various core distances in showers having Haverah Park ground parameter $\rho(500) = 0.2\ m^{-2}$.

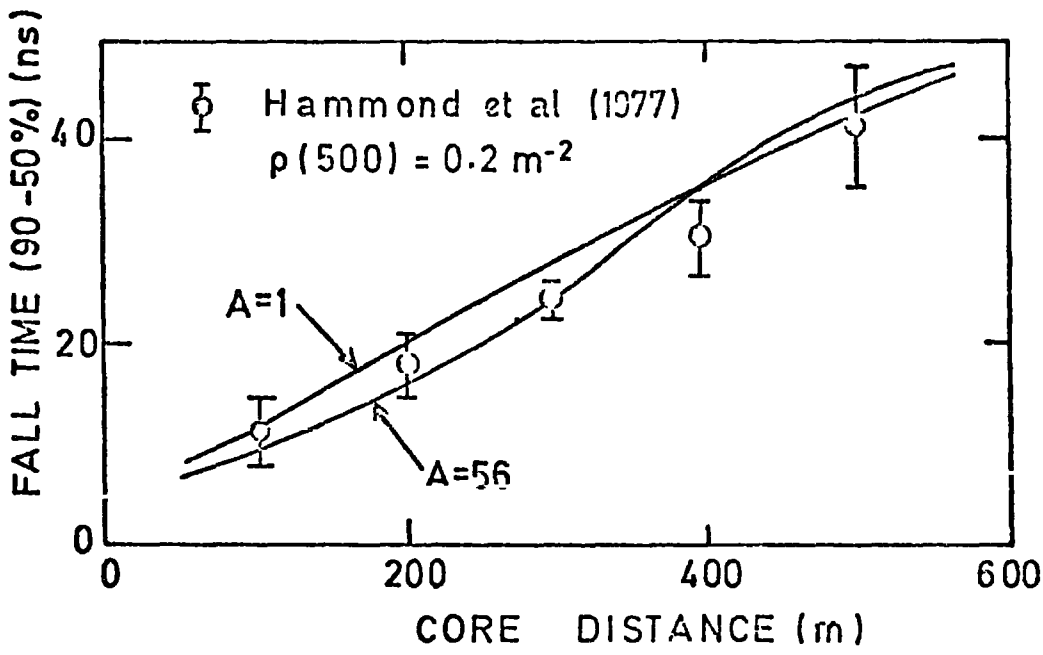

FIGURE 7-9· The average fall times of the air Cerenkov pulses recorded at various distances in showers having Haverah Park ground parameter $\rho(500) = 0.2\ m^{-2}$.

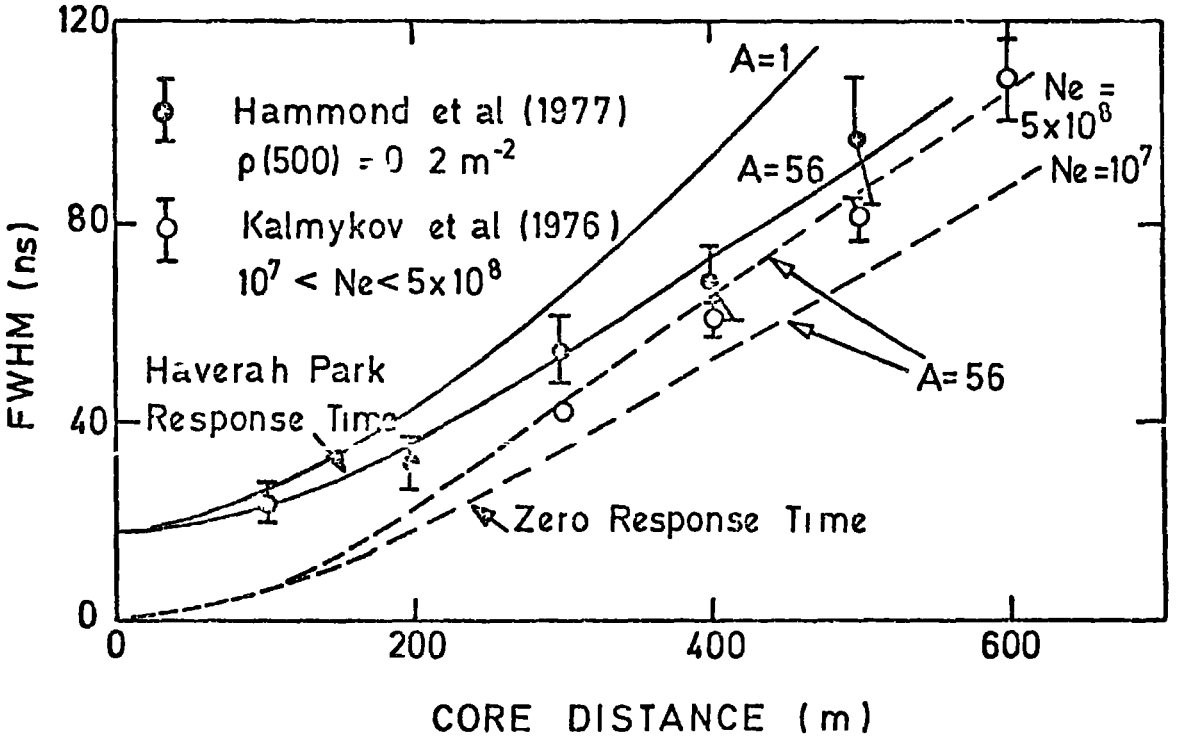

FIGURE 7-10· The average full width at half maximum of the air Cerenkov pulses as a function of core distance measured at Haverah Park with $\rho(500) = 0.2\ m^{-2}$ (Hammond et al) and the Yakutsk array (Kalmykov et al), for showers of size $10^7 < N_e < 5 \times 10^8$ are compared with the results of the present simulations.

predictions of the scaling model fit the data for the rising and falling edges of the pulse adequately, independent of the primary mass. For FWHM, however, the data of Hammond et al show a preference for the earlier cascade development appropriate to heavy primary nuclei. The sensitivity arises from the changing width of the pulse near the peak.

The data on FWHM of the pulse reported recently by Kalmykov et al (1976) are also shown in figure 10. When it is noted that these authors have corrected their data for the effects of the bandwidth of their detectors, their data are also seen to be well represented by the present simulations (iron nucleus primaries)for a detector with zero response time. Here the predictions, indicated by broken lines, are for showers with electron number ranging from 10^7 to 5×10^8, to be consistent with the measurements. This is in agreement with the authors own interpretation (Kalmykov et al (1977)). Measurements of the shape of the Cerenkov light pulse, requiring no accurate knowledge of the detector absolute gain (and thus no normalization) provide one of the best tests of models.

The depth of initiation of the electron cascade (and hence the hadron cascade) is reflected by the radius of curvature of the atmospheric Cerenkov light front. This can be well measured without the sampling problems which characterise many measurements of the particle front. When the light front is defined as the time at which 10% of the total light signal has arrived, a radius of curvature for measurements in the range 100 - 500 m from the core of 7.5 ± 0.3 km was observed by Hammond et al (1977a) in a sample of showers of mean $\rho(500) = 0.9$ vert. equiv. muons m^{-2}. The simulations give a corresponding radius of curvature of 7.1 km for proton primaries and 8.2 km for iron nucleus primaries.

7-1.4 Lateral distribution of electrons

Measurements of the lateral distribution of electrons have been made

by Towers (1971), Armitage (1973) and Strutt (1976) at sea level at Haverah Park for showers of fixed ρ(500) using flashtubes and scintillators. Their data are shown in figure 11 where they are compared to the result of the present simulations. The calculated lateral distribution structure function is seen to be steeper than the data, the discrepancy being greatest near the core. This failure to explain satisfactorily the shape of the distribution function for electrons is a persisting problem in the interpretation of shower data. The problem is not confined to these measurements (see e.g. Hillas et al (1971)).

The review of data by Atrashkevich et al (1977) provides detailed information on the lateral distribution of all charged particles for showers of fixed N_e. Unfortunately, calculations of lateral distributions in showers of fixed N_e are not available from the present work.

7-1.5 The Haverah Park water Cerenkov detector response

The large area water Cerenkov particle detectors are unique to the Haverah Park array and have been extensively studied over the years (see e.g. Edge et al (1973)). The lateral distribution of the signal recorded by these detectors (a complicated combination of the electron-photon and muon fluxes) is now well known. The structure function of an average shower of $\rho(500) = 1.0\ m^{-2}$ is shown in figure 12, where it is compared to the result of the simulations for an iron nucleus primary and a proton primary with energies giving the same ρ(500). A further measure of the shape which has been employed at the Haverah Park experiment, particularly for the investigation of fluctuations, is B(100), the ratio of the signal at 100 m to that at 600 m from the core. The mean value according to Edge (1976), for such a shower is 145, compared with a predicted value of ∽450 for iron nucleus initiated showers and ∽600 for proton initiated showers from the present simulations.

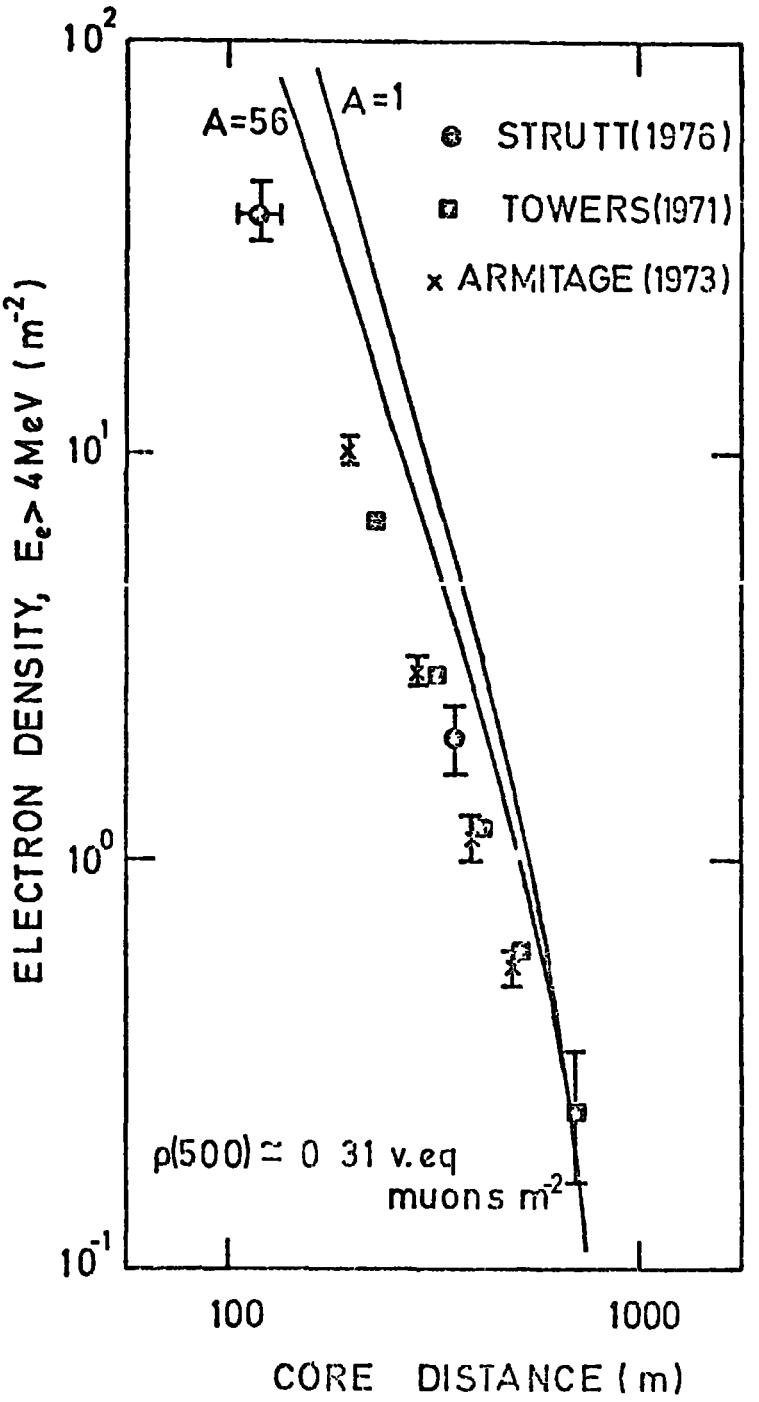

FIGURE 7-11 The measured lateral distribution of electrons is compared to the results of simulations at a primary energy corresponding to $\rho(500) = 0.31\ m^{-2}$.

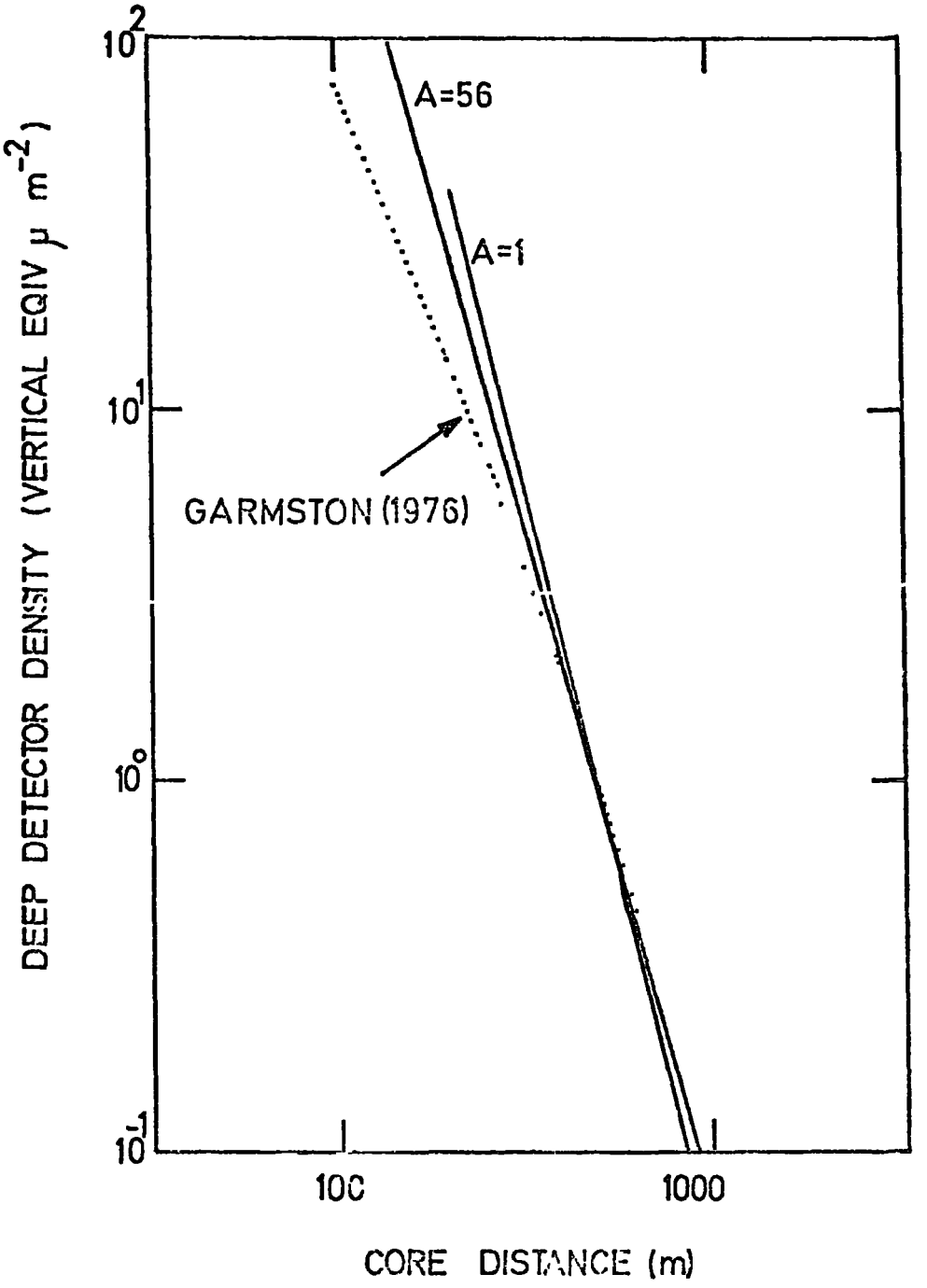

FIGURE 7-12· The average lateral distribution for the response of the Haverah Park water Cerenkov detectors is compared to the results of simulations at a primary energy corresponding to $\rho(500) = 1.0\ m^{-2}$.

A feature of the water Cerenkov detector response for which no simulation results have yet given a satisfactory explanation, is the relative insensitivity of the shape of the structure function to the primary energy of the shower. No evidence exists for any measured change in B(100) with primary energy over ~3 decades in energy (Garmston (1976)). In contrast, calculations with the scaling model indicate a change in B(100) of ~50% per decade around 10^{18} eV, corresponding to a steepening of the lateral distribution as energy increases. A similar steepening is a feature of several calculations based on various models (e.g. Hillas et al (1971), Dixon et al (1974)). Simulations show a strong correlation between depth of shower maximum and the water Cerenkov detector signal near the core but little or no correlation between depth of shower maximum and ρ(600) (Dixon and Turver (1974)). Thus it is possible to attribute the calculated increase of B(100) to the approach of the average depth of shower maximum toward the observation level as shower energy increases.

Conversely, the lack of dependence of the shape of the signal on energy in observed showers would suggest that the average depth of shower maximum does not change with energy in real showers. In contrast to this expectation, Barrett et al (1977) infer from measurements of the rise time of the signal in the water Cerenkov detectors that the depth of shower maximum increases at a rate of 90 $\pm$ 10 g cm^{-2} per decade of primary energy. This apparent conflict between these two measures of shower development should provide a clue to the correct model of particle physics/composition.

Barrett et al (1977) have also inferred the fluctuations in depth of maximum for showers of fixed energy from observations of fluctuations in the rise time of the water Cerenkov detector signal. They obtain an r.m.s. deviation of 70 $\pm$ 10 g cm^{-2} for showers of average primary energy

8×10^{17} eV. According to the authors, such large fluctuations rule out a primary beam of pure heavy nuclei. These fluctuations might arise from an admixture of a few protons in a predominantly heavy beam or from intrinsic fluctuations in proton initiated showers with a high multiplicity model.

A similar result for flutuations in N_μ for showers of fixed N_e is discussed in section 7-2.3.

7-1.6 The ratio of muon density to water Cerenkov detector response

A large area muon sensitive scintillation detector and a water Cerenkov detector (sensitive to muons and the soft, i.e. electron-photon component) are co-located at the centre of the Haverah Park array. The ratio of the response of the two detectors $\rho_\mu(r)/\rho_c(r)$ has been reported by Armitage (1973) and Strutt (1976) for core distances in the range 100 - 500 m. Values of this quantity for showers with $\rho(500)$ in the range 0.32 - 2.18 vertical equivalent muons m^{-2} are shown in figure 13. The response of the array (determined by the trigger and the array geometry) is such that the most probable distance of the core from the centre of the array increases with the primary energy of the shower. Therefore, the dependence of $\rho_\mu(r)/\rho_c(r)$ on core distance calculated for proton and iron nucleus primaries at two primary energies (solid lines) is shown in figure 13 as is the result of an attempt based on the known response of the Haverah Park array to take into account the likely increase of primary energy with core distance for the data (dashed line). The simulations for proton primaries are inconsistent with these data and, although a more satisfactory fit results, there is still some disagreement between simulations with scaling and iron nucleus primaries, particularly near the core. However, the allowance for a systematic change in primary energy with distance clearly demonstrates the sensitivity of the shape of the $\rho_\mu(r)/\rho_c(r)$ plot to the primary energy.

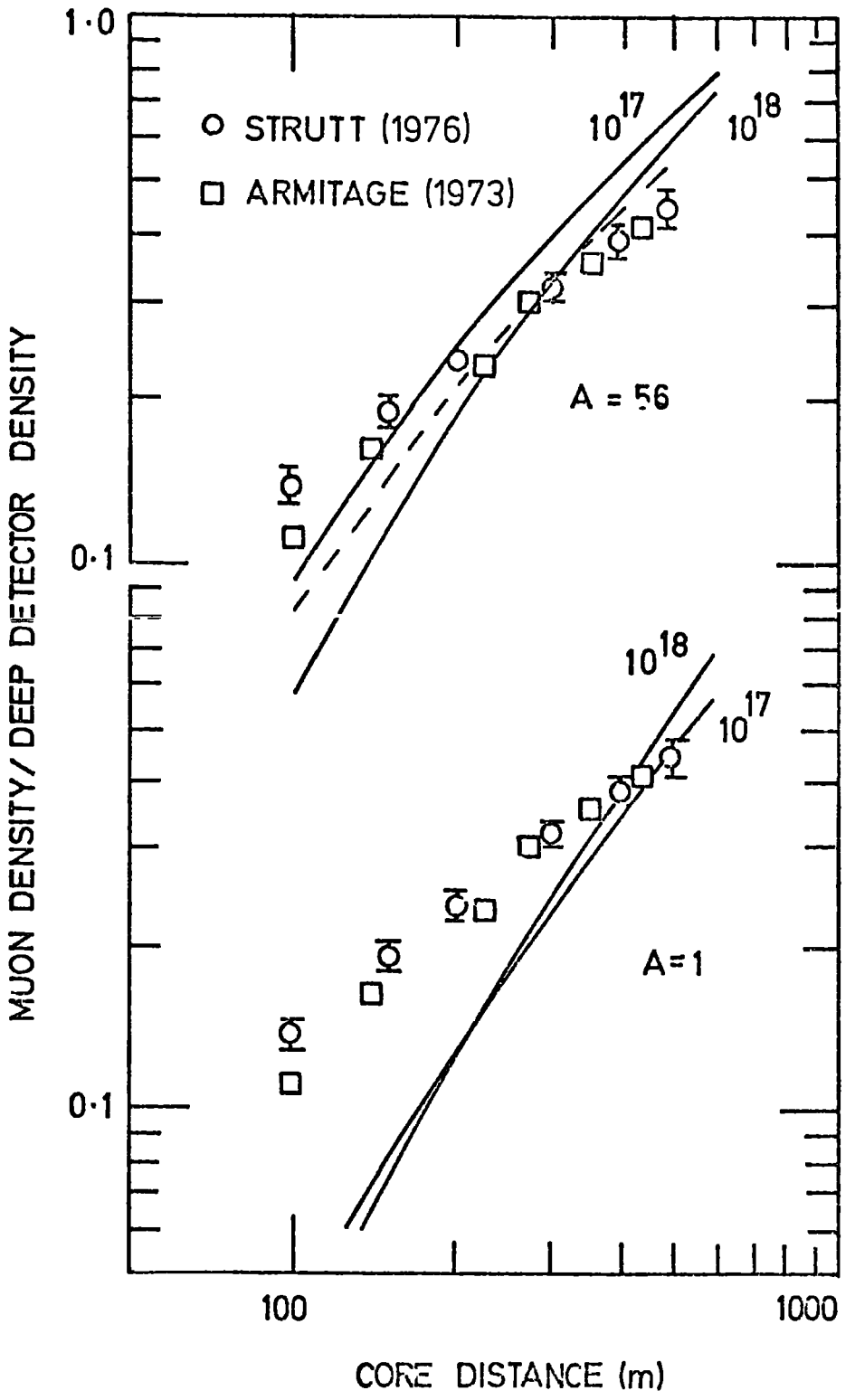

FIGURE 7-13· The average ratio of muon density to Haverah Park water Cerenkov detector response as a function of core distance is compared to the results of simulations. The numbers attached to the curves are the primary energies (eV).

7-2 INTERPRETATION OF SHOWERS AT 10^{15}-10^{17} eV

In the past, tests of scaling based on comparisons of calculated shower development with observational data have been made with showers which range in primary energy roughly from 10^{15} to 10^{17} eV. The tests have been based on average shower development (primarily the electromagnetic component), on the muon content of showers, and on certain (at present restricted) measures of fluctuations in shower properties. In this section the extent to which various primary compositions together with scaling are consistent with EAS data in this energy range will be examined.

7-2.1 Average shower development from the method of constant intensity cuts

The most complete set of data that reflects average shower development in the range 10^{15} - 10^{17} eV is from the Chacaltaya experiment. A revised summary of the data was presented at the Calgary Conference by La Pointe et al (1968), and this has been adopted as the basic data set (see figure 14). Hillas (1975) has summarised most measurements relevant to cascade development and found that the Chacaltaya results are representative and are also the most extensive set of data.

It is important to emphasise that the development curves in figure 14 are not directly observed averages for groups of showers of fixed primary energies, E_o. Because any array must be at a fixed depth in the atmosphere (530 g cm^{-2} in this case) the information about longitudinal development must be obtained indirectly. This has been done by selecting showers incident from different zenith angles (and hence at various atmospheric depths along the shower axis). The showers are grouped in families with the same frequency. Shower development can be obtained in this way for depths ranging from the vertical depth of the array x_o = 530 g cm^{-2} to $x_o \sec \theta_{max}$ (800 - 1200 g cm^{-2} depending here on shower size). If showers at a given rate originate from primaries

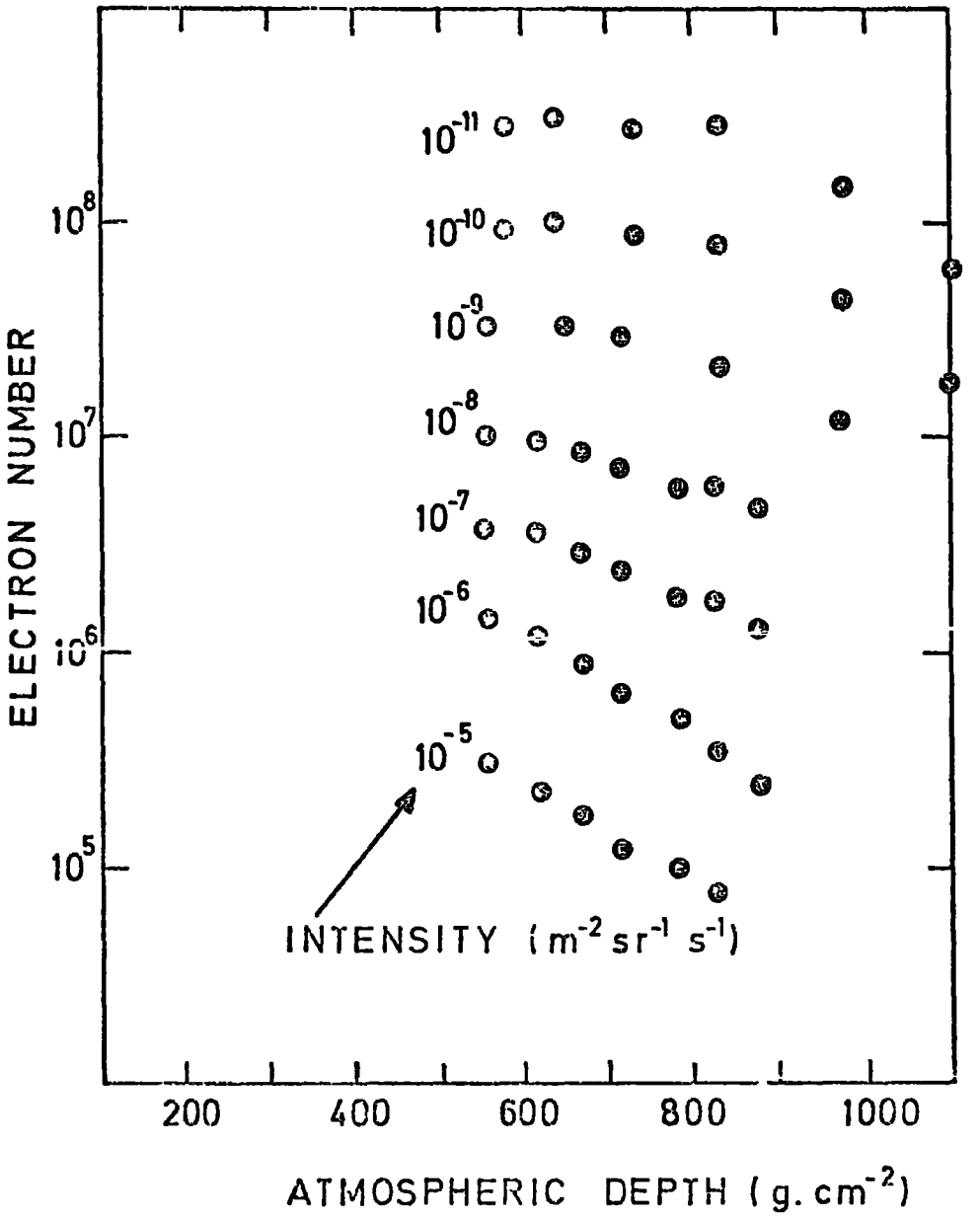

FIGURE 7-14 The longitudinal electron cascade development obtained at the Chacaltaya array using the constant intensity cut method by La Pointe et al (1968).

of similar energy, then the size versus depth curves in figure 14 correspond to the true average development of showers of an energy corresponding to the integral intensity I (m^{-2} s^{-1} sr^{-1}) in the primary spectrum.

Because of fluctuations (for example in depth of shower initiation and in shower development) coupled with the steep primary spectrum, however, this is not the case (Dedenko (1975)). It can be shown (Gaisser and Hillas (1977)) that development curves obtained by the method of constant intensity cuts (as in figure 14) correspond to a good approximation to $N_{r.m.s.}$, rather than to the average size, $\bar{N}$, of showers of fixed primary energy. Gaisser and Hillas find that the maximum of $\bar{N}$ is about 20-40 g cm^{-2} lower in the atmosphere than $N_{r.m.s.}$ It was shown in chapter 3 that the difference between $N_{r.m.s.}$ and $\bar{N}$ is negligible for iron-nucleus primaries.

In view of the preceding discussion, $\bar{N}$ is calculated for showers of fixed primary energy for comparison with the Chacaltaya curves of figure 14. The results are shown in figure 15. The results for iron nucleus primaries are very similar to those first obtained by Gaisser (1974a) under essentially the same assumptions. Each calculated development curve has been normalized at one depth (600 g cm^{-2}). This amounts to assigning an energy to a quoted intensity (and thus calibrating the energy spectrum). The energy assignments obtained are compared in table 1 with those of Hillas (1975). Hillas' energy assignments were made primarly on the basis of considerations of ionization in a rather model-independent fashion. The close similarity between the two results suggests the absence of gross errors in the energetics of the calculation.

The data shown in figure 14 are often characterised by depth of maximum cascade development as a function of primary energy, as shown in figure 2. The maximum is not actually seen for the lower energy cuts in the Chacaltaya data. The only measurement of shower development

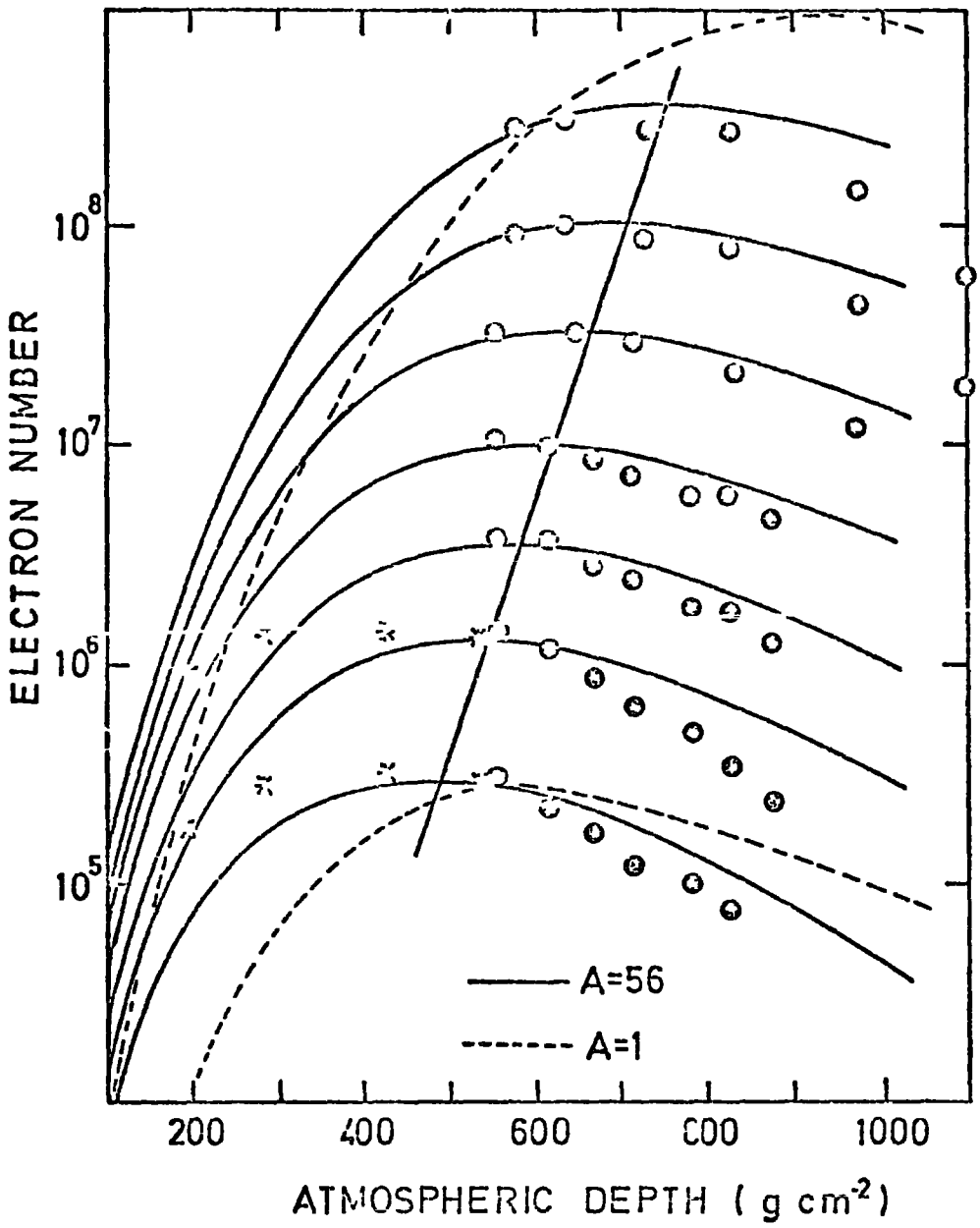

FIGURE 7-15 The longitudinal electron cascade development curves from the present work are compared to experimental development curves obtained by La Pointe et al (1968) (•) and Antonov and Ivanenko (1975) (*).

Integral flux (m^{-2} sr^{-1} s^{-1})	Energy derived from energy deposition by Hillas (eV)	Energy estimate from present work (eV)
10^{-6}	(1.9×10^{15})	(1.8×10^{15})
10^{-7}	5.9×10^{15}	7.5×10^{15}
10^{-8}	1.6×10^{16}	1.9×10^{16}
10^{-9}	5.5×10^{16}	6.5×10^{16}
10^{-10}	1.7×10^{17}	1.9×10^{17}
10^{-11}	5.5×10^{17}	5.5×10^{17}

TABLE 7-1 Energies assigned to the longitudinal development curves obtained in the Chacaltaya experiment

that significantly extends the range of the Chacaltaya measurements is that of Antonov and Ivanenko (1975) and Antonov (1974) who have measured the size spectra of small showers at aeroplane altitudes (200-550 g cm^{-2}), at which depth the showers have barely reached maximum. They have normalised the spectra to the two smallest constant intensity curves as reported by the Chacaltaya group at the London Conference (Bradt et al (1966)), ($I = 10^{-5}$ and $I = 10^{-6}$ m^{-2} s^{-1} sr^{-1}). Their data for these intensities are shown as * in figure 15. Note, however, that the lowest energy point is based upon data which had been deleted from the presentation of the Chacaltaya group at the Calgary Conference in 1967. Assigning depths of maximum and corresponding uncertainties to the constant intensity cut curves is still to some extent a matter of taste. For this reason the locus of the maxima of the computed showers is shown as solid line in figure 15.

Olejn czak et al (1977) have, however, gone further. They have calculated a value for the effective atomic mass A_{eff} from a depth of maximum vs. E_o plot (including Antonov points) by estimating what atomic mass is needed to bring their caclulated depth of maximum down to the observed depth of maximum. They find a lower limit of A = 200. Such a calculation, however, involves exponentiating all the uncertainty and error (including use of calculated $\bar{N}$ rather than $N_{r.m.s.}$) involved in obtaining an estimate of depth of maximum from the data. This can be seen by noting that the calculated value of x_{max} for a nucleus of mass A is approximately given by

$$x_{max} = C + B \ln (E_o/A) \qquad 1$$

Then A_{eff} is obtained by requiring x_{max} (calculated) = x_{max} (observed) i.e.

$$A_{eff} = E_o \exp \frac{C - x_{max}(\text{observed})}{B} \qquad 2$$

where $B \approx 37$ gm cm^{-2}. It is therefore preferable to compare the results

of a model calculation directly with the data as in figure 15. Doing this, no significant inconsistency is found between the Chacaltaya data and the prediction for scaling and iron primaries, although there appears to be a suggestion that observed showers attenuate more rapidly than calculated ones. The lowest two curves are systematically steeper than the caculation. However, the lowest (10^{-5}) curve is not included in the revised data of La Pointe et al (1968) and Hillas (1975) has noted previously that the next (10^{-6}) development curve may be anomalous and cannot be represented by a physical model.

Another way of presenting what is essentially the same data is to tabulate $N_{max}/N_{sea\ level}$, as has been done by Wdowczyk (1975). Results derived directly from the data (figure 14) are shown in table 2 where they are compared with results from the present simulations and the estimates made by Wdowczyk from the composite development curves of Antonov and Ivanenko (1975). The latter were obtained by normalising the aeroplane experiments (Antonov and Ivanenko (1973) and Antonov (1974)) to the first presentation at the London Conference of the Chacaltaya data (Bradt et al (1966)), including the cut at 10^{-5} m^{-2} s^{-1} sr^{-1}, which was not reported in the revised data presented at Calgary (La Pointe et al (1968)). Again, scaling with proton primaries is clearly ruled out by all considerations, but calculations for iron-nucleus primaries with scaling give a good account of this feature of shower development (except possibly at the lowest energies) as should be expected from the satisfactory agreement shown in figure 15.

7-2.2 Measurements of muon densities

It was shown in chapters 3 and 4 that the muon and electron longtiduinal development are fundamentally different the muon component grows to a plateau in N_μ and then the number of muons declines rather slowly. In contrast, N_e grows to a maximum then dies away rather rapidly (see, for

Integral flux (m^{-2} sr^{-1} s^{-1})	$N_{max}/N_{s.l.}$			
	Chacaltaya data	Calculations Fe	p	Wdowczyk (1975)
10^{-5}		7.36	3.57	12
10^{-6}	13	4.82	2.16	10
10^{-7}	4.7	3.57	1.73	6.3
10^{-8}	3.5	2.70	1.45	4.3
10^{-9}	3.2	2.23	1.21	3.4
10^{-10}	2.9	1.83	1.10	
10^{-11}	2.6	1.67	1.05	

TABLE 7-2 Calculated values of shower size at maximum to size at sea level $N_{max}/N_{s.l}$ are compared to estimates based on the Chacaltaya data (La Pointe et al (1968)) and estimates by Wdowczyk (1975) based on the development curves of Antonov and Ivanenko (1975).

example, figure 5 of chapter 1). Since showers in the range 10^{15} - 10^{17} eV are generally observed at sea level and are well past maximum, this means that N_μ/N_e (see figure 2) is in principle a sensitive measure of average longitudinal development and of fluctuations in development. However, because of the large and correlated fluctuations, it is essential to be quite clear about what is actually measured.

Typical measurements of the muon flux in EAS are made with one (or at best a few) muon detectors of several tens of m^2 total area in conjunction with an array of many detectors that measure primarily the soft component. Thus, what is often measured is the muon density at a particular distance (or distances) from the shower core. For each shower the core is located by fitting the densities in the electron detectors to a semi-empirical lateral distribution, which at the same time defines N_e for the shower. Showers are then binned by N_e and a lateral distribution is built up from measurements of $\rho_\mu(r)$ at various core distances, r, in many showers in the same size bin. In this way an average muon lateral distribution characteristic of showers in a given size range is constructed.

7-2.3 Comparison with calculations of lateral distributions

The results of such an analysis for showers of size 10^5 - 10^6 (nominal size 2×10^5), 10^7 - 5×10^7 (nominal size 2×10^7) and $\gtrsim10^5$ (nominal size 4.5×10^5) and for muons with $E_\mu > 10$ GeV are shown in figure 16 (Khristiansen et al (1971)). The result of a similar analysis for showers of size $\gtrsim 3.16 \times 10^4$ normalised to $N = 10^6$ and for muons with $E_\mu > 2$ GeV is shown in figure 17 (Staubert et al (1969)). As has already been seen (figure 1), scaling completely fails to explain the relatively high abundance of muons if the primaries are all or mostly protons. The solid lines in figures 16 and 17 show calculations with a

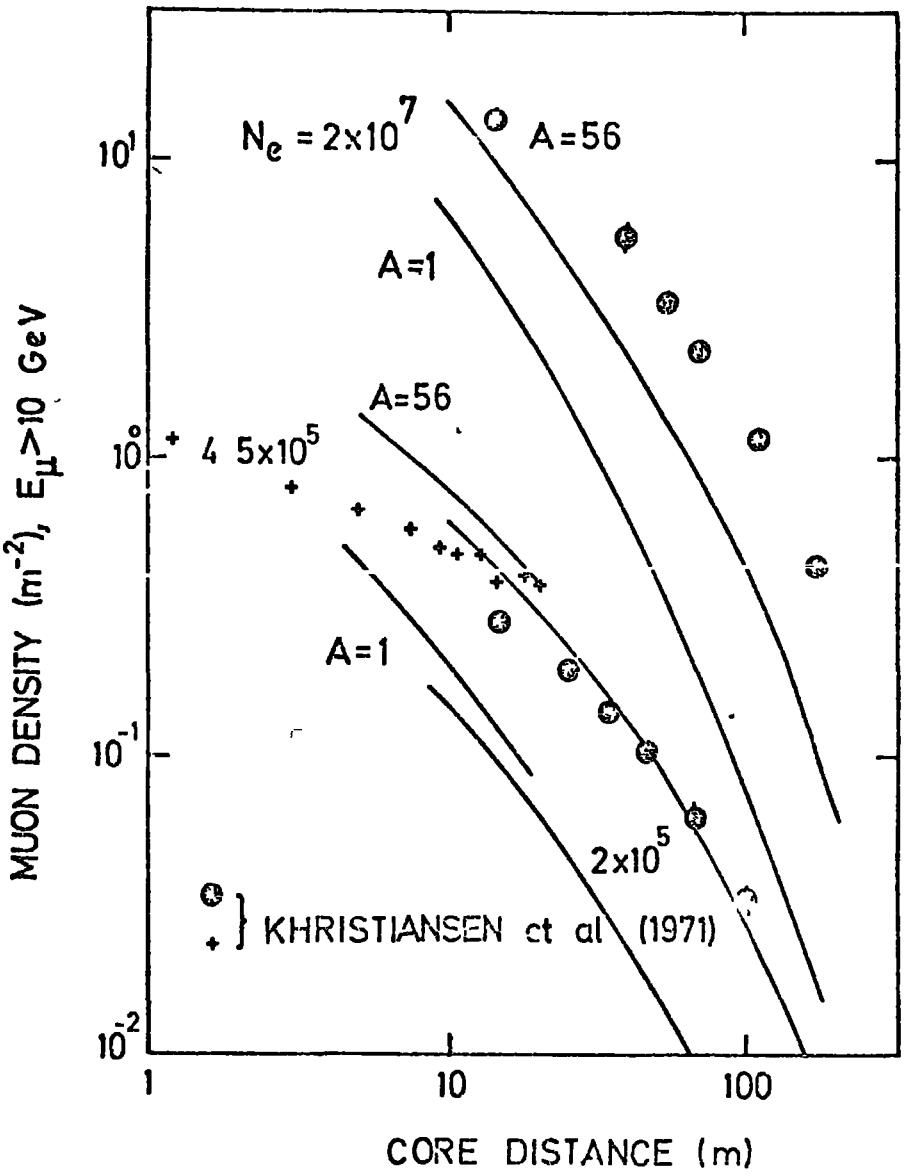

FIGURE 7-16 The measured lateral distribution of muons with energy greater than 10 GeV is compared to the results of simulations at primary energies corresponding to $N_e = 2 \times 10^5$ and $N_e = 2 \times 10^7$.

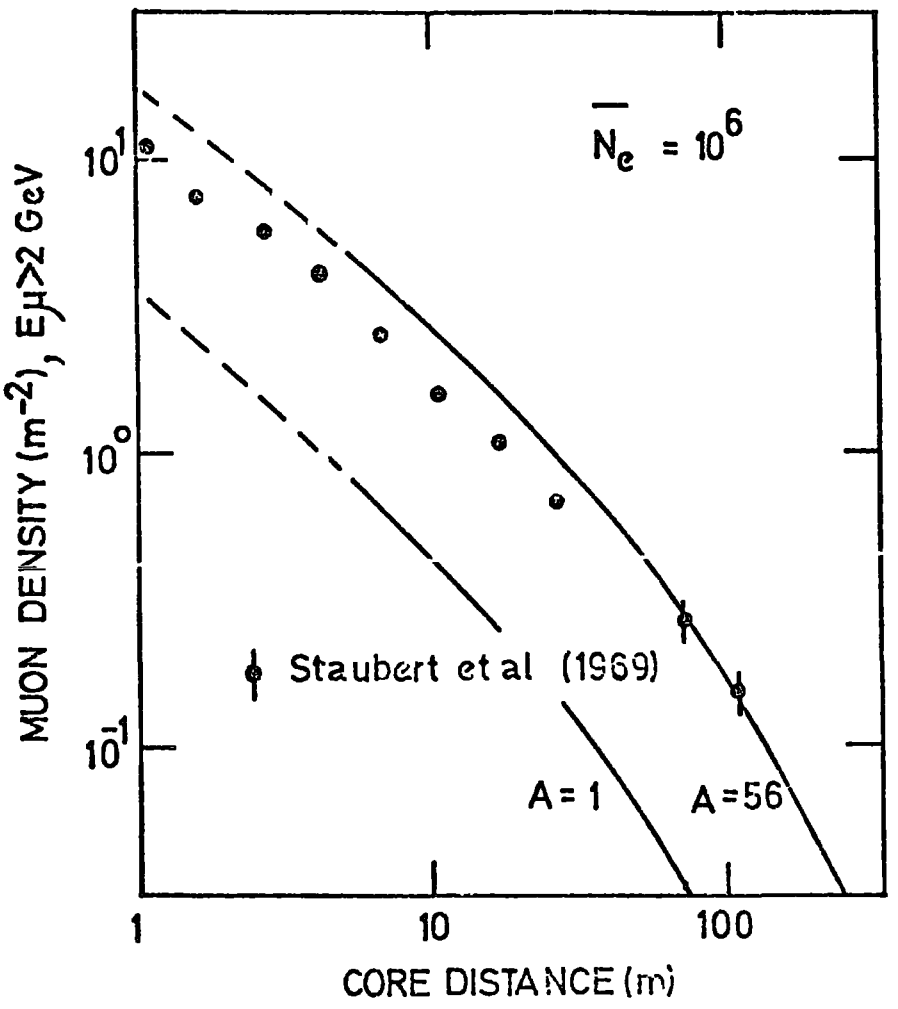

FIGURE 7-17 The measured lateral distribution of muons with energy greater than 2 GeV is compared to the result of simulations at a primary energy corresponding to $\overline{N}_e = 10^6$.

scaling model assuming both proton and iron nucleus primaries. The scaling model with iron primaries is seen to be able to account for the data, the shape of the lateral distribution being in better agreement near the core with the data of Staubert et al who suggest that the observed flattening of lateral distributions near the core in other experiments is probably due to an underestimation of core location errors Analogous quantities at 10^{17} - 10^{18} eV are compared to the predictions of the same model in figures 3 and 4. It is noted that the threshold energies are different in the four cases.

Because of fluctuations among showers of given E_o, together with a rapidly falling primary spectrum (given by $N_o(>E_o) = E_o^{-\gamma}$, $1.5<\gamma<2$), showers of fixed primary energy have not the same characteristics as showers of fixed N_e. The correct calculation involves assuming a primary spectrum, generating showers with energies chosen randomly from this distribution, binning the results by N_e and then looking at properties of the generated muons. For heavy primaries, fluctuations are small so that it is reasonable to compare muon charactertistics for calculated showers grouped by E_o with data binned by N_e, as has been done in figures 16 and 17. For a mixed composition, however, fluctuations may well be important even if the fraction of protons is small in a given energy bin. This is because selection of showers of given N_e at a certain depth favours deeply penetrating proton showers of relatively low primary energy.

7-2.4 Total Muon number

It is traditional to define a total integral number of muons for each shower, N_μ ($>E_\mu$), by using the average distribution function described above to assign a total N_μ to each measured $\rho_\mu(r)$. In Khristiansen et al (1971) this is done by scaling the measured ρ up or down in energy to one of the average lateral distribution curves at $N_e = 2 \times 10^5$ or $N_e = 2 \times 10^7$ according to $N_\mu \propto N_e^{0.78}$. This is the way in which the

N_μ - N_e plot shown earlier (figure 1) was obtained. The best fit to these data is $N_\mu(E_\mu>10$ GeV) $\propto N_e^{0.78}$ in contrast to simulations using the scaling model with proton or iron-nucleus primaries shown in figure 1 which have a power law of N_μ ($E_\mu > 10$ GeV) $\propto N_e^{0.62}$. This same discrepancy is reflected in figure 16 by the fact that the calculated lateral distribution for large showers is somewhat below the data. It is possible that the discrepancy in slope may, to some extent, be alleviated by the effects of fluctuations in the presence of a mixed primary composition, as noted in the next section.

The shape of the calculated integral energy spectrum is shown to be in good agreement with experiment at low primary energies in figure 18 where a compilation of total muon number, $N_\mu(>E_\mu)$, from various experiments at $N_e \approx 10^6$ by Gaisser and Maurer (1972) is given. Also included are recent measurements by Vernov et al (1977).

7-2.5 Fluctuations in muon number at fixed shower size

Even though fluctuations in N_μ for fixed E_o are expected to be relatively small, fluctuations in N_μ for fixed N_e need not be small especially for proton primaries. This is because of the steep attenuation of N_e with depth in the region of observation folded into the steep primary spectrum. Since N_μ is well correlated with E_o in each shower, the fluctuations in N_e can lead to large fluctuations in N_μ for fixed N_e. Figure 19 shows the data of Vernov et al (1969) for the relative dispersion σ/N_μ. Several authors (Kalmykov and Khristiansen (1975), Olejniczak et al (1977)) have pointed out that such large fluctuations rule out a pure iron nucleus composition in the range 10^{15} - 10^{17} eV. Elbert et al (1976) point out that there are two solutions to this problem either a predominantly iron nucleus composition with a small admixture of protons or other light nuclei or a composition of nearly all protons. In the former case the fluctuations

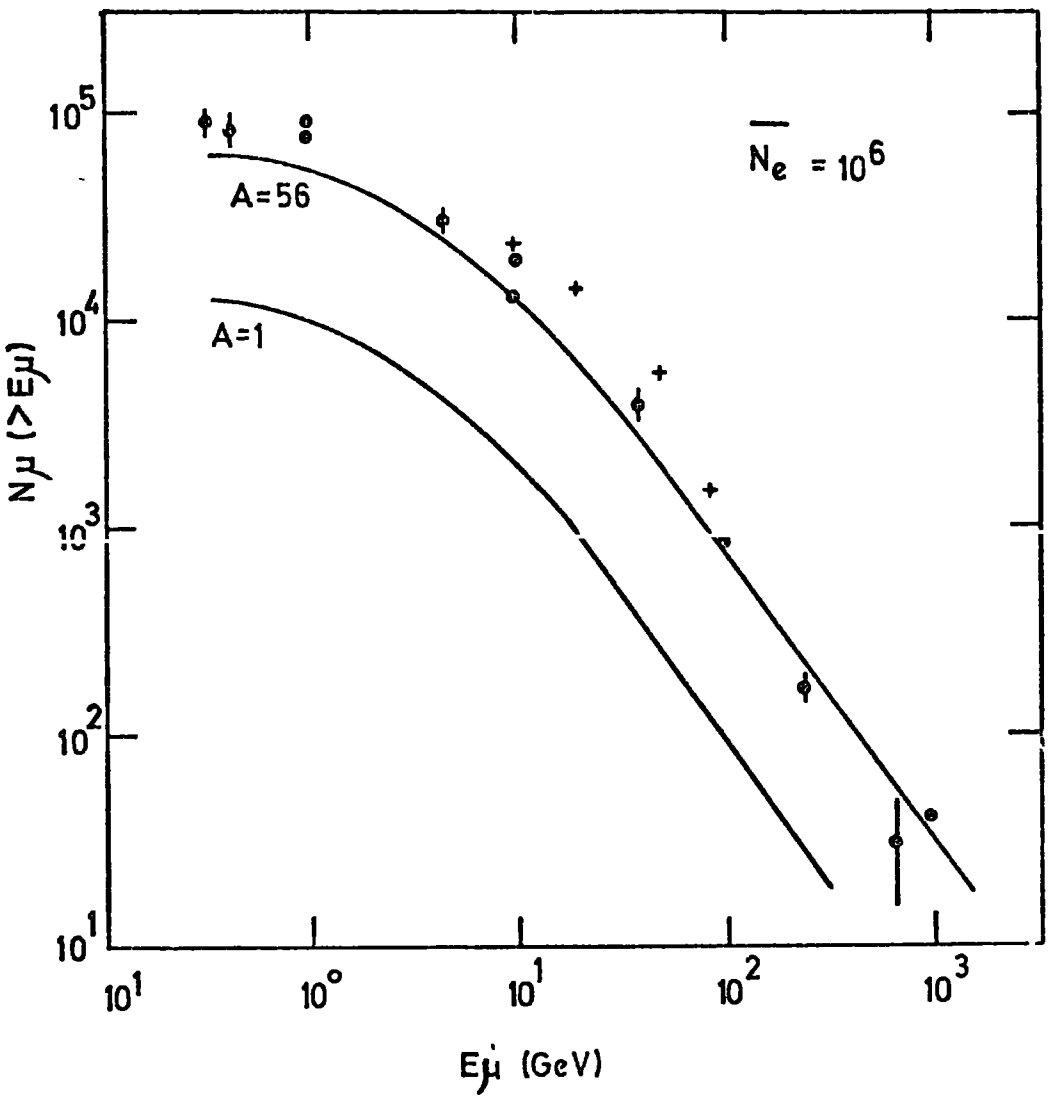

FIGURE 7-18 A compilation of total muon number, $N_\mu\ (>E_\mu)$ by Gaisser and Maurer (1972) (•) and additional data from Vernov et al (1977) (+) is compared to the integral energy spectrum of muons simulated at a primary energy corresponding to $\bar{N}_e = 10^6$.

arise largely from the mixture and in the latter case largely from the large fluctuations in development characteristic of proton showers. The curves in figure 19 have been obtained from a scaling model by Elbert et al (1976). They are able to bracket the data by varying the composition. Pure protons or pure iron primaries both give too little fluctuation. A standard mixed composition gives too much fluctuation. Predominantly iron primaries with about 10-20% protons give agreement with the data. The measurements by Barrett et al (1977) of fluctuations in cascade development based on the rise time of the Haverah Park water Cerenkov detector pulses were noted in section 7-1.5. Again, in the authors interpretation a choice of models and masses exist to explain these data on showers of mean energy 8×10^{17} eV. One possibility is $\sim$80% iron nuclei and 20% protons. The authors believe that the case of primaries being predominantly protons is preferable and that if this is so, a significant departure from Feynman scaling is required to understand other EAS data.

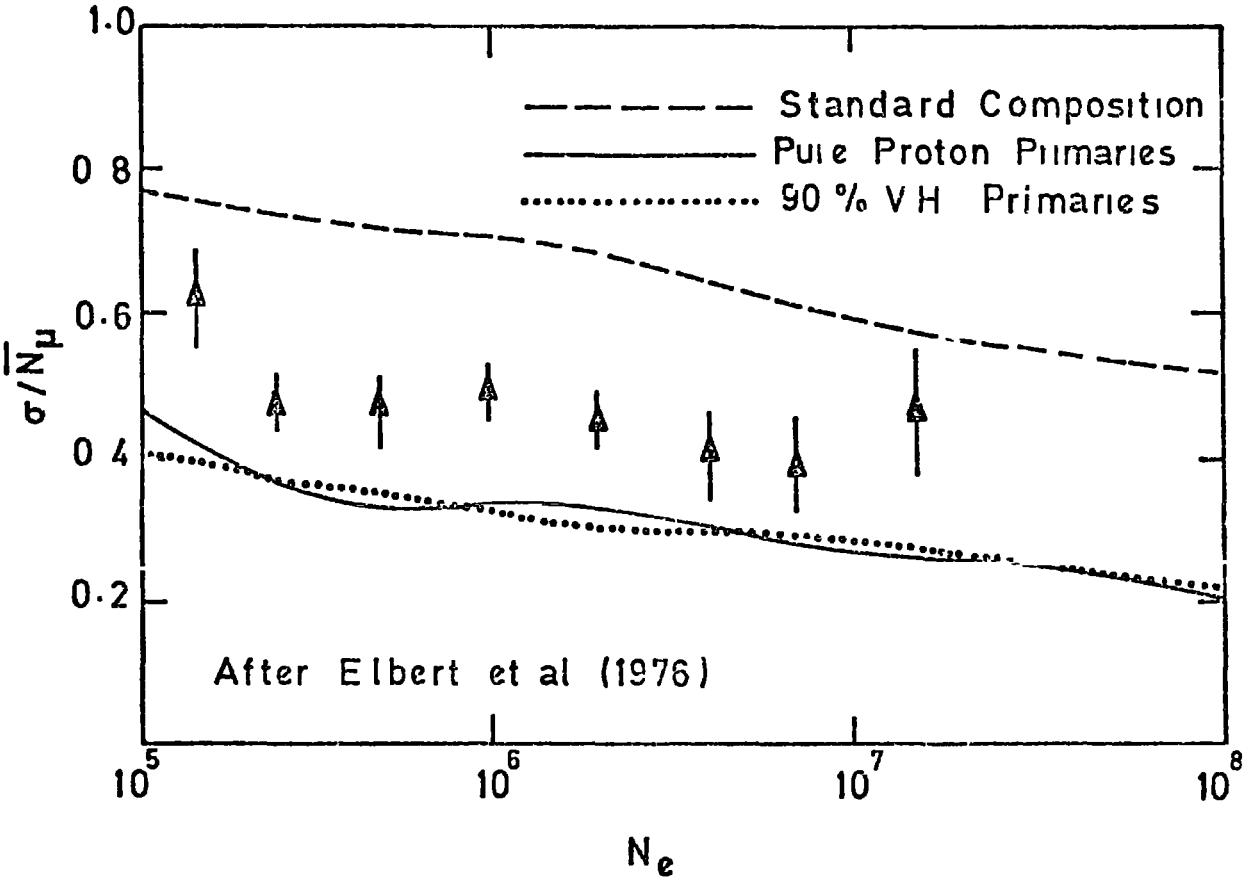

FIGURE 7-19 The measured relative dispersion in muon number as a function of shower size (from Vernov et al (1969)) is compared to that calculated by Elbert et al for various primary compositions.

CHAPTER EIGHT

CONCLUSIONS

INTRODUCTION

There is considerable contemporary interest in particle interactions at those high energies accessible only through the study of cosmic ray extensive air showers, i.e., $E \gtrsim 1000$ TeV. The interpretation of air shower data, however, involves consideration also of the nature of the primary particles. An attempt has been made recently by Gaisser, Protheroe and Turver (1977, and in preparation) to clarify and, as far as is possible, separate the particle physics and astrophysics aspects of air shower studies. Their conclusions are reproduced here in part. Success in this may lead to information on the primary particle mass - a long standing goal of high energy astrophysics. It may also be expected to lead to information about gross features of particle interactions at energies up to $\sim 10^{18}$ eV, a region which may never be explored by accelerators. It is emphasised, however, that it is not possible on the basis of existing work to disentangle completely the particle physics from the astrophysical implications of extensive air shower data. Thus an important goal of this work is to delineate the direction in which further experiment and analysis is required.

A review and clarification of the siutation for primary energies ranging from 10^{15} - 10^{18} eV is particularly timely from the point of view of the high energy physics for several reasons. For example, the design of the new generation of accelerators presently under consideration may benefit from hints about the behaviour of particles at high energies, especially since results on multi-particle production at 100-1000 GeV are now clearly in focus, and scaling provides a woll-defined extrapolation that

is amenable to test at high energy. This is especially so since it has become clear recently that nuclear effects in the light atmospheric nuclei will not seriously obsure matters.

In this chapter the question as to whether the development of air showersat energies up to 10^{18} eV is consistent with particle physics scaled up in energy from accelerator data at 100 - 1000 GeV is considered. The comparison of detailed simulations with a broad range of observational data which was made in chapter 7 suggested that many aspects of shower development are indeed consistent with scaling for particle physics provided the mass composition is as at $\sim 10^{12}$eV per nucleus (where $A_{eff} \approx 10$). Certain other data are, however, consistent with the scaling model only if the primaries are predominantly heavy nuclei, such as iron. Indeed, it is found that scaling and heavy primaries can account well for recent measurements of Cerenkov radiation in large cosmic ray showers as well as for the observed rapid development of the electron cascade and the large magnitude of the muon to electron ratio. However, in many of these experiments the sensitivity is to the development of the electron cascade and not directly to the mass of the primary particle. Other models considered, with different primary mass compositions but with similar electron cascade development, would therefore give predictions which would agree equally well with these data.

Some aspects of showers, particularly the energy dependence of both the muon to electron ratio and the lateral distribution of the Haverah Park water Cerenkov detector response are inconsistent with Feynman scaling even if the primaries are all heavy nuclei.

8-1 THE FEYNMAN SCALING MODEL AT EAS ENERGIES

The comparisions between model predicitions and air shower data that were made in chapter 7, and mentioned above, fall into two groups: those that refer to measurements derived from the electromagnetic component and those that reflect the muon component, and in particular the low

energy muons.

The characteristics of the first group are governed by the energetic π^o component, which in turn is determined by the fragmentation region of the momentum distribution of particles produced in high energy nuclear interactions. The scaling model may account for these properties provided that, in some cases, the primary mass composition is weighted towards the heavy nuclei.

It is found, however, that the second group of measurements that depend on the low energy muons in air showers cannot be accounted for by Feynman scaling with any feasible model for the primary composition. These measurements include the energy dependence of the muon to electron ratio (to the extent that it is not obscured by selection effects arising from fluctuations in the presence of a mixed primary composition) for primary energies ranging from 10^{15} to 10^{17} eV, and the observed insensitivity to the primary energy of the shape of the lateral distribution of the Haverah Park water Cerenkov detector response, for primary energies ranging from 10^{17} - 10^{20} eV. The discrepancies between the predictions of the scaling model and these measurements may indicate a deficiency of low energy muons in the model simulations for showers of given primary energy. Such a deficiency could be accounted for by a deficiency of pions produced in the central region of the momentum distribution in high energy nuclear interactions. To test this idea, a series of calculations based on the Landau hydrodynamical model (Landau (1953)) has been made. This model is characterised by an energy dependent enhancement of pion production in the central region such that the multiplicity is proportional to $E^{\frac{1}{4}}$ rather than ln E, as for Feynman scaling.

8-2 THE LANDAU MODEL AT EAS ENERGIES

It has been pointed out that the Landau hydrodynamical model provides

a good representation of the data in the ISR energy range (Andersson et al (1976)). A series of calculations has been made using a simplified version of the Landau model (described in Chapter 2) to examine the effects of adopting this model on EAS calculations.

As expected, use of a model with multiplicity proportional to $E^{\frac{1}{4}}$, changes the calculated results in the desired direction. In no case, however, is an acceptable fit to the data given if the primaries are protons. For iron nucleus primaries, changes to the electron cascade development are, as expected, small typically at 10^{17} eV, the depth of electron cascade maximum is reduced by $\sim$50 g cm^{-2}.

A model giving greater enhancement of pion production in the central region than the Landau model, resulting in a multiplicity of $E^{0.33}$, was also described in chapter 2. As expected, this model has been found to give even better agreement with some of the data. The longitudinal electron cascade predicted for both the Landau and $E^{0.33}$ models with iron nucleus primaries are compared in figure 1 with the Chacaltaya data. Results using the $E^{0.33}$ model with proton primaries are also shown and it is seen that, particularly at low primary energies, the early development arising from a heavy primary composition is still required to give agreement with the data.

In figure 2 a comparison is made between the results of the Landau and the $E^{0.33}$ models for iron nucleus primaries and the observed lateral distribution of muons with energy greater than 10 GeV (Khristiansen et al (1971)). Both the above models give a better representation of the data than the scaling model (see figure 16 of chapter 7) but, particularly for the $E^{0.33}$ model, agreement could be obtained with the data for less massive primaries. The predictions obtained using the $E^{0.33}$ model for the lateral distribution of the Haverah Park water Cerenkov response at a primary energy corresponding to $\rho(500)=1$ m^{-2} are seen in figure 3 to

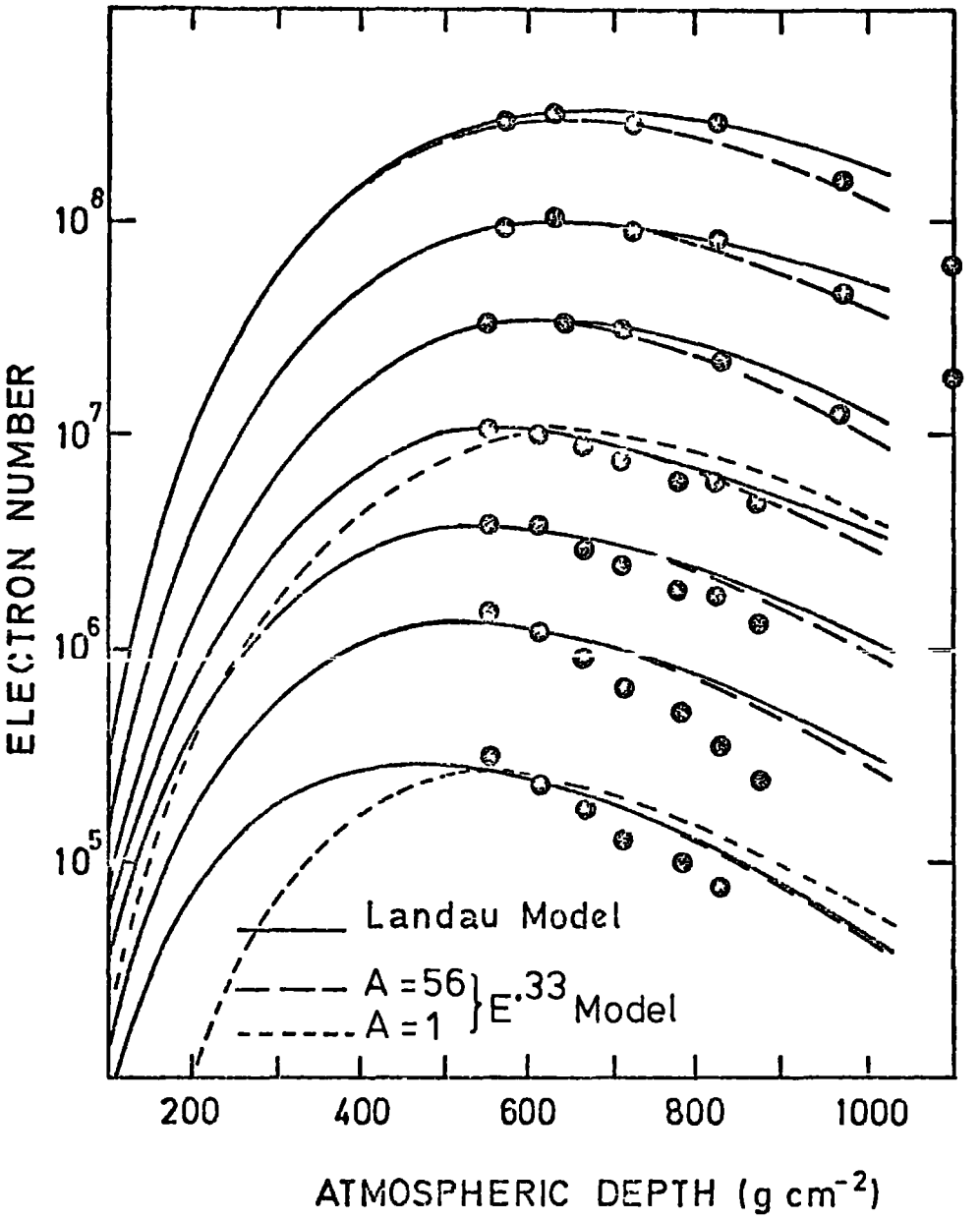

FIGURE 8-1 The longitudinal electron cascade development curves predicted from the Landau model (for A=56) and $E^{0.33}$ model (A= 1 and 56) are compared to the experimental development curves obtained by La Pointe et al (1968)

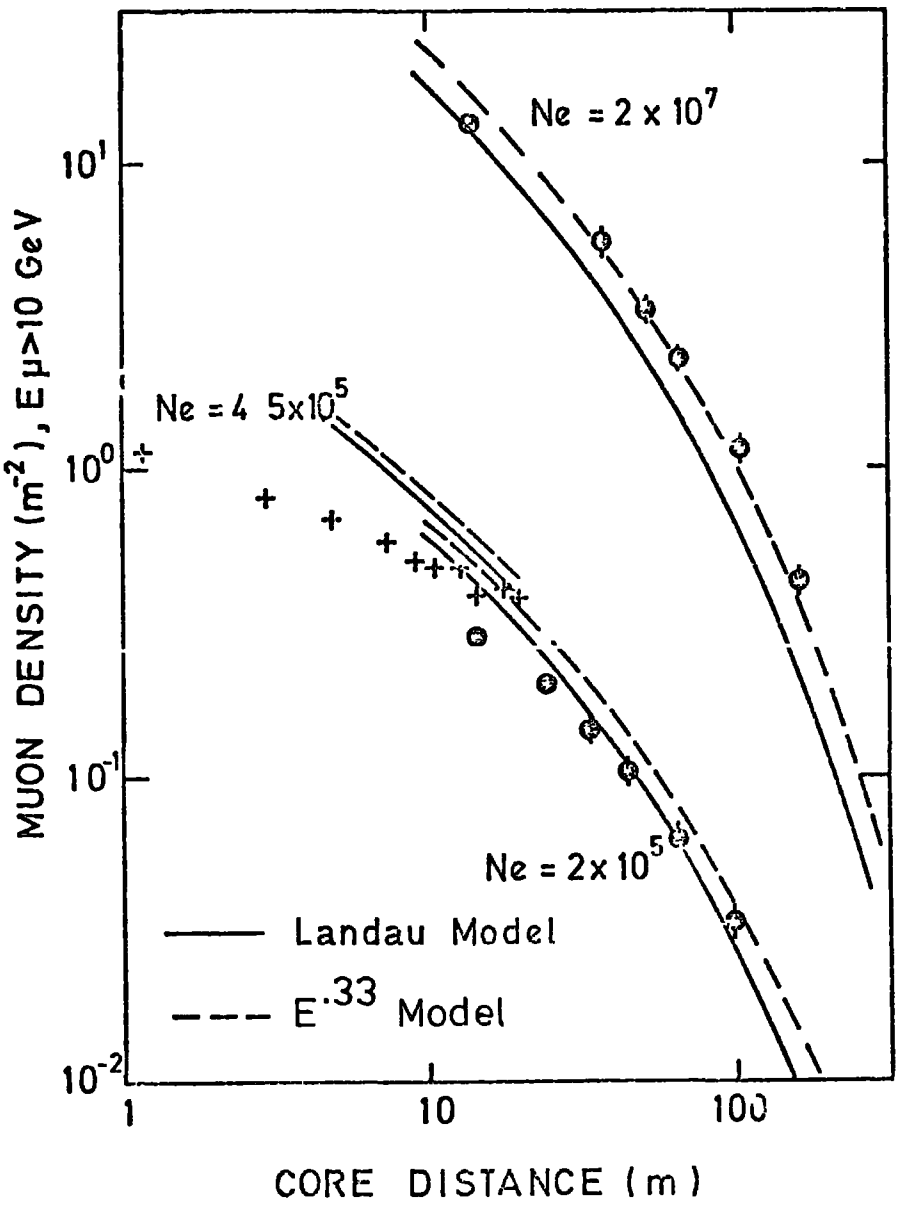

FIGURE 8-2 The lateral distribution of muons with energy greater than 10 GeV (Khristiansen et al (1971)) is compared to the predicted lateral distribution for iron nucleus primaries using the Landau and $E^{0.33}$ models at two values of N_e.

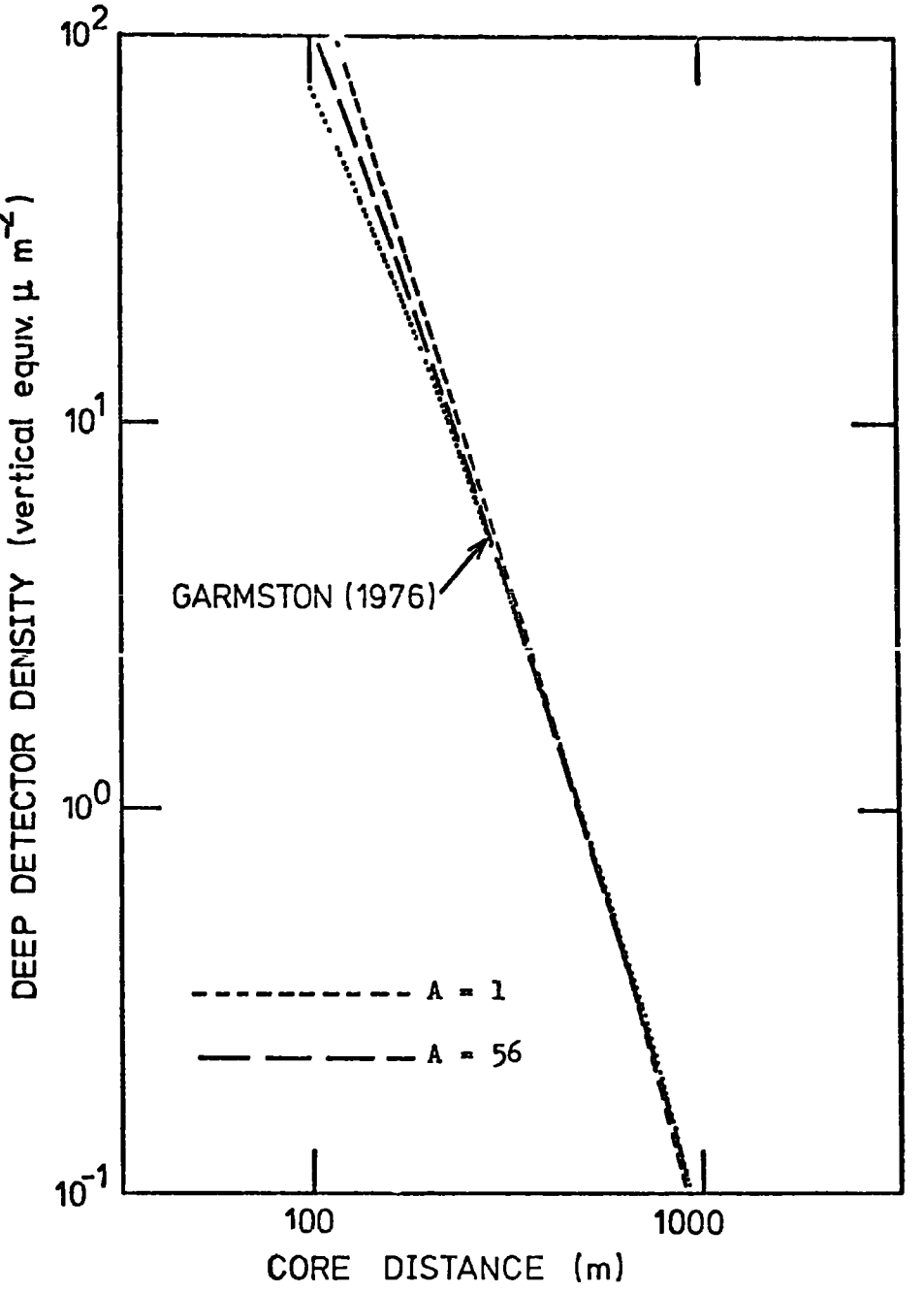

FIGURE 8-3 The average lateral distribution for the Haverah Park water Cerenkov detectors is compared that predicted using the $E^{0.53}$ model (A=1 and 56) at a primary energy corresponding to $\rho(500) = 1\ m^{-2}$.

be in better agreement with the data than the scaling model predictions (see figure 12 of chapter 7). This improvement is due to the earlier shower development obtained with this model and the larger relative contribution of the (broadly spread) muon component to the water Cerenkov detector response. The rate of change of B(100) with primary energy is, as expected, reduced with a value of ~25% per decade for the $E^{0.33}$ model at a primary energy of 10^{18} eV. This is in better agreement with the observed insensitivity of B(100) to primary energy than the predictions of the scaling model (~50% increase per decade of primary energy).

These preliminary results have indicated the general improvement in the agreement between predictions and data that arise when models which preserve scaling in the fragmentation region, but have enhanced pion production in the central region, are used. It is suggested that future work should include a more detailed study of the effects of adopting, these models in air shower calculations.

8-3 IMPLICATIONS FOR PARTICLE PHYSICS ABOVE 1000 TeV

It appears that, on balance, a picture with scaling in the fragmentation region (limiting fragmentation) and enhanced multiplicity due to increased production of pions in the central region, together with a primary composition as at 10^{12} eV, may account for most air shower observations. There are two notable exceptions to this overall picture. Both the average electron cascade development (figure 15 of chapter 7) and the muon to electron ratio (figure 16 of chapter 7) appear to require a significantly heavier composition than $A_{eff} = 10$ to accommodate Feynman scaling or the Landau model comfortably.

If the discrepancies between calculated and observed showers are to be accounted for by changes in strong interactions rather than by a heavy primary composition then the nature of strong interactions at EAS energies

would deviate drastically from that expected from accelerator data, and must include a breakdown of scaling in the fragmentation region. A mild violation of scaling in the central region only (as in the Landau model) would be insufficient if the primaries are predominantly protons and light primary nuclei. Models with extremely high multiplicities such as $\langle n \rangle \propto E^{\frac{1}{2}}$ (achieved when the energy is converted into matter moving slowly in the CM system - the kinematic limit) are required for a light primary composition in order to give sufficiently rapid shower development. This is achieved by a rapid degradation in energy of the hadronic cascade.

A shower parameter which is particularly sensitive to the multiplicity in high energy interactions independently of primary mass (to a reasonable approximation) is the elongation rate, defined as $\Delta x_{max} / \Delta \log E_p$ (i.e. the change in depth of electron cascade maximum per decade increase in primary energy). One objection to models with extremely high multiplicities, apart from their lack of theoretical motivation (Gaisser (1977)), is that they lead to low elongation rates e.g. for an $E^{\frac{1}{2}}$ model the elongation rate is $\sim$40 - 50 g cm^{-2}(see e.g. Olejniczak et al (1977a)). Preliminary indications (Barrett et al (1977) and Protheroe and Turver (1977)) suggest that the elongation rate is 80 - 90 g cm^{-2} at energies in the range 2×10^{17} eV to 5×10^{18} eV. This higher value is consistent with a scaling model, regardless of primary mass.

8-3.1 The effects of a rising cross section

The effect of a rising cross section is to cause showers to develop more rapidly, mainly because the mean depth of first interation is higher in the atmosphere. Various extrapolations have been made for the increase with energy of the proton-proton total cross section observed at the ISR (as discussed in chapter 2) and the effect of an energy dependent mean free path on the longitudinal electron cascade development has been described in chapter 3.

A mean free path in air for protons at 10^{17} eV of $\sim$55 g cm^{-2} is obtained for a conservative extrapolation with a ln E dependence (cross section (iii) in figure 18 of chapter 2). The effect of this energy dependent cross section is to reduce the depth of electron cascade maximum for 10^{17} eV showers by $\sim$45 g cm^{-2} for proton primaries and by $\sim$ 15 g cm^{-2} for iron nucleus primaries. With such a modification to the scaling model, proton primaries are still precluded by the Chacaltaya electron cascade measurements and the measured muon to electron ratio. For heavy primaries the effect of the increased cross section is small but may remove the slight discrepancies that exist between the predictions for iron nucleus primaries and some of the data.

8-3.2 Photoproduction of pions

EAS calculations including the effects of the photoproduction of pions have been made by Protheroe McComb and Turver (1977, in preparation) using the model of nuclear interactions of photons described in chapter 3. Interest in this process arises since pions produced in such interactions may form a source of low energy muons additional to those from the usual processes. The additional number of muons from this source in showers simulated with the scaling model was given in chapter 4.

The most important consequences of this process arise for showers simulated with primary energies greater than 10^{18} eV as a consequence of the large number of photons in the cascade and the increased proximity of the cascade maximum to ground level. The increase in the muon density at a core distance of 600 m could cause an increase, for a given primary energy, in the value of the Haverah Park ground parameter $\rho(600)$. This is of limited consequence for the above comparisions, since most of the data considered are at energies around 10^{17} eV.

In particular, there is no significant change in the relationship between the observed number of muons with energy greater than 10 GeV and electron number (Kalmykov and Khristiansen (1975)), since the number of additional muons arising from the photoproduction process is small (due to the low primary energy of the data) and lacking in high energy particles (see chapter 4).

Perhaps the most important effect of the increased muon density from this source will be on the relation between the Haverah Park ground parameter and primary energy, which may become energy dependent at the highest energies. To estimate this effect, the additional muon component was assumed to vary with primary energy as $E_p^{1.12}$. The power low exponent of 1.12 arises from the approximate proportionality, between the photo-produced pion component and primary energy, being enhanced by the energy dependence of the depth of maximum of the additional muon component. The energy dependence of the "normal" muon component is strongly model dependent and ranges from $E_p^{0.7}$ to $E_p^{0.9}$. Conventionally the Haverah Park ground parameter $\rho(600)$ has been assumed to be proportional to primary energy

$$\rho(600) \approx 10^{-18} E_p \quad m^{-2} \qquad 1$$

where E_p is the primary energy (eV). Taking the more conservative estimate of the energy dependence of the "normal" muon component and normalising to the data on the muon to water Cerenkov detector response ratio at $\sim 10^{17}$ eV yields approximately

$$\rho_\mu(600) \approx 5 \times 10^{-2} \left\{\frac{E_p}{10^{17}}\right\}^{0.82} \quad m^{-2}, \qquad 2$$

for the muon density at 600 m from the core. The additional muon component gives

$$\Delta\rho_\mu(600) \approx 10^{-2} \left\{\frac{E_p}{10^{17}}\right\}^{1.12} \quad m^{-2}, \qquad 3$$

with a fractional increase in $\rho_\mu(600)$ of $\sim 0.2(E_p/10^{17})^{0.3}$ and a corresponding fractional increase in $\rho(600)$ of $\sim 0.2\ \rho(600)^{0.3}$ if the muon to Cerenkov ratio is assumed to be independent of energy.

The primary energy spectrum measurements of Cunningham et al (1977) have been modified to allow for the effects of photomeson production as described above and are shown in figure 4. The modification was made by converting the measured $\rho(600)$ to the $\rho(600)$ expected if photomeson production were negligible by using,

$$\rho(600)_{normal} \approx \rho(600)\left[\ 1 + 0.2\rho(600)^{0.3}\ \right]^{-1} \qquad 4$$

It is suggested that additional muons originating in the photoproduction of pions may allow a primary energy spectrum with a simple power law to be consistent with the spectrum of the ground parameter, $\rho(600)$, showing a flattening at the highest observed values. The adoption of any preferred primary energy spectrum must, however, await further detailed considerations of this effect.

8-4 CONSEQUENCES FOR PRIMARY MASS COMPOSITION

Throughout this chapter, the difficulty of disentangling the effects of the primary mass composition from the effects of the high energy particle physics have been highlighted. An attempt to clarify the situation has been made in table 1 where an attempt has been made to answer the question "Is scaling acceptable at EAS energies?" for each set of data considered in chapter 7, and for three widely differing models of primary composition. The models of primary composition considered here are 1) light nuclei ($A \sim 1$), 2) mixed composition with $A_{eff} \sim 10$ (representative of the composition around 10^{12} eV per nucleus), and 3) heavy nuclei ($A \sim 56$). In general the predictions for the mixed composition would be midway between those for A = 1 and A = 56 in the figures of chapter 7 but, in some cases, the shower selection effects

10^{15} - 10^{17}	Muon content of showers	No	No	No	1, 16	A~56 best but primary energy dependance wrong.
10^{15} - 10^{17}	Fluctuations in Muon number at fixed Shower size	No	No	No	19	Require mixed composition with ~80-90% very heavy nuclei
10^{15} - 10^{18}	Electron cascade development	No	No	Maybe	15	A~56 best (~ 70 g cm^{-2} out)
10^{17}	Momentum spectrum of muons	No	Yes	Yes	5	
2×10^{17}	Lateral distribution of low energy muons	No	Yes	Yes	3, 4	
2×10^{17}	Lateral distribution of atmospheric Cerenkov radiation	Yes	Yes	Yes	7	
3×10^{17}	Time structure of atmospheric Cerenkov light pulse	No	Maybe	Yes	8, 9, 10	FWHM (top of pulse) sensitive to cascade development.
10^{17} - 10^{18}	Muon density - Haverah Park water Cerenkov detector density ratio	No	No	Yes	13	
10^{17} - 10^{18}	Height of origin of muons	No	Maybe	Yes	6	
10^{17} - 10^{18}	Lateral distribution of electrons	No	No	No	11	All models give too steep lateral distribution.
10^{17} - 10^{20}	Response of Haverah Park water Cerenkov detectors	No	No	No	12	Predicted lateral distribution too steep and energy dependent

TABLE 8-1. An attempt to summarise the consequences for primary composition of the comparison between the predictions and air shower data made in chapter 7.

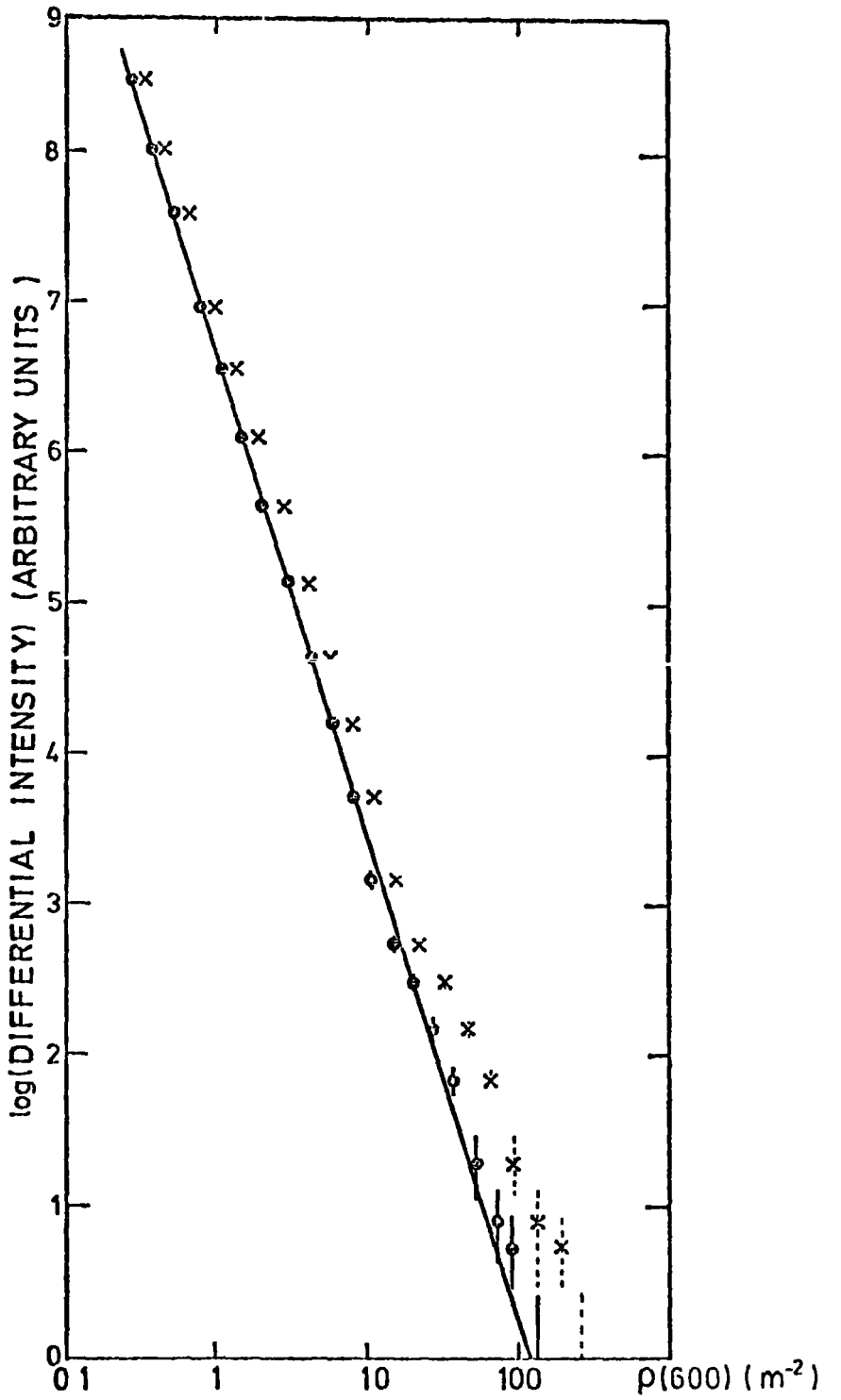

FIGURE 8-4 The primary spectrum measurements of Cunningham et al (1977) (x) have been modified to allow for the effects of photomeson production (o) as discussed in section 8-1.5.

of the detector array due to fluctuations in the presence of a mixed primary composition may alter this.

The results of earlier calculations (Gaisser and Maurer (1972) and Wdowczyk and Wolfendale (1972, 1973)) which suggested that the scaling model could not give agreement with the EAS data for a primary proton composition are confirmed by this more detailed comparison of simulations with a wider range of experimental data.

The acceptability of scaling with a mixed composition is more difficult to determine. It is unlikely that this model can account for the observed rapid electron cascade development or the observed energy dependence of of the muon to electron ratio, paricularly as fluctuations will bias toward the more deeply penetrating light nuclei because of the steep primary energy spectrum. It is on the electron cascade development and the muon to electron ratio of proton initiated showers, however, that the Landau model and/or a rising cross section have their greatest effect and, in these circumstances, a mixed composition may be acceptable.

A heavy primary composition appears to have the greatest success in reproducing the EAS data but a definitive answer to the question posed above must await calculations which include the selection effects due to fluctuations in the presence of a steep primary energy spectrum. These effects have been shown to be important by Elbert et al (1976) who find that with a scaling model only a mixed composition is capable of reproducing the data on the fluctuations in muon number at fixed shower size.

8-5 CONCLUSION

Computer simulations have been made of many aspects of large cosmic ray showers using recent models of hadronic collisions. The results of these simulations have been compared with a broad range of experimental data considering, where possible, the response of the detectors. No model

of primary composition and particle physics appears, at present, to be consistent with all the reported air shower data. A primary proton composition and scaling is inconsistent with most aspects of the data, but many aspects of the data would be consistent with a heavier primary composition (e.g., $A_{eff} \sim 10$). With a very heavy composition (e.g., $A \sim 56$), the scaling model would give a consistent picture on an even broader front.

The position may be clarified by future calculations made to include the effects of fluctuations. Detailed results on fluctuations in cascade development from a new series of experiments may lead to a tentative identification of the mean primary mass number. Perhaps the most promising of these are the "Fly's Eye" experiment (Bergeson et al (1975)), direct observations of electron cascade through studies of time structure of atmospheric Cerenkov light pulses (Hammond et al (1977a)) and data from a number of experiments at the Haverah Park air shower array. Results from the giant air shower array now under construction in Japan (Kamata et al (1977)) will also be important.

In conclusion, when information on the general features of strong interactions are obtained using the next generation of particle accelerators (ISABELLE at Brookhaven National Laboratory and the proposed collider/doubler at Fermilab) it will be possible to infer with greater reliability the gross features of the primary mass composition up to $\sim 10^{15}$ eV and beyond (after making more reasonable extrapolations from the accelerator data).

APPENDIX A

THE ENERGY DEPENDENCE OF THE MULTIPLICITY FOR SCALING MODELS

In this appendix, the well known logarithmic energy dependence of the mean multiplicity for scaling models is demonstrated. The mean multiplicity of charged pions, $\langle n_\pi \rangle$, is calculated from the inclusive cross section for pion production in pion-nucleon interactions, $F_{\pi\pi}(x)$ given in chapter 2.

The mean multiplicity of pions in pion-nucleon interactions is given by:

$$\langle n_\pi \rangle \approx \int_{E_{min}}^{E_{max}} \frac{F_{\pi\pi}(x)}{E_\pi} \, dE_\pi \qquad 1$$

$$= \int_{E_{min}}^{E_{max}} \left\{ \frac{F_{\pi\pi}(0)}{E_\pi} - \frac{F_{\pi\pi}(x) - F_{\pi\pi}(0)}{E_\pi} \right\} dE_\pi \qquad 2$$

$$\therefore \quad \langle n_\pi \rangle \approx F_{\pi\pi}(0) \ln \left\{ \frac{E_{max}}{E_{min}} \right\} - \int_{E_{min}}^{E_{max}} \frac{F_{\pi\pi}(x) - F_{\pi\pi}(0)}{E_\pi} dE_\pi \qquad 3$$

Now $$E_{max} \approx E_o \ , \qquad 4$$

$$E_{min} \approx m_\pi c^2 , \qquad 5$$

and $$x \approx \begin{cases} E_\pi / E_o & \text{for } E_\pi \gg m_\pi c^2 \\ \dfrac{-\langle m_{\pi t}^2 \rangle c^2}{2 m_p E_\pi} & \text{for } E_\pi \ll E_o \end{cases} \qquad 6$$

$$\therefore \quad \frac{dE_\pi}{E_\pi} \approx \begin{cases} dx/x & \text{for } E_\pi \gg m_\pi \\ -dx/x & \text{for } E_\pi \ll E_o \end{cases} \qquad 7$$

hence $$\langle n_\pi \rangle \approx F_{\pi\pi}(0) \ln \left\{ \frac{E_o}{m_\pi c^2} \right\} - \int_{-1}^{1} \frac{F_{\pi\pi}(x) \quad F_{\pi\pi}(0)}{|x|} dx \qquad 8$$

The integrand is plotted in figure 1 and theintegral has been obtained from the area

$$\int_{-1}^{1} \frac{F_{\pi\pi}(x) \quad - F_{\pi\pi}(0)}{|x|} dx \approx 10.0 \qquad 9$$

Substitution of this result and $F_{\pi\pi}(0) = 2.19$ into equation 8 gives,

$$\langle n_\pi \rangle = 2.19 \quad \ln E_o - 5.688 \qquad 10$$

where E_o is the projectile energy in GeV.

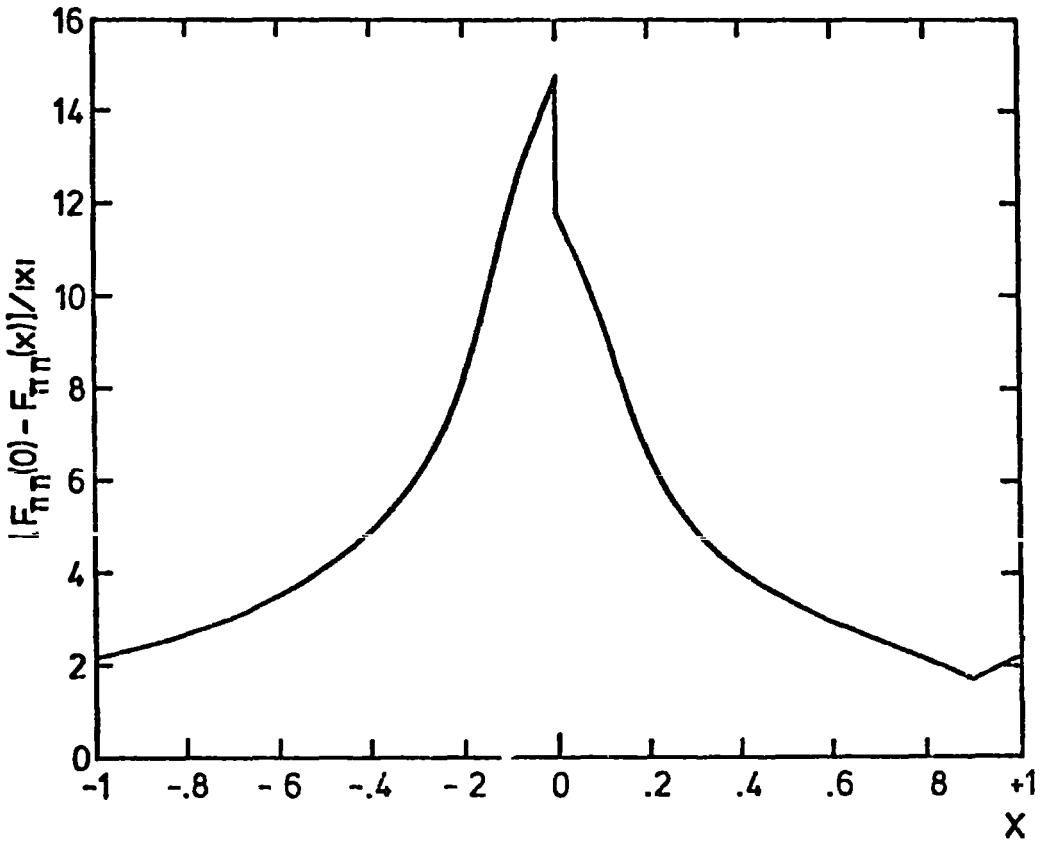

FIGURE A-1 The integrand of equation 9 plotted against x.

APPENDIX B

NUMERICAL SIMULATION OF LOW ENERGY PION CASCADES

In this appendix a method for the numerical simulation of the low energy pion component is described. This method has been used to determine the production spectra of charged and neutral pions, $\phi_{\pi^c}(x,E)$ and $\phi_{\pi^o}(x,E)$ (i.e. PITOT (IH, IE) and PIZOT (IH, IE) as defined in section 2-7 of chapter 2) resulting from the cascade of pions produced with energies below the Monte Carlo threshold energy, E_t (see section 2-7 of chapter 2).

The probability that a pion which was produced in the depth bin at x_j and in the energy bin at E_j (below the Monte Carlo threshold) will interact in the depth bin at x_i ($> x_j$) to produce a pion in the energy bin at E_i ($\leq E_j$) is

$$P(x_j,E_j \rightarrow x_i, E_i) \approx P_s(x_i, x_j, E_j)\, P_i(x_i - x_j) F(E_i,E_j) \qquad 1$$

where $P_s(x_i, x_j, E_j)$ is the probability of surviving decay from depth x_j to x_i for a pion of enery E_j, and $P_i(x_i - x_j)$ is the probability of a pion at depth x_j interacting in the depth bin at x_i. $P_s(x_i, x_j, E_j)$ and $P_i(x_i - x_j)$ are given below

$$P_s(x_i, x_j, E_j) \approx \exp\left\{ -(h_j - h_i) / \tau_\pi \gamma\beta c \right\} \qquad 2$$

where h_i is the altiude (m) at depth x_i,

τ_π is the mean pion lifetime (s),

βc is the velocity (m s^{-1}) of a pion with energy E_j

$$\gamma = (1 - \beta^2)^{-1}$$

$$P_i(x_i - x_j) = \exp\left\{-(x_i - x_j)/\lambda\right\}\left\{ \exp(\Delta x/2\lambda) - \exp(-\Delta x/2\lambda)\right\} \qquad 3$$

where λ is the mean free path for pion air-nucleus interactions ($g\ cm^{-2}$)

and $F(E_i,E_j)$ is the probability per interation of a pion being produced with energy in the bin centred on E_i if the interaction energy is E_j. (Equations 2 and 3 are not valid if $x_i = x_j$ or $E_i = E_j$ but more accurate formulae for the survival and interaction probabilities, have been used for these cases in the present calculations.)

Hence $\phi_{\pi^c}(x_i, E_i)$ and $\phi_{\pi^o}(x_i, E_i)$ may be modified to include pions produced as a result of the cascade of pions with energies below the Monte Carlo threshold, E_t, by summing the above probabilities over all pairs of energies E_i and E_j and all pairs of depths x_i and x_j in the order specified below

$$x_j = x_1, x_2, x_3, \ldots\ldots\ldots x_{40}$$

$$x_i = x_j, x_{j+1}, x_{j+2}, \ldots\ldots\ldots x_{40}$$

$$E_j = E_t, E_{t-1}, E_{t-2}, \ldots\ldots\ldots E_1$$

$$E_i = E_j, E_{j-1}, E_{j-2}, \ldots\ldots\ldots E_1$$

$$\phi_{\pi^c}(x_i,E_i) \longleftarrow \left\{\phi_{\pi^c}(x_i,E_i) + \frac{2}{3}\ \phi_{\pi^c}(x_j,E_j,)P(x_j,E_j \rightarrow x_i,E_i)\right\} \qquad 4$$

$$\phi_{\pi^o}(x_i,E_i) \longleftarrow \left\{\phi_{\pi^o}(x_i,E_i) + \frac{1}{3}\ \phi_{\pi^c}(x_j,E_j)\ P(x_j,E_j \rightarrow x_i,E_i)\right\} \qquad 5$$

The summation is made in the above order to simulate the cascade since then the probability of pions in (x_j,E_j) being responsible indirectly for the production of pions in (x_i,E_i) (by intermediate interations) is included.

APPENDIX C

THE APPROXIMATION A OPERATORS

The numerical solution of the electron-photon cascade equations under approximation A by the step-by-step method was described in chapter 3. In this appendix the approximation A operators ee_1, eg_1, ge_1 and gg_1 (see equation 19 of chapter 3) are given.

Since the energy bins used in the calculation are of finite width, it is necessary to make an assumption about the differential energy spectra of particles within an energy bin. Over small ranges of energy and thickness the differential spectra depend on energy according to a power law with exponent $-(s + 1)$ (Rossi (1952)). s is the age parameter of the shower, taken here as 1 since a particle has greatest probability of being at shower maximum. The derivation is therefore based on the following assumptions

$$\psi_{rad}(v) = K v^{-1} - K + v, \qquad 1$$

$$\psi_{pair}(v) = K v^{2} - Kv + 1, \qquad 2$$

$$f(E') = \frac{E_p \; E'^{-1}}{(F - 1/F)}, \qquad 3$$

where $K = (4/3 + 2b)$, equations 1 and 2 are based on equations 16 and 17 of chapter 3, and $f(E')$ is the differential energy spectrum of particles in an energy bin such that $E_p/F < E' < FE_p$. The operators have been calculated and given in equations 4 to 11

$$ee_i = C \left\{ K \sum_{l=2}^{\infty} \alpha_l \alpha_{l+1} \beta^l + \alpha_1 \alpha_2 \beta - \alpha_2 \alpha_3 \beta^2 \right\}, \qquad 4$$

$$eg_1 = C \left\{ K \alpha_1 \ln F^2 - K \alpha_1 \alpha_2 \beta + \alpha_2 \alpha_3 \beta^2 \right\}, \qquad 5$$

$$ge_1 = 2C \left\{ K \alpha_3 \alpha_4 \beta^3 - K \alpha_2 \alpha_3 \beta^2 + \alpha_1 \alpha_2 \beta \right\}, \qquad 6$$

$$gg_1 = 0, \qquad 7$$

$$ee_o = 1 - \sum_{i=1}^{\infty} ee_i \quad , \qquad 8$$

$$eg_o = C\left\{\frac{\alpha_1}{2} + \frac{\alpha_2}{F} - \frac{\alpha_3}{2F^2} - \frac{K}{F} \ln F^2\right\} , \qquad 9$$

$$ge_o = 2C\left\{(1- K/6)\ \alpha_1 - \frac{K\alpha_4}{3F^3} + \frac{K\alpha_3}{2F^2} - \frac{\alpha_2}{F}\right\} , \qquad 10$$

$$gg_o = 1 -(1 - K/6)\ (F - 1/F)C, \qquad 11$$

where

$$C = \frac{\Delta t}{(F - 1/F)} ,$$

$$\alpha_J = \frac{(F^J - 1/F^J)}{J} ,$$

$$\hat{\beta} = F^{-2i}.$$

REFERENCES

Albrow M.G., et al (CERN-Holland-Lancaster-Manchester Collaboration) (1974) Nucl. Phys., B73, 40.

Allan H.R., Crannell C.J., Shutie P.F. and Sun M.P. (1975) Proc. 14th Int. Conf. Cosmic Rays, Munich, 6, 3071.

Alper B., et al (British-Scandinavian Collaboration) (1975) Nucl. Phys., B100, 237.

Amati D., Fubini S and Stanghellini A. (1962) Nuovo Cimento, 26, 896.

Anderson C.D. (1932) Science, 76, 238.

Anderson C.D. and Neddermeyer S.H. (1934) Proc. Int Conf. Phys., London, 1, 171.

Andersson B., Jarlskog G and Damgaard G. (1976) Nucl. Phys., B112, 413.

Antinucci M., Bertin A., Capiluppi P., D'Agostino-Bruno M., Rossi A.M., Vannini G., Giacomelli G. and Bussiere A (1973) Nuovo Cimento Letters, 6, 121.

Antonov R.A. (1974) Soviet Nucl. Phys., 19, 1053.

Antonov R.A. and Ivanenko I.P. (1975) Proc. 14th Int. Conf. Cosmic Rays, Munich, 8, 2708.

Armitage M.L. (1973) PhD. thesis, University of Nottingham.

Astrashkevich V.B., Vedeneev O.V., Kulikov G.V., Solovjeva V.I. and Khristiansen G.B. (1977) Proc. 15th Int. Conf. Cosmic Rays, Plovdiv, 8, 142.

Auger P., Maze R and Grivet-Meyer T. (1938) C.R. Acad. Sci. (Paris), 206, 1721.

Barclay F.R. and Jelley J.V. (1956) The Oxford Conf. on EAS, AERE, Harwell, p. 74.

Barrett M.L., Watson A.A., Wild P. and Wilson J.G. (1975) Proc. 14th Int. Conf. Cosmic Rays, Munich, 8, 2753.

Barrett M.L., Walker R., Watson A.A. and Wild P. (1977) Proc. 15th Int. Conf. Cosmic Rays, Plovdiv 8, 172.

Baxter A.J. (1969) J. Phys. A, 2, 50.

de Beer J.F., Holyoak B., Wdowczyk J. and Wolfendale A.W. (1966) Proc. Phys. Soc., 89, 567.

Benecke J., Chou T.T., Yang C.N. and Yen E. (1969) Phys. Rev., 188, 2159.

Berger Ch., Dick G., Erlewein W., Lubelsmeyer K , Paul L., Meyer-Wachsmuth H. and Schultz von Dratzig A. (1973) Phys. Lett., 47B, 377.

Bergeson H.E., Boone J.C. and Cassiday G.L. (1975) Proc. 14th Int. Conf. Cosmic Rays, Munich, 8, 3059.

Bergeson H.E., Cassiday G.L., Chiu T.-W., Cooper D.A., Elbert J.W., Loh E.C., Steck D., West W.J., Linsley J. and Mason G.W. (1977) Phys. Rev. Lett., 39, 847.

Bethe H.A. and Heitler W. (1934) Proc. Roy. Soc., A146, 83.

Blau M. and Wambacher H. (1937) Nature, 140, 585.

Blobel V., et al (Bonn-Hamburg-Munich Collaboration) (1974) Nucl. Phys., B69, 454.

Boley F.I., Bunn J.H., Palsedge J.A. and Pereve J.H. (1961) Phys. ReV., 124, 1205.

Boley F.I. (1964) Rev. Mod. Phys., 36, 792.

Bosetti P., et al (Aachen-Berlin-Bonn-CERN-Cracow-Heidelberg-Warsaw Collaboration) (1973) Nucl. Phys., B54, 141.

Bosia G., Marmgelli M. and Navarra G. (1972) Nuovo Cimento, 9B, 201.

Bosia G., Navarra G., Saavedra O., Bohm E. and Cachon A. (1973) Proc. 13th Int. Conf. Cosmic Rays, Denver, 4, 2375.

Bothe W. and Kolhorster W. (1929) Zeits. fur Physik, 56, 751.

Bradt H., Clark G., La Pointe M., Domingo V., Escobar I., Kamata K., Murakami K., Suga K. and Toyoda Y. (1966) Proc. 9th Int. Conf. Cosmic Rays, London, 2, 715.

Brennan M.H., Malos J., Millar D.D. and Wallace C.S. (1958) Nature, 182, 973.

Brown R.H., Camerini V., Fowler P.H., Heitler W., King D.T. and Powell C.F. (1949) Phil. Mag., 40, 862.

Browning R. and Turver K.E. (1977) Nuovo Cimento, 38A, 223.

Bunner A.N. (1967) PhD. thesis, Cornell University.

Burfeindt H., Buschhorn G., Genzel H., Heide P., Kotz U., Mess K.-H., Schmuser P., Sonne B., Vogel G., and Wilk B.H. (1973) Phys. Lett., 43B, 345.

Busza W., Elias J.E., Jacobs D.F., Swartz P.A., Young C.C. and Sogard M.R. (1975) Phys. Rev.Lett., 34, 836.

Butcher J.C. and Messel H. (1958) Phys. Rev., 112, 2096. and (1960) Nucl. Phys., 20, 15.

Capella A. and Krzywicki A. (1977) Laboratoire de Physique Theorique et Particules Elementaries, Paris, ref. LPTPE 77/31.

Capiluppi P., Giacomelli G., Rossi A.M., Vannini G., and Bussiere A. (1974) Nucl. Phys., B70, 1.

Carruthers P. and Minh Duong-van (1973) Phys. Rev., D8, 859.

Cassiday G.L., Bergeson H.E., Chiu T.W., Cooper D.A., Elbert J.W., Loh E.C., Steck D., West W.J., Mason G.W., Boone J. and Linsley J. (1977) Proc. 15th Int. Conf. Cosmic Rays, Plovdiv, 8, 258. and (1977a) Proc. 15th Int. Conf. Cosmic Rays, Plovdiv, 8, 270.

Castagnoli C., Locci M.A., Picchi P. and Verri G. (1967) Nucl. Phys., B2, 369.

Castagnoli C., Picchi P. and Locci M.A. (1972) Nuovo Cimento, 9B, 213.

Cerenkov P.A. (1934) Dokl. Akad. Nauk., 2, 451.

Cerenkov P.A. (1937) Dokl. Akad. Nauk., 14, 101.

Cleghorn J.F., Freier P.S. and Waddington C.J. (1968) Can. J. Phys., 46, S572.

Cocconi G., Loverdo A. and Tongiorgi V. (1946) Phys. Rev., 70, 852.

Cocconi G., Koester L.G. and Perkins D H. (1961) Lawrence Rad. Lab. Seminars, 28, pt.2, UCID-144, 1.

Cox R.T. (1944) Phys. Rev., 66, 106.

Crawford D.F. and Messel H. (1962) Phys. Rev., 128, 2352

Cunningham G., Pollock A.M.T., Reid R.J.O. and Watson A.A. (1977) Proc. 15th Int. Conf. Cosmic Rays, Plovdiv, 2, 303.

Dar A. and Tran Thran Van (1976) Phys. Lett., B65, 455.

Dedenko L.G. (1966) Proc. 9th Int. Conf. Cosmic Rays, London, 2, 662 and (1975) Proc. 14th Int. Conf. Cosmic Rays, Munich, 8, 2857.

Diddens A.N. (1974) Proc. 17th Int. Conf. High Energy Phys., London, p. I-41.

Dixon H.E. (1974) PhD. thesis, University of Durham.

Dixon H.E., Machin A.C., Pickersgill D.R., Smith G.J. and Turver K.E. (1974) J. Phys. A, 7, 1010.

Dixon H.E., Earnshaw J.C., Hook J.R., Hough J.H., Smith G.J., Stephenson W. and Turver K.E. (1974a) Proc. Roy. Soc., A339, 133.

Dixon, H E., Turver K.E. and Waddington C.J. (1974b) Proc. Roy. Soc., A339, 157.

Dixon H.E. and Turver K.E. (1974) Proc. Roy. Soc., A339, 171.

Dyakonov M.N., Knurenko S.P , Kolosov V.A., Krasilnikov D.D., Kulakovskaya V.P., Kuzmin A.I., Orlov V.A., Sleptsov I. Ye., Yefimov N.N. and Yegorov T.A. (1973) Proc. 13th Int. Conf. Cosmic Rays, Denver, 4, 2389.

Earnshaw J.C., Machin A.C., Pickersgill D.R. and Turver K.E. (1973) J. Phys. A, 6, 1244.

Edge D.M., Evans A.C., Garmston H.J., Reid R.J.O., Watson A.A., Wilson J.G. and Wray A.M., (1973) J. Phys. A, 6, 1612.

Edge D.M. (1976) J. Phys. G, 2, 433.

Efimov N.N., Krasilnikov D.D., Khristiansen G.B., Shikalov F.V. and Kuzmin A.I. (1973) Proc. 13th Int. Conf. Cosmic Rays, Denver, 4, 2378.

Eisner A.M., Caldwell D.O., Cumalat J.P., Kendall B.N., McPharlin T.P., Morrison R.J. and Murphy F.V. (1974) Phys. Rev. Lett., 33, 865.

Elbert J.W., Mason G.W., Morrison J.L. and Narasimham V.S (1976) J. Phys. G, 2, 971.

Elbert J.W., Bergeson H.E., Cassiday G.L., Chiu T.W., Cooper D.A., Loh E.C., Steck D., West W.J., Mason G.W., Boone J and Linsley J. (1977) Proc. 15th Int. Conf. Cosmic Rays, Plovdiv, 8, 264.

Elterman L. (1968) Air Force Cambridge Res. Labs., ref. AFC RL-68-0153.

Fermi E. (1950) Prog. Theor. Phys., 5, 570.

Feynman R.P. (1969) Phys. Rev. Lett., 23, 1415.

Fishbane P. M. and Trefil J.S. (1973) Phys. Rev. Lett., 31, 734.

Fishbane P.M., Gaisser T.K., Maurer R.H. and Trefil J.S. (1974) Phys. Rev., D9, 3083.

Fomin Yu. A. and Khristiansen G.B. (1971) Soviet J. Nucl. Phys., 14, 360.

Frank I.M. and Tamm Ig. (1937) Dokl. Akad. Nauk., 14, 109.

Frazer W.R., Ingber L., Mehta C.H., Poon C.H., Silverman D., Stowe K., Ting P.D. and Yesian H.J. (1972) Rev. Mod. Phys., 44, 284.

Freier P.S. and Waddington C.J. (1975) Astropnys. and Space Sci., 38, 419.

Galbraith W. and Jelley J.V. (1953) Nature, 171, 349.

Gaisser T.K. and Maurer R.H. (1972) Phys. Lett., 42B, 444. and (1973) Phys. Rev. Lett., 30, 1264.

Gaisser T.K. (1974) J. Franklin Inst., 298, 271 and (1974a) Nature, 248, 122.

Gaisser T.K., Protheroe R.J. and Turver K.E. (1977) Proc. 15th Int. Conf. Cosmic Rays, 8, 314.

Gaisser T.K. and Hillas A.M. (1977) Proc. 15th Int. Conf. Cosmic Rays, Plovdiv, 8, 353.

Gaisser T.K. (1977) Proc. 15th Int. Conf. Cosmic Rays, Plovdiv, Rapporteur paper.

Garmston, H.J. (1976) Ph.D. Thesis, University of Leeds.

Geiger H. and Muller W. (1928) Die Naturwiss, 16, 617.

Gibson A.I. (1976) M.Sc. thesis, University of Durham.

Ginsberg V.L. (1940) Zh. fiz. SSSR, 2, 441.

Gol'danskii V.I. and Zhdanov G.B. (1954) J.E.T.P., 26, 405.

Gottfreid K. (1976) Phys. Rev. Lett., 32, 957.

Greisen K. (1956) Prog. Cosmic Ray Phys., 3, 1.

Greisen K. (1966) Proc. 9th Int. Conf. Cosmic Rays, London, 2, 609.

Grieder P.K.F. (1977) Revista del Nuovo Cimento, 7, 1 and (1977a) Proc. 15th Int. Conf. Cosmic Rays, 8, 326.

Grindlay J. (1974) Harvard College Obsy. and Smithsonian Ast. Obsy., Center for Astrophys. Preprint Series No 150

Guettler K. et al (British-Scandinavian-MIT Collaboration) (1976) Phys. Lett., 64B, 111.

Guzhavin V.V., Ivanenko I.P., Makarov V.V., Roganova T.M. and Fedorova G.F. (1975) Proc. 14th Int. Conf. Cosmic Rays, Munich, 8, 3024.

Hammond R.T., Orford K.J., Shearer J A.L., Turver K.E., Waddoup W.D. and Wellby D.W. (1977) Proc. 15th Int. Conf. Cosmic Rays, Plovdiv, 8, 281.

Hammond R.T., Protheroe R.J., Orford K.J., Shearer J.A.L., Turver K.E., Waddoup W.D. and Wellby D.W. (1977a) Proc. 15th Int. Conf. Cosmic Rays, Plovdiv, 8, 287.

Hara T., Ishikawa F., Kawaguchi S., Miura Y., Nagano M., Suga K. and Tanahashi G. (1969) Proc. 11th Int. Conf. Cosmic Rays, Budapest (Acta. Phys. Acad. Sci. Hung., 29, Suppl. 3, 369 (1970)).

Hess V. (1912) Physik. Zeitschr, 13, 1804.

Hillas A.M. (1966) Proc. 9th Int. Conf. Cosmic Rays, London, 2, 758.

Hillas A.M., Marsden D.J., Hollows J.D. and Hunter H.W. (1971) Proc. 12th Int. Conf. Cosmic Rays, Hobart, 2 1001.

Hillas A.M. (1972) "Cosmic Rays", pub. by Pergamon Press, Oxford and (1975) Phys. Reports, 20C, 59.

Hillas A.M. and Lapikens J. (1977) Proc. 15th Int. Conf. Cosmic Rays, Plovdiv, 8, 460.

Ivanenko I.P., Makarov V.V. and Hein I.A. (1976) Acad. of Sci. of U.S.S.R., P.N Lebedev Phys. Inst., Preprint ref. 98.

Jelley J.V. and Galbraith W. (1953) Phil. Mag., 44, 619 and (1955) J. Atmos. Terrest. Phys., 6, 304.

Jelley J.V. (1968) Prog. in Cosmic Ray Phys., 9, 41.

Kalmykov N.N. and Khristiansen G.B. (1975) Proc. 14th Int. Conf. Cosmic Rays, Munich, 8, 2861.

Kalmykov N.N., Prosin V.V. and Khristiansen G.B. (1975a) Proc. 14th Int. Conf. Cosmic Rays, Munich, 8, 3034.

Kalmykov N.N., Khristiansen G.B., Nechin Yu.A., Prosin V.V., Efimov N.N. and Grigoriev V.M. (1976) paper presented at 5th European Symposium on Cosmic Rays, Leeds, September 1976.

Kalmykov N.N., Khristiansen G.B., Nechin Yu.A., Prosin V.V., Grigoriev V.M. and Efimov N.N. (1977) Proc. 15th Int. Conf. Cosmic Rays, Plovdiv, 8, 244.

Kamata K. et al (Akeno group) (1977) Proc. 15th Int. Conf. Cosmic Rays, Plovdiv, 8, 501.

Kaye G.W.C. and Laby T.H. (1966) "Tables of Physical and Chemical Constants", 13th ed., pub. by Longmans, London.

Kellerman W. (1976) Phys. Bull., June 1976, p. 249.

Khristiansen G.B., Vedeneev O.V., Kulukov G.V. Nazarov V.I. and Solovjeva V.I. (1971) Proc. 12th Int. Conf. Cosmic Rays, Hobart, 6, 2097.

Khristiansen G.B., Kulikov G.V., Lebedev A.P., Silaev A.A., Solovieva V.I., Sirodzev N. and Makhmudov B.M. (1977) Proc. 15th Int. Conf. Cosmic Rays, Plovdiv, 8, 148.

Kolhorster W. (1914) Deutsh. Phys. Gesell. Verh., 16, 719.

Krieger A.S. and Bradt H.V. (1969) Phys. Rev., 185, 1629.

Landau L.D. (1953) Izv. Akad. Nauk. SSSR, 17, 51.

La Pointe M., Kamata K., Gaebler J., Escobar J., Domingo V., Suga K., Murakami K., Toyoda Y. and Shibata S. (1968) Can. J. Phys. 46, S68.

Lattes C.M.G., Occialini G.P.S. and Powell C.F. (1947) Nature, 160, 453.

Leader E. and Maor U. (1973) Phys. Lett., 43B, 505.

Linsley J. (1973) Proc. 13th Int. Conf. Cosmic Rays, Denver, 4, 2506.

Luke D and Soding P. (1971) Springer Tracts in Mod. Phys., 59, 39.

Malos J., Millar D.D. and Wallace C.S. (1962) J. Phys. Soc. Japan, 17, 114, Suppl. A - III.

Marsden D.J. (1971) Ph.D. thesis, University of Leeds.

Mason G.W., Bergeson H.E., Cassiday G L., Chiu T.W., Cooper D.A., Elbert J.W., Loh E.C., Steck D., West W.J., Boone J. and Linsley J. (1977) Proc. 15th Int. Conf. Cosmic Rays, Plovdiv, 8, 252.

Masuda N. (1977) Phys. Rev., D15, 1314.

Messel H., Smirnov A.D., Varfolomeer A.A., Crawford D.F. and Butcher J.C. (1962) Nucl. Phys., 39, 1.

Messel H. and Crawford D.F. (1970) "Electron-photon Shower Distribution Function Tables for Lead, Copper and Air Absorbers", pub. by Pergamon Press, Oxford.

Moffeit K.C., Ballam J., Chadwick G.B., Della-Negra M., Gearhart R., Murray J.J., Seyboth P., Sinclair C.K., Skillicorn I.O., Spitzer H, Wolf G., Bingham H.H., Fretter W.B., Podolsky W.J., Rabin M.S., Rosenfeld A.H., Windmolders R., Yost G.P. and Milburn R.H. (1972) Phys. Rev., D5, 1603.

Morrison D.R.O. (1973) Proc. Roy. Soc., A335, 461.

Nash T. (1977) ref. FERMILAB-Conf-77/61-EXP 2021.000.

Neddermeyer S.H. and Anderson C.D. (1937) Phys. Rev., 51, 884.

Nishimura J. (1967) Handbuch der Physik, Vol. XLVI/2, 1. (Springer-Verlag, Berlin)

Olejniczak J., Wdowczyk J. and Wolfendale A.W. (1977) J.Phys. G, 3, 847.

Olejniczak J., Wdowczyk J. and Zujewska E. (1977a) Proc. 15th Int. Conf. Cosmic Rays, Plovdiv, 8, 393.

Orford K.J. and Turver K.E (1976) Nature, 264, 727.

Orth C.D., Buffington A., Mast T.S. and Smoot G.F. (1977) Phys. Rev Lett., in the press.

Porter L.G., Earnshaw J.C., Tielsch-Cassel E., Ahlstrom J.C. and Greisen K. (1970) Nucl. Instrum. Methods, 87, 87.

Protheroe R.J., Smith G.J. and Turver K.E. (1975) Proc. 14th Int. Conf. Cosmic Rays, Munich, 8, 3008.

Protheroe R.J. and Turver K.E. (1977) Proc. 15th Int. Conf. Cosmic Rays, Plovdiv, 8, 275.

Richards J.A. and Nordheim L.W. (1948) Phys. Rev., 74, 1106.

Rieke G. (1969) Proc. 11th Int. Conf. Cosmic Rays, Budapest (Acta. Phys. Acad. Sci. Hung., 29, Suppl. 3, 601 (1970))

Roberg J. and Nordheim L.W. (1949) Phys. Rev., 75, 444.

Rossi B. (1932) Naturwiss, 20, 65 and (1933) Zeits f. Phys., 82, 151.

Rossi B., Hilberry N. and Hoag J.B. (1940) Phys. Rev., 57, 461.

Rossi B. and Greisen K. (1941) Rev. Mod. Phys., 13, 240.

Rossi B. and Nereson N. (1942) Phys. Rev., 62, 417.

Rossi B. (1952) "High Energy Particles", pub. by Prentice-Hall Inc., New York.

Sitte K. (1962) Nuovo Cimento, 24, 86 and (1969) Proc. 11th Int. Conf. Cosmic Rays, Budapest (Acta Phys. Acad. Sci. Hung., 29, Suppl.3, 389 (1970)).

Skobelzyn D. (1927) Zeits. f. Phys., 43, 371.

Smith G.J. and Turver K.E. (1973) J. Phys. A, 6, L121.

Snyder H.S. (1949) Phys. Rev., 76, 1563.

Staubert R., Trumper J., Wiedecke L, Wolter W., Bohm E., Fritze R., Mie F. and Samorski M. (1969) Proc. 11th Int. Conf. Cosmic Rays, Budapest (Acta Phys. Acad. Sci. Hung., 29, Suppl. 3, 661 (1970)).

Sternheimer R.M. (1959) Phys. Rev., 115, 137.

Stuart R.B. (1976) Ph.D. thesis, University of Nottingham.

Swanson W.P., Davier M., Derado I., Fries D.C., Liu F.F., Mozley R.F., Odian A.C., Park J., Villa F. and Yount D.E. (1971) Phys. Rev. Lett., 27, 1472.

Tanahashi G., Goorevich L., Horton L., McCusker C.B.A., Rapp P. and Winn M.M. (1975) Proc. 14th Int. Conf. Cosmic Rays, Munich, 8, 3058.

Tennent R.M. (1967) Proc. Phys. Soc., 92, 622.

Tomaszewski A. and Wdowczyk J. (1975) Proc. 14th Int. Conf. Cosmic Rays, Munich, 8, 2899.

Towers L. (1971) Ph.D. thesis, University of Leeds.

Trilling G.H. (1974) Proc. 9th Rencontre de Moriond, 1, 423.

Turver K.E. (1975) Proc. 14th Int. Conf. Cosmic Rays, Munich, 8, 2851.

Vernov S.N., Khristiansen G.B., Abrosimov A.T., Kalmykov N.N., Kulikov G V., Solovieva V.I., Fomin Yu.A. and Khrenov B.A. (1977) Proc. 15th Int. Conf. Cosmic Rays, Plovdiv, 8, 320.

Wdowczyk J. and Wolfendale A.W. (1972) Nature, 236, 29 and (1973) J. Phys. A, 6, 1594.

Wdowczyk J. (1975) Proc. 14th Int. Conf. Cosmic Rays, Munich, 11, 4002.

Weise W. (1974) Phys. Reports, 13, 53.

Whitmore J. (1976) Phys. Reports, 27C, 188.

Williams E.J. (1939) Proc. Roy. Soc., A169, 531. and (1940) Phys. Rev., 58, 292.

Williams E.J. and Roberts G.E. (1940) Nature, 145, 102.

Wilson C.T.R. (1901) Proc. Roy. Soc., 68, 151.

Wilson K.G. (1963) Acta. Phys. Austr., 17, 37.

Wolfendale A.W. (1975) in "The Origin of Cosmic Radiation", p.1, ed. by J.L. Osborne and A.W. Wolfendale, pub. by D.Reidel, Dordrecht-Holland.

Yodh G.B., Pal Y. and Trefil J.S. (1972) Phys. Rev. Lett., 28, 1005.

Zatsepin V.I. and Chudakov A.E. (1962) Soviet Phys., J.E.T.P., 15, 1126.

ACKNOWLEDGEMENTS

I thank Professor A.W. Wolfendale F.R.S. for provision of the facilities of the Physics Department of the University of Durham and for his encouragement throughout the course of this work. I am also indebted to my supervisor, Dr.K.E.Turver for his continual encouragement and advice.

I am very grateful to the director and staff of the Bartol Research Foundation of the Franklin Institute, and particularly to Dr.T.K.Gaisser, for their hospitality during my visit to Swarthmore, Pennsylvania in July and August of 1976. Dr.Gaisser is also thanked for much encouragement, many stimulating discussions and for reading chapter 2 of this thesis.

I thank my colleagues David Wellby, Ian Gibson David Waddoup, Rick Hammond, Andy Shearer and Lowry McComb for their friendship and for many useful discussions. Lowry McComb is also thanked for pointing out some consequences of photomeson production and for assistance with some of the computing.

The staff of the Computer Unit of the University of Durham are thanked for the provision of computing facilities and for programming advice. The Science Research Council is thanked for providing a Research Studenship.

Finally, I thank Mrs.C.G.Rowes for her careful typing of this thesis.

12 MAR 1978
SECTION LIBRARY